

Nonclassical Excitation and Quantum Interference in a Three Level Atom

Thesis by

Nikos Photakis Georgiades

In Partial Fulfillment of the Requirements

for the Degree of

Doctor of Philosophy

California Institute of Technology

Pasadena, California

1998

(Submitted December 1, 1997)

© 1998

Nikos Photakis Georgiades

All Rights Reserved

Acknowledgements

A person hardly ever walks the path of learning alone. To complete my Ph.D. in Physics was a dream and a goal inspired more than fifteen years ago while I was still at high school learning my first physics from an excellent teacher, Ms. Georgia Stylianou, who not only encouraged but also promoted my interests in science. Alongside with my high school teacher, at the dawn of my scientific awakening, the fascinating TV series Cosmos by Prof. Carl Sagan triggered my curiosity and brought my young and unshaped mind in front of the amazing wonders of the universe. Since then many wonderful teachers have taken me under their wings and taught me science. Among the most prominent of them were some of my college professors at the University of Pennsylvania to whom I would like to give special thanks: Prof. Rex Rivolo, Prof. Borris Lerner, Prof. Paul Soven and Prof. Fay Ajzenberg-Selove. My undergraduate research advisor Prof. Argun G. Yodh needs special mention since he was the one who introduced me to the world of scientific research and guided my first steps through a “real” scientific project. However, I would not have been able to write this thesis if it were not for one more teacher of mine, a professor at Caltech, with whom I spent the last six years developing my scientific skill and personality. This professor is, of course, none other than my research advisor Prof. H. Jeff Kimble. From Professor Kimble not only did I learn physics, but I also learned about scientific integrity, about being a hard and fair judge, about being competitive and the meaning of being a “good scientist.” Prof. Kimble has been to me a teacher, a raw model, a guide and a friend. For all that he has offered me, I would like to express to him my gratitude, appreciation and very special thanks. In addition to my advisor, of extreme importance to my graduate school career was our entire research group that often felt as an extended family within which I could seek help, recognition and comfort. My “lab mentor” (now a professor at Aarhus University in Denmark), Prof. Eugene Polzik, I need to mention and thank separately for all the things he has taught me and the trust he

has put into me. In addition, I must thank a whole army of other people that passed through our labs during my years at Caltech and who deserve special mention too. Here, with apologies to all not mentioned, I will only list a few: Dr. Sylvania Pereira, Dr. Rob Thompson, Dr. Quentin Turchette, Hideo Mabuchi, Christina Hood, David Vernooy, Dr. Scott Parkins, Dr. Mike Chapman, Prof. Ken Librecht, Dr. Phill Williams and Dr. Keichi Edamatsu. I also want to thank my fiancé Christina Bender for her love, support and encouragement. Alongside her, numerous friends helped me throughout the years to feel needed and loved. They, too, played a very important role in helping me reach my goal. The most important people in my life I left to thank last. These are none other than my family. My father Photakis, who unfortunately did not live to see me completing my goal, but who took an enormous pride knowing that one day I will get my Ph.D. My mother Ute who loves me and struggles to do everything possible for me, and my brothers Akis and Paul. Especially to my Father and my Mother, I would like to dedicate with all my love this thesis as a very small token of appreciation for all that they have done for me.

Abstract

Non-classical properties and quantum interference (QI) in two-photon excitation of a three level atom ($|1\rangle$, $|2\rangle$, $|3\rangle$) in a ladder configuration, illuminated by multiple fields in non-classical (squeezed) and/or classical (coherent) states, is studied. Fundamentally new effects associated with quantum correlations in the squeezed fields and QI due to multiple excitation pathways have been observed. Theoretical studies and extrapolations of these findings have revealed possible applications which are far beyond any current capabilities, including ultrafast nonlinear mixing, ultrafast homodyne detection and frequency metrology. The atom used throughout the experiments was Cesium, which was magneto-optically trapped in a vapor cell to produce a Doppler-free sample. For the first part of the work the $|1\rangle \rightarrow |2\rangle \rightarrow |3\rangle$ transition (corresponding to the $6S_{1/2}F = 4 \rightarrow 6P_{3/2}F' = 5 \rightarrow 6D_{5/2}F'' = 6$ transition) was excited by using the quantum-correlated signal (\mathcal{E}_s) and idler (\mathcal{E}_i) output fields of a subthreshold non-degenerate optical parametric oscillator, which was tuned so that the signal and idler fields were resonant with the $|1\rangle \rightarrow |2\rangle$ and $|2\rangle \rightarrow |3\rangle$ transitions, respectively. In contrast to excitation with classical fields for which the excitation rate as a function of intensity has always an exponent greater than or equal to two, excitation with squeezed-fields has been theoretically predicted to have an exponent that approaches unity for small enough intensities. This was verified experimentally by probing the exponent down to a slope of 1.3, demonstrating for the first time a purely non-classical effect associated with the interaction of squeezed fields and atoms. In the second part excitation of the two-photon transition by three phase coherent fields \mathcal{E}_1 , \mathcal{E}_2 and \mathcal{E}_0 , resonant with the dipole $|1\rangle \rightarrow |2\rangle$ and $|2\rangle \rightarrow |3\rangle$ and quadrupole $|1\rangle \rightarrow |3\rangle$ transitions, respectively, is studied. QI in the excited state population is observed due to two alternative excitation pathways. This is equivalent to nonlinear mixing of the three excitation fields by the atom. Realizing that in the experiment the three fields are spaced in frequency over a range of 25 THz, and extending this

scheme to other energy triplets and atoms, leads to the discovery that ranges up to 100's of THz can be bridged in a single mixing step. Motivated by these results, a master equation model has been developed for the system and its properties have been extensively studied.

Contents

| | |
|---|------------|
| Acknowledgements | iii |
| Abstract | v |
| 1 Introduction | 1 |
| 1.1 The Three “ <i>Eras</i> ” of my Research | 2 |
| 1.2 Three-Level Energy Submanifold in Cs ¹³³ | 4 |
| 1.3 Basic Experimental Concepts | 5 |
| 1.3.1 Magneto-Optical Trap | 6 |
| 1.3.2 High Precision Spectroscopy of the $6D_{5/2}$ State in Cs ¹³³ | 6 |
| 1.3.3 Optical Parametric Oscillator | 8 |
| 1.4 Squeezed Light and Atoms | 10 |
| 1.4.1 Two-Photon Excitation Rate with Nonclassical Fields: Theory and Experiment | 10 |
| 1.4.2 Linear Two-Photon Excitation Rate with Nonclassical Fields: Analysis, Statistics and Results | 14 |
| 1.5 Quantum Interference | 15 |
| 1.5.1 Multiple Field Two-Photon Excitation and Quantum Interference | 16 |
| 1.5.2 Ultrafast Homodyne Detection | 17 |
| 1.5.3 Atoms as Ultrafast Nonlinear Mixers | 18 |
| 1.6 Summary | 19 |
| | |
| I BASIC EXPERIMENTAL CONCEPTS | 20 |
| | |
| 2 Magneto-Optical Trap | 21 |
| 2.1 Geometry | 21 |

| | | |
|----------|---|-----------|
| 2.2 | Trapping Beams | 23 |
| 2.3 | Magnetic Fields | 24 |
| 2.4 | Alignment | 25 |
| 2.4.1 | MOT Alignment | 25 |
| 2.4.2 | Excitation Fields | 26 |
| 2.4.3 | Imaging | 27 |
| 2.5 | Summary | 28 |
| 3 | High Precision Spectroscopy of the $6D_{5/2}$ State in Cs | 29 |
| 3.1 | Two-Photon Spectroscopy in a MOT vs. in a Vapor Cell | 30 |
| 3.2 | Experimental Setup | 34 |
| 3.2.1 | Locking and Scanning (Block I) | 34 |
| 3.2.2 | Detection and Data Acquisition (Block IV) | 37 |
| 3.3 | Theory of hf Structure for the $6D_{5/2}$ State | 39 |
| 3.4 | Results | 40 |
| 3.4.1 | The a and b Coefficients | 42 |
| 3.4.2 | Linewidths | 43 |
| 3.4.3 | AC Stark Shift of the Ground State | 44 |
| 3.4.4 | “Cross-Talk” between hf States | 45 |
| 3.5 | Summary | 47 |
| 4 | Optical Parametric Oscillator | 48 |
| 4.1 | OPO Configuration | 49 |
| 4.1.1 | Cavity Elements | 49 |
| 4.1.2 | Beam Paths | 51 |
| 4.1.3 | OPO Locking | 52 |
| 4.1.4 | Triangular Cavity | 52 |
| 4.2 | Degenerate Operation | 54 |
| 4.2.1 | Phase-Sensitive Gain | 54 |
| 4.2.2 | Squeezing Spectra | 59 |
| 4.2.3 | Summary of the DOPO Results | 64 |

| | | |
|--|--|---------------|
| 4.3 | Non-Degenerate Operation | 65 |
| 4.3.1 | Operation | 66 |
| 4.3.2 | Performance | 68 |
| 4.4 | Summary | 72 |
| II SQUEEZED LIGHT AND ATOMS | | 74 |
| 5 | Two-Photon Excitation Rate with Nonclassical Fields: Theory and Experiment | 75 |
| 5.1 | Theory | 76 |
| 5.1.1 | “Simple” Theory | 76 |
| 5.1.2 | “Full” Theory | 79 |
| 5.1.3 | Classical versus Nonclassical Effects | 80 |
| 5.2 | Experiment | 83 |
| 5.2.1 | Setup | 83 |
| 5.2.2 | ON/OFF Protocol | 84 |
| 5.2.3 | Background | 86 |
| 5.2.4 | Data | 87 |
| 5.2.5 | Control Experiment | 90 |
| 5.3 | Summary | 92 |
| 6 | Two-Photon Excitation Rate with Nonclassical Fields: Analysis, Statistics and Results | 94 |
| 6.1 | Statistical Analysis Part I: Functional Form of R_2 vs. R_1 | 94 |
| 6.1.1 | Fitting Procedure | 94 |
| 6.1.2 | The \bar{S} statistic | 98 |
| 6.1.3 | The \bar{C} statistic | 99 |
| 6.1.4 | f_Q vs f_{Q+L} | 100 |
| 6.2 | Statistical Analysis Part II: The G factor | 101 |
| 6.3 | “Knee” Position | 105 |

| | | |
|---------------------------------|---|------------|
| 6.4 | Combining all Data | 109 |
| 6.5 | Summary | 113 |
| III QUANTUM INTERFERENCE | | 114 |
| 7 | Multiple-Field, Two-Photon Excitation and Quantum Interference | 115 |
| 7.1 | The 3-level Atom and Excitation Scheme | 117 |
| 7.2 | Perturbative Analysis | 119 |
| 7.2.1 | Equation of Motion | 119 |
| 7.2.2 | Solution for ρ_{33} and QI | 121 |
| 7.3 | “Full” Theory | 124 |
| 7.3.1 | Hamiltonian Formalism | 124 |
| 7.3.2 | Equation of Motion | 126 |
| 7.3.3 | Solution | 128 |
| 7.4 | QuInC | 131 |
| 7.5 | Experiment | 132 |
| 7.6 | Multiphoton Excitations | 136 |
| 7.7 | Internal State Correlations | 137 |
| 7.8 | Summary | 139 |
| 8 | Ultrafast Homodyne Detection | 140 |
| 8.1 | Theory | 144 |
| 8.1.1 | Excitation Field | 144 |
| 8.1.2 | Hamiltonian Formulation and Master Equation | 145 |
| 8.1.3 | Equations of Motion | 148 |
| 8.1.4 | Solution for the Atomic Populations | 149 |
| 8.2 | Experiment | 152 |
| 8.3 | Summary | 156 |
| 9 | Atoms as Ultrafast Nonlinear Mixers | 157 |
| 9.1 | Characterization of Atomic Nonlinear Mixers | 158 |

| | | |
|-----------|--|------------|
| 9.1.1 | ANM Frequency Response with Fixed Excitation Power | 159 |
| 9.1.2 | ANM Frequency Response with Variable Excitation Power | 162 |
| 9.2 | Database of Atomic Nonlinear Mixers | 163 |
| 9.3 | Frequency Metrology | 165 |
| 9.4 | Optical Communication | 168 |
| 9.5 | Summary | 169 |
| 10 | Epilogue | 170 |
| A | OPO Gain for the Single and Double-Sided Cavity | 173 |
| A.1 | Degenerate OPO (DOPO) | 173 |
| A.1.1 | Probe Injected Through M_1 | 176 |
| A.1.2 | Probe Injected Through M_{out} | 176 |
| A.2 | Non-Degenerate OPO (NDOPO) | 177 |
| A.2.1 | Probe Injected Through M_1 | 180 |
| A.2.2 | Probe Injected Through M_{out} | 180 |
| A.3 | Summary | 181 |
| B | Nonclassical Two-Photon Experiment: Data Plots, Fits and Fit Parameters | 182 |
| B.1 | Exp. 11-17-94 (Nonclassical Excitation) | 183 |
| B.2 | Exp. 11-29-94 (Nonclassical Excitation) | 184 |
| B.3 | Exp. 12-06-94 (Nonclassical Excitation) | 185 |
| B.4 | Exp. 12-20-94a (Nonclassical Excitation) | 186 |
| B.5 | Exp. 12-20-94b (Nonclassical Excitation) | 187 |
| B.6 | Exp. 12-22-94 (Coherent Excitation) | 188 |
| B.7 | Exp. 01-12-95 (Coherent Excitation) | 189 |
| C | Results from Numerical Integration of the Master Equation for the Nonclassical Two-Photon Excitation Experiment | 190 |
| C.1 | Master Equation | 190 |
| C.2 | Parameters and Notation | 191 |

| | |
|--|------------|
| C.3 Results | 193 |
| C.4 “Knee Position” | 195 |
| D Effect of Detunings on the “Knee” Position in the Nonclassical Two-Photon Excitation Experiment | 199 |
| Bibliography | 201 |

List of Figures

| | | |
|-----|---|----|
| 1.1 | A three-level system is realized by considering an “ <i>isolated</i> ” energy submanifold of an alkali atom. | 2 |
| 1.2 | The three-level energy submanifold in atomic Cesium which was used in our experiments. | 5 |
| 1.3 | MOT setup: five trapping beams, T_1, \dots, T_5 , and one repumping beam are responsible for cooling the atoms. A pair of coils with antiparallel currents, I , produce a magnetic field gradient which in concert with the light force confine the atoms in a localized region in space. | 7 |
| 1.4 | NDOPO setup for producing nonclassical light. | 9 |
| 1.5 | Interaction of atoms with classical and squeezed vacuum, shown as circles and ellipses, respectively. | 11 |
| 1.6 | (a) Classical and (b) quantum excitation of a two-photon transition. | 12 |
| 1.7 | Experimental observation of two-photon excitation with (a) quantum correlated and (b) classical fields. The units of the counting rates, $R_2^{Squeezed}$ and $R_2^{Coherent}$, are detected <i>photons/sec</i> . The solid lines are fits to the data of the form of Eqs.(1.3) and (1.4), while the dotted lines are the linear and quadratic components plotted separately for the fit to the non-classical data. The $x - axis$ is a measure of the intensity in arbitrary units. | 15 |
| 1.8 | Excitation of a two-photon transition by three phase-coherent lasers leads to quantum interference. | 16 |
| 2.1 | The $xy - plane$ geometry of the MOT. | 22 |
| 2.2 | Imaging of the trap. A one-to-one telescope collects light from the MOT and refocuses it onto the APD. | 26 |

| | | |
|-----|--|----|
| 3.1 | Doppler free spectroscopy: (a) using counter propagating beams in a vapor cell, (b) using co-propagating beams in a MOT. | 31 |
| 3.2 | Focusing geometry of the excitation beam. Notice that the volume of excited atoms that is imaged may be smaller than the diameter of the trap. | 32 |
| 3.3 | Experimental setup. | 35 |
| 3.4 | Hyperfine structure of atomic Cs^{133} | 41 |
| 3.5 | Hyperfine spectrum of the $6D_{5/2}$ state in Cs^{133} | 42 |
| 3.6 | Linewidth of the hf components of the $6D_{5/2}$ state as a function of power of the excitation beam. | 43 |
| 3.7 | Two-photon excitation spectra, which show Stark shifts and power broadening due to perturbation of the ground state by the trapping beams. a) Trapping beams are OFF, b) Trapping beams ON, total power $P_T^{(b)} \sim 3.1 \text{ mW}$, c) Trapping beams ON, total power $P_T^{(c)} \sim 10.4 \text{ mW}$. The power of the 884 nm , two-photon excitation beam, is 3.3 mW in each case. | 45 |
| 3.8 | Cross-talk m as a function of the probe frequency ω ($\omega = 0$ is the resonant frequency with the $F'' = 6$ state). | 47 |
| 4.1 | A basic OPO consists of a non-linear crystal, $\chi^{(2)}$ inside an optical cavity. The OPO is pumped by a laser at frequency ω_p and generates a signal and idler output at frequencies ω_s and ω_i , respectively. | 49 |
| 4.2 | OPO geometry. | 50 |
| 4.3 | Experimental setup to generate squeezed light. | 53 |
| 4.4 | Phase-sensitive gain of a coherent beam transmitted through the DOPO. | 55 |
| 4.5 | OPO gain G_+ vs. the dimensionless pumping parameter x^2 . The solid line is the theoretical prediction ($G_+ = (1 - x)^{-2}$) with no free parameters. | 56 |

| | | |
|------|--|----|
| 4.6 | OPO gain G_- vs. the dimensionless pumping parameter x^2 . The solid line is the theoretical prediction ($G_- = (1 + x)^{-2}$) with no free parameters. | 57 |
| 4.7 | The product G_+G_- versus the dimensionless pumping parameter x^2 . The solid line is the theoretical prediction $G_+G_- = (1 - x^2)^{-2}$ | 58 |
| 4.8 | OPO amplification gain G_+ versus deamplification G_- for all measurements. The solid line is the theoretical prediction $G_+ = G_- (2\sqrt{G_-} - 1)^{-2}$ | 59 |
| 4.9 | Balanced homodyne detector. | 61 |
| 4.10 | A typical spectrum of squeezing. | 62 |
| 4.11 | The squeezed ($\Delta X_- = 1 + S_-$) versus the antisqueezed ($\Delta X_+ = 1 + S_+$) quadratures of the OPO output. The solid line is the minimum uncertainty relation $\Delta X_+ \Delta X_- = 1$ | 64 |
| 4.12 | The squeezed ($\Delta X_- = 1 + S_-$) versus the antisqueezed ($\Delta X_+ = 1 + S_+$) quadratures of the OPO output calculated taking into account an extra efficiency factor ζ_x . The solid line is the minimum uncertainty relation $\Delta X_+ \Delta X_- = 1$ | 65 |
| 4.13 | Schematic representation of double resonance in the NDOPO. The vertical lines denote longitudinal modes of the OPO cavity for the two wavelengths λ_s (solid lines) and λ_i (dotted lines), which are separated by λ_s and λ_i , respectively. As the cavity length is changed, the resonances of the two wavelengths move relative to each other until they coincide and to produce another double resonance. | 67 |
| 4.14 | When the OPO cavity is doubly resonant with the injected ω_{852} and conjugate $\omega_{442} - \omega_{852}$ frequencies, there is amplification of the injected beam. | 68 |
| 4.15 | Sequence of measurements to determine the OPO gain: (a) no-gain measurement of the transmitted power V_o ; (b) combined power of the amplified 852 nm and generated 917 nm beams, $V_{852+917}$; (c) amplified power of the injected beam at 852 nm alone, V_{852} ; (d) generated power of the idler beam at 917 nm alone, V_{917} | 69 |

- 4.16 Plot of the gain measurements of the idler beam $G_{917}^{\text{exp}1}$ versus $G_{917}^{\text{exp}2}$, which were determined by two independent methods. For the data to be consistent, they must fall on the diagonal $G_{917}^{\text{exp}1} = G_{917}^{\text{exp}2}$ 71
- 4.17 Idler gain G_{917}^{exp} versus signal gain G_{852}^{exp} . The solid line is the theoretical prediction for the relation of the two, namely $G_{917}^{\text{exp}} = G_{852}^{\text{exp}} \left(1 - \frac{1}{\sqrt{G_{852}^{\text{exp}}}} \right)$. 72
- 5.1 Two-photon excitation by non-classical fields: a three-level atom $\{|1\rangle, |2\rangle, |3\rangle\}$ is illuminated by the signal and idler (ω_s, ω_i) output beams from an NDOPO, and they are near resonance with the $|1\rangle \rightarrow |2\rangle$ and $|2\rangle \rightarrow |3\rangle$ transitions, respectively $(\omega_s \simeq \omega_{12}$ and $\omega_i \simeq \omega_{23})$ 75
- 5.2 The output field E_{out} of the OPO is related to the input state E_{in} via the transformation $E_{out} = \mu E_{in} + \nu E_{in}^\dagger$ 77
- 5.3 Quadrature space of the squeezed states of the electromagnetic field. Curve (i) indicates minimum uncertainty states which satisfy $\Delta X_- \Delta X_+ = 1$. Curve (ii) corresponds to thermal states for which $\Delta X_- = \Delta X_+ > 1$. Curves (iii) and (iv) are for states with $\Delta X_+ = 1$ and $\Delta X_- = 1$, respectively. States in region (a) are forbidden by the uncertainty relation. States in region (b) are quantum squeezed states characterized by the fact that either $\Delta X_+ < 1$ or $\Delta X_- < 1$. States in region (c) are classically squeezed states with both $\Delta X_+ \geq 1$ and $\Delta X_- \geq 1$ and also with unequal quadratures $\Delta X_- \neq \Delta X_+$. The special state $\Delta X_- = \Delta X_+ = 1$ corresponds to the electromagnetic vacuum. 82
- 5.4 Experimental setup for two-photon excitation with non-classical fields. 83
- 5.5 a) With the trapping beams turned ON, the rate R_1 is proportional to the intensity of the idler field. b) When the trapping beams are turned OFF, the rate R_2 is proportional to the two-photon excitation rate by the signal and idler beams from the NDOPO. 85
- 5.6 Gating of the photon counter. Gate A corresponds to the OFF and Gate B to the ON phases of the experiment. 88

| | | |
|-----|--|-----|
| 5.7 | Setup for generating two coherent beams at 852 <i>nm</i> and 917 <i>nm</i> in resonance with the $6S_{1/2}F = 4 \rightarrow 6P_{3/2}F' = 5$ and $6P_{3/2}F' = 5 \rightarrow 6D_{5/2}F'' = 6$ transitions, respectively. | 92 |
| 6.1 | R_2 versus R_1 from the nonclassical two-photon excitation experiment of 12/20/94-b. The solid line is a quadratic plus linear fit (f_{Q+L}) and the dotted line is a quadratic fit (f_Q). | 102 |
| 6.2 | R_2 versus R_1 from the two-photon classical excitation experiment of 12/22/94. The solid line is a quadratic fit (f_Q) to the data. | 103 |
| 6.3 | One photon counting rate R_1 versus the OPO gain G_{852} from the data of 11/29/94. The solid line is a fit of the form $R_1 = \alpha_1 (\sqrt{G_{852}} - 1)$ | 104 |
| 6.4 | Two-photon counting rate R_2 versus the OPO gain G_{852} from the data of 11/29/94. The solid line is a fit of the form $R_2 = \alpha_2 (\sqrt{G_{852}} - 1) + \alpha_3 (\sqrt{G_{852}} - 1)^2$. The dashed lines shows the quadratic fit of the form $R_2 = \alpha'_3 (\sqrt{G_{852}} - 1)^2$ | 105 |
| 6.5 | Gain at the knee position G_s^{knee} for the non-classical excitation experiments. The solid line at $G = 1.33$ is the prediction from the full theory and is approximately the same as the value predicted from the theory of Ficek and Drummond. The solid line at $G = 1.41$ is the average of the experimental values and the two dotted lines symmetrically around it are the 1σ error bars. | 108 |
| 6.6 | Excited state population ρ_{33} due to nonclassical two-photon excitation as a function of OPO output intensity expressed in terms of the intracavity photon number for the idler field, n_{917} . The solid line is the full theory and the dotted lines are the linear and quadratic asymptotes to the theory. The data points are the normalized data from the five experiments. | 110 |
| 6.7 | Residuals of the normalized data (a) relative to the quadratic and (b) relative to the linear asymptotes to the theory. | 111 |

| | | |
|-----|---|-----|
| 7.1 | The two-photon transition $ 1\rangle \rightarrow 3\rangle$ is excited by three fields via two alternative excitation pathways, which lead to QI. | 116 |
| 7.2 | Quantum Interference Calculator (QuInC) is available on the WWW at http://www.cco.caltech.edu/~qoptics/QIHome/QuInC/QuInC.html | 131 |
| 7.3 | Setup for the QI experiment. | 133 |
| 7.4 | Fluorescence from the $6D_{5/2}F'' = 6 \rightarrow 6P_{3/2}F' = 5$ transition as a function of time for excitation of the atoms in the MOT by a combination of three coherent beams with corresponding wavelengths 852 nm , 917 nm and 884 nm . The phase of the 884 nm beam is modulated with a PZT at a frequency $\frac{\omega_m}{2\pi} \simeq 11\text{ Hz}$ | 134 |
| 7.5 | Multiphoton excitation with multiple lasers $\{\omega_1, \omega_2, \dots, \omega_k\}$. Several excitation paths $\{\mathbf{X}_1, \mathbf{X}_2, \dots, \mathbf{X}_m\}$ contribute to the overall excited state population ρ_{nn} , resulting in QI. | 136 |
| 7.6 | Atomic state populations ρ_{11} , ρ_{22} and ρ_{33} as functions of the phase Θ , calculated from the full theory model using $\alpha = \sqrt{\frac{3}{15}}$, $\delta_1 = -\frac{30}{\sqrt{45}}$, $\delta_2 = -\frac{10}{\sqrt{45}}$, $\delta_0 = \frac{\delta_1 + \delta_2}{2}$ and $\Omega_1 = \Omega_2 = Q_o = 2$ | 138 |
| 8.1 | Two-photon excitation by a combination of a coherent RO field with frequency ω_o , in resonance with the two-photon $ 1\rangle \rightarrow 3\rangle$ transition, and the signal and idler outputs of an NDOPO at frequencies ω_s and ω_i in resonance with the dipole $ 1\rangle \rightarrow 2\rangle$ and $ 2\rangle \rightarrow 3\rangle$ transitions, respectively. | 141 |
| 8.2 | a) Homodyne detection of squeezing. b) Detection of nonclassical correlations with QI where an atom is utilized as a nonlinear mixer. . . | 142 |
| 8.3 | Experimental setup for observation of QI with squeezed light. . . . | 153 |
| 8.4 | Power spectrum $R(f)$ of the photocounting time series I_F . a) Control spectrum with the squeezing turned off for which no modulation at either ω_m or $2\omega_m$ is observed; b) spectrum with the squeezing on for which a peak at frequency $2\omega_m$ appears. | 155 |

| | | |
|-----|---|-----|
| 9.1 | A three level atom acting as a nonlinear mixer. Three input fields at frequencies ω_1 , ω_2 and ω_3 are “mixed” to result in a “demodulated” output signal. | 158 |
| 9.2 | Frequency response of ρ in (a), (b) and (c) and \mathcal{V} in (d), (e) and (f) as functions of the detuning δ . Solid lines are for $\delta_1 = \delta$, $\delta_2 = 0$, $\delta_0 = 0$; dotted lines are for $\delta_1 = 0$, $\delta_2 = \delta$, $\delta_0 = 0$; dashed lines are for $\delta_1 = 0$, $\delta_2 = 0$, $\delta_0 = \delta$. The value of $\alpha = \sqrt{\frac{\gamma_2}{\gamma_3}}$ is for (a) and (d) $\alpha = \sqrt{\frac{1}{10}}$, for (b) and (e) $\alpha = \sqrt{\frac{5}{3}}$ and for (c) and (f) $\alpha = \sqrt{\frac{10}{1}}$. Note that δ is in units of $\gamma = \sqrt{\gamma_2\gamma_3}$ | 160 |
| 9.3 | Full width at half maximum $\Delta_{FWHM}^{(i)}$, $i = 0, 1, 2$ for the visibility \mathcal{V} as a function of $\alpha = \sqrt{\frac{\gamma_2}{\gamma_3}}$. Note that $\Delta_{FWHM}^{(i)}$ is in units of $\gamma = \sqrt{\gamma_2\gamma_3}$ | 162 |
| 9.4 | From the three possible two-photon excitation schemes, Ξ , V and Λ , only the first one is considered here. The other two also exhibit QI and could be also used as nonlinear mixers. | 164 |
| 9.5 | ANM characteristics for the sideband-to-carrier separation Δf versus the carrier wavelength λ_c for the database of 6900 transitions in the alkali elements. The circled point corresponds to the experimental demonstration with $\lambda_c \simeq 884 \text{ nm}$ and $\Delta f \simeq 12.5 \text{ THz}$ | 166 |
| 9.6 | By frequency sum and difference generation and harmonic conversion ($\omega_i \pm \omega_j$), an initial set of reference frequencies Ω_o together with the target frequency ω_t results after k stages of nonlinear transformations into a new set of frequencies Ω_k . From Ω_k the three “best” frequencies $\{\omega_a, \omega_b, \omega_c\}$ for the particular application are chosen. | 167 |
| A.1 | DOPO configuration. | 174 |
| A.2 | NDOPO configuration. | 178 |
| B.1 | a) R_2 vs. R_1 data from the 11-17-94 experiment. The solid line is the best linear plus quadratic fit and the dashed line the best quadratic fit. b) Quadratic plus linear residual, define in Eq. (B.1) c) Quadratic residual, defined in Eq. (B.2) | 183 |

- B.2 a) R_2 vs. R_1 data from the 11-29-94 experiment. The solid line is the best linear plus quadratic fit and the dashed line the best quadratic fit. b) Quadratic plus linear residual, define in Eq. (B.1) c) Quadratic residual, defined in Eq. (B.2) 184
- B.3 a) R_2 vs. R_1 data from the 12-06-94 experiment. The solid line is the best linear plus quadratic fit and the dashed line the best quadratic fit. b) Quadratic plus linear residual, define in Eq. (B.1) c) Quadratic residual, defined in Eq. (B.2) 185
- B.4 a) R_2 vs. R_1 data from the 12-20-94a experiment. The solid line is the best linear plus quadratic fit and the dashed line the best quadratic fit. b) Quadratic plus linear residual, define in Eq. (B.1) c) Quadratic residual, defined in Eq. (B.2) 186
- B.5 a) R_2 vs. R_1 data from the 12-20-94b experiment. The solid line is the best linear plus quadratic fit and the dashed line the best quadratic fit. b) Quadratic plus linear residual, define in Eq. (B.1) c) Quadratic residual, defined in Eq. (B.2) 187
- B.6 a) R_2 vs. R_1 data from the 12-22-94 experiment. The solid line is the best linear plus quadratic fit and the dashed line the best quadratic fit. b) Quadratic plus linear residual, define in Eq. (B.1) c) Quadratic residual, defined in Eq. (B.2) 188
- B.7 a) R_2 vs. R_1 data from the 01-12-95 experiment. The solid line is the best linear plus quadratic fit and the dashed line the best quadratic fit. b) Quadratic plus linear residual, define in Eq. (B.1) c) Quadratic residual, defined in Eq. (B.2) 189

- C.1 a) Circles: Excited state population ρ_{33} as a function of the intracavity photon number of the idler mode n_b from numerical integration of the master equation by A. S. Parkins. b) Solid line: “Phenomenological” fit to the numerical data of the form $\rho_{33}^{(1)} = \alpha n_b + \beta n_b^2 \left(1 - \gamma e^{-\frac{n_b}{\delta}}\right)$. c) Dashed line: Best linear plus quadratic fit to the numerical data of the form $\rho_{33}^{(2)} = \alpha' n_b + \beta' n_b^2$. d) Insert: Ratio of the two fits shown in (b) and (c), $\frac{\rho_{33}^{(1)}}{\rho_{33}^{(2)}}$ 194
- C.2 Log-log slope $\frac{d \log \rho_{33}}{d \log n_b}$ as a function of the idler intracavity photon-number n_b . a) Slope of $\rho_{33}^{(1)}$ (solid line); b) slope of $\rho_{33}^{(2)}$ (dashed line); c) slope of ρ_{33}^{FD} ($\eta \ll 1$) (dotted line). 196

List of Tables

| | | |
|-----|---|-----|
| 4.1 | Raw data of P , G_+ and G_- for the experiments of 2/11/94, 4/2/94, 5/2/94 and 8/4/94. Note that P is in mW | 60 |
| 4.2 | Size of the squeezing R_- and antisqueezing R_+ relative to the shot noise in linear units. Corrections for the finite level of the shot noise have been included. P is the pump power in mW | 63 |
| 4.3 | Gain measurements for the NDOPO. | 70 |
| 5.1 | Excitation with non-classical fields, data from experiment 11/17/94. | 89 |
| 5.2 | Excitation with non-classical fields, data from experiment 11/29/94. | 90 |
| 5.3 | Excitation with non-classical fields, data from experiment 12/06/94. | 91 |
| 5.4 | Excitation with non-classical fields, data from experiment 12/20/94-a. | 91 |
| 5.5 | Excitation with non-classical fields, data from experiment 12/20/94-b. | 92 |
| 5.6 | Excitation with coherent fields, data from experiments on 12/22/94 and 1/12/95. | 93 |
| 6.1 | Significant levels S and $\chi^{(2)}$ values for fits to the test functions. The number of free parameters $n - d$ in the experiments of $\{11/17/94, \dots, 1/12/95\}$ are for f_Q equal to $\{18, 7, 12, 6, 11, 8, 9\}$ and for f_{Q+C} , f_P and f_{Q+L} equal to $\{17, 6, 11, 5, 10, 7, 8\}$ | 97 |
| 6.2 | Fit parameters and OPO gain at the knee position, G_s^{knee} , for the non-classical excitation experiments. | 107 |
| C.1 | Data from numerical integration of the master equation appropriate for the nonclassical excitation experiment of Ch. 4 and 5. (From private communication with A. S. Parkins, Feb. 1995). | 193 |
| D.1 | “Knee” position and detunings: data from numerical integration of the master equation for two-photon excitation with nonclassical fields. | 200 |

Chapter 1 Introduction

It may be argued that an atom, especially an alkali with a single electron in its outer shell, is a very simple physical system. In addition, if one considers only an isolated sub-manifold of few (three in our case) of its energy levels, as in Fig. 1.1, then the dynamics of this atom under the influence of electromagnetic (EM) fields should be readily understood. Yet, such a simple system has given us enough material to investigate, keeping us occupied for the last six years. In fact, the simplicity of the three-level system of Fig. 1.1 has been the ideal test bench for the investigation of otherwise very complicated phenomena. During this time and with the aid of such an atom, some very fundamental concepts and principles in the field of Quantum Optics and Atomic and Molecular Physics have been uncovered. The journey of exploration through this very simple three-level atomic system and the discoveries made along the way are the subject of my Thesis.

More specifically, using a three-level atom, a variety of new phenomena associated with the interaction of atoms with various states of the EM field have been studied. As part of the work, experimental techniques have been developed, nonclassical phenomena have been observed, the system has been studied theoretically and the acquired knowledge was extended to practical applications with implications in a variety of fields. The emphasis of the work was divided among two principle subjects: the investigation of quantum effects associated with the interaction of atoms with quantum states of the EM field and the quantum features of the interaction of the atoms with multiple single-mode coherent states of the EM field. A combination of these two subjects sparked further developments and, as a result, observations have been made of otherwise out of reach nonclassical correlation of fields separated in frequency by $25 THz$.

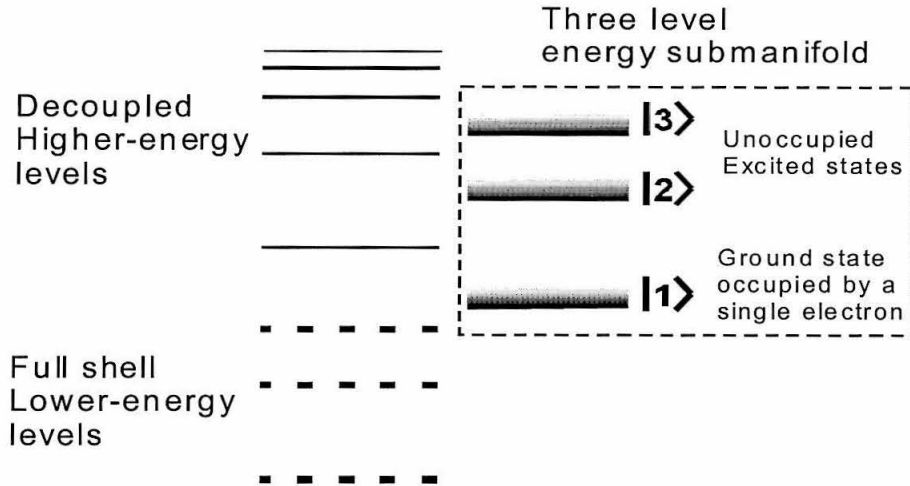


Figure 1.1: A three-level system is realized by considering an “*isolated*” energy submanifold of an alkali atom.

The intent is to cover in this Thesis the basic milestones and explain the physical principles of this work. The journey takes us from basic understanding of a three-level atom to notions such as nonclassical two-photon excitation, quantum interference in multiphoton excitation and the use of atoms as ultra-fast non-linear mixers. These subjects will all be explained in due time in the subsequent chapters, but before getting into the details, in the remainder of this chapter a brief overview of the things to come will be outlined.

1.1 The Three “*Eras*” of my Research

Reflecting back on the work of the last six years, I see that my Thesis is naturally divided into three “*eras*” which I will conveniently use as break points in the discussion of our research. The first “*era*” I call “*Basic Experimental Concepts.*” During this time some of the fundamental experimental techniques and methods needed for the subsequent work were developed. At this preliminary stage a magneto-optical trap (MOT) was constructed to cool and trap atoms in order to produce a Doppler-free

sample for the subsequent experiments. Following this, the capability to perform high-resolution spectroscopy on the atoms in the MOT was developed and measurements of the previously unresolved internal structure of the third excited state of the atom were performed. Finally, a unique facility capable of producing frequency tunable squeezing was modified to match the needs of the research program that followed. During this *era* the foundations of my experimental skills were put into place.

The next “*era*” was the time when one of the most challenging tasks in Quantum Optics, namely the observation of nonclassical effects associated with the interaction of squeezed light with atoms, was undertaken. This *era* I call “*Squeezed Light and Atoms.*” During this time pioneering experiments were performed and for the first time complemented with observations, theoretical predictions that existed for more than a decade.[1] Here an example of nonclassical behavior of atoms interacting with squeezed light as manifested in two-photon excitation by correlated pairs of photons was demonstrated. In particular, the excitation rate as a function of intensity was measured to deviate from the classical quadratic law and was observed to asymptotically approach a linear dependence in accordance with theory. Until today, the work of this era has been the only successful attempt, and with the exception of an alternative, relatively unsuccessful approach also implemented by us,[2] it remains the only experiment on the subject.

Finally we come to the third “*era,*” the *era* of “*Quantum Interference.*” This has been the most productive *era* of my graduate career, where as a well “seasoned” student I have produced the bulk of my work. During this time, by modifying the previous experiment, a two-photon transition was excited by using multiple photons. As a result there were more than one possible excitation pathway, which lead to Quantum Interference (QI). Not long after the initial observations, it was realized that this could have profound implications in several fields. The key idea is that atoms act as ultrafast nonlinear mixers due to QI. First by applying these findings to frequency metrology, we proposed novel techniques for bridging large frequency gaps in single steps. Then we applied our results to optical communications and obtained a patent for our work. Subsequently, we also proposed to use the atoms in a novel

homodyne scheme and presented a proof-of-principle experiment in support of our claim. Finally, in order to lay some solid ground for future work on the subject, we have theoretically analyzed the details of our system by solving the master equation that produced models valid in a large range of parameters.

With this prelude in mind we now turn to the more technical discussion. The next section is devoted to introducing the atomic system used throughout our experiments, while the following three sections are an overview of the science of each of the *eras* mentioned above. Here, the goal is to relate to the reader the main concepts and key ideas that will appear in the rest of the Thesis and summarize the content of the various chapters. The interested reader may then refer for more details to the subsequent chapters.

1.2 Three-Level Energy Submanifold in Cs¹³³

The particular atom that was used throughout our experiments is atomic Cesium-133. The relevant transitions that comprise the three-level energy submanifold of Fig. 1.1 are the $6S_{1/2}F = 4$, $6P_{3/2}F' = 5$ and $6D_{5/2}F'' = 6$ states, as shown in Fig. 1.2. To familiarize further the reader with the atomic system of Fig. 1.2, it is worthwhile to introduce at this point the notation and parameters which will be used repeatedly throughout the rest of this Thesis. First, the simplifying notation $\{|1\rangle, |2\rangle, |3\rangle\}$ is employed to denote the energy levels $\{6S_{1/2}F = 4, 6P_{3/2}F' = 5, 6D_{5/2}F'' = 6\}$. Then the eigenfrequencies of the system are defined to be

$$\omega_{ij} \equiv \frac{E_i - E_j}{\hbar}, \quad (1.1)$$

where E_i is the energy of each state. The eigenfrequencies for the atom in Fig. 1.2 have corresponding wavelengths equal to $\lambda_{21} \simeq 852 \text{ nm}$, $\lambda_{32} \simeq 917 \text{ nm}$ and $\lambda_{31} \simeq 442 \text{ nm}$. The FWHM atomic linewidths are $\gamma_2 \simeq 5 \text{ MHz}$ and $\gamma_3 \simeq 3 \text{ MHz}$ and correspond to the decay rates of the $|2\rangle \rightarrow |1\rangle$ and $|3\rangle \rightarrow |2\rangle$ transitions respectively. Finally, an

important parameter of the system is Δ , which is defined to be

$$\Delta \equiv \left| \omega_{21} - \frac{\omega_{31}}{2} \right| = \left| \omega_{32} - \frac{\omega_{31}}{2} \right|. \quad (1.2)$$

Stated differently, Δ is a measure of the degree of non-degeneracy in the system which for our case is equal to $\Delta \simeq 25 \text{ THz}$.

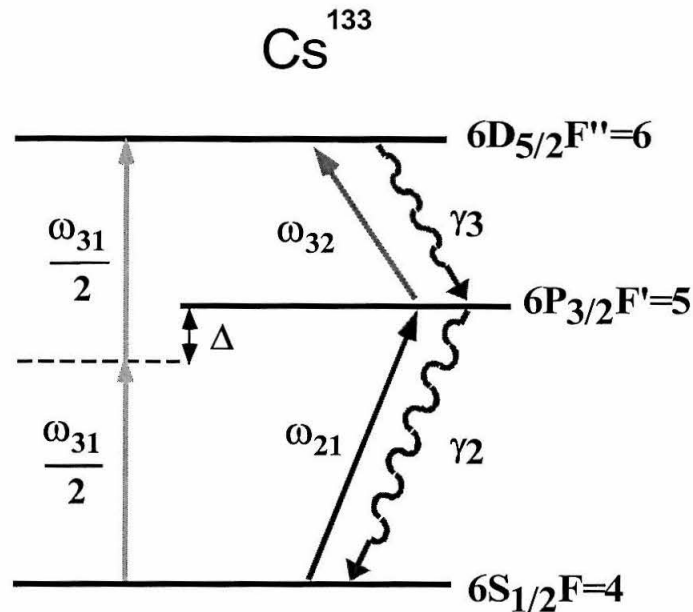


Figure 1.2: The three-level energy submanifold in atomic Cesium which was used in our experiments.

1.3 Basic Experimental Concepts

In the first part of the Thesis the basic lab set-up that was used throughout the experiments will be described. This set-up consists of two main components: a frequency tunable source of squeezed light [3, 4] that generates nonclassical states of the EM field and a magneto-optical trap (MOT) [5, 6] that provides a Doppler-free atomic sample for the experiments.

1.3.1 Magneto-Optical Trap

Starting from the first part of the experimental set-up, the magneto-optical trap (MOT) shown schematically in Fig. 1.3 is formed by a combination of optical and magnetic fields. In particular, five laser beams (two with opposite directions along the z -axis, and three in the perpendicular plane, spaced by 120° from each other) together with a repumping beam, are responsible for cooling the atoms down to the Doppler limit of $120 \mu K$. In addition, a pair of coils with anti-parallel currents produces a magnetic field gradient, which in concert with light forces produces a potential well in which the atoms are confined. Although this is a well established technique for cooling and trapping, [5, 6] some of the discussion will nevertheless be devoted in the particular realization in our own experiments in order to document the parameters and characteristics of the apparatus. To give a general idea of the trap that we had in our disposal, it is worth noting at this point that the physical size of the MOT was of the order of $0.1 - 0.3 \text{ mm}$ in diameter, it had a temperature close to the Doppler cooling limit of about $120 \mu K$, its density was estimated to be of the order of 10^9 atoms/cm^3 and hence the number of atoms in the MOT was of the order of $500 - 15,000$.

1.3.2 High Precision Spectroscopy of the $6D_{5/2}$ State in Cs^{133}

Continuing the discussion of the preliminary phase of our research, I will then describe a classical spectroscopy experiment which was performed in order to study the $6D_{5/2}$ state of Cs . [7] This exercise was a very crucial initial step in our work for a couple of reasons. First, in order to realize an isolated three-level energy submanifold, it is important to know the internal (hyperfine) structure of the states involved in the transitions. However, as it turned out, the $6D_{5/2}$ level had not been carefully studied in the past, and the only available reference [9] until then quoted an accuracy for the measurements of only 30%. In addition, for the experiments that followed it was very important to learn how to perform spectroscopy on the MOT which is a very powerful tool in the field of high precision spectroscopy. [8, 10, 11]

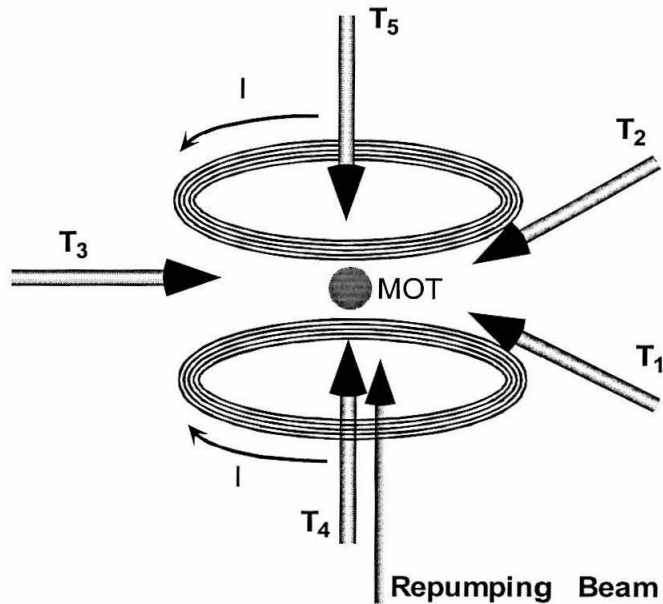


Figure 1.3: MOT setup: five trapping beams, T_1, \dots, T_5 , and one repumping beam are responsible for cooling the atoms. A pair of coils with antiparallel currents, I , produce a magnetic field gradient which in concert with the light force confine the atoms in a localized region in space.

Turning now to the actual spectroscopy experiment, it is noted that it was performed by exciting the two-photon transition $6S_{1/2}F = 4 \rightarrow 6D_{5/2}F''$ by a tunable Ti:Sapphire laser and then observing the emitted fluorescence from the cascade decay back to the ground state. In particular, monitoring of the excited state population was achieved by observing the fluorescence emitted from the $6D_{5/2}F'' \rightarrow 6P_{3/2}F' = 5$ transition. The main outcome of these measurements was the determination of the hyperfine structure (hfs) of the $6D_{5/2}$ level as characterized in first order by the magnetic dipole a and in second order by the electric quadruple b coefficients. These coefficients were measured to be $a = -4.69 \pm 0.04 \text{ MHz}$ and $b = 0.18 \pm 0.73 \text{ MHz}$.

Here, the solution to two main experimental problems that were crucial in the following experiments will also be discussed. First, there was the issue of AC Stark shifts of the ground level and power broadening due to the strong trapping beams.

This was solved by implementing a chopping cycle (at 4 *KHz*) for the trapping beams and performing the measurements only during the OFF part of the cycle. However, even the ON part of the cycle was interesting and by comparing spectra obtained during the ON and OFF parts of the cycle, useful information about the magnitude of the Stark shifts and power broadening have been extracted.

A second problem that needed special attention was the signal-to-noise (S/N) ratio of the measurements. First an efficient technique for the observation of the fluorescence from the $6D_{5/2}F'' \rightarrow 6P_{3/2}F' = 5$ transition had to be devised and then the background light (mostly from scattering from the trapping beams which even during the OFF part of the cycle was enough to produce noticeable signals) had to be dealt with. In addition, during the ON part of the cycle the detector was oversaturating and was not recovering fast enough for the measurements to be made accurately during the OFF part of the cycle. However, by realizing that the wavelength of the trapping beams is 852 *nm*, while that of the $6D_{5/2}F'' \rightarrow 6P_{3/2}F' = 5$ transition was close to 917 *nm* and by using an interference (notch) filter centered at 917 *nm*, good isolation was provided that helped to overcome these difficulties by eliminating the background to acceptable levels and avoiding detector saturation from 852 *nm* light.

1.3.3 Optical Parametric Oscillator

The last chapter of Part I refers to the subthreshold optical parametric oscillator (OPO) which was the source of radiation for the experiments that followed. The operation of the OPO in two modes, the degenerate (DOPO) and non-degenerate (NDOPO), will be discussed. The setup, particularly of the NDOPO which is relevant for the experiments, consists of a very complex set of optical elements, alignment procedures, optimization techniques and electronic feedback loops (see Fig.1.4), all of which when put together could be a Thesis by themselves! In addition, when one starts to consider the properties and actual behavior of the output of the OPO as compared to the theoretical predictions, even further complications arise. Luckily

there exists a lot of theoretical [12, 13] as well as experimental [3, 4] work on the subject and most of the setup was already in place. Hence, the emphasis here will be on the operation of the OPO and measurements that were taken to characterize its properties. In addition the modifications that have been introduced and operating details will be outlined.

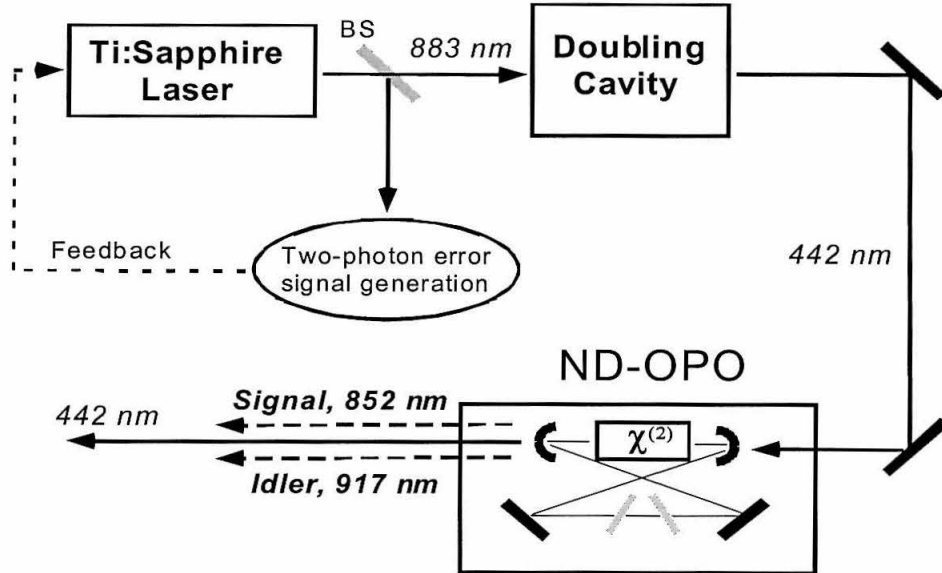


Figure 1.4: NDOPO setup for producing nonclassical light.

Perhaps the most important modification in the system of Ref. [3, 4] is the fact that in this case the OPO was operating in a non-degenerate mode producing signal and idler beams that were separated in frequency by $25 THz$ and had respective wavelengths of 852 and $917 nm$. Not only was it a challenge to operate the OPO cavity in this large non-degenerate mode (which effectively means that the cavity had to be in double resonance with the signal and idler frequencies), but also the signal and idler frequencies had to be resonant with the $|1\rangle \rightarrow |2\rangle$ and $|2\rangle \rightarrow |3\rangle$ transitions, respectively, for the nonclassical spectroscopy experiments to be feasible. These challenges are unique tasks that had to be accomplished for the first time.

Finally, performance measurements that characterize the NDOPO and comparison

with theoretical predictions will be discussed. In particular, measurements of the spectrum of squeezing for the degenerate OPO that verify the uncertainty relation for conjugate quadratures of the electromagnetic field will be presented, and data on phase-sensitive gain will be shown and compared to phase-sensitive amplification and deamplification from theory. As it turns out these measurements indicate small discrepancies from theory that one needs to be aware of.

1.4 Squeezed Light and Atoms

After this preliminary phase in Part II, the subject of nonclassical interaction of squeezed light and atoms will be addressed. After a brief outline of the theory, the experiment will be described and explicit procedures used to treat the raw data will be given. Following this, statistical analysis of the results and conclusions from the experiment will be discussed.

1.4.1 Two-Photon Excitation Rate with Nonclassical Fields: Theory and Experiment

At this point, precluding the work to be presented later, it is worth noting that since the seminal work of Milburn [14, 15] and Gardiner [16] who showed for the first time that nonclassical effects arise when atoms are exposed to quantum reservoirs, there has been considerable effort in the theoretical community to unveil as many of these phenomena as possible.[17] In particular, in the original work of Gardiner [16] we see the first example where a phase-sensitive sub-natural linewidth is predicted for a two-level atom interacting with squeezed vacuum. In this example the degree and phase of squeezing as well as the efficiency with which it is coupled to the atom are crucial determining factors to the size of the effect. Figure 1.5 depicts schematically the original idea.

Following the above footsteps, theorists have since then predicted an abundance of nonclassical phenomena associated with the interaction of atoms with nonclas-

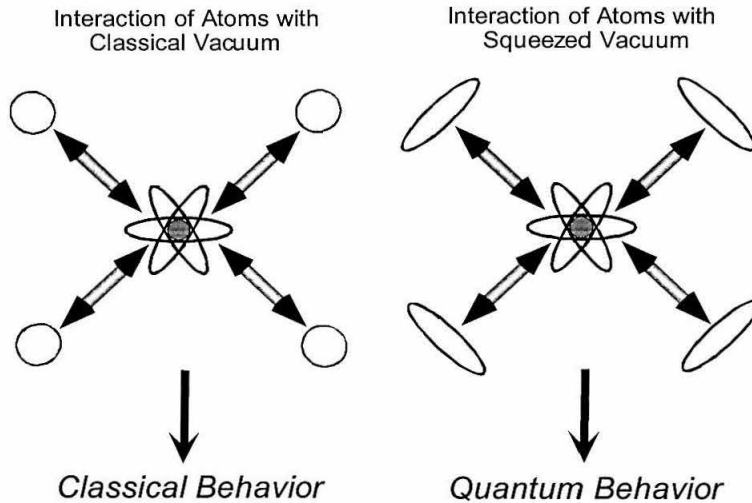


Figure 1.5: Interaction of atoms with classical and squeezed vacuum, shown as circles and ellipses, respectively.

sical fields. These examples include resonance fluorescence of atoms in squeezed vacuum,[18, 19, 20, 21, 22] optical bistability in squeezed vacuum,[23] optical pumping with squeezed light,[24] photon echoes and revivals,[25, 26] lasers pumped by squeezed light,[27, 28, 29, 30] gain without inversion,[31] electromagnetically induced transparency, [32] numerous cavity QED examples in the presence of squeezed light,[33, 34, 35, 36, 37] laser cooling with squeezed light,[38] cooperative effects,[39, 40, 41] and finally effects associated with two-photon excitation by correlated pairs of photons,[42, 43, 44, 45, 46, 47] which is the subject of our own work.

The experiment to be presented here tests the prediction of several authors [42, 43, 44, 45] that the rate of two-photon excitation R_2 as a function of the excitation intensity I deviates from the usual quadratic form and becomes asymptotically linear for small enough intensities

$$R_2^{Squeezed} = \alpha_1 I^2 + \alpha_2 I , \quad (1.3)$$

provided that the exciting fields are in a nonclassical state such as the state of the

NDOPO output. Here α_1 and α_2 are constants of the same order of magnitude. Recall that for classical fields the two-photon excitation rate versus intensity is quadratic and is given by

$$R_2^{Classical} = \beta_1 I^2, \quad (1.4)$$

where β_1 is again a constant.

As an intuitive physical interpretation of this phenomenon, one may envision the two-photon excitation process $|1\rangle \rightarrow |3\rangle$ as a two-step process, where the atom makes first a $|1\rangle \rightarrow |2\rangle$ followed by a second $|2\rangle \rightarrow |3\rangle$ transitions. Referring to Fig. 1.6(a) this process is shown to take place in the presence of two independent lasers of frequencies ω_1 and ω_2 , tuned near resonance with the ω_{21} and ω_{32} eigenfrequencies, respectively. In Fig. 1.6(b) the same process takes place with the same frequencies ω_1 and ω_2 produced in this case from an NDOPO.

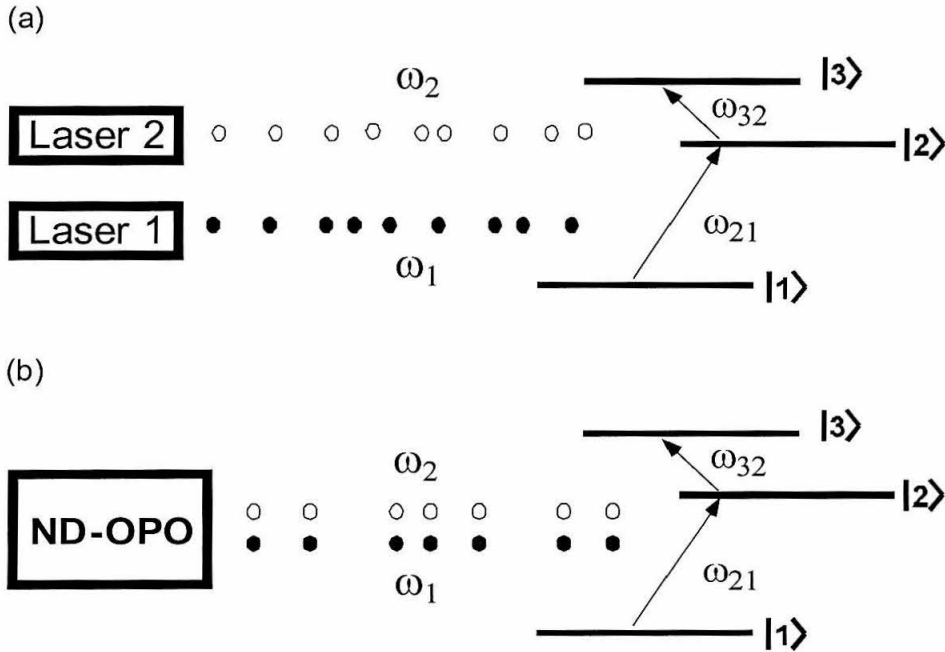


Figure 1.6: (a) Classical and (b) quantum excitation of a two-photon transition.

Loosely speaking in a language of photons as billiard balls, in the first case of Fig.

1.6(a) the probability distribution of time spacing between photons is for each of the two lasers Poissonian. Hence, the probability distribution of arrival times between pairs of ω_1 and ω_2 photons at the location of the atom is also Poissonian with the mean spacing scaling proportionally to the intensity I . Therefore, once the atom absorbs an ω_1 photon has to “wait” for a certain time (given by a Poissonian distribution) for a second ω_2 photon to arrive. During this dwell time, however, it may decay back to the ground state reducing in this way the overall excitation probability. Since each absorption probability is proportional to the intensity I of the corresponding beam, it is natural to expect that the overall $|1\rangle \rightarrow |3\rangle$ transition probability is the product of the two and hence classically it is proportional to I^2 . [77]

However, the situation is different for excitation with light emitted from an NDOPO, Fig. 1.6(b). In this case photons in the ω_1 and ω_2 beams are “perfectly” correlated and hence pairs of ω_1 and ω_2 photons arrive at the side of the atom simultaneously, reducing the probability for decay of the atom from the intermediate state back to the ground state. Because of the lack of “dwell” time, the excitation probability from correlated pairs of photons is then proportional to the intensity I rather than the square of the intensity I^2 . Nevertheless, the possibility of excitation from a pair of uncorrelated photons still exists and hence as in the first case this process will still have a term proportional to I^2 , justifying in this way the quadratic contribution in Eq. (1.3).

To realize experimentally the above described two-photon excitation with correlated pairs of photons, the atoms in the MOT have been excited by the output of the NDOPO and then by observing the fluorescent decay of the atoms from the $|3\rangle \rightarrow |2\rangle$ transition, a measure of the excited state population was obtained. Having overcome all other technical problems of trapping the atoms, tuning the NDOPO so that to generate signal and idler photons in resonance with the $|1\rangle \rightarrow |2\rangle$ and $|2\rangle \rightarrow |3\rangle$ transitions, respectively, and having aligned all the beams, there was still a major problem to overcome, namely data acquisition.

In order to be able to observe the nonclassical behavior of the atoms, i.e., the linear component of Eq. (1.3), we have to probe the rate of two-photon excitation at small

enough intensities where the linear term dominates over the quadratic. Defining arbitrarily the “knee” point to be the point at which the contributions from the linear and quadratic parts of Eq. (1.3) become equal, we find that the corresponding intensity is about 0.001 mW/cm^2 while the saturation intensity is of the order of 1 mW/cm^2 . Hence, it is clear that at the region of interest, the atoms will be excited very weakly and therefore the excited state population will be very small. Taking into account the total detection efficiency, which was not more than few percent, the signals at the relevant region are of the order of 1 photons / sec . Given a background count of the order of $4 - 5 \text{ photons / sec}$ (primarily dominated by the dark counts of the detector) it is clear that the observation of this effect is non trivial. Nevertheless, by using several experimental and statistical techniques to check against possible pitfalls, we were finally able to show convincingly that the nonclassical behavior of the atoms as manifested in Eq. (1.3) has been observed.[48, 49]

1.4.2 Linear Two-Photon Excitation Rate with Nonclassical Fields: Analysis, Statistics and Results

In Fig. 1.7 we see a typical example of data obtained from our experiments, with an obvious deviation from the quadratic law for excitation with squeezed light contrary to that of excitation with classical light. Note that significant deviations from the quadratic dependence occur for counting rates close to 1 photon/sec . “To convince the jury” that an asymptotically linear dependence is predicted from our data, significant effort was given in the statistical analysis of the data. To combine the knowledge acquired from different experiments, two different statistics have been defined and detailed analysis of the data showed that a linear plus quadratic model is the “most likely” to describe the data. Furthermore, identical numerical treatment and statistical analysis of control experiments with coherent excitation suggests that these data are as expected governed by the classical quadratic law. Hence a case is built in favor of the nonclassical model. The details of these arguments and the procedures followed will be carefully outlined.

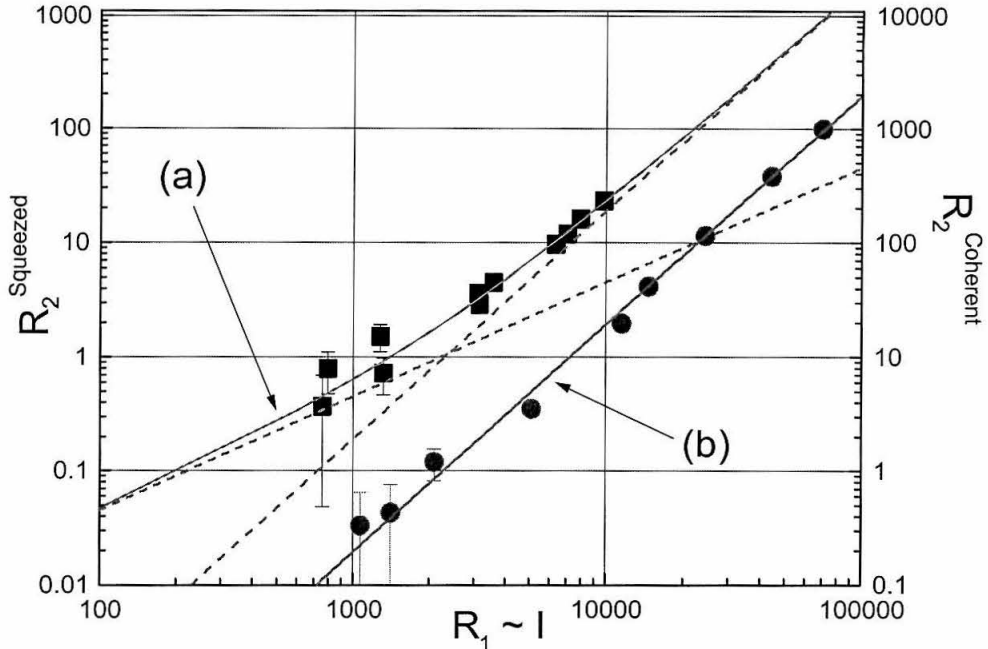


Figure 1.7: Experimental observation of two-photon excitation with (a) quantum correlated and (b) classical fields. The units of the counting rates, $R_2^{Squeezed}$ and $R_2^{Coherent}$, are detected *photons/sec*. The solid lines are fits to the data of the form of Eqs.(1.3) and (1.4), while the dotted lines are the linear and quadratic components plotted separately for the fit to the non-classical data. The x - $axis$ is a measure of the intensity in arbitrary units.

1.5 Quantum Interference

In Part III quantum interference (QI) in two-photon excitation subject to illumination by multiple fields is investigated. First, theory developed to describe the process is outlined and then a proof-of-principle experiment is presented. By extending these ideas to nonclassical excitation, the possibility for ultrafast homodyne detection is explored and another experiment is presented. Finally, applications of the QI scheme in frequency metrology and optical communications with atoms utilized as ultrafast nonlinear mixers are suggested.

1.5.1 Multiple Field Two-Photon Excitation and Quantum Interference

The basic idea of QI in two-photon excitation is shown in Fig. 1.8 where a three-level atom is excited from its ground state $|1\rangle$ to the third excited state $|3\rangle$ in the presence of three exciting fields. The frequencies of these fields, ω_1, ω_2 and ω_o , are chosen so they are near resonance with the atomic eigenfrequencies ω_{21}, ω_{32} and $\frac{\omega_{31}}{2}$, respectively. Therefore, the atom can be excited via two alternative pathways: a stepwise cascade of two dipole absorptions from the ω_1 and ω_2 fields or a simultaneous two-photon absorption from the ω_o field. In the case that the probability amplitudes of these two excitation pathways are coherent, we expect to observe QI as in any other quantum mechanical system. The particular manifestation of QI is in terms of the excited state population ρ_{33} , which is modulated depending on the relative phase of the excitation amplitudes.

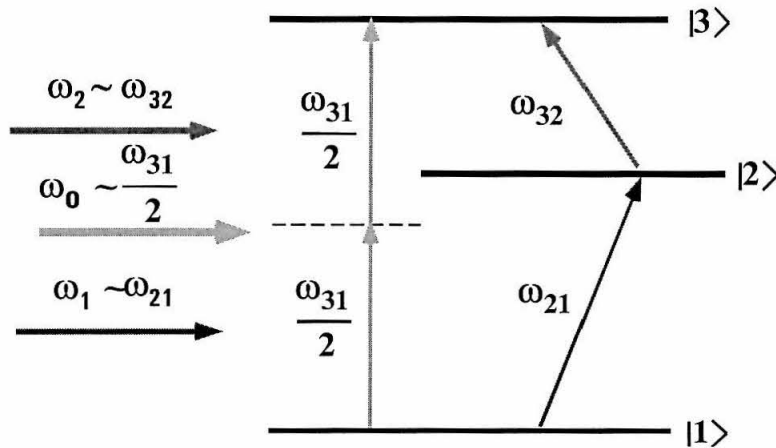


Figure 1.8: Excitation of a two-photon transition by three phase-coherent lasers leads to quantum interference.

More quantitatively it has been shown by solving the master equation of the system in the perturbative (weak-field excitation) limit that the excited state population

ρ_{33} is given by

$$\rho_{33} = \mathbf{X}_1^2 + 2\mathbf{X}_1\mathbf{X}_2 \cos \Phi + \mathbf{X}_2^2 . \quad (1.5)$$

Here \mathbf{X}_1 and \mathbf{X}_2 are the probability amplitudes for the two alternative excitation pathways and Φ is a relative phase between the three excitation lasers at the site of the atom. The form of Eq. (1.5) indicates interference as in any generic interference experiment and, since \mathbf{X}_1 and \mathbf{X}_2 are quantum mechanical probability amplitudes, the process is governed by quantum interference.

The next step is to extend the theory to the strong-field excitation limit. Here the master equation is solved with a more general approach sacrificing some of the simplicity of the perturbative solution in favor of generality. As a result the solution is given by a matrix equation valid for both strong and weak excitation, which, although not analytic, requires only numerical inversion of an 8×8 matrix to produce readily numerical results that can be studied. To further aid researchers in the field, an interactive Java based calculator has been constructed and is made available on the WWW.[50]

Complementing the above theory, a proof-of-principle experiment with observations of QI is presented. In particular, an example where the excited state population was monitored as a function of the relative phase of the three lasers used for excitation is shown. The observation of ρ_{33} shows a clear sinusoidal modulation, the contrast of which was measured to be about 0.3. To compare to theory, calculations based on the experimental parameters are performed and test the models developed earlier.

1.5.2 Ultrafast Homodyne Detection

The next subject in the discussion is ultrafast homodyne detection using atoms as ultrafast nonlinear mixers. The goal here is to observe the quantum correlations of fields that are separated in frequency by large intervals. For example, for the output of the NDOPO in the two-photon experiment (see Fig. 1.6(b)), the signal and idler beams are separated by 25 THz. In order to prove that indeed we have nonclassical correlations between these two fields, we must in principle be able to form and observe

the beatnote of these two fields with respect to a reference oscillator (RO), which in this case is the ω_o field. However, current technology limits the mixing with a cutoff of a few tens of GHz and hence the correlations in question are far beyond any observational capabilities. Yet, the atom behaves as a non-linear mixer itself. Therefore, by modifying the example of Fig. 1.8 so that ω_1 and ω_2 are the signal and idler photons from the NDOPO and keeping the ω_o field in a classical coherent state, the atom is utilized as an ultrafast mixer to demodulate the beatnote of the quantum fields with RO the ω_o beam. As a result observations of these ultrahigh frequency correlations are reported. Unfortunately, observing the correlations and proving that they are nonclassical are two disjoint tasks, and although they have been observed, there is still a question of principle regarding the proof that they are nonclassical. In addition to the experimental observations, theory to study in more detail the consequences of this scheme is presented.

1.5.3 Atoms as Ultrafast Nonlinear Mixers

Finally, some other applications of the notion of ultrafast atomic mixers are presented. The frequency response of the atomic mixers is quantified with the perturbation theory developed earlier. Applications in frequency metrology are discussed and a proposal for a novel technique for establishing new frequency standards is suggested. Extending the discussion even further, we show that the idea could be commercialized with implications in the field of optical communications. This latest idea has also been the motivation behind submitting a patent for the work. In support of these applications, an extensive database of 6900 different three-level submanifolds from the alkali elements *Li*, *Na*, *K*, *Rb* and *Cs* which can be used in schemes similar to that of Fig. 1.8 has been constructed. A search algorithm has been developed based upon the database. Given any target wavelengths in the range of 200 – 2000 *nm* that needs to be measured, the algorithm considers all possible combinations and suggests an optimal strategy for achieving the goal.

1.6 Summary

From this outline of topics to be discussed in the remaining of the Thesis, it is clear that the study of a three-level system has been proven to be very fruitful and has helped in the investigation of several new phenomena in the course of our research. During our work we have uncovered nonclassical interactions with atoms, we have seen QI in two-photon excitation, and we have utilized atoms as nonlinear mixers to perform tasks not possible with any other techniques. Before continuing, however, I would like to mention that we also performed several cavity QED experiments in order to investigate the interaction of atoms with squeezed light.[2] These projects, however, are somewhat disjoint from the rest of the subjects covered in this Thesis and, in addition, they have been extensively covered in Quentin Turchette's Ph.D. Thesis. For these reasons I will ignore this part of our work, which nevertheless was a significant effort.

With this introduction to the subjects and science to be described in the rest of the Thesis, we now enter a more detailed discussion of the various topics.

Part I

BASIC EXPERIMENTAL CONCEPTS

Chapter 2 Magneto-Optical Trap

A crucial component of all our experiments was the magneto-optical trap that provided a Doppler free sample of trapped atoms for our studies. In this chapter the particular realization of the MOT implemented in our research will be described. However, the main purpose here is not to describe the physical principles dictating the operation of the MOT,[5, 6] but rather to document the parameters and procedures used in our own setup.

2.1 Geometry

As noted in the introduction, Section 1.3.1, the MOT was constructed implementing a five-beam configuration, Fig. 1.3. These beams were arranged so that two of them were counter propagating along the z – *axis*, while the other three were on the xy – *plane*, spaced from each other by about $120^\circ \pm 20^\circ$. This particular configuration (somehow unusual compared to the traditional six-beam MOT), was chosen mostly due to the constraints of the available geometry in the xy – *plane* as shown in Fig. 2.1.

The trapping chamber was a spectroscopic glass cell made by Uvonic, with fairly good optical quality windows and dimensions $\sim 5\text{cm} \times 1\text{cm} \times 1\text{cm}$. The wall thickness was roughly 1 *mm*. This cell was connected to a Cs source which was kept at a low temperature of about -10 to 0 °C in order to reduce the Cs vapor pressure. In addition, a 2 *l/s* ion pump was connected to the system and sustained a pressure in the chamber of about $\lesssim 10^{-7}$ Torr. Note that the loading time of the trap strongly depends on the Cs pressure, since it is proportional to the total number of Cs atoms near the cooling “zone,” while the lifetime of the trap depends strongly on the background pressure, since the main loss mechanism is background collisions.

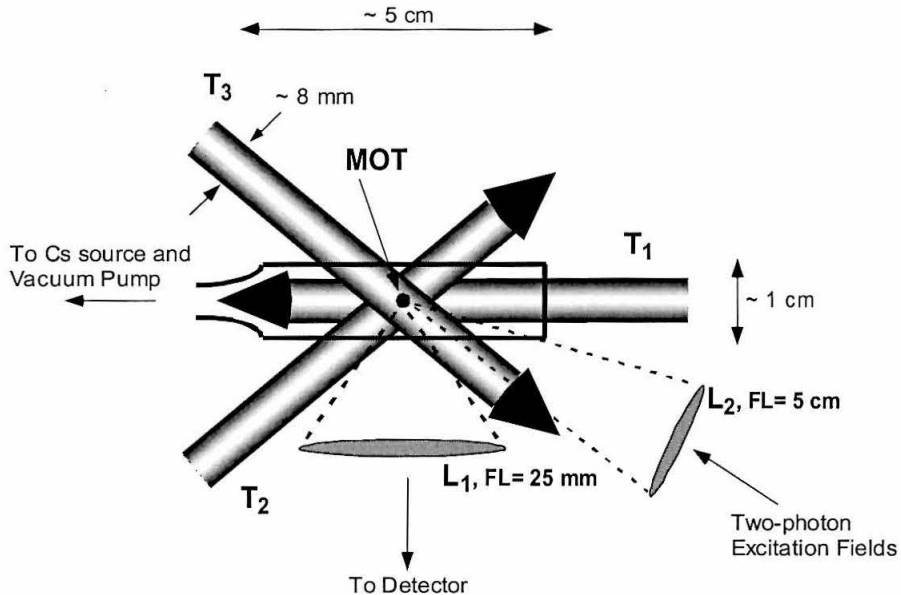


Figure 2.1: The xy – $plane$ geometry of the MOT.

The trapping beams were adjusted to a size as big as possible, about 6 – 8 mm in diameter. Note that the total number of atoms in the trap grows as the 4th power of the trapping beam diameter; [53, 54] hence, it was crucial for us to have large beams in order to accumulate enough atoms.

The geometry of the xy – $plane$ in the vicinity of the MOT (Fig. 2.1) is completed with the addition of two more elements, the lenses L_1 and L_2 shown on Fig. 2.1. Lens L_1 is a collimating lens, positioned at a distance equal to one focal length from the MOT, and its function is to collect light for imaging purposes. In order to have efficient light collection, the diameter of this lens was chosen to be comparable to its focal length (note that efficient collection beyond this point becomes impractical due to lens manufacturing difficulties for the working distances required in our experiment (~ 25 mm)). This condition imposed certain geometry constraints, since the lens should not obscure the trapping beams entering the trapping cell, but also it should not sit at the path of other beams that go through the cell because it would then collect that light and send it to the detector causing saturation. An additional constraint

is that the lens should be parallel to one of the cell’s windows in order to reduce aberrations which are important because the collected light must be re-focused onto a detector with fairly small active area (diameter $\sim 150 \mu m$).

Lastly, we have the lens L_2 , which is responsible for focusing the excitation fields onto the atoms in the MOT. This lens was chosen to be of focal length equal to 5 *cm* and was placed almost along the T_3 trapping beam. Note that this has no impact in bringing the trapping beams into the trap, nor does it influence any other part of the MOT setup.

2.2 Trapping Beams

The five trapping beams of Fig. 1.3 are all derived from a single “homemade” diode laser,[55] tuned to about 10 *MHz* below the $6S_{1/2}F = 4 \rightarrow 6P_{3/2}F' = 5$ transition of Cs and locked to the signal from a saturated absorption cell. The corresponding wavelength of this frequency in air was measured by a wavemeter to be $\lambda_T \simeq 852.360 \text{ nm}$, although variations in room temperature and humidity result in variations of this measurement by as much as $\pm 0.003 \text{ nm}$. The power of each of these beams was about 1 – 2 *mW*, corresponding to intensities close to saturation, but the exact power was not so crucial for the trap performance. However, some care was taken in arranging that all beams have about the same power so that the optical forces will be roughly balanced. The polarization of these beams was adjusted to be as close to circular as possible, with the helicity of the three coplanar beams in the *xy* – *plane*, opposite from the helicity of the beams along the *z* – *axis*. However, due to reflections of the beams at “funny” angles from various mirrors as well as polarization selective reflection from the cell walls, the polarization of these beams was in fact elliptical with asymmetry ratios as large as 3 : 2.

In addition to the five trapping beams, we also had a repumping beam, derived from a commercially available diode laser. This laser was sometimes free running and sometimes locked, but in either case tuned close to the $6S_{1/2}F = 3 \rightarrow 6P_{3/2}F' = 4$ transition in order to prevent depletion of the $6S_{1/2}F = 4$ state from which trapping

occurs. Due to the tight geometry we had to work with, as shown in Fig. 2.1, we chose to send the repumping beam along one of the other trapping beams. Most of the time this beam was sent along the T_1 beam (Fig. 2.1), although at the early stages of our experiments we also tried to send it along the z - *axis* as shown in Fig. 1.3. The power of this beam was a few mW ; its size was comparable to the trapping beams; and its polarization was arbitrary.

2.3 Magnetic Fields

While cooling occurs by optical forces, confinement in a MOT is due to optical forces adding in concert with magnetic field gradients. In fact, the trap forms at the zero point of a magnetic field gradient, achieved by a set of anti-Helmholtz coils, parallel to the xy - *plane* and through which anti-parallel currents run. The optimum geometry of these coils is described in Ref. [56] and is such that the ratio of the diameter of the coils to the separation between them is about 1.6. Note that from symmetry and the divergence-free property of magnetic fields $\nabla \cdot B = 0$, it follows that $\frac{\partial B}{\partial x} = \frac{\partial B}{\partial y} = -2\frac{\partial B}{\partial z}$. The difference in sign for the magnetic field gradient in the xy - *plane* from that along the z - *axis* is also the reason why the helicity of the trapping beams in the z direction must be opposite from the rest. Note that reversing the direction of the current in both coils results in a sign flip for all components of the magnetic field gradient. Therefore, from an operational point of view, the first time the trap is constructed, one arranges the helicities of the beams as described and then checks whether or not a trap is formed. If it is not, then the most likely reason is that either the coils are not positioned correctly with respect to the trapping beams or that the current is reversed. In the second case, flipping the current direction readily fixes the problem. The magnetic field gradients used in our experiments were of the order of $\frac{\partial B}{\partial x} \approx 4 - 8$ Gauss/cm.

2.4 Alignment

The last thing about the MOT is alignment. This was one of the most tedious tasks that had to be addressed every time the trap was turned on and was crucial in performing successful experiments. Hence, alignment needs some special attention.

2.4.1 MOT Alignment

The first thing we had to do was to align the trapping beams and position the anti-Helmholtz coils (which were fixed on an xyz translation stage) in order to achieve a “nicely shaped” trap. Although so far a MOT has been implicitly described as a “nice” sphere, Figs. 1.3 and 2.1, this could not have been further from the truth. In particular, in an ideal case the trap should be an ellipsoid, since confinement in the axial (z) direction is twice as much as that along the planar (x and y) directions (recall that $\frac{\partial B}{\partial x} = \frac{\partial B}{\partial y} = -2\frac{\partial B}{\partial z}$).

In practice, however, a nice ellipsoidal shape is very difficult to achieve because of interferometrically sensitive alignment of the trapping beams that set interference fringes in the vicinity of the MOT. In addition, imbalances in polarization and power of the trapping beams causes further complications. Only after careful alignment, and most importantly by monitoring the shape and behavior of the MOT from two perpendicular directions, were nicely shaped traps obtained. For the purposes of monitoring, two CCD cameras that imaged the trap from the top and side views were implemented. Note that sometimes it is possible to have an image of the trap from one direction that looks nice, but viewed from a perpendicular direction is completely out of shape. Notice that in order to image the trap we had to introduce to the already crowded geometry even more optical elements.

An additional test for “good” alignment was the modulation by 30 – 50% of the magnetic field gradient by turning up and down the current. If this procedure did not produce any erratic movements in the position and shape of the trap, then this was a further indication of a stable and well aligned trap.

2.4.2 Excitation Fields

The second major alignment issue that had to be addressed was the intersection of the two-photon excitation fields with the MOT. This was a major “targeting” exercise since the trap had a size of $0.1 - 0.3 \text{ mm}$ while the excitation fields were focused down to $\sim 7 \mu\text{m}$. Note that this tight focusing was necessary in order to achieve high intensities throughout the trap diameter as explained in Ref. [7].

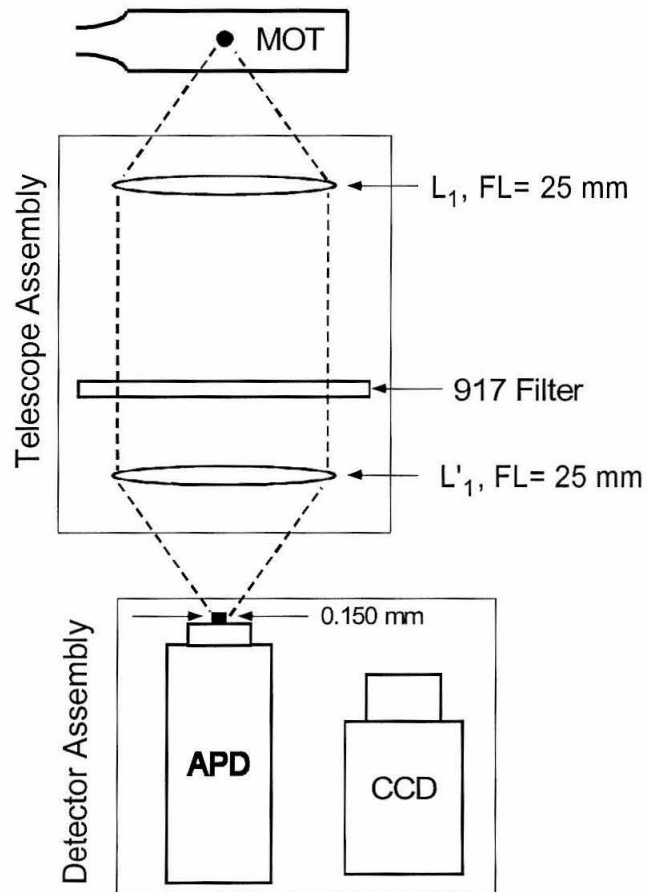


Figure 2.2: Imaging of the trap. A one-to-one telescope collects light from the MOT and refocuses it onto the APD.

Lens L_2 in Fig. 2.1 was positioned on an xyz translation stage and by moving

it we could steer the direction of the excitation fields with respect to the MOT. To monitor the “targeting”, the two CCD cameras that imaged the trap were used to observe the path of a strong 852 *nm* beam sent along the path of the excitation fields.¹ This beam left a bright trail of fluorescent light while traversing the vapor cell and hence its path could be seen. Note that due to contrast problems the trapping beams had to be turned off during this procedure. To know the MOT’s location, a mark of its position was placed on the TV monitors. Also note that when aiming was right and the trap was turned back on, the 852 targeting beam blow the trap away since it delivered unbalanced, high intensity radiation to the MOT. In this procedure it was also crucial to monitor the targeting alignment from two perpendicular views since a single view could lead to alignment at the front or at the back of the trap.

2.4.3 Imaging

Finally, the last alignment task was to position correctly the imaging system shown in Fig. 2.2 in front of the trap (note that the lens L_1 is the same as that of Fig. 2.1). This imaging system consists of two parts, the telescope assembly and the detector assembly. Each of these two parts was mounted independently on its own *xyz* translation stage.

The telescope assembly consists of two identical lenses, L_1 and L'_1 , which collected fluorescent light from the MOT and then refocused it down onto the detector which in this case was an avalanche photodiode (APD). Between the two lenses there are 917 *nm* interference filters in order to block the 852 radiation. More details about the telescope system will be given in the next chapter. The detector assembly consisted of the APD and a CCD camera which were mounted together on a *xyz* translational stage as well. The task was then to first position the telescope so that it will be centered with respect to the MOT and also to be at the right distance from it. Then the APD had to be correctly positioned so that it was situated at the image point of the telescope. This was a tiresome procedure, not only because the trap position

¹The 852 *nm* targeting beam was transmitted through the OPO so that it had the “correct beam path” relative to the signal and idler beams.

could change from day to day, but also because the APD detector was so small (150 μm in diameter).

The operational way around this problem was to utilize the CCD camera on the detector assembly. First the CCD camera which has a large active area would be used to image the trap through the telescope. When a clear image was achieved then the telescope was situated correctly and was properly aligned with the CCD camera. Then the CCD camera would be moved so that the trap image was at the center of a monitor at a fixed mark. Then since the APD is fixed relative to the CCD camera, it was always a matter of a fixed xyz displacement of the whole detector assembly to bring the APD at the right place. Of course in practice we had to find this reference displacement for the first time, but even after the reference offset was established, the outlined procedure would only bring the APD to the near vicinity of the image of the MOT. So finally fine tuning of the alignment was necessary using the signal from the APD. Nevertheless, this method greatly simplified the imaging alignment and it was crucial in making the experiment work.

2.5 Summary

In this chapter, a brief review of the specifics of the MOT used in the following experiments was presented. The main goal in building the MOT was not to achieve ultracold temperatures or very long lifetimes or in any other way “a state of the art” trap, but rather to prepare a dense sample of cold atoms on which experiments could be performed. As such, the MOT described was more than adequate and, although constructed without fancy vacuum chambers, very stable lasers, large beams or very precise magnetic field gradients, it was still a very good MOT for all our purposes.

Chapter 3 High Precision Spectroscopy of the $6D_{5/2}$ State in Cs

Although a lot is known about the atomic structure of alkali elements, not all of their energy levels have been probed or carefully measured. One of the main reasons for this incompleteness, is of course, the availability of laser frequencies near the corresponding eigenfrequencies. In the case shown in Fig. 1.2, the $6D_{5/2}$ level in atomic Cs was such an unexplored state. In particular, prior to our work, the hyperfine (hf) structure of this level was only poorly known, with the hf splitting measured with an accuracy of only 30% [9] while the linewidth has been only theoretically predicted. [57] Both of these parameters are crucial throughout all of our subsequent experiments; first because the hf splitting defines the interaction with other states, which could promote our three-level model to a more complex system of more than three eigenstates, and second because the atomic linewidth is a crucial parameter in all theoretical calculations that will follow. With the results to be presented here, the hf splitting is determined with an experimental accuracy of 1% and the atomic linewidth to 7%.

The study of the $6D_{5/2}$ state in Cs was limited prior to our work for two main reasons: the lack of laser frequencies near the eigenfrequency of the transition and the fact that to reach the $6D_{5/2}$ level from the ground state ($6S_{1/2}$) requires a two-photon absorption which is a much weaker process than usual one-photon absorptions. These problems were solved with progress in laser technology and in magneto-optical trapping. In particular, the resonant frequency for the two-photon transition $6S_{1/2} \rightarrow 6D_{5/2}$ corresponds to a laser wavelength close to 884 nm, which is at the edge of the operating region of our Ti:Sapphire laser.¹ On the other hand, spectroscopy on the MOT simplified the problem of two-photon absorption.

¹Today, commercial Ti:Sapphire lasers have operating ranges that can easily reach 920 nm.

3.1 Two-Photon Spectroscopy in a MOT vs. in a Vapor Cell

Conventional two-photon studies [58, 59] are usually carried out by implementing a scheme where the excitation fields enter the sample via two counter-propagating directions, Fig. 3.1(a). Hence, an atom absorbing a photon from each beam undergoes an almost Doppler free transition ($\omega'_1 + \omega'_2 \simeq \omega_1 + \omega_2$, assuming $\omega_1 \simeq \omega_2$) therefore making possible the observation of the internal structure of the state without the Doppler broadening that smears it out.² However, this method is not completely Doppler free because of subtleties introduced by the requirement to focus tightly the excitation beams in order to reach high enough intensities for the weak two-photon transition to take place. Contrary to this situation, spectroscopy on the MOT does not require counter propagating beams and also does not suffer from the problem of tight focusing because the atoms are cold, Fig. 3.1(b). Moreover, in the subsequent experiments the two-photon transition is excited by non-degenerate frequencies (852 *nm* and 917 *nm*) and hence counter propagation would not have completely solved the Doppler broadening problem since $\omega'_1 + \omega'_2 \simeq \omega_1 + \omega_2 + |(k_1 - k_2) \cdot v| \neq \omega_1 + \omega_2$ for widely spaced ω_1 and ω_2 .

An additional advantage of using a MOT, rather than a vapor cell, is that a MOT provides an atomic sample that is well localized. This is important for several reasons: first because focussing of the excitation beams must be such that there is almost uniform intensity across the sample, second because these beams must be tightly focused onto the atoms in order to reach high enough intensities and third because imaging is easier for a well localized sample. The first requirement is obvious in order to make intensity dependent measurements as in the nonclassical experiment described in Chapter 5. The second one becomes also obvious when one realizes that in the nonclassical experiment, the excitation rate is extremely small due to the low power (~ 1 *pW*) of the nonclassical fields. Finally, the third reason is justified since

²It is also possible to absorb two co-propagating photons. In this case there is going to be twice as much Doppler shift and this will contribute towards a broad residual Doppler background.

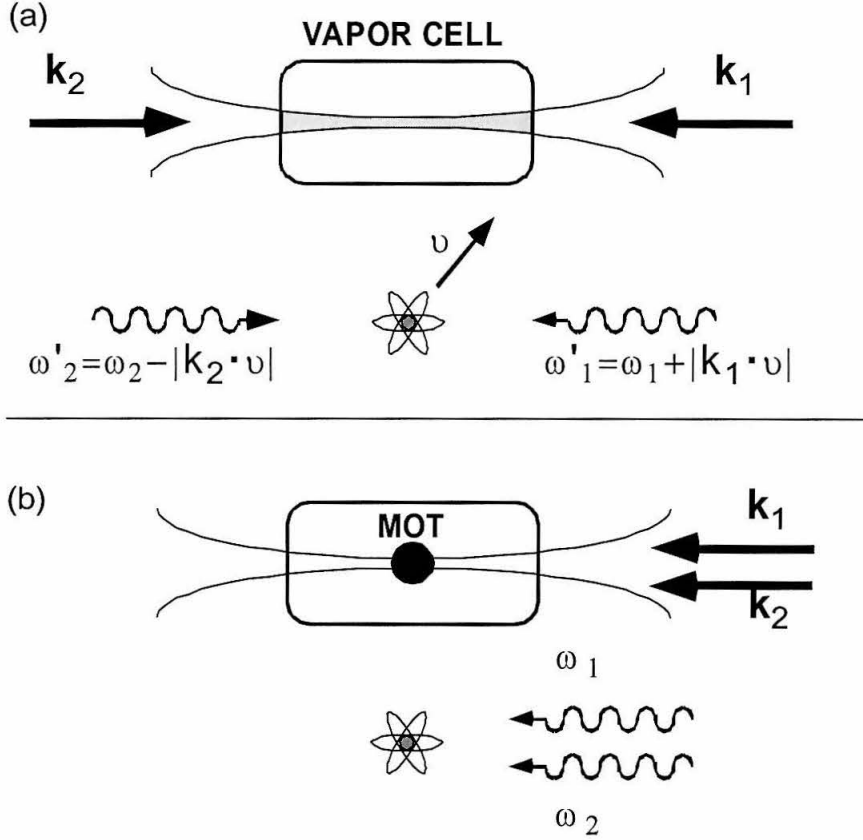


Figure 3.1: Doppler free spectroscopy: (a) using counter propagating beams in a vapor cell, (b) using co-propagating beams in a MOT.

the active area of the avalanche photodiode (APD) is only $150 \mu m \times 150 \mu m$.

To see how a localized sample is better than a vapor cell, one needs to consider, in addition to the above requirements, the total fluorescence signal I_F from the sample, which for an optically thin sample is given by

$$I_F = \frac{2\Gamma_2 P_o^2 n_a \xi}{\lambda} \arctan\left(\frac{L}{2z_o}\right) \quad (3.1)$$

as described in Ref. [7]. Here P_o is the excitation power, λ , the excitation wavelength, ξ is the overall collection and detection efficiency, Γ_2 , the two-photon cross section (defined by $R_2 = \Gamma_2 I_o^2$ with R_2 the two-photon excitation rate for an intensity I_o)

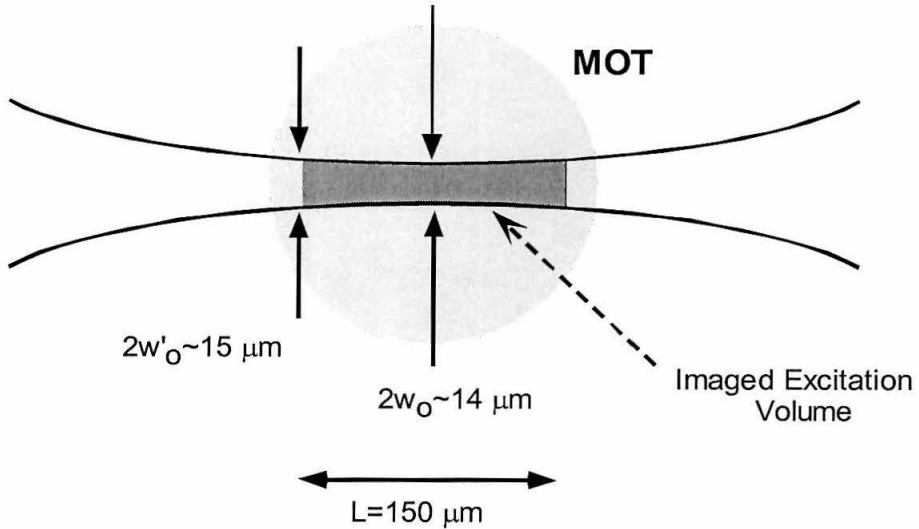


Figure 3.2: Focusing geometry of the excitation beam. Notice that the volume of excited atoms that is imaged may be smaller than the diameter of the trap.

and $z_o = \frac{\pi w_o^2}{\lambda}$, the Rayleigh length.[7] The waist of the excitation beam is given by w_o , and the length of the excitation volume is equal to L (see Fig. 3.2).

In the experiment the waist size was $w_o \simeq 7 \mu m$ and the length of the volume of excited atoms that was imaged was $L \simeq 150 \mu m$. Hence, $z_o \simeq 175 \mu m$ and $\arctan\left(\frac{L}{2z_o}\right) \simeq 0.4$. Note that the maximum value that the arctan can take is $\frac{\pi}{2}$. Also note that with this choice of parameters, the intensity variation across the imaged volume due to the beam divergence is less than 18%, as could easily be calculated from the geometry of Fig.3.2 (for a complete discussion on the Gaussian profile of laser beams, see Ref. [60]).

Despite of all these advantages, there is however a major disadvantage in doing spectroscopy with a MOT versus with a vapor cell. This is the decrease in density n_a and hence decrease in the overall signal I_F (notice the two scale proportionally to each other, Eq. (3.1)). In particular, for the MOT in the experiment the density is $n_a^{MOT} \sim 10^9 \text{ atoms/cm}^3$ while for “better” traps values of $10^{10} - 10^{12}$ are possible. In

contrast, a vapor cell of Cs heated up to $100^\circ C$ will have a vapor pressure of $\sim 7 \times 10^{-4}$ Torr, which corresponds to $n_a^{vapor} \sim 10^{13}$ atoms/cm³. Therefore, the atomic sample density for an experiment in the MOT is of the order of a 10000 smaller than what could have been in a vapor cell! However, not all of this gain in density can be utilized, and, in particular, two important factors cancel out a large portion of it: the residual Doppler broadening and the detuning from the intermediate state.

First, the residual Doppler broadening due to the non-degeneracy of the excitation beams, which was not included in Eq. (3.1), has to be taken into account. Notice that this is important for the experiments to be described because the excitation beams with wavelengths of 852 nm and 917 nm are separated by a large frequency interval. The magnitude of the residual Doppler broadening is of the order of $\sim |k_1 - k_2| v_{rms}(T)$, where $v_{rms}(T)$ is the rms velocity of the atoms at temperature T . For $100^\circ C$, this Doppler broadening is found to be about 7 times the linewidth, hence, the signal would decrease by roughly the same amount.

The second factor that reduces the overall two photon excitation signal is the detuning of the fields from the intermediate level. In particular, while for stationary atoms the excitation fields at 852 nm and 917 nm are resonant with the $|1\rangle \rightarrow |2\rangle$ and $|2\rangle \rightarrow |3\rangle$ transitions, respectively, in the case of moving atoms each of the two fields is detuned from the corresponding transition due to Doppler shifts. Although, in the case of counter-propagating beams, the overall two-photon transition ($|1\rangle \rightarrow |3\rangle$) is kept resonant (except for the residual Doppler broadening described above), the fact that the individual one-photon transitions ($|1\rangle \rightarrow |2\rangle$ and $|2\rangle \rightarrow |3\rangle$) are off-resonance will significantly reduce the two-photon excitation probability. The detuning from the intermediate state is of the order of $\Delta_D \sim \frac{|k_1+k_2|}{2} v_{rms}(T)$ which in our case is roughly equal to 60 atomic linewidths of the intermediate state. Hence, the signal I_F will be reduced approximately by a factor of $\Delta_D^2 \simeq 3600$.

Combining all these factors (i.e., density, residual Doppler broadening and detuning from the intermediate state) implies that using a MOT, instead of a vapor cell at $100^\circ C$, will result in signals roughly 2.5 times bigger. Clearly for better traps this factor increases significantly. In addition, the 852 nm and 917 nm beams are

generated in our experiment in co-propagating directions which makes it difficult to separate and implement a vapor cell scheme with counter-propagating beams such as that shown in Fig. (3.1). A further argument against using a vapor cell is that due to the residual Doppler broadening due to the non-degeneracy of the excitation beams, the hf states $6D_{5/2}F'' = 6$ and $6D_{5/2}F'' = 5$ start to mix, and, hence, the three-level system becomes a four level system, which complicates the interpretation of the results.

3.2 Experimental Setup

Turning now to the complete experimental setup, the main components of the spectroscopy experiment are shown in Fig. 3.3. The setup can be divided into four Blocks (I-IV) of different functional roles in the experiment. Block I is responsible for locking and scanning the master laser to the right transition for the two-photon experiments. Block II is the master laser producing the main beam for the excitation of the atoms. Block III is the trapping setup described in the previous chapter. Block IV is the detection and data acquisition part of the experiment.

Although each of these Blocks deserves special attention, here only Blocks I and IV will be described in detail. Block II is a standard Ti:Sapphire setup that has been discussed in the past [3, 4] and consists mainly of an Ar:Ion laser that pumps a homemade ring cavity containing the Ti:Sapphire crystal. Block III has already been discussed in the previous chapter. Therefore, the discussion will now concentrate on Blocks I and IV.

3.2.1 Locking and Scanning (Block I)

The capability of locking the master laser (Ti:Sapphire) to the two-photon transition and, in particular, to be able to choose a specific hf component was a crucial requirement throughout our experiments. In addition, for the spectroscopy of the $6D_{5/2}$ level, it was also crucial to be able to scan continuously the Ti:Sapphire laser (while keeping it locked) across the frequency range spanned by the hf components of the

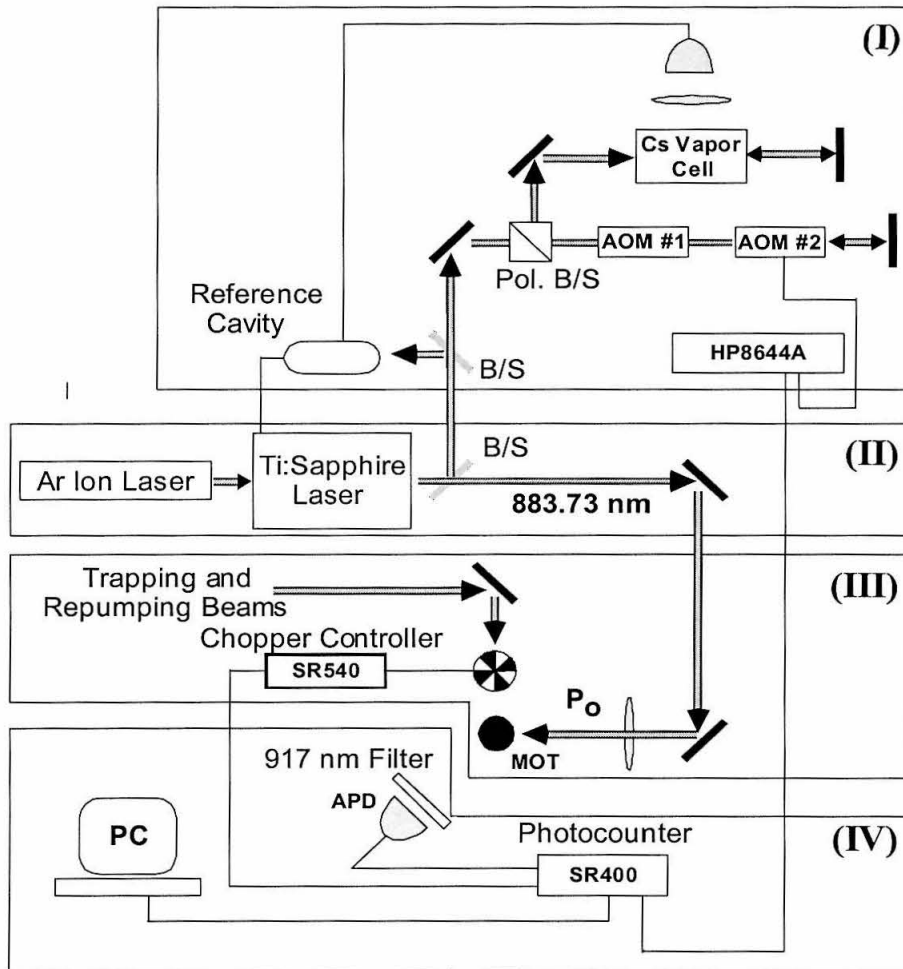


Figure 3.3: Experimental setup.

$6D_{5/2}$ state which is about 140 MHz . To lock the Ti:Sapphire a two step process is implemented, where first the Ti:Sapphire is locked a stable, high finesse cavity with linewidth of about 50 KHz and second the cavity is locked to the atomic transition. Direct locking of the Ti:Sapphire to the atomic transition was also possible and sometimes was used, but because the atomic linewidth is about 3 MHz , this lock is not as “tight” or robust as the first one. Once locked the laser was scanned by using tunable acousto-optic modulators as described below.

The locking signal was produced by observing the fluorescence from a Doppler

free two-photon absorption, $6S_{1/2}F = 4 \rightarrow 6D_{5/2}F''$ in a vapor cell which was heated to about $50^\circ C$ and through which an intense ($\sim 100 \text{ mW}$) beam was double passed. A detector placed at the top of the cell collected the fluorescence from the atoms; see Block I in Fig. 3.3. Note that a special oven had to be built for heating the cell since without a “full-jacket” oven, any cold spots on the cell and, in particular, the windows could easily be coated with Cs making them opaque. Hence, the oven was constructed in such a way so as to leave only three small holes for the excitation beams to get in and for the fluorescent signal to get out. The quality of the fluorescent signal from the cell was somewhat broadened, but still was good enough to distinguish all hf components, which were well separated in frequency, and enabled us to clearly choose which one to lock to. Because the $F'' = 6$ hf component was the strongest, throughout all our experiments the laser was always locked to this transition.

To tune the Ti:Sapphire, the frequency selection elements in the laser (thick and thin etalons and birefringent filter) were tuned so that the emitted light had a wavelength close to $\lambda_o \simeq 883.729 \text{ nm}$. An inseparable part of the tuning procedure was a wavemeter that guided us. Once the laser was close to λ_o , it was locked to the free standing reference cavity. The fine tuning was accomplished by scanning one of the mirrors of the cavity and having the laser follow until it reached the two-photon resonance $6S_{1/2}F = 4 \rightarrow 6D_{5/2}F'' = 6$. At this point the cavity was locked to the two-photon signal and hence the Ti:Sapphire was locked to the same transition as well. Note that the reading for the two-photon wavelength deviated from day to day from the above value of λ_o by as much as $\pm 0.002 \text{ nm}$ because of temperature and humidity variations in the room (the wavemeter measures wavelengths in air).

The next task was to devise a way to scan the Ti:Sapphire laser across all hf components F'' of the $6S_{1/2}F = 4 \rightarrow 6D_{5/2}F''$ transition. This was done by using a locking beam that was frequency shifted from the Ti:Sapphire frequency. In particular, in Fig. 3.3 Block I, we see that the vapor cell is pumped by the locking beam, which has first been double passed through two acousto-optic modulators, AOM1 and AOM2. Since the Ti:Sapphire is always locked to a signal corresponding to the $6S_{1/2}F = 4 \rightarrow 6D_{5/2}F'' = 6$ transition, the frequency of this locking beam is always

on resonance with this transition, i.e., $2\omega_{Lock-Beam} = \omega_{31}$, where ω_{31} is the eigenfrequency of the $6S_{1/2}F = 4 \rightarrow 6D_{5/2}F'' = 6$ transition. However, this beam is shifted from the Ti:Sapphire frequency by $\delta\omega$, i.e., $\omega_{Lock-Beam} = \omega_{Ti:Sapphire} + \delta\omega$ which implies that $2\omega_{Ti:Sapphire} = \omega_{31} - 2\delta\omega$. The reason for using two AOM's is that in order to scan around ω_{31} and since each AOM operates at a large offset frequency (~ 80 MHz in our case), a single AOM would not work. However, two AOM's, one that upshifts the frequency and the other that downshifts it, with a net offset equal to 0 results in tunability around zero offset. Then by scanning one of the two AOM's using the *HP8644A* function generator, the Ti:Sapphire frequency was scanned around the $\frac{\omega_{31}}{2}$ frequency. Note that because of the double passing of the beams from the AOM's, the frequency scan is twice that provided by the function generator.

3.2.2 Detection and Data Acquisition (Block IV)

We now turn to Block IV of Fig. 3.3 that shows the detection and data acquisition components of the experiment. The rate of two-photon excitation of the $6S_{1/2}F = 4 \rightarrow 6D_{5/2}F''$ transition was monitored by observing the fluorescent decay from the $6D_{5/2}F'' \rightarrow 6P_{3/2}F' = 5$ transition which has a wavelength close to $\lambda_2 \simeq 917$ nm. The observation at λ_2 was very convenient because all other laser beams in the experiment were at different wavelengths. Recall that the two-photon excitation $6S_{1/2}F = 4 \rightarrow 6D_{5/2}F''$ has eigenfrequency corresponding to a wavelength $\lambda_o \simeq 884$ nm while the trapping lasers, resonant with the $6S_{1/2}F = 4 \rightarrow 6P_{3/2}F' = 5$, have wavelength $\lambda_1 \simeq 852$ nm, see Fig. 1.2. Hence, by using 917 nm interference (notch) filters to isolate the detector, only the radiation from the $6D_{5/2}F'' \rightarrow 6P_{3/2}F' = 5$ decay is measured.

Before proceeding to the description of the rest of Block IV, the mechanical chopper, which is actually part of Block III, must be discussed in more detail. This chopper was placed in the path of the trapping and repumping beams and was synchronized so that both beams are chopped ON/OFF simultaneously. This means that the beam sizes had to be about the same at the chopper side and small compared to the size

of the chopper slots so that the transit time between the ON and OFF parts of the cycle would be small. The experiment has then two phases: the ON (trapping beams ON) phase during which the MOT is maintained and the OFF (trapping beams OFF) phase, during which the measurements are performed. Note that ON/OFF chopping is needed for two reasons, first because even though one or two 917 nm interference filters are placed in front of the APD, there is still noticeable background during the ON part of the cycle, and second because when the beams are ON, there is significant light perturbation (Stark shift and power broadening) to the atoms in the MOT. The operating speed for ON/OFF cycle was 4 KHz.

Returning now to Block IV, the output of the APD was fed into the SR400 photon counter which was interfaced with a PC using the manufacturer's control software. In addition to the signal from the APD, a trigger signal from the chopper was also fed into the SR400 to synchronize the data acquisition with the ON and OFF parts of the experimental cycle. Data acquisition was gated and provided two streams of data, the ON and OFF sequences. The trigger signal for the gating was provided by a photodiode placed at the exit path from the trapping cell of the T_2 trapping beam; see Fig. 2.1.

Finally, to perform frequency dependent measurements, frequency markers are needed that coincide with the scanning of the Ti:Sapphire laser. These markers were provided by the function generator HP8644A that was used to scan the Ti:Sapphire and were imported onto the computer through the photon counter. Note that the SR400 counter has only two gates, A and B. Hence, the signal was either for both the OFF and ON parts of the experimental cycle or for one of them and the frequency markers. The first case was used to measure the relative shift of the spectra with and without the trapping beams so that the Stark shift and power broadening due to the trapping beams can be quantified. The second case was implemented to get an absolute frequency calibration and measure the spacing of the hf components.

3.3 Theory of hf Structure for the $6D_{5/2}$ State

Before presenting the results of the spectroscopy experiment it is worth briefly reviewing the theory of hf structure as applied to the $6D_{5/2}$ level. On this subject one can find references in many graduate level Quantum Mechanics textbooks as well as in more advanced books on the subject.[61, 62, 63] Recall that the hf structure is the result of the coupling of the nuclear magnetic moment I with the total angular momentum of the electron J and that the hf Hamiltonian is given by

$$H_{hf} = \hbar \left[a (\mathbf{I} \cdot \mathbf{J}) + b \left(\frac{3 (\mathbf{I} \cdot \mathbf{J})^2 + \frac{3}{2} (\mathbf{I} \cdot \mathbf{J}) - I J (I + 1) (J + 1)}{2I J (2I - 1) (2J - 1)} \right) + \dots \right] + H_{hf}^Z. \quad (3.2)$$

Here a is the magnetic dipole and b the electric quadrupole coefficients in a multipole expansion while higher order terms are ignored. The term H_{hf}^Z is the Zeeman splitting in the presence of magnetic fields, which is negligible for the magnetic fields in our case.

For Cs^{133} the nuclear magnetic moment is $I = \frac{7}{2}$ and the state of interest $6D_{5/2}$ has $J = \frac{5}{2}$. Hence, when I is combined with J under the quantum mechanics rules for addition of angular momentum, we find that the $6D_{5/2}$ state has six hf components, with corresponding quantum numbers $F'' = 1, 2, 3, 4, 5, 6$. Assuming that the energy shift of each of these levels from the unperturbed state is given by $\Delta E_{F''} = \hbar \delta\omega_{F''}$, one can easily plug in Eq. (3.2) the values for I and J to obtain the position of the various hf energy levels. In particular, it can be shown that

$$\delta\omega_1 = -\frac{45}{4}a + \frac{15}{28}b, \quad (3.3)$$

$$\delta\omega_2 = -\frac{37}{4}a + \frac{1}{4}b, \quad (3.4)$$

$$\delta\omega_3 = -\frac{25}{4}a - \frac{1}{14}b, \quad (3.5)$$

$$\delta\omega_4 = -\frac{9}{4}a - \frac{3}{10}b, \quad (3.6)$$

$$\delta\omega_5 = \frac{11}{4}a - \frac{37}{140}b, \quad (3.7)$$

and

$$\delta\omega_6 = \frac{35}{4}a + \frac{1}{4}b. \quad (3.8)$$

Notice that, as it should be, the center of gravity of these hf components is the same as the unperturbed level, i.e., $\sum_{F''} \Delta E_{F''} (2F'' + 1) = 0$.

Finally, from Eqs. (3.3)-(3.8) it can be shown that the splittings $\delta\omega_{ij} \equiv \delta\omega_i - \delta\omega_j$ of the hf components are equal to

$$\delta\omega_{12} = -2a + \frac{2}{7}b, \quad (3.9)$$

$$\delta\omega_{23} = -3a + \frac{9}{28}b, \quad (3.10)$$

$$\delta\omega_{34} = -4a + \frac{8}{35}b, \quad (3.11)$$

$$\delta\omega_{45} = -5a - \frac{1}{28}b, \quad (3.12)$$

and

$$\delta\omega_{56} = -6a - \frac{18}{35}b. \quad (3.13)$$

As it turns out $a < 0$ and since $b \ll a$ (recall that a and b correspond to successive orders in a multipole expansion), it is clear from Eqs. (3.3)-(3.8) that the energy level of the $F'' = 1$ hf component is the highest, while that of $F'' = 6$ is the lowest.

3.4 Results

Figure 3.4 shows the hf structure of the three energy levels of atomic Cs^{133} that we are considering. The three hf components shown in bold face are the ones that will be used to realize a three-level system in the subsequent experiments. As has already been explained, for the purpose of the current spectroscopy experiment on the $6D_{5/2}$ state, the atoms have been excited using a tunable laser around $\lambda_o \simeq 884 \text{ nm}$ of power P_o . The rate of two-photon excitation was monitored by measuring the fluorescence intensity I_F at $\lambda_F = 917 \text{ nm}$ from the $6D_{5/2}F'' \rightarrow 6P_{3/2}F' = 5$ decay. The trapping beams, which are turned off during the measurements so that they would not perturb

the atomic energy levels, are resonant with the $6S_{1/2}F = 4 \rightarrow 6P_{3/2}F' = 5$ transition, have wavelength $\lambda_T \simeq 852 \text{ nm}$ and total power (sum of powers of all five trapping beams, see Fig. 1.3) P_T .

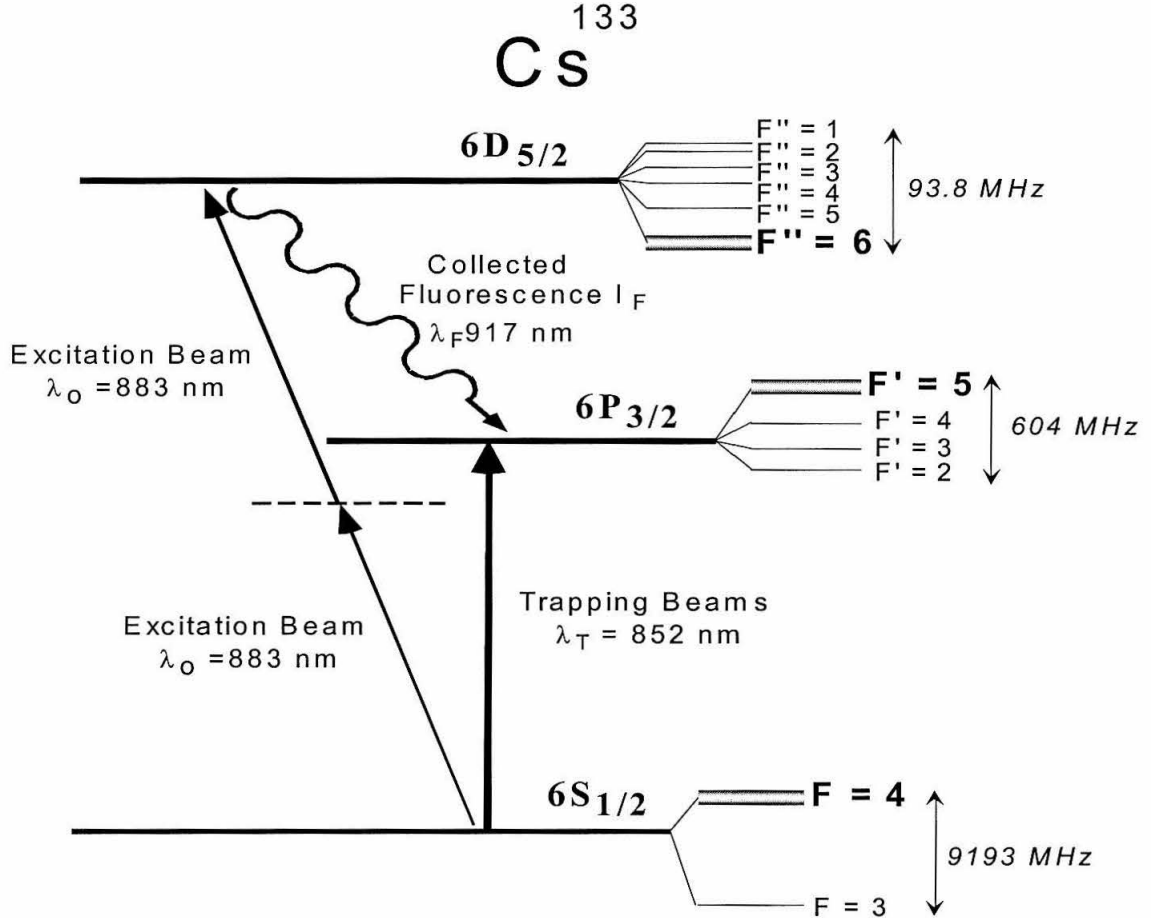


Figure 3.4: Hyperfine structure of atomic Cs^{133} .

Figure 3.5 shows a typical spectrum obtained from this experiment. Notice that because of the two-photon selection rule $|F - F''| \leq 2$, the $6D_{5/2}F'' = 1$ state is inaccessible from the ground state $6S_{1/2}F = 4$ and hence only five hf components can be observed. Also note that to scan across a frequency range ω of the hf components in Fig. 3.5, we only need to tune the frequency of the λ_o excitation beam by $\frac{\omega}{2}$ since the excitation is a two-photon process. Numerous spectra such as the one of Fig. 3.5

have been obtained and have been analyzed by fitting to them multi-Lorentzian curves with variable peak positions, peak amplitudes and linewidths. Then, by compiling the data various results about the $6D_{5/2}$ state of atomic Cs^{133} are derived.³

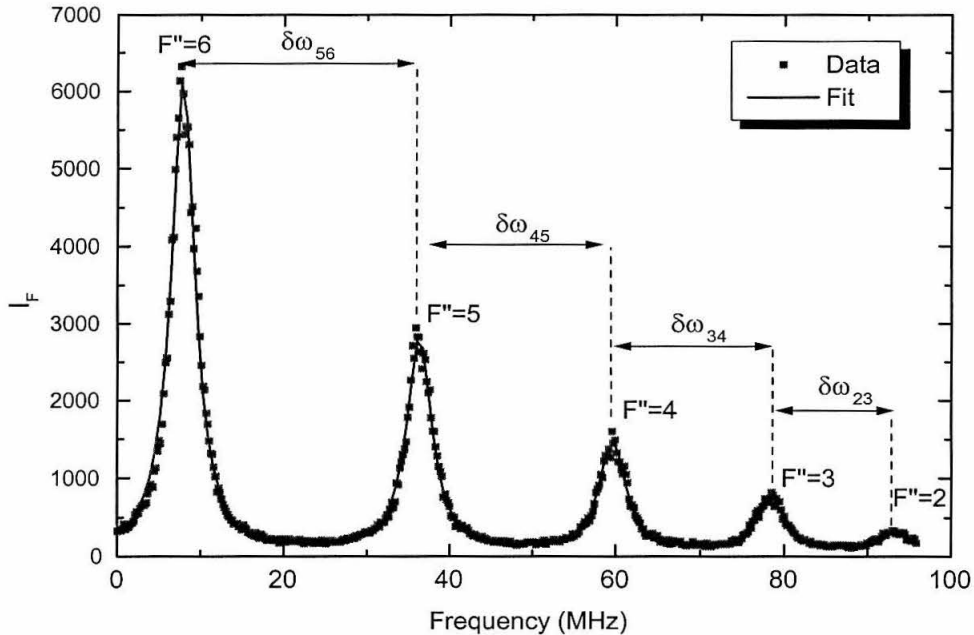


Figure 3.5: Hyperfine spectrum of the $6D_{5/2}$ state in Cs^{133} .

3.4.1 The a and b Coefficients

The first goal is to measure the magnetic dipole a and electric quadrupole b coefficients that characterize the hf structure of the $6D_{5/2}$ as described by Eqs. (3.3)-(3.8). To do so we compiled all our results for the various splittings (obtained by multi-Lorentzian fits to spectra similar to that of Fig. 3.5), and by averaging all available data we arrived at the best estimates for each of the hf splittings. Given the relation of these splittings to the a and b coefficients as described by Eqs. (3.10)-(3.13), we thus have an overspecified system of four equations with two unknowns. Performing a standard

³The raw data and details about the analysis (multi-Lorentzian fits and least square procedure) can be found in Lab Book # 3 of NPhG, p. 56-83.

least square fit to this data gives the best fit values for the a and b coefficients. The derived values are $a = -4.69 \pm 0.04 \text{ MHz}$ and $b = 0.18 \pm 0.73 \text{ MHz}$. Contrasting our results with the previous measurement of $a = -3.6 \pm 1.0 \text{ MHz}$, [9] we see that in addition to a 30-fold improvement in accuracy, we have also pinpointed a to a value that is 1σ away from the previous measurement.

3.4.2 Linewidths

The next atomic property to be measured is the natural linewidth of the hf components. Because this measurement is subject to power broadening from the excitation beam, we have chosen to make measurements as a function of power P_o and extrapolate the data back to zero power. Figure 3.6 shows our data along with the extrapolated value of $\gamma_3 = 3.2 \pm 0.2 \text{ MHz}$ [7] and the theoretically predicted value of $\gamma_3^{\text{Theory}} = 2.5 \text{ MHz}$ [57] which is significantly different from the measurement.

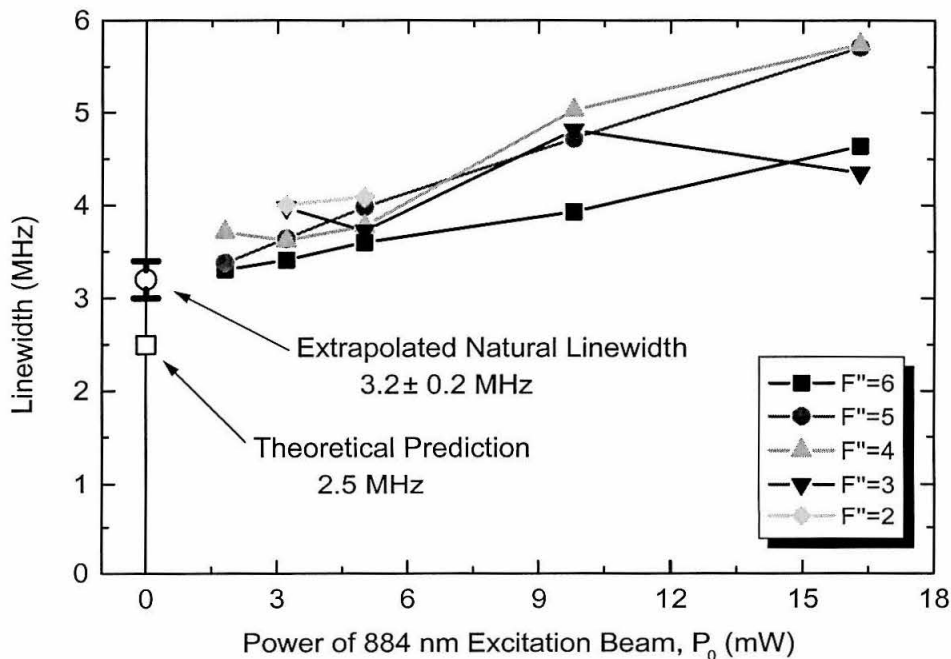


Figure 3.6: Linewidth of the hf components of the $6D_{5/2}$ state as a function of power of the excitation beam.

3.4.3 AC Stark Shift of the Ground State

As described earlier, the experiment is performed in two steps: first the trap is formed using intense 852 *nm* fields (resonant with the $6S_{1/2}F = 4 \rightarrow 6P_{3/2}F' = 5$ transition) and then by turning OFF these beams the measurements are taken. However, it is also possible to take measurements while the trapping beams are ON, but because the trapping beams Stark shift the ground state, we expect the excitation spectrum taken with the trapping beams ON to be shifted relative to that taken with the trapping beams OFF. Figure 3.7 demonstrates this with three spectra taken under different conditions. The first spectrum (a) is taken with the trapping beams OFF and hence serves as benchmark for the unshifted spectrum. The other two spectra (b) and (c) are taken with the trapping beams ON and as expected they are shifted (and broadened) relative to (a). The total power of the trapping beams is $P_T^{(b)} \simeq 3.1$ *mW* and $P_T^{(c)} \simeq 10.4$ *mW* for the (b) and (c) spectra, respectively.

To quantify the power broadening and Stark shift of the ground state as a function of trapping beam power, we use the shifted spectra (b) and (c) shown in Fig. 3.7. In particular, for spectrum (b) we find that the mean shift of the various hf components relative to those of spectrum (a) is about 3.4 *MHz*, while for spectrum (c) it is about 8.4 *MHz*. The Stark shift $\Delta^{Stark} = cP_T$ is proportional to the power P_T of the perturbing (trapping) field, where c is a constant of proportionality. Therefore, the value of c is estimated from spectrum (b) to be 1.1 *MHz/mW* and from spectrum (c) to be 0.81 *MHz/mW*. Taking a simple average of the two yields a value of $c = 0.95$ and hence $\Delta^{Stark}(P) \simeq (0.95 \frac{MHz}{mW}) P$.

Similarly, the mean power broadening is estimated for each of the two spectra and it is found that for spectrum (b) the mean linewidth of the hf components is $\gamma^{(b)} \sim 1.9\gamma$ while for spectrum (c) is about $\gamma^{(c)} \sim 3.3\gamma$, where $\gamma \simeq 3.8$ *MHz* is the linewidth from spectrum (a). Notice that γ is not the natural linewidth because the two-photon excitation beam at $\lambda_o = 884$ *nm* has power $P_o \simeq 3.3$ *mW* and causes a non-negligible power broadening of 0.6 *MHz*. The power broadening of the ground state due to the trapping beams can then be expressed as $\gamma(P_T)^2 = \gamma^2 + kP_T$, [64]

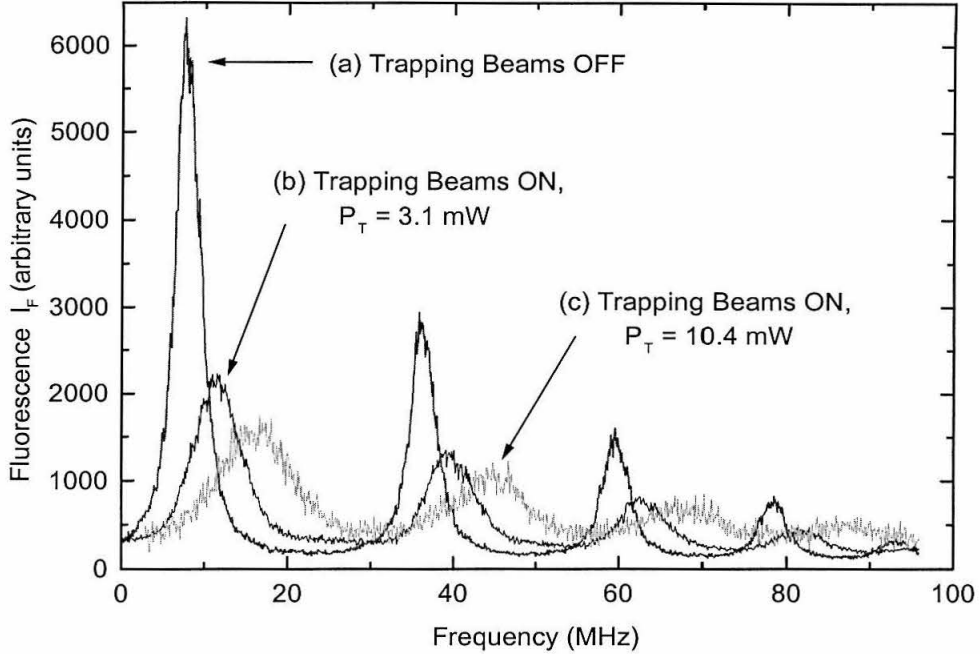


Figure 3.7: Two-photon excitation spectra, which show Stark shifts and power broadening due to perturbation of the ground state by the trapping beams. a) Trapping beams are OFF, b) Trapping beams ON, total power $P_T^{(b)} \sim 3.1 \text{ mW}$, c) Trapping beams ON, total power $P_T^{(c)} \sim 10.4 \text{ mW}$. The power of the 884 nm , two-photon excitation beam, is 3.3 mW in each case.

where γ is the linewidth from spectrum (a), P_T the power of the trapping beams and k a constant of proportionality. Hence, from spectrum (b) the value of k is estimated to be $0.85\gamma^2/\text{mW}$ while spectrum (c) gives in good agreement with (b) that $k \sim 0.95\gamma^2/\text{mW}$. Therefore, an average estimate of the power broadening of the ground state due to the trapping beams is given by $\gamma(P_T) \simeq \gamma\sqrt{1 + \frac{P_T}{1.1\text{mW}}}$.

3.4.4 “Cross-Talk” between hf States

The concept of “cross-talk” (mixing) between different hf components is an important constraint for realizing a pure three-level system. For example, if the atoms are to be excited from the $6S_{1/2}F = 4$ level via a two-photon absorption and the excitation laser is tuned somewhere between the $F'' = 6$ and $F'' = 5$ energy levels, then the

resulting absorption S will be primarily due to the sum of absorptions that lead to the $F'' = 6$ and $F'' = 5$ levels. Hence, the upper level must be described as a non-degenerate two-level manifold, and the overall atomic system is not any more an isolated three-level system. To quantify in simple terms this mixing we can define the total absorption S to be the incoherent sum of five absorptions, S_6, S_5, S_4, S_3 and S_2 corresponding to excitations to the various $F'' = 6, 5, 4, 3$ and 2 levels, respectively. Then $S = S_6 + S_5 + S_4 + S_3 + S_2$ and the mixing of the $F'' = 2, 3, 4$ and 5 into the $F'' = 6$ level may be quantified by the ‘‘cross-talk’’ ratio defined to be $m \equiv \frac{S_5+S_4+S_3+S_2}{S_6}$ which needs to be as small as possible. Since each of the S_i has a Lorentzian shape (see Fig. 3.5) of about the same linewidth $\gamma \sim 3 \text{ MHz}$, we have that

$$m \simeq \frac{\frac{A_2\gamma^2}{\gamma^2+(\omega-\delta\omega_{26})^2} + \frac{A_3\gamma^2}{\gamma^2+(\omega-\delta\omega_{36})^2} + \frac{A_4\gamma^2}{\gamma^2+(\omega-\delta\omega_{46})^2} + \frac{A_5\gamma^2}{\gamma^2+(\omega-\delta\omega_{56})^2}}{\frac{A_6\gamma^2}{\gamma^2+\omega^2}}, \quad (3.14)$$

where ω is the frequency of the excitation laser relative to the frequency of the $F'' = 6$ component and $\delta\omega_{i6}$ are the frequency splittings between the $F'' = 6$ and $F'' = i$ hf components. The amplitudes A_i are the amplitudes of the various components of Fig. 3.5 and are roughly equal to $\frac{A_2}{A_6} : \frac{A_3}{A_6} : \frac{A_4}{A_6} : \frac{A_5}{A_6} = 0.5 : 0.25 : 0.13 : 0.04$. The splittings $\delta\omega_{i6}$ are equal to $\{\delta\omega_{26}, \delta\omega_{36}, \delta\omega_{46}, \delta\omega_{56}\} \simeq \{84.4, 70.4, 51.6, 28.1\} \text{ MHz}$.

Figure 3.8 shows the ‘‘cross-talk’’ m versus the probe frequency ω . When $\omega = 0$ then the excitation laser is on exact resonance with the $F'' = 6$ hf component and the m is close to minimum ($m(\omega = 0) \simeq 0.008$). On the contrary when $\omega = \delta\omega_{i6}$ then the contribution comes mostly from the $F'' = i$ hf component and in that case $m > 40$. Clearly, if we want to have the atom as a purely three-level system, we must constraint ω to be close to resonance with the $F'' = 6$ hf component. Setting a rather arbitrary limit of 5% for the allowed contribution to the absorption S from other hf states ($F'' < 6$) constraints the deviation from resonance for the excitation frequency to be $-11 \lesssim \omega \lesssim 6 \text{ MHz}$.

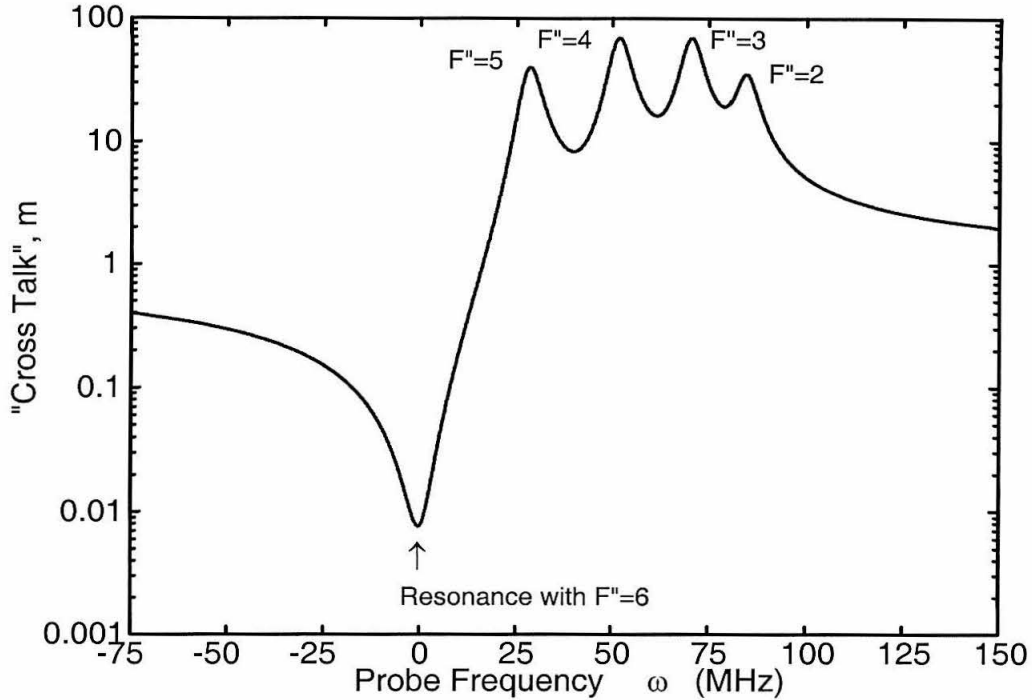


Figure 3.8: Cross-talk m as a function of the probe frequency ω ($\omega = 0$ is the resonant frequency with the $F'' = 6$ state).

3.5 Summary

In this chapter the investigation of the $6D_{5/2}$ state of atomic Cs^{133} has been presented. By developing capabilities for two-photon spectroscopy in a magneto-optical trap, we were able to determine accurately the hf structure of the $6D_{5/2}$ level and measure several things. In particular, we measured to 1% the magnetic dipole a and electric quadrupole b coefficients that determine the hf splittings. We also measured the natural linewidth and estimated the Stark shift and power broadening of the ground state due to the trapping beams. Finally, we quantified the “cross-talk” of the hf components in two-photon excitation.

Chapter 4 Optical Parametric Oscillator

In the previous two chapters the experimental techniques that have been developed to perform our experiments and in particular the procedures implemented to monitor the two-photon excitation of a three-level atom have been described. In this chapter the focus will be on the source of nonclassical radiation, which throughout the subsequent experiments will be a subthreshold optical parametric oscillator (OPO).

Optical parametric oscillators have been used for many years in quantum optics to generate and study nonclassical states of light.[65, 66, 67, 68] In fact, a very large portion of quantum optics involves, in one way or the other, the use of some sort of an OPO which makes virtually impossible the complete coverage of all aspects of OPO's in the present discussion. Instead, the discussion here concentrates on the particular OPO used in our own experiments and a detailed description of its various modes of operation will be given.

In its most general form, an OPO is simply a nonlinear crystal, characterized by a non-linearity $\chi^{(2)}$, placed inside an optical cavity in-order to build up the signal and idler output fields. This basic configuration is shown in Fig. 4.1 where, in addition to the crystal and the cavity, the pump laser at frequency ω_p and the generated signal and idler fields at frequencies ω_s and ω_i , respectively, are also shown.

From energy conservation the relation $\omega_p = \omega_s + \omega_i$ must be satisfied. Note that the frequencies ω_s and ω_i must be in resonance with the optical cavity while the pump frequency is usually not, although cases where ω_p builds up around the OPO have been considered.[69, 70] Also note that as a result of the conversion of a single pump photon into two (signal and idler), the two output photons are highly correlated with each other. These correlations give rise to the nonclassical nature of the OPO output and the squeezed spectrum that characterizes it.

Depending on whether or not the signal and idler frequencies are degenerate, the OPO is said to operate in a degenerate mode (DOPO) for which $\omega_s = \omega_i = \frac{\omega_p}{2}$, or in a

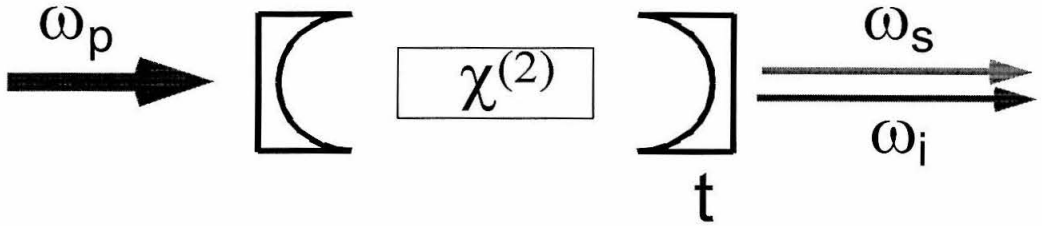


Figure 4.1: A basic OPO consists of a non-linear crystal, $\chi^{(2)}$ inside an optical cavity. The OPO is pumped by a laser at frequency ω_p and generates a signal and idler output at frequencies ω_s and ω_i , respectively.

non-degenerate mode (NDOPO) for which $\omega_s \neq \omega_i$. The output coupler of the OPO has field transmissivity t (see Fig. 4.1) which translates to a cold cavity (i.e., without the pump) linewidth for the OPO of $\gamma_{OPO} \equiv \gamma_o$. Note that the cavity linewidth changes when the pump is on; see Ref. [12].

4.1 OPO Configuration

4.1.1 Cavity Elements

Turning now to our OPO, we begin the discussion by describing the geometry configuration in the experiments shown in Fig. 4.2. Contrary to the simplified OPO of Fig. 4.1, the geometry implemented in our experiments is a folded ring cavity (composed of the mirrors M_{IN} , M_{OUT} , M_1 and M_2) and is the same geometry that was used in previous experiments by our group.[3, 4] The main reason for using a ring cavity is that the total intracavity losses in a ring configuration are only half of those in a standing wave cavity, while the folded configuration permits the angles of incidence on the mirrors to be kept small in order to avoid birefringence from the curved mirrors (M_{IN} and M_{OUT}) that effectively acts as a loss mechanism. The nonlinear material that was used is a $KNbO_3$ crystal of about 10 *mm* length.¹

¹In the lab this crystal was marked as C15. Its properties were carefully measured by E. S. Polzik. However, over time the quality of the crystal degraded and during our experiments apparent bulk defects, “stripes” inside the crystal, were present. For a summary of the properties of the crystal,

The OPO is usually operating at one of two pump frequencies corresponding to pump wavelengths of $\lambda_P \simeq 426 \text{ nm}$ and $\lambda_p \simeq 442 \text{ nm}$, respectively. For the first case ($\lambda_P \simeq 426 \text{ nm}$) the OPO was always operated in the degenerate mode, producing correlated signal and idler beams at $\lambda_s = \lambda_i \simeq 852 \text{ nm}$, while in the second case ($\lambda_p \simeq 442 \text{ nm}$) the OPO was used as either a DOPO with $\lambda_s = \lambda_i \simeq 884 \text{ nm}$ or as a NDOPO with $\lambda_s \simeq 852 \text{ nm}$ and $\lambda_i \simeq 917 \text{ nm}$. In both cases the mirrors M_{IN} , M_1 and M_2 are high reflectors for the IR (signal and idler) frequencies and transmit the pump frequency ($t_{426}^2 \simeq t_{442}^2 \gtrsim 0.95$). The output coupler M_{OUT} has IR transmission $t_{852}^2 \simeq 0.105$ for the case $\lambda_P \simeq 426 \text{ nm}$ and $t_{852}^2 \simeq t_{884}^2 \simeq t_{917}^2 \simeq 0.07$ for the case $\lambda_p \simeq 442 \text{ nm}$ and also transmits the pump. To switch between the two, the mirror M_{OUT} is physically replaced.

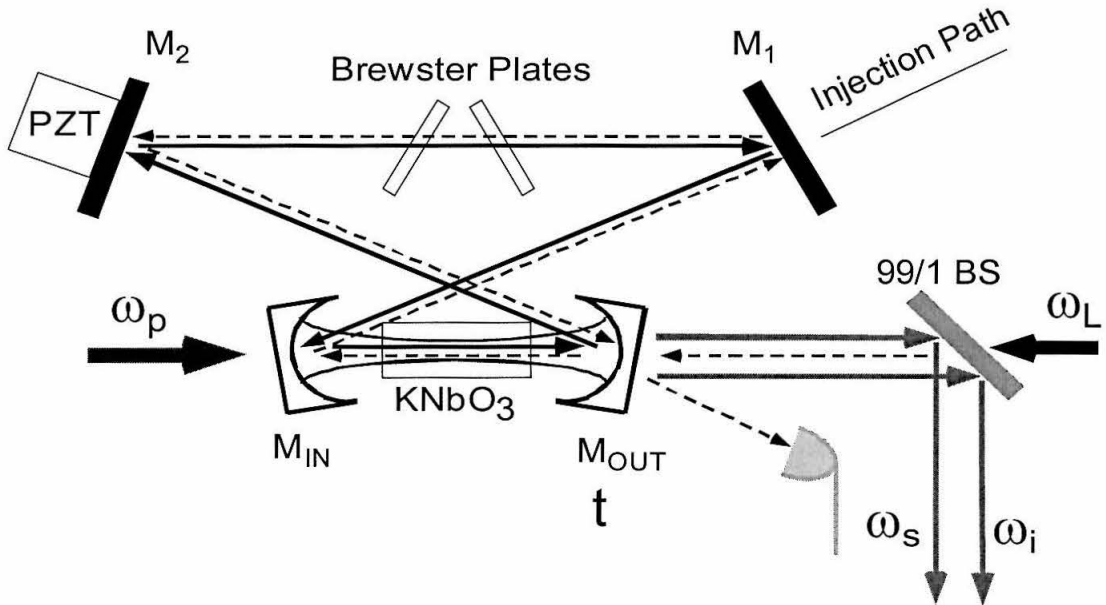


Figure 4.2: OPO geometry.

The total passive losses (in power) of the cavity are usually less than 0.5% and see the list compiled by E. S. Polzik in Lab Book # 7 of N.Ph.G., p. 35.

those due to light induced absorption about 1%. [71] Therefore, the total power losses (including the output coupler transmission t) are about $\delta_L \simeq 12\%$ for the case of operating the OPO with a pump frequency corresponding to $\lambda_p \simeq 426 \text{ nm}$ and $\delta_L \simeq 8.5\%$ for the case of $\lambda_p \simeq 442 \text{ nm}$. Hence, the finesse of the cavity, given by $\mathcal{F} = \frac{\pi\sqrt{1-\delta_L}}{1-\sqrt{1-\delta_L}}$, is $\mathcal{F} \simeq 50$ for the case of $\lambda_p \simeq 426 \text{ nm}$ and $\mathcal{F} \simeq 71$ for $\lambda_p \simeq 442 \text{ nm}$. The total length of the OPO cavity is about $L \simeq 46 \text{ cm}$ and hence the free spectral range is $FSR = \frac{c}{L} \simeq 650 \text{ MHz}$ from which we calculate the cold cavity linewidth $\gamma_o = \frac{FSR}{\mathcal{F}}$ to be $\frac{\gamma_o}{2\pi} \simeq 13 \text{ MHz}$ for the case when we operate the OPO with $\lambda_p \simeq 426 \text{ nm}$ and $\frac{\gamma_o}{2\pi} \simeq 9 \text{ MHz}$ for $\lambda_p \simeq 442 \text{ nm}$. Note that γ_o is the FWHM value of the linewidth.

The last element in the cavity is a set of Brewster windows fixed on two counter rotating tilt mounds. The purpose of this set of plates is to tune dispersively the length of the OPO so that in the NDOPO operating mode double resonance for the desired ω_s and ω_i frequencies can be achieved. These windows are positioned with respect to the beam path at an angle close to the Brewster angle so as to minimize losses. The reason for using two instead of just one is of course to avoid misalignment due to beam displacement of the OPO as the plates are tilted.

4.1.2 Beam Paths

Because of the ring configuration of the OPO, there are two distinct counter-propagating paths within the cavity (see Fig. 4.2). The main path is defined by the direction of the pump field and it is also the direction of the signal and idler propagation. The opposite path is used for locking the OPO, and a beam counter propagating to the signal and idler is reflected from the output coupler M_{OUT} onto the locking detector. In order to minimize the degradation of the signal and idler beams, the locking beam is brought into the OPO through a 99/1 beamsplitter.

One more injected beam through M_1 (along the direction of the signal and idler propagation) serves as a probe beam to measure the phase-sensitive gain of the OPO and to check if the OPO is in resonance with the atomic transitions (see below). This beam is turned off during the experiments.

4.1.3 OPO Locking

To lock the OPO we implement the well established FM stabilization technique of Ref. [72]. Here the locking beam (like all other beams originating from the master-laser which is the Ti:Sapphire) has FM sidebands at $\pm 27.5 \text{ MHz}$. When reflected from the OPO, this locking beam is detected on a fast photodiode, the photocurrent of which is demodulated by mixing with a signal from the RF generator at 27.5 MHz . The demodulated signal is amplified, high-pass filtered and fed into a HV amplifier that drives the PZT of M_2 so that the cavity stays in resonance with the locking frequency ω_L .

To avoid any cross-talk of the locking beam with the signal and idler frequencies due to backscattering, the locking frequency ω_L is detuned by about 240 MHz from the master-laser (Ti:Sapphire). This is achieved by double passing the locking beam through a tunable acousto-optic modulator. Then the OPO is locked to one of the transverse spatial modes of the locking beam that coincides with the longitudinal modes of the signal and idler beams that we want the cavity to be resonant with. Note that the master-laser frequency is ω_o , the OPO pump frequency (generated by doubling of the Ti:Sapphire laser frequency) is $2\omega_o$, the signal and idler frequencies are $\omega_{s,i} = \omega_o \pm \Delta$ and the locking beam that also originates from the same Ti:Sapphire laser has frequency $\omega_L \simeq \omega_o + 240 \text{ MHz}$; see Fig. 4.3. Hence, in the degenerate operation of the OPO, $\omega_{s,i} = \omega_o \neq \omega_L$, while for the NDOPO we have that $|\omega_{s,i} - \omega_L| \gg 240 \text{ MHz}$ since $\Delta \gg 240 \text{ MHz}$. In other words, in both the DOPO and NDOPO, the locking beam frequency is at least 240 MHz away from the signal and idler frequencies minimizing in this way the possibility of contaminating the squeezing by unwanted radiation.

4.1.4 Triangular Cavity

Finally, to complete the discussion about the OPO setup, notice that in Fig. 4.3 the pump beam passes through a triangular cavity on its way from the doubling cavity to the OPO. This cavity is used as a transfer cavity to modematch the pump beam

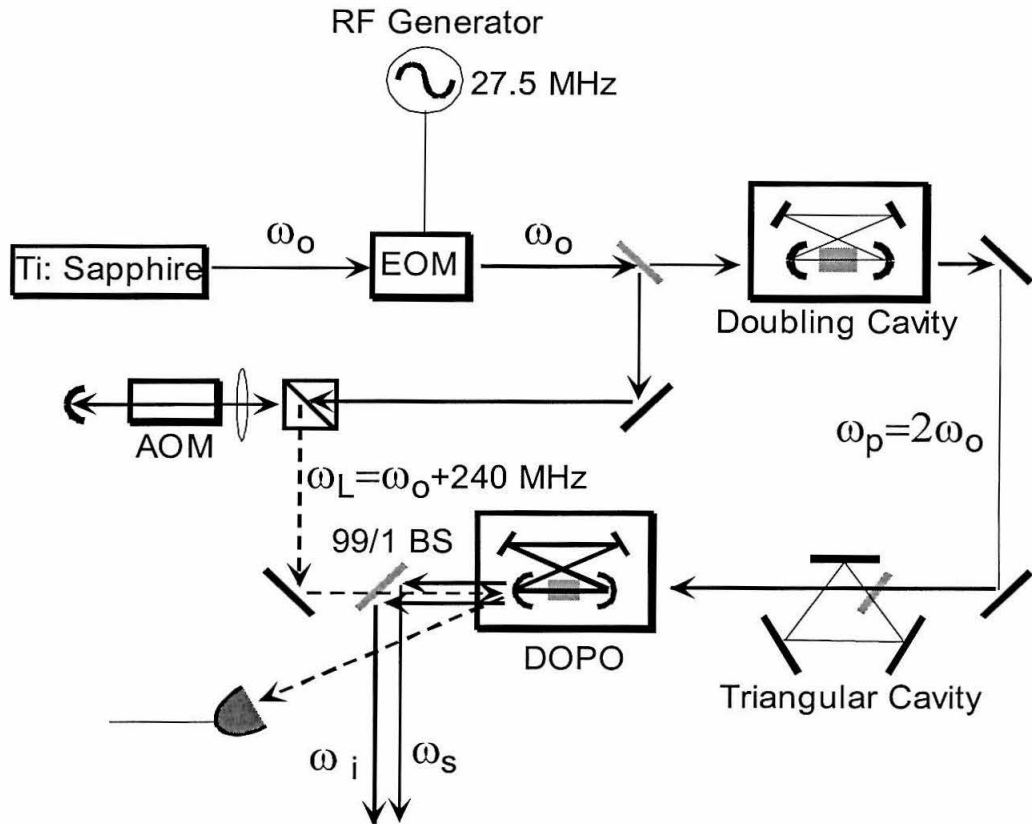


Figure 4.3: Experimental setup to generate squeezed light.

to the OPO. To do this, the pump from the doubling cavity is modematched to the triangular cavity. Then, by injecting into the OPO an IR beam (at frequency ω_o), counter-propagating to the direction of the signal and idler beams, we generate light at the pump frequency $\omega_p = 2\omega_o$. This beam is propagating in the opposite direction of the pump and goes to the triangular cavity to which is also then modematched. Hence, the pump from the doubling cavity is modematched to the OPO. The transfer cavity just described is crucial for aligning the pump to the OPO since the OPO cavity is not resonant with the pump and hence could not be directly modematched to it.

4.2 Degenerate Operation

Having described in detail the experimental realization of the OPO, we now turn our attention to its performance characterization in the two modes of operation, the DOPO and NDOPO. Theory for both operating modes can be found in Ref. [12]. The discussion begins in this section with the DOPO, and in the next section the NDOPO will be described.²

From the analysis of Ref. [12], it follows that all OPO output characteristics (both for the DOPO as well as the NDOPO) can be expressed in terms of the pumping parameter x defined by

$$x \equiv \sqrt{\frac{P}{P_{th}}}, \quad (4.1)$$

and the OPO cold cavity linewidth γ_o . Here P is the pump power and P_{th} is the threshold power above which the OPO starts to lase. The parameter x is the same as what the authors in Ref. [12] call $\coth \frac{s}{2}$, which for practical reasons we choose to express here in terms of power instead of fields since power is what we experimentally measure.

4.2.1 Phase-Sensitive Gain

In the degenerate mode (either with $\lambda_p \simeq 426$ or $\lambda_p \simeq 442$), the DOPO was characterized on a day to day basis in terms of the phase-sensitive gain G_{\pm}^{exp} , experimentally defined by

$$G_{\pm}^{\text{exp}} \equiv \frac{V_{\pm}}{V_o}. \quad (4.2)$$

The gain G_{\pm}^{exp} corresponds to the maximum power amplification (+) and maximum power deamplification (−) of a small injected coherent signal at frequency $\frac{\omega_p}{2}$, that enters the OPO cavity through M_1 (see Fig. 4.2). This beam is phase coherent with

²Note, however, that the phase sensitive gain derived in Ref. [12], **DOES NOT** apply in our case, because the derivation is based on the assumption of a single port cavity (i.e., same input and output ports). In our case, the two ports are different, M_1 and M_{out} (see Fig. 4.2). Notice, also, that Fig. 1 of Ref. [12] is misleading and does not correspond to the equations the authors derive for the phase sensitive amplification, i.e., Eq. 15 and Eq. 46 in Ref. [12]. The easiest way to see this discrepancy is to turn off the gain and observe that, contrary to the two sided cavity, the entire field transmits (see Eq. 15 in Ref. [12])! More details can be found in Appendix A.

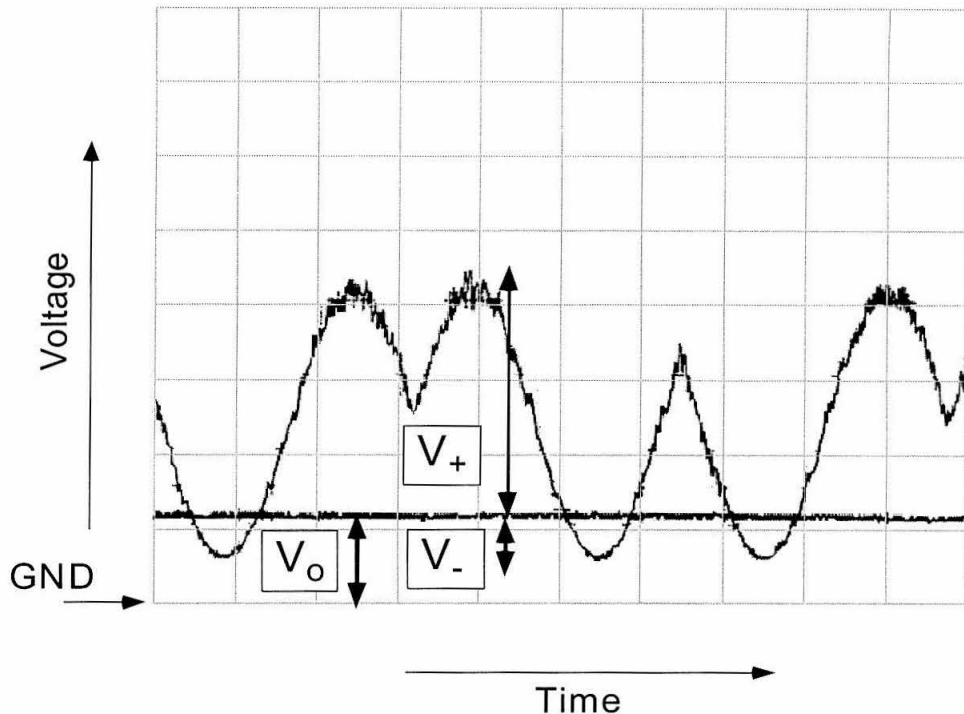


Figure 4.4: Phase-sensitive gain of a coherent beam transmitted through the DOPO.

the pump (i.e., originates from the Ti:Sapphire laser of Fig. 4.3) and is injected along the injection path of Fig. 4.2. The transmission of this beam is observed at the signal/idler output port of the OPO. In the presence of the pump this signal is amplified or deamplified depending on its relative phase to the pump. By modulating this phase, with a PZT along the injection path, we observe a periodic output with maximum value V_+ and minimum V_- (see Fig. 4.4). These values, compared to the no-gain value V_o , give G_{\pm}^{exp} as described by Eq. (4.2). Here an important experimental detail is that to determine correctly V_o we should NOT block the pump power (which of course turns the gain off) but rather detune the temperature of the crystal to a place where there is no phase matching and hence no gain from the OPO. This is important because the presence of the pump introduces non-linear losses due to light-induced absorption, so that if the blue is blocked in order to measure V_o , its value will in fact be overestimated.

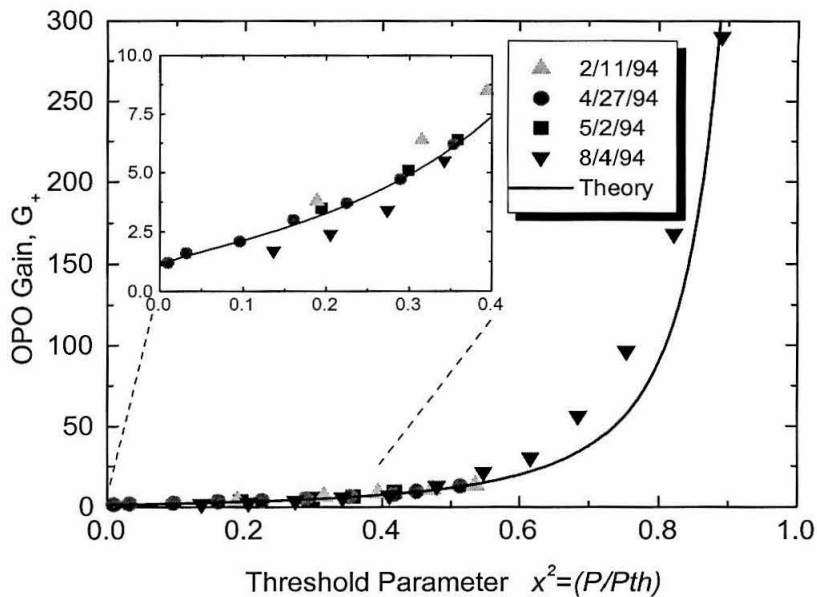


Figure 4.5: OPO gain G_+ vs. the dimensionless pumping parameter x^2 . The solid line is the theoretical prediction ($G_+ = (1 - x)^{-2}$) with no free parameters.

Expressed in terms of the pumping parameter x , the phase-sensitive gain for the DOPO can be shown from Ref. [73] (Eqs. 1-4) and Ref. [74] to be equal to

$$G_{\pm} = \frac{1}{(1 \mp x)^2} \quad (4.3)$$

and hence the relation

$$G_+ G_- = \frac{1}{(1 - x^2)^2} \quad (4.4)$$

must hold; see Appendix A.³ Clearly, by measuring G_{\pm} the value of the pumping parameter x can be inferred, which is important in estimating the rest of the properties

³Note that for a single-sided cavity in which the injected beam enters and escapes the cavity from the same mirror (i.e., same input and output ports), the gain is given by Eq. 15 of Ref. [12], which reduces to

$$G_{\pm} = \left(\frac{1 \pm x}{1 \mp x} \right)^2,$$

and which further implies that

$$G_+ G_- = 1.$$

This expression can also be derived from Refs. [73] and [74] and details of the derivation are shown in Appendix A.

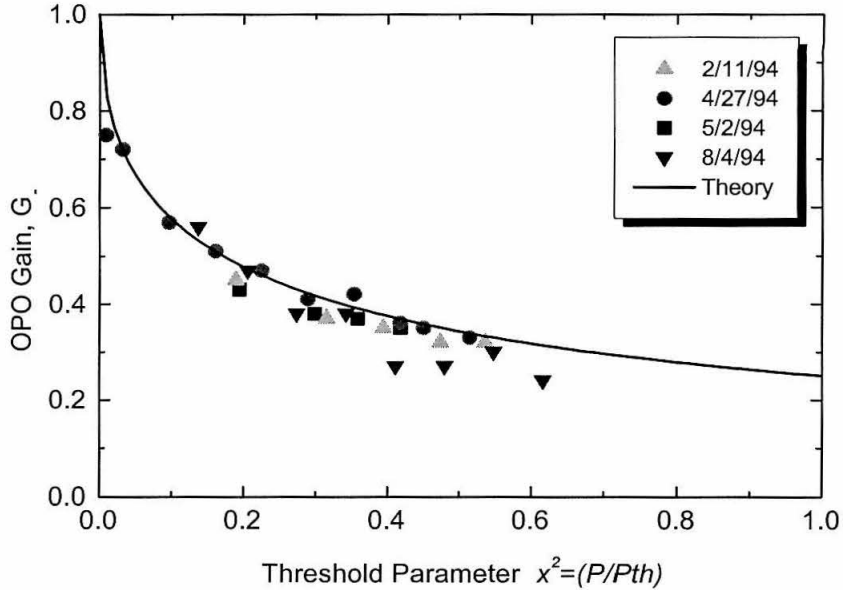


Figure 4.6: OPO gain G_- vs. the dimensionless pumping parameter x^2 . The solid line is the theoretical prediction ($G_- = (1 + x)^{-2}$) with no free parameters.

of the OPO. In particular, inverting Eq. (4.3) for x gives

$$x = \left| 1 - \frac{1}{\sqrt{G_{\pm}}} \right|. \quad (4.5)$$

In addition to the day to day measurements of G_+ through which the performance of the OPO was monitored, specific experiments were conducted to quantify better the issues described above. In particular, measurements have been taken of G_{\pm} versus P in three occasions (2/11/94, 4/27/94, 5/2/94) with $\lambda_p \simeq 426$ and once (8/4/94) with $\lambda_p \simeq 442$. The data are compiled in Table 4.1 and plots of them are shown in Figs. 4.5, 4.6, 4.7 and 4.8.

To put all the data together, the following two-step procedure has been applied: a) the G_+ versus P data from each experiment are fitted to Eq. (4.3) to get P_{th} ; b) the P axis of the data is rescaled to x by normalizing P by P_{th} for each experiment. Having performed this normalization the data, although taken at different days, which could mean different conditions, i.e., potentially different P_{th} , can be presented on the

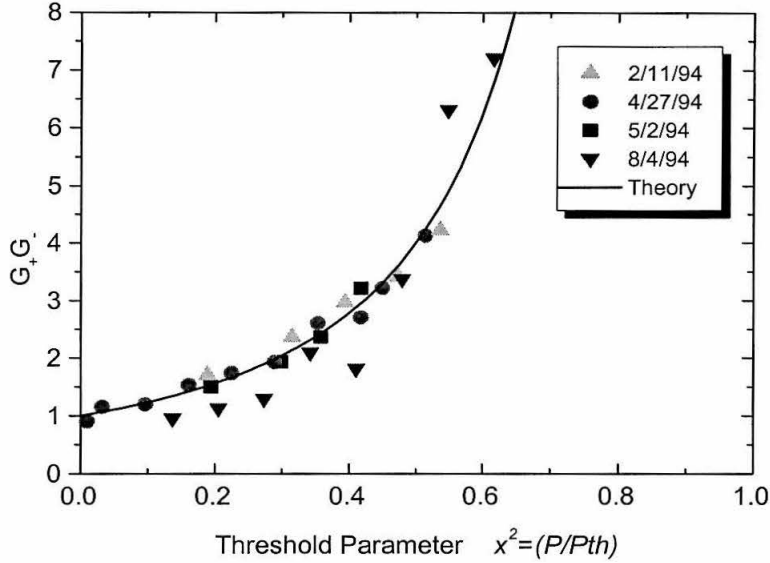


Figure 4.7: The product G_+G_- versus the dimensionless pumping parameter x^2 . The solid line is the theoretical prediction $G_+G_- = (1 - x^2)^{-2}$.

same graph. The threshold powers extracted from fitting Eq. (4.3) to the data are $P_{th}^{2/11/94} \simeq 335 \text{ mW}$, $P_{th}^{4/27/94} \simeq 311 \text{ mW}$, $P_{th}^{5/2/94} \simeq 317 \text{ mW}$ and $P_{th}^{8/4/94} \simeq 146 \text{ mW}$. Clearly, the first three data sets have similar threshold powers, while the last one has a much lower value which is due to the different output couplers used. In particular, the first three experiments, for which the pump wavelength was $\lambda_P \simeq 426 \text{ nm}$, were performed with a 10.5% output coupler, resulting in an OPO linewidth of $\gamma_{OPO}^{426} \simeq 13 \text{ MHz}$, while the last experiment, for which $\lambda_P \simeq 442 \text{ nm}$, was performed with a 7% output coupler, resulting in an OPO linewidth about $\gamma_{OPO}^{442} \simeq 9 \text{ MHz}$ (see Sec. 4.1.1). Since the threshold power for the OPO scales as the square of the cavity linewidth (see Ref. [12] and Appendix A), we expect that the threshold in the case of $\lambda_P \simeq 426 \text{ nm}$ (first three experiments with 10.5% output coupler) to be $(\frac{13}{9})^2 \simeq 2.1$ times bigger than in the case of $\lambda_P \simeq 442 \text{ nm}$ (last experiment with 7% output coupler) in accordance with the observations.

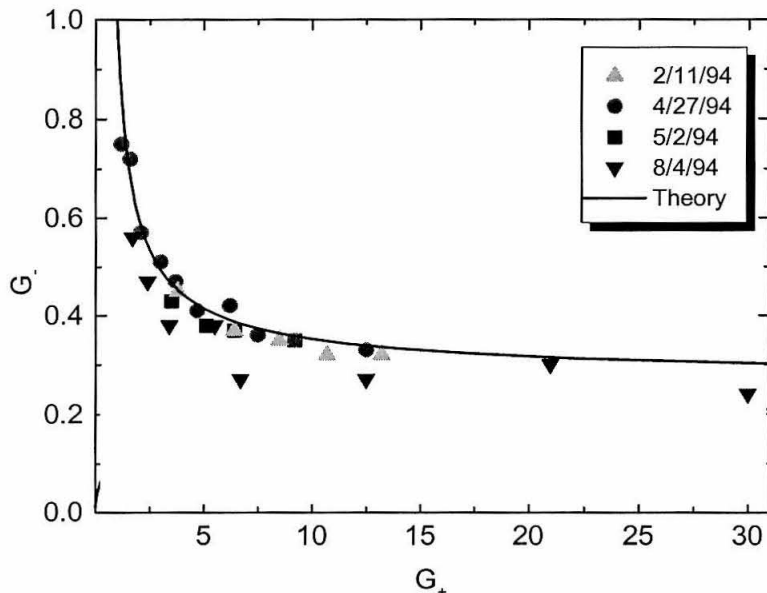


Figure 4.8: OPO amplification gain G_+ versus deamplification G_- for all measurements. The solid line is the theoretical prediction $G_+ = G_- (2\sqrt{G_-} - 1)^{-2}$.

4.2.2 Squeezing Spectra

In addition to the gain measurements, we have also observed squeezing directly using a usual balanced homodyne setup as shown in Fig. 4.9.[75, 76] A typical spectrum obtained from such a measurement is shown in Fig. 4.10. The shot-noise level W_o is about 10 dB above the electronics noise. When the squeezing is unblocked, the modulated trace in Fig. 4.10 is observed, which is an indication of squeezing. The fact that there is noise suppression below the shot-noise level is a signature of quantum squeezing. The frequency with which the modulation occurs is twice that of the modulation on the PZT of Fig. 4.9.[13] The maximum noise suppression W_- and the maximum noise enhancement W_+ correspond to the sizes of the squeezed and antisqueezed quadratures, respectively.

Systematic homodyne measurements of squeezing as a function of the pump power P were performed twice, once on 2/11/94 and once on 4/27/94 along with the phase-sensitive gain measurements mentioned earlier. In both cases the homodyne detector

| 2/11/94 | | | 4/27/94 | | | 5/2/94 | | | 8/4/94 | | |
|---------|-------|-------|---------|-------|-------|--------|-------|-------|--------|-------|-------|
| P | G_+ | G_- | P | G_+ | G_- | P | G_+ | G_- | P | G_+ | G_- |
| 60 | 3.8 | 0.45 | 3 | 1.2 | 0.75 | 65 | 3.5 | 0.43 | 20 | 1.7 | 0.56 |
| 100 | 6.4 | 0.37 | 10 | 1.6 | 0.72 | 100 | 5.1 | 0.38 | 30 | 2.4 | 0.47 |
| 125 | 8.5 | 0.35 | 30 | 2.1 | 0.57 | 120 | 6.4 | 0.37 | 40 | 3.4 | 0.38 |
| 150 | 10.7 | 0.32 | 50 | 3.0 | 0.51 | 140 | 9.2 | 0.35 | 50 | 5.5 | 0.38 |
| 170 | 13.2 | 0.32 | 70 | 3.7 | 0.47 | | | | 60 | 6.7 | 0.27 |
| 180 | 14.0 | 0.31 | 90 | 4.7 | 0.41 | | | | 70 | 12.5 | 0.27 |
| 190 | 14.3 | 0.31 | 110 | 6.2 | 0.42 | | | | 80 | 21.0 | 0.30 |
| | | | 130 | 7.5 | 0.36 | | | | 90 | 30.0 | 0.24 |
| | | | 140 | 9.2 | 0.35 | | | | 100 | 56.0 | - |
| | | | 160 | 12.5 | 0.33 | | | | 110 | 96.0 | - |
| | | | | | | | | | 120 | 168.0 | - |
| | | | | | | | | | 130 | 290.0 | - |

Table 4.1: Raw data of P , G_+ and G_- for the experiments of 2/11/94, 4/2/94, 5/2/94 and 8/4/94. Note that P is in mW .

was balanced at 3 MHz (to avoid the laser's technical noise) and had noise suppression of about 35 dB . To observe the squeezing, the spectrum analyzer was set to zero span, center frequency 3 MHz , resolution bandwidth 100 KHz and video bandwidth 1 KHz . The overall detection efficiency was $\zeta = \eta^2 \alpha t_{tr} t_{out} \simeq 0.71$, where $\eta \simeq 0.93$ was the homodyne visibility at each port of the 50/50 BS (Fig. 4.9, note that a cleaning cavity for the LO mode was not used), $\alpha \simeq 0.95$ was the detector quantum efficiency (measured by Akira Furusawa in Oct. 1997, about two years after the experiments took place), $t_{tr} \simeq 0.96$ was the transport efficiency and $t_{out} \simeq 0.87$ was the escape efficiency from the OPO. Figure 4.10 is typical of the squeezing spectra from the experiments of 2/11/94 and 4/27/94.

The quantities of interest from the data are W_{\pm} (shown in Fig. 4.10), from which the sizes R_{\pm} (see Eq. (4.7) below) of the squeezed and antisqueezed quadratures relative to the shot-noise level can be calculated. Notice that the W 's are in a log scale while the R 's are linear quantities. Furthermore, matters are somewhat complicated by small corrections to W_{\pm} due to the finite shot-noise level above the electronics noise floor which was $W_o \simeq 10$ dB for experiment 2/11/94 and $W_o \simeq 8$ dB for 4/27/94. To derive the transformation between the W 's and the R 's, we begin by defining the electronic noise floor to be at a level on the spectrum analyzer y_e , the shot-noise at y_o ,

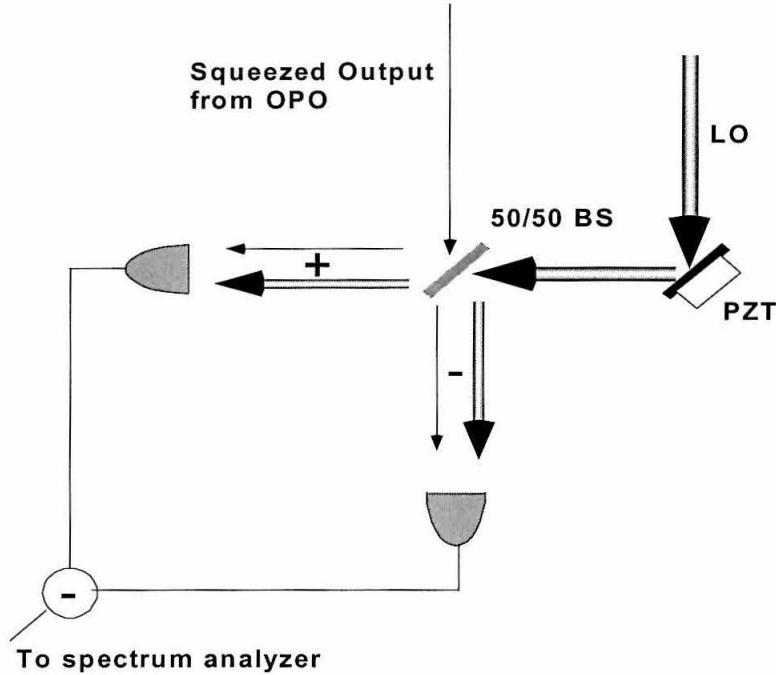


Figure 4.9: Balanced homodyne detector.

the maximum squeezing at y_- and the maximum antisqueezing at y_+ ; see Fig. 4.10. Hence, $W_0 = y_o - y_e$ and $W_{\pm} = y_{\pm} - y_o$. Let $x_{o,\pm}$ be the size (in linear scale) of the shot-noise, antisqueezing and squeezing without the contribution from the electronics noise. Then,

$$y_{o,\pm} = 10 \log \left(x_{o,\pm} + 10^{\frac{y_e}{10}} \right) \Rightarrow x_{o,\pm} = 10^{\frac{y_{o,\pm}}{10}} - 10^{\frac{y_e}{10}}, \quad (4.6)$$

where the contribution of the electronics noise is included via the term $10^{\frac{y_e}{10}}$ and is assumed to add incoherently to the values of $x_{o,\pm}$. Therefore, R_{\pm} is calculated to be

$$R_{\pm} \equiv \frac{x_{\pm}}{x_o} = \frac{10^{\frac{y_{\pm} - y_e}{10}} - 1}{10^{\frac{y_o - y_e}{10}} - 1} = \frac{10^{\frac{W_{\pm} + W_o}{10}} - 1}{10^{\frac{W_0}{10}} - 1}. \quad (4.7)$$

The experimental uncertainties for R_{\pm} , defined to be $e_{R_{\pm}}$, are easily calculated from

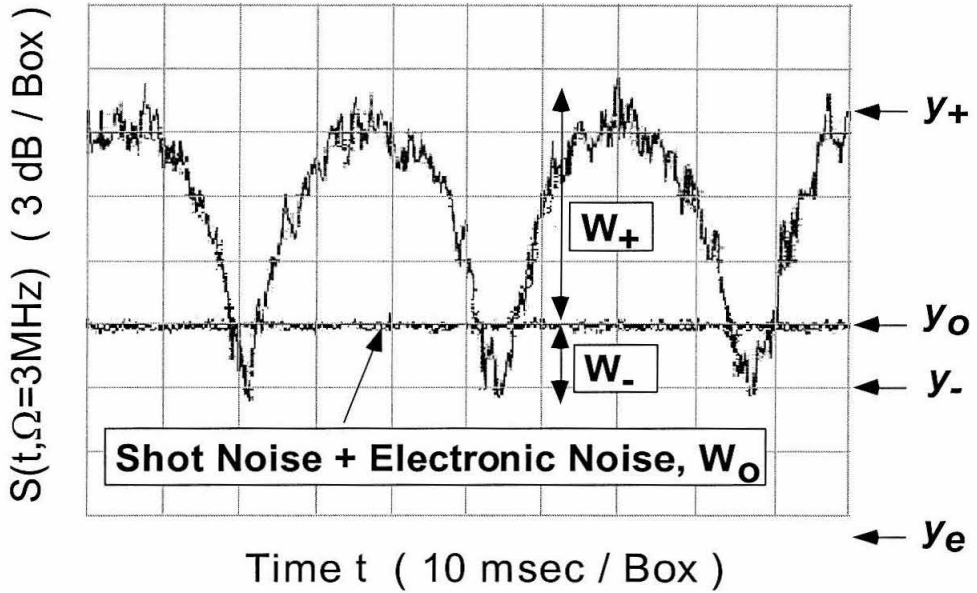


Figure 4.10: A typical spectrum of squeezing.

the experimental uncertainties $e_{W_{\pm}}$ of W_{\pm} to be

$$e_{R_{\pm}} = \left| \frac{dR_{\pm}}{dW_{\pm}} \right| e_{W_{\pm}} = 0.23 R_{\pm} e_{W_{\pm}}, \quad (4.8)$$

where it is assumed that there is no uncertainty in W_o . Note that both the values of W_{\pm} as well as their associated uncertainties $e_{W_{\pm}}$ have been extracted (“by eye”) from plots similar to that in Fig. 4.10. Table 4.2 lists the values of R_{\pm} and the associated errors $e_{R_{\pm}}$ for the experiments of 2/11/94 and 4/27/94.

Next, the size of the two conjugate quadratures of the electromagnetic field $\Delta X_{\pm}(\Omega)$ are calculated, which as shown in Ref. [13] are equal to

$$\Delta X_{\pm}(\Omega) = 1 + S_{\pm}(\Omega) \quad (4.9)$$

| 2/11/94 | | | 4/27/94 | | |
|---------|-------------------|-------------------|---------|-------------------|-------------------|
| P | $R_+ \pm e_{R_+}$ | $R_- \pm e_{R_-}$ | P | $R_+ \pm e_{R_+}$ | $R_- \pm e_{R_-}$ |
| 100 | 5.72 ± 0.65 | 0.42 ± 0.05 | 3 | 1.41 ± 0.16 | 0.78 ± 0.07 |
| 125 | 6.43 ± 0.74 | 0.41 ± 0.05 | 10 | 1.61 ± 0.15 | 0.67 ± 0.06 |
| 150 | 7.40 ± 0.85 | 0.38 ± 0.05 | 30 | 2.24 ± 0.10 | 0.62 ± 0.03 |
| 170 | 9.35 ± 1.07 | 0.45 ± 0.05 | 50 | 2.94 ± 0.20 | 0.56 ± 0.03 |
| 180 | 10.26 ± 1.18 | 0.37 ± 0.04 | 70 | 3.32 ± 0.15 | 0.56 ± 0.03 |
| 190 | 10.50 ± 1.20 | 0.39 ± 0.04 | 90 | 3.84 ± 0.17 | 0.54 ± 0.05 |
| | | | 110 | 4.23 ± 0.19 | 0.51 ± 0.05 |
| | | | 130 | 5.34 ± 0.37 | 0.51 ± 0.05 |
| | | | 140 | 6.05 ± 0.42 | 0.50 ± 0.03 |
| | | | 160 | 6.97 ± 0.80 | 0.47 ± 0.06 |

Table 4.2: Size of the squeezing R_- and antisqueezing R_+ relative to the shot noise in linear units. Corrections for the finite level of the shot noise have been included. P is the pump power in mW .

and satisfy the uncertainty relation

$$\Delta X_+(\Omega) \Delta X_-(\Omega') \geq \delta(\Omega - \Omega'). \quad (4.10)$$

Here Ω is the frequency of observation (3 MHz in our case) and S_{\pm} is shown (see Ref. [13]) to be related to R_{\pm} by

$$R_{\pm}(\Omega) = 1 + \zeta S_{\pm}(\Omega), \quad (4.11)$$

where $\zeta \simeq 0.71$ is the overall homodyne efficiency. From these relationships the uncertainty relation for the quadratures of the field is written in terms of the experimentally measured quantities R_{\pm} :

$$\left(1 + \frac{R_+ - 1}{\zeta}\right) \left(1 + \frac{R_- - 1}{\zeta}\right) \geq 1. \quad (4.12)$$

Note that for minimum uncertainty states $\Delta X_+ \Delta X_- = 1$ and as we approach perfect squeezing $S_+ \rightarrow \infty$ while $S_- \rightarrow -1$.

Figure 4.11 shows the data plotted as the squeezed quadrature $\Delta X_+ = 1 + S_+$ versus the antisqueezed quadrature $\Delta X_- = 1 + S_-$. As we can see, the data exhibit

quantum squeezing (i.e., $\Delta X_- < 1$) but they do not fall on the minimum uncertainty curve. One explanation of this discrepancy is that there is an extra loss factor that has not been accounted for. By assuming that $\zeta_{TOT} = \zeta \cdot \zeta_x$ with the extra

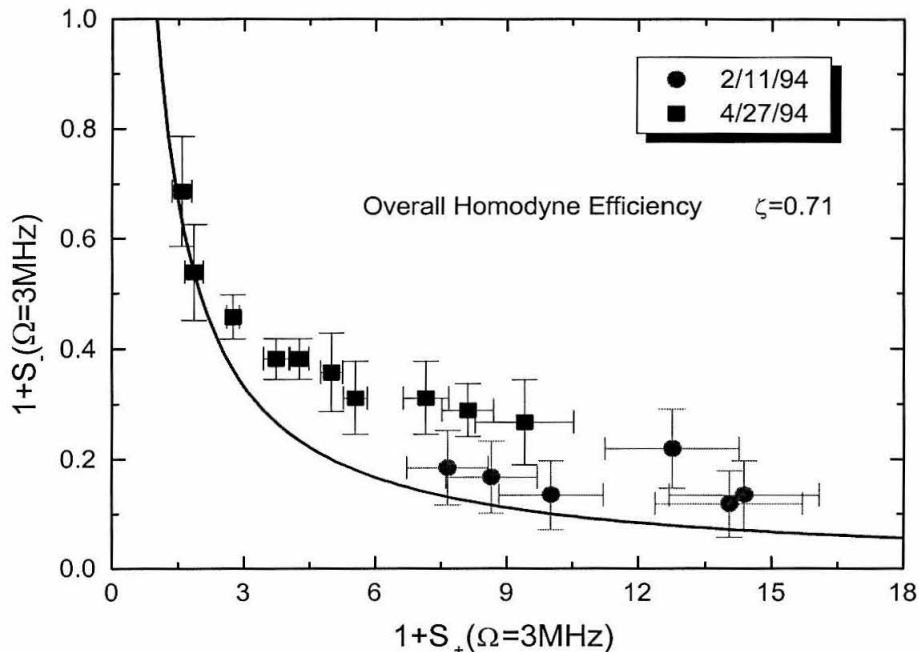


Figure 4.11: The squeezed ($\Delta X_- = 1 + S_-$) versus the antisqueezed ($\Delta X_+ = 1 + S_+$) quadratures of the OPO output. The solid line is the minimum uncertainty relation $\Delta X_+ \Delta X_- = 1$.

factor ζ_x introduced to account for a missing efficiency, the data are fitted to the minimum uncertainty relation to obtain ζ_x , which gives that for the experiment of 2/11/94 $\zeta_x = 0.93$ and for 4/27/94 $\zeta_x = 0.79$. Figure 4.12 shows ΔX_+ versus ΔX_- as calculated from Eqs. (4.9)-(4.11) taking into account the extra factor ζ_x , with now very good agreement.

4.2.3 Summary of the DOPO Results

Recapitulating the results for the performance measurements of the DOPO, we note that two independent types of experiments were performed, the phase-sensitive gain

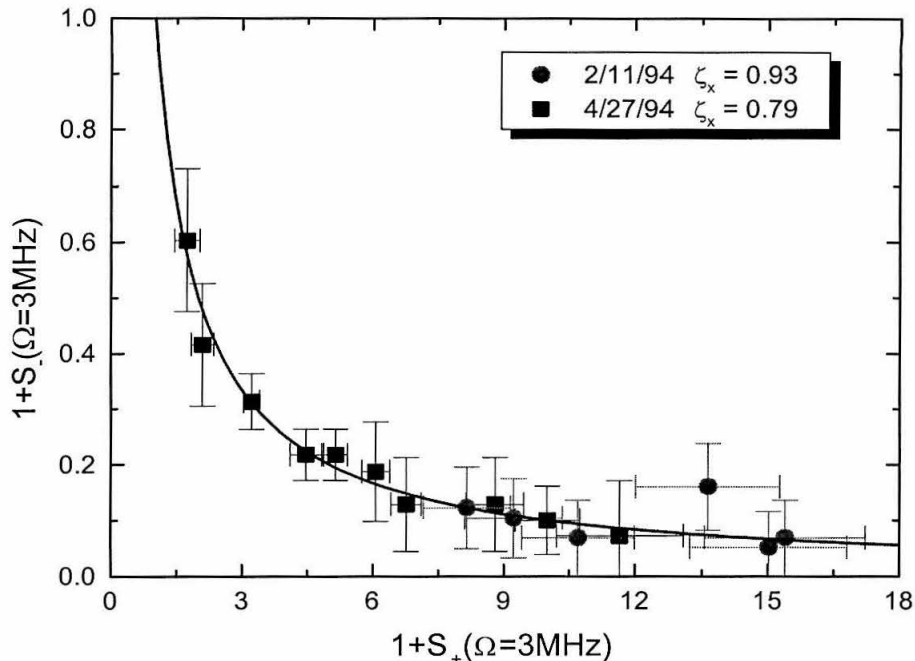


Figure 4.12: The squeezed ($\Delta X_- = 1 + S_-$) versus the antisqueezed ($\Delta X_+ = 1 + S_+$) quadratures of the OPO output calculated taking into account an extra efficiency factor ζ_x . The solid line is the minimum uncertainty relation $\Delta X_+ \Delta X_- = 1$.

measurements and the direct homodyne detection of squeezing. In the first case, the phase-sensitive gain measurements are in good agreement with theory, while in the case of squeezed spectra a small discrepancy with theory has been detected. However, this difference can be bridged by assuming some extra loss factor which has not been accounted for otherwise and which degrades the squeezing. For the experiment of 4/24/94, the loss factor that resolves the discrepancy is $1 - \zeta_x = 0.21$, while for the experiment of 2/11/94 the factors that adjust the data to the theory is $1 - \zeta_x = 0.07$.

4.3 Non-Degenerate Operation

Turning now to the NDOPO, we will first discuss its operation and tuning so that the output signal and idler beams have corresponding wavelengths $\lambda_s \simeq 852 \text{ nm}$ and $\lambda_i \simeq 917 \text{ nm}$ in resonance with the $6S_{1/2}F' = 4 \rightarrow 6P_{3/2}F' = 5$ and $6P_{3/2}F' = 5 \rightarrow$

$6D_{5/2}F'' = 6$ transitions in Cs , respectively. Following that we will concentrate on the characterization and day-to-day monitoring of the performance of the NDOPO. Neither the operation nor the characterization are easy tasks mainly due to the fact that the signal and idler frequencies differ by $25 THz$. First to tune the NDOPO, we must bring the OPO cavity to double resonance with the signal and idler wavelengths $\lambda_s \simeq 852 nm$ and $\lambda_i \simeq 917 nm$. Then to deduce the squeezing produced, we must rely on phase-sensitive gain measurements since direct observation of the spectrum of squeezing is not possible. Note that nonclassical correlations exist between the signal and idler frequencies which are separated by $\omega_s - \omega_i \simeq 25 THz$ and hence are well beyond the detection capabilities of any conventional photodetector.

4.3.1 Operation

In order to tune the OPO cavity to double resonance with $\lambda_s \simeq 852 nm$ and $\lambda_i \simeq 917 nm$, the Brewster plates in Fig. 4.2 are used to scan the length of the OPO. Double resonance is achieved when the optical path lengths L_s and L_i of the signal and idler beams are simultaneously equal to integer multiples of the corresponding wavelengths λ_s and λ_i , i.e., when $L_s = p\lambda_s$ and $L_i = q\lambda_i$, where p and q are integers. Assuming that the indices of refraction for the two wavelengths in the Brewster plates are the same, the double resonance condition may be written as $p\lambda_s = q\lambda_i$. Realizing that $\frac{\lambda_s}{\lambda_i} \simeq \frac{13}{14}$ implies that if there is a double resonance in the OPO cavity for some physical cavity length L_o , then the next double resonance will be at $L_o + 13\lambda_i \simeq L_o + 14\lambda_s$. Hence, by changing the length of the OPO by at most $dL_o \simeq 13\lambda_i \simeq 14\lambda_s \simeq 12 \mu m$ should result in a subsequent double resonance; see Fig. 4.13. Because the required scanning length of $12 \mu m$ to reach double resonance is beyond the scanning range of the PZT, the Brewster plates are used, which provide a much larger tuning range. Note that if the ratio of the two wavelengths is not “close” to a ratio of two small integers, then the length L_o must be tuned by much more than $12 \mu m$ before a double resonance is reached. Actually, because the ratio is not exactly $13/14$, it has been found that a scanning range of the order of $100\lambda_s$ was required before the double

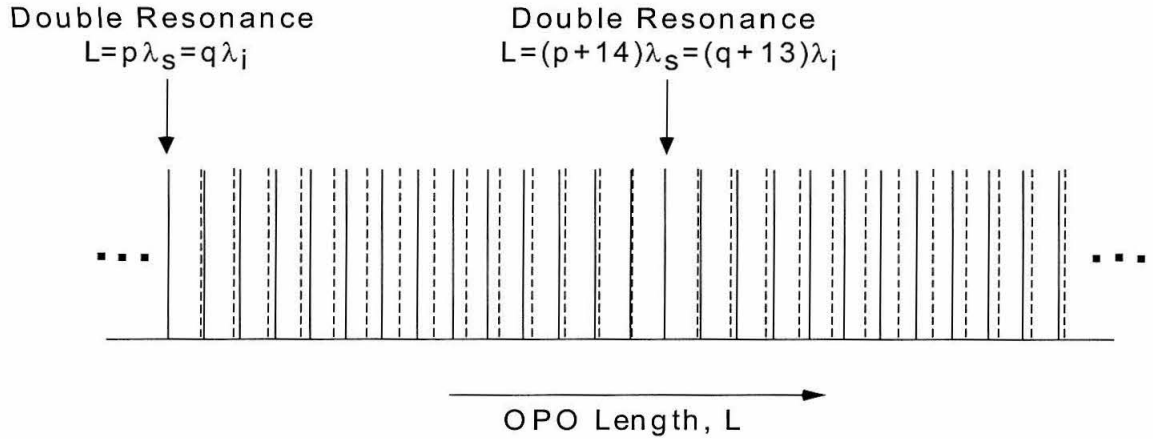


Figure 4.13: Schematic representation of double resonance in the NDOPO. The vertical lines denote longitudinal modes of the OPO cavity for the two wavelengths λ_s (solid lines) and λ_i (dotted lines), which are separated by λ_s and λ_i , respectively. As the cavity length is changed, the resonances of the two wavelengths move relative to each other until they coincide and to produce another double resonance.

resonance was optimized for the finesse of our cavity.

To monitor the tuning to the double resonance, a small coherent probe beam is injected into the OPO. The injected beam originates from an independent diode laser tuned at the $\lambda_{852} = 852 \text{ nm}$ resonance of the $6S_{1/2}F = 4 \rightarrow 6P_{3/2}F' = 5$ transition in Cs, hence having the desired frequency for the signal beam. Simultaneously, the OPO is pumped at frequency $\lambda_p = 442 \text{ nm}$, obtained by doubling the frequency of the Ti:Sapphire laser which is locked to the two-photon transition $6S_{1/2}F' = 4 \rightarrow 6D_{5/2}F'' = 6$ ($\lambda_{884} = 884 \text{ nm}$). Then, as the cavity length is scanned, successive double resonances of ω_{852} with $\omega_{442} - \omega_{852}$ are reached, at which points the transmission of the injected beam exhibits amplification; see Fig. 4.14. This of course happens because at double resonance some of the pump photons at ω_{442} are converted to two photons of frequencies $\omega_s = \omega_{852}$ and $\omega_i = \omega_{442} - \omega_{852}$ and hence the ω_{852} beam is amplified. By optimizing the gain of the injected ω_{852} beam and locking to that point, the length of the OPO cavity is fixed so that it is doubly resonant with $\omega_s = \omega_{852}$

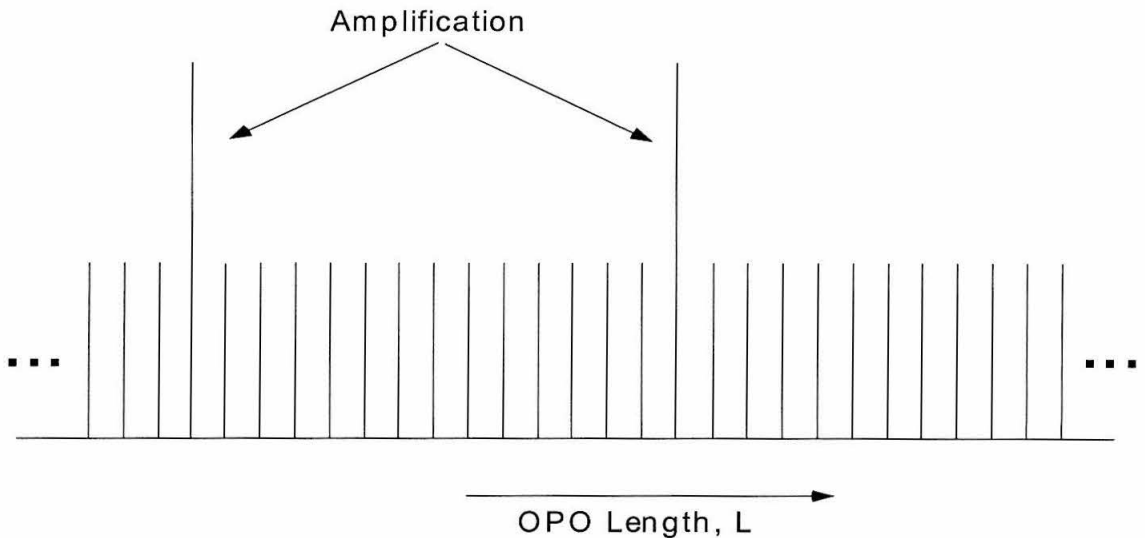


Figure 4.14: When the OPO cavity is doubly resonant with the injected ω_{852} and conjugate $\omega_{442} - \omega_{852}$ frequencies, there is amplification of the injected beam.

and $\omega_i = \omega_{442} - \omega_{852}$. Since ω_{852} is resonant with the $6S_{1/2}F = 4 \rightarrow 6P_{3/2}F' = 5$ transition and since $\omega_{442} = 2\omega_{884}$ is resonant with the $6S_{1/2}F = 4 \rightarrow 6D_{5/2}F'' = 6$ transition, it follows that the $\omega_i = \omega_{917} = \omega_{442} - \omega_{852}$ is the eigenfrequency of the $6P_{3/2}F' = 5 \rightarrow 6D_{5/2}F'' = 6$ transition. Hence, the OPO signal and idler frequencies are $\omega_s \simeq \omega_{852}$ and $\omega_i \simeq \omega_{917}$ are in approximate resonance with the two atomic transitions of interest.

4.3.2 Performance

To monitor the NDOPO performance we observe in a series of measurements the gain at the signal and idler frequencies. In particular, we look at the transmission of the injected beam and measure its power in four different configurations; see Fig. 4.15. First, by detuning the crystal temperature, the no-gain transmitted power of the ω_{852} beam V_o is obtained; Fig. 4.15a. Next, the temperature is tuned to the phase matching point and the amplified power of the combined signal and idler beams $V_{852+917}$ is observed; Fig. 4.15b. Note that as the OPO cavity is scanned, several

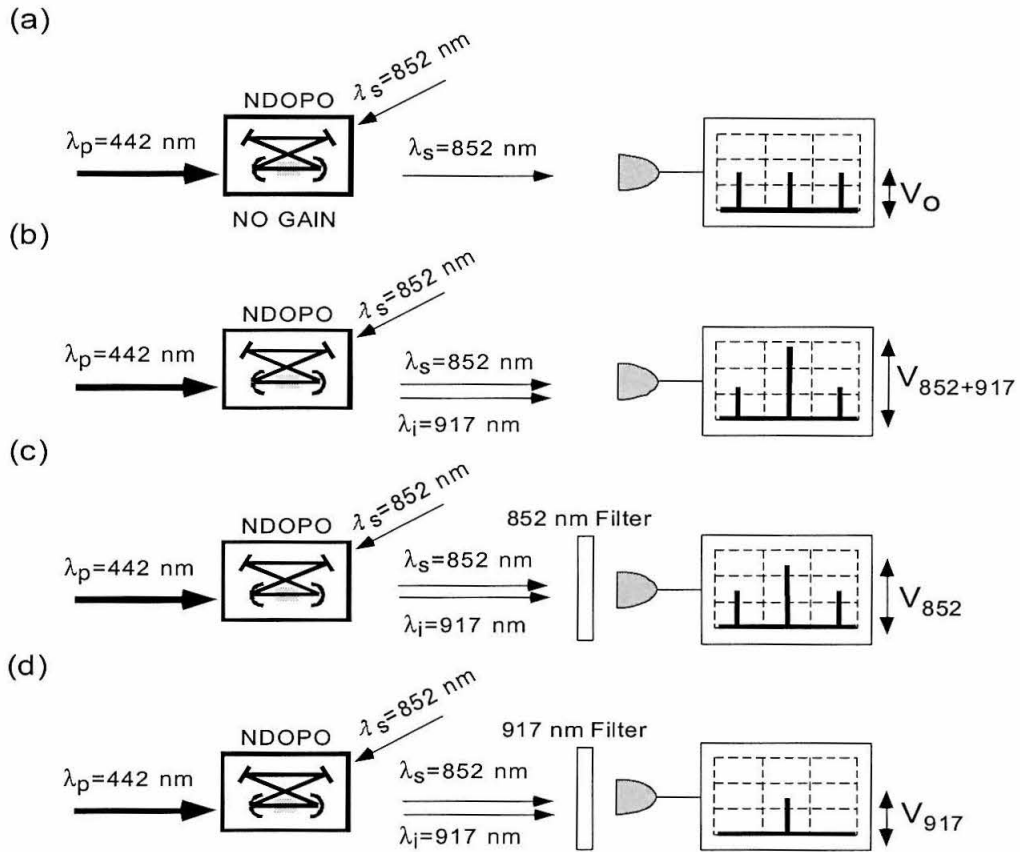


Figure 4.15: Sequence of measurements to determine the OPO gain: (a) no-gain measurement of the transmitted power V_o ; (b) combined power of the amplified 852 nm and generated 917 nm beams, $V_{852+917}$; (c) amplified power of the injected beam at 852 nm alone, V_{852} ; (d) generated power of the idler beam at 917 nm alone, V_{917} .

longitudinal resonances of the injected beam appear, but only the one for which there is double resonance exhibits gain. In the third measurement only the amplified signal beam power V_{852} is observed by inserting an 852 nm filter in the path of the OPO output, Fig. 4.15c. Finally, in the last step, by replacing the 852 nm with a 917 nm filter, the generate idler power V_{917} is observed, Fig. 4.15d.

Combining these measurements for the various V 's, the gain (maximum amplifi-

| 11/29/94 | | | 12/06/94 | | | 12/20/94 | | |
|------------------------|--------------------------|--------------------------|------------------------|--------------------------|--------------------------|------------------------|--------------------------|--------------------------|
| G_{852}^{exp} | $G_{917}^{\text{exp 1}}$ | $G_{917}^{\text{exp 2}}$ | G_{852}^{exp} | $G_{917}^{\text{exp 1}}$ | $G_{917}^{\text{exp 2}}$ | G_{852}^{exp} | $G_{917}^{\text{exp 1}}$ | $G_{917}^{\text{exp 2}}$ |
| 4.60 | 2.75 | 3.13 | 3.33 | 1.87 | 2.00 | 6.07 | 2.93 | 4.25 |
| 3.16 | 1.15 | 1.25 | 2.00 | 1.00 | 0.95 | 3.67 | 2.33 | 2.25 |
| 2.25 | 1.03 | 0.78 | 1.40 | 0.80 | 0.43 | 1.83 | 0.67 | 0.63 |
| 1.75 | 0.28 | 0.42 | 1.17 | 1.33 | 0.20 | 1.67 | 0.83 | 0.45 |
| 1.50 | 0.26 | 0.26 | 2.66 | 1.34 | 1.75 | 1.68 | 0.82 | 0.63 |
| 1.25 | 0.22 | 0.20 | 6.67 | 5.33 | 5.00 | 3.75 | 0.85 | 1.50 |
| 1.25 | 0.18 | 0.16 | 4.00 | 3.00 | 2.25 | 1.35 | 0.18 | 0.22 |
| 3.00 | 0.57 | 0.71 | 2.00 | 1.40 | 0.75 | 2.41 | 0.53 | 0.68 |
| | | | 1.50 | 0.70 | 0.38 | 3.27 | 1.40 | 1.53 |
| | | | | | | 1.27 | 0.08 | 0.14 |
| | | | | | | 5.22 | 0.28 | 2.81 |
| | | | | | | 1.43 | 0.39 | 0.31 |
| | | | | | | 2.31 | 0.80 | 0.75 |

Table 4.3: Gain measurements for the NDOPO.

cation) is defined for the signal and idler beam to be

$$G_{852}^{\text{exp}} \equiv \frac{1}{T_{852}} \frac{V_{852}}{V_o} \quad (4.13)$$

and

$$G_{917}^{\text{exp 1}} \equiv \frac{V_{852+917} - \frac{1}{T_{852}} V_{852}}{V_o}, \quad (4.14)$$

where T_{852} is the power transmission of the 852 filter in the measurement of Fig. 4.15c. In addition, the measurements of Fig. 4.15d give a second estimate of G_{917} , namely

$$G_{917}^{\text{exp 2}} \equiv \frac{1}{T_{917}} \frac{V_{917}}{V_o}, \quad (4.15)$$

where T_{917} is the power transmission of the 917 filter. Note that in the above discussion it is assumed that the quantum efficiency of the detector at 852 nm and 917 nm is the same.

Systematic data for the gain of the signal and idler beams have been recorded on three occasions, 11/29/94, 12/06/94 and 12/20/94, during the nonclassical two-photon excitation experiment. The data are shown in Table 4.3. To check for consistency of the measurements, we first plot in Fig. 4.16 $G_{917}^{\text{exp 1}}$ versus $G_{917}^{\text{exp 2}}$. The data

fall on the diagonal $G_{917}^{\text{exp}1} = G_{917}^{\text{exp}2}$ (as they should) and hence we take for the value of the gain of the idler beam the average of the two $G_{917}^{\text{exp}} = \frac{1}{2} (G_{917}^{\text{exp}1} + G_{917}^{\text{exp}2})$.

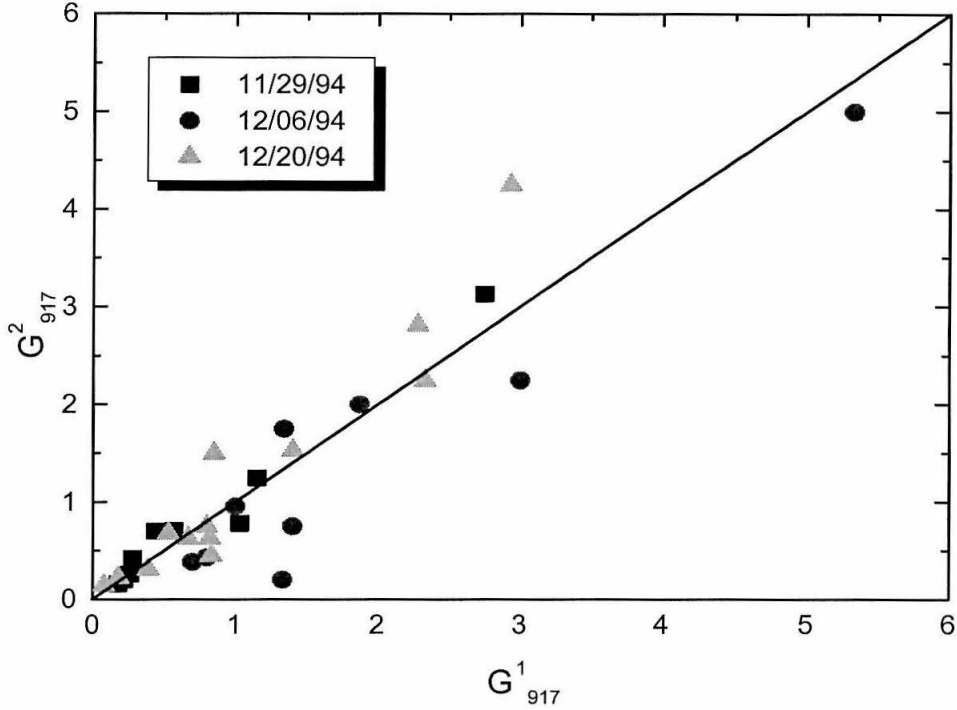


Figure 4.16: Plot of the gain measurements of the idler beam $G_{917}^{\text{exp}1}$ versus $G_{917}^{\text{exp}2}$, which were determined by two independent methods. For the data to be consistent, they must fall on the diagonal $G_{917}^{\text{exp}1} = G_{917}^{\text{exp}2}$.

The theory for the NDOPO is slightly different from that of DOPO. Following the discussion of Appendix A, we find that the gain of the signal and idler beams of a NDOPO are given by

$$G_s = \frac{1}{(1-x^2)^2} \quad (4.16)$$

and

$$G_i = \frac{x^2}{(1-x^2)^2}, \quad (4.17)$$

from which it follows that

$$G_i = G_s \left(1 - \frac{1}{\sqrt{G_s}} \right) \quad (4.18)$$

Here x is the pumping parameter as defined by Eq. (4.1) and all the losses in the OPO

are assumed to be the same in both the signal and idler frequencies; see Appendix A. Therefore, to check whether or not the data are consistent with theory, we plot in Fig. 4.17 the gain of the idler beam G_{917}^{exp} versus the gain of the signal beam G_{852}^{exp} . Clearly, there is good agreement and the discrepancies that are present (especially for the experiment of 12/06/94) could probably be explained by unequal losses for the signal and idler frequencies in the OPO.

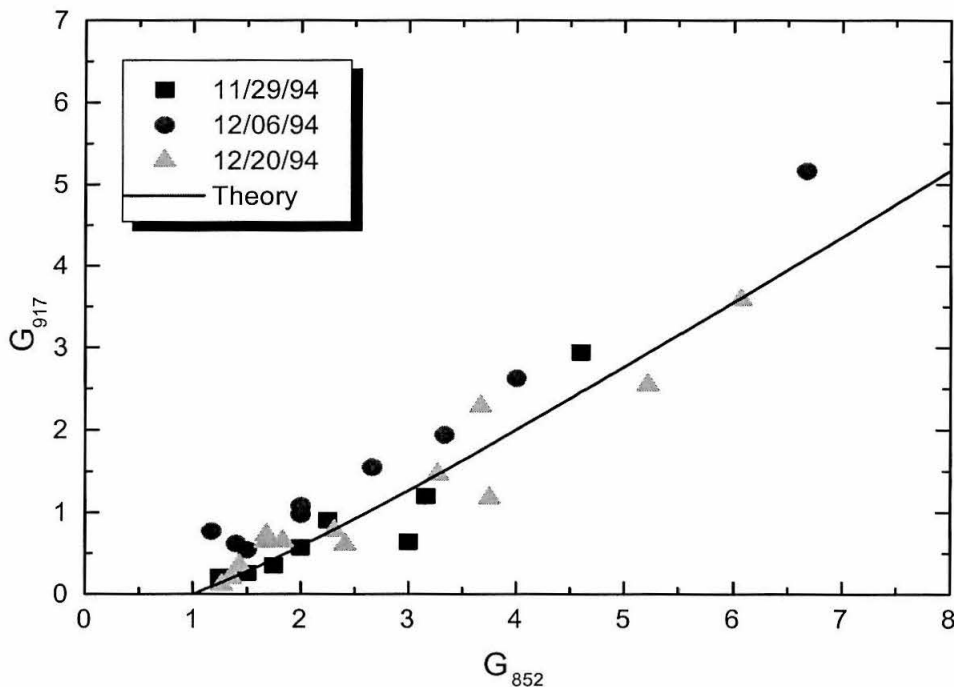


Figure 4.17: Idler gain G_{917}^{exp} versus signal gain G_{852}^{exp} . The solid line is the theoretical prediction for the relation of the two, namely $G_{917}^{\text{exp}} = G_{852}^{\text{exp}} \left(1 - \frac{1}{\sqrt{G_{852}^{\text{exp}}}} \right)$.

4.4 Summary

The focus of this chapter has been the description and characterization of the OPO used in our experiments. Two main modes of operation have been discussed, the DOPO and NDOPO. A compilation of all available data from various experiments al-

allows us to compare theory with experiment and to quantify the discrepancies between the two. In particular for the DOPO we find that the phase-sensitive gain measurements are in agreement with theory, while the homodyne spectra of squeezing deviate from theory by up to 20% which could be due to an unaccounted detection efficiency. For the NDOPO there is a more limited set of data which nevertheless again shows agreement between the gain measurements and theory.

Part II

SQUEEZED LIGHT AND ATOMS

Chapter 5 Two-Photon Excitation Rate with Nonclassical Fields: Theory and Experiment

One of the most challenging tasks in quantum optics is the observation of the interaction of nonclassical states of the electromagnetic field with atoms.[14, 15, 16, 17] Three main factors contribute to the overall difficulty of this type of experiment: the creation of nonclassical states of the electromagnetic field in resonance with atoms, the efficient illumination of the atoms by these states and the efficient monitoring of the interaction. As mentioned in the introduction, predictions for nonclassical

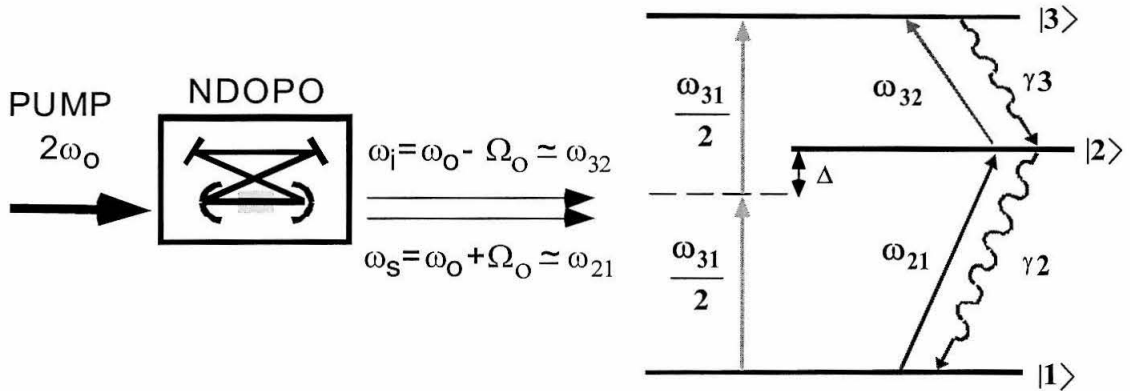


Figure 5.1: Two-photon excitation by non-classical fields: a three-level atom $\{|1\rangle, |2\rangle, |3\rangle\}$ is illuminated by the signal and idler (ω_s, ω_i) output beams from an NDOPO, and they are near resonance with the $|1\rangle \rightarrow |2\rangle$ and $|2\rangle \rightarrow |3\rangle$ transitions, respectively ($\omega_s \simeq \omega_{12}$ and $\omega_i \simeq \omega_{23}$).

effects associated with the interaction of squeezed states with atoms have existed in abundance for more than a decade, but the difficulties outlined above have limited

experimental work to a minimum. To the present day there is only one experiment demonstrating such an effect [48, 49] and this will be discussed in the present and next chapters.

Two-photon excitation of a three-level atom by the signal and idler outputs of an OPO (Fig. 5.1) was predicted to exhibit nonclassical behavior by several authors.[42, 43, 44, 45] In particular, it has been shown that the rate of two-photon excitation as a function of intensity approaches asymptotically a linear dependence for small enough intensities. The basic principle behind our experiment along with an intuitive interpretation of the phenomenon was presented in the introduction. In the following section (Section 5.1) a more accurate but brief description of the underlying theory is presented with emphasis on what constitutes a nonclassical effect. In Section 5.2 the setup, protocols and data of the experiment (including a control experiment) will be discussed. The analysis is deferred to the next chapter.

5.1 Theory

5.1.1 “Simple” Theory

It has been known since the early work of Mollow in 1968 [77] that the rate of two-photon excitation R_2 is proportional to the fourth-order correlation function of the excitation field \hat{E} ,

$$R_2 \propto \left\langle \hat{E}^\dagger(t + \tau) \hat{E}^\dagger(t + \tau) \hat{E}(t) \hat{E}(t) \right\rangle. \quad (5.1)$$

In our case, the excitation field is the output of an NDOPO $\hat{E}_{out} \equiv \hat{E}_q$ which can be expressed in terms of the transformation

$$\hat{E}_q(\Omega) = \mu(\Omega) \hat{E}_V(\Omega) + \nu(\Omega) \hat{E}_V^\dagger(-\Omega), \quad (5.2)$$

of the input field $\hat{E}_{in} \equiv \hat{E}_V$, taken to be the vacuum state so that $\langle \hat{E}_V(\Omega) \rangle = 0$ (see Fig. 5.2). The quantities $\hat{E}_q(t)$ and $\hat{E}_q(\Omega)$ are related to each other by the Fourier

transform

$$\widehat{E}_q(t) = \int \widehat{E}_q(\Omega) e^{-i\Omega t} d\Omega. \quad (5.3)$$

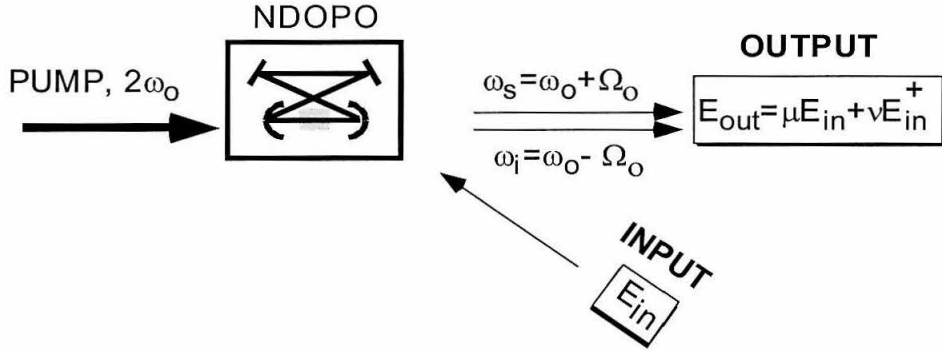


Figure 5.2: The output field E_{out} of the OPO is related to the input state E_{in} via the transformation $E_{out} = \mu E_{in} + \nu E_{in}^\dagger$.

The parameters μ and ν are broadband functions of the frequency Ω and fully describe the output properties of the OPO.¹ In particular, $\{\mu(\Omega), \nu(\Omega)\}$ are centered (peak) at the signal and idler frequencies at $\omega_s = \omega_o + \Omega_o$ and $\omega_i = \omega_o - \Omega_o$ and have bandwidth similar to the OPO linewidth. Without loss of generality ν is taken to be real and $\mu \equiv |\mu| e^{i\phi}$. In addition, from the commutation relation

$$\left[\widehat{E}_q(\Omega), \widehat{E}_q^\dagger(\Omega') \right] = \delta(\Omega - \Omega'), \quad (5.4)$$

it follows that

$$|\mu(\Omega)|^2 - |\nu(\Omega)|^2 = 1. \quad (5.5)$$

It can also be shown that $\{\mu, \nu\}$ are related to the more common squeezing parameters

¹The parameters $\{\mu, \nu\}$ are related to the squeezing parameter s of M. J. Collet and R. Loudon, J. Opt. Soc. Am. **B4**, 1525 (1987) via

$$|\mu| = \cosh \frac{s}{2} \text{ and } |\nu| = \sinh \frac{s}{2}.$$

M and N in the literature by

$$M(\Omega) = \mu(\Omega) \nu(\Omega) \quad (5.6)$$

and

$$N(\Omega) = |\nu(\Omega)|^2 . \quad (5.7)$$

Here the parameters M and N are the field autocorrelation function and occupation photon number of the squeezed output of the OPO as defined by the correlation functions

$$\langle \widehat{E}_q(\Omega) \widehat{E}_q(\Omega') \rangle \equiv M(\Omega) \delta(\Omega + \Omega') \quad (5.8)$$

and

$$\langle \widehat{E}_q^\dagger(\Omega) \widehat{E}_q(\Omega') \rangle \equiv N(\Omega) \delta(\Omega - \Omega') . \quad (5.9)$$

Expanding Eq. (5.1) and applying these definitions leads to

$$R_2 \propto |\nu|^4 + \xi |\mu|^2 |\nu|^2 = N^2 + \xi |M|^2 , \quad (5.10)$$

where ξ is a constant of order unity. For minimum uncertainty states M and N are related to each other by $M^2 = N(N+1)$ and hence

$$R_2 \propto \alpha'_1 N^2 + \alpha'_2 N \approx \alpha_1 I^2 + \alpha_2 I , \quad (5.11)$$

which is in agreement with Eq. (1.3). Here of course I is the intensity of the squeezed beam which is proportional to the occupation number N and also for simplicity we have assumed that $N_s = N_i = N$ where N_s and N_i are the photon numbers in the signal and idler beams.² Note that N_s and N_i are not necessarily the same if the corresponding losses in the OPO are unequal.

²Strictly speaking, the output intensity of the OPO is proportional to the photon flux, and is given by $I \propto \frac{1}{2\pi} \int d\Omega' e^{i(\Omega - \Omega')t} N(\Omega)$. Therefore, in general $I \approx N$ and the bandwidth of the OPO cavity (i.e. lineshape of $N(\Omega)$) has to be properly accounted for with the above integration. Nevertheless, for small values of N , the two quantities are proportional to each other, i.e., $1 \gg N \sim I$. For more details see Appendix C.

5.1.2 “Full” Theory

Following a more accurate theoretical description of the system, the authors in Ref. [44, 45] have integrated the master equation and derived a more complicated expression for R_2 in terms of the excited state population ρ_{33}

$$R_2 \propto \rho_{33} = \frac{v^2(\theta) N_s \{1 - v(\theta) N_s + [1 + \beta - \beta v(\theta)] N_i\}}{[\beta + \beta v(\theta) N_i + v(\theta) N_s] \{1 + v(\theta) [2N_s + N_i - 3v(\theta) N_i]\}}, \quad (5.12)$$

(see Eq. (23) in Ref. [45]). The parameter β is the ratio of the atomic linewidths as defined by $\beta \equiv \frac{\gamma_3}{\gamma_2}$ where γ_2 and γ_3 are the linewidths of the second and third excited states, respectively, ($6P_{3/2}F' = 5$ and $6D_{5/2}F'' = 6$ in our case, see Fig. 5.1). Here the quantity $v(\theta)$ is defined by

$$v(\theta) \equiv \frac{1}{2} \left[1 - \frac{1}{4} (3 + \cos^2 \theta) \cos \theta \right], \quad 0 \leq \theta \leq \pi \quad (5.13)$$

and accounts for imperfect coupling of the atoms with the squeezed vacuum which is mainly due to the finite focusing angle θ of the OPO output onto the atoms. In our experiments $v(\theta) \ll 1$ and hence by expanding Eq. (5.12) and assuming that $N_s = N_i = N$, we arrive at

$$\rho_{33} \simeq \frac{v^2(\theta)}{\beta} [(1 + \beta) N_s N_i + N_s] + O[v^3(\theta)] \simeq \frac{v^2(\theta)}{\beta} [(1 + \beta) N^2 + N], \quad (5.14)$$

which can also be written as

$$\rho_{33} \simeq v^2(\theta) \left[N^2 + \frac{1}{\beta} |M|^2 \right]. \quad (5.15)$$

Clearly, Eqs. (5.11) and (5.15) have the same functional dependences in N , which as advertised for small enough N grow linearly with intensity. An important feature of Eq. (5.14) is that even for inefficient coupling of the atoms to the squeezed vacuum ($v(\theta) \rightarrow 0$), this nonclassical effect persists since the functional dependence of the excitation rate versus intensity is not altered. This is not the case in examples such as the one originally considered by Gardiner [16] for which efficient coupling was

essential in preserving the nonclassical effects. This feature of two-photon excitation by nonclassical fields is extremely important from an experimental point of view because of the difficulties in achieving efficient coupling.

Preluding the experiment that will be discussed in the next section, it is noted that the price to pay for small values of $v(\theta)$ is that the overall detection signal, which scales proportionally to $v^2(\theta)$, becomes very small. In our case $\theta \simeq 5^\circ$ and hence Eq. (5.14) predicts that the excitation population is $\rho_{33} \approx 1.4 \times 10^{-5} \left(\frac{8}{5}N^2 + N\right)$. In order to observe the transition from the quadratic N^2 to the linear dependence N , the experiment must be performed in the region where $\frac{8}{5}N^2 \approx N$, i.e., for $N \approx \frac{5}{8}$ and hence at the region of interest $\rho_{33} \approx 2 \times 10^{-5}$. Because the overall detection efficiency is also small $\zeta_{tot} \sim 0.01$ and given that the detection channel (which in our case is the decay from the upper to the intermediate states $|3\rangle \rightarrow |2\rangle$) has linewidth $\gamma_3 \approx 3$ *MHz*, the expected counting rate at the region of interest is of the order of

$$R_2 \approx \zeta_{tot}\gamma_3\rho_{33} \sim 0.5 / \text{sec} ! \quad (5.16)$$

Clearly, detecting 0.5 photons per second is not an easy task which is one of the reasons why this type of experiment is extremely difficult.

5.1.3 Classical versus Nonclassical Effects

Before describing the experiment, it is worth discussing what constitutes a nonclassical as compared to a classical effect. This question has to be clearly addressed if one is to claim that nonclassical effects have been observed. Setting the standard, throughout our research in both our attempts to such effects,[2, 48] we have used the strong criterion that nonclassical atomic effects are atomic features that can only be observed in interaction of atoms with nonclassical states of the electromagnetic field. Although this definition would apply to all nonclassical electromagnetic states, here we are only considering the limited class of nonclassical states, the so called squeezed states, for which the threshold for being nonclassical is defined to be the condition $\Delta X_- < 1$. Here, ΔX_- is the minimum variance of the generalized field quadrature

X_θ , defined by

$$X_\theta \equiv \widehat{E}_q e^{-i\theta} + \widehat{E}_q^\dagger e^{i\theta} \quad (5.17)$$

and where \widehat{E}_q is the operator for the field under consideration, which in our case is the squeezed output of the OPO; see Ref. [13].

To explore the phase space of field quadratures, we consider the plane spanned by the orthogonal quadratures $\Delta X_- \equiv Var(X_0)$ and $\Delta X_+ \equiv Var(X_{\frac{\pi}{2}})$ and discuss the various regions, keeping in mind the uncertainty relation $\Delta X_- \Delta X_+ \geq 1$. Figure 5.3 shows this quadrature space with a cartoon like representation of the various types of states, which in addition to the quantum squeezed states, also include thermal and classically squeezed states.

The states shown in Fig. 5.3 can also be distinguished from each other in terms of the parameters M and N (defined by Eqs. (5.8) and (5.9)). Recall that M describes the autocorrelation of the fields and hence is a measure of the asymmetry in the quadrature space while N is the occupation photon number and hence describes the overall “size” of the states. The classification in terms of M and N is then as follows:

- Electromagnetic vacuum, $\Delta X_+ = \Delta X_- = 1 \Leftrightarrow M = N = 0$,
- Thermal states, $\Delta X_+ = \Delta X_- > 1 \Leftrightarrow M = 0, N > 0$,
- Classically squeezed states, $\Delta X_+ \neq \Delta X_-$, $\Delta X_\pm \geq 1 \Leftrightarrow 0 < M \leq N$
- Quantum squeezed states, $\Delta X_+ \neq \Delta X_-$, $\{\Delta X_\pm > 1 \text{ and } \Delta X_\mp < 1\} \Leftrightarrow N < M \leq \sqrt{N(N+1)}$

In summary, the criterium for having a quantum squeezed state is restricted in the limited range

$$N < M \leq \sqrt{N(N+1)}. \quad (5.18)$$

Returning now to the expression for two-photon excitation, Eq. (5.15), we note that it applies not only to quantum squeezing but also to all other states in the plane in Fig. 5.3. Therefore, it is easy to see that for all non-quantum squeezed states (i.e.,

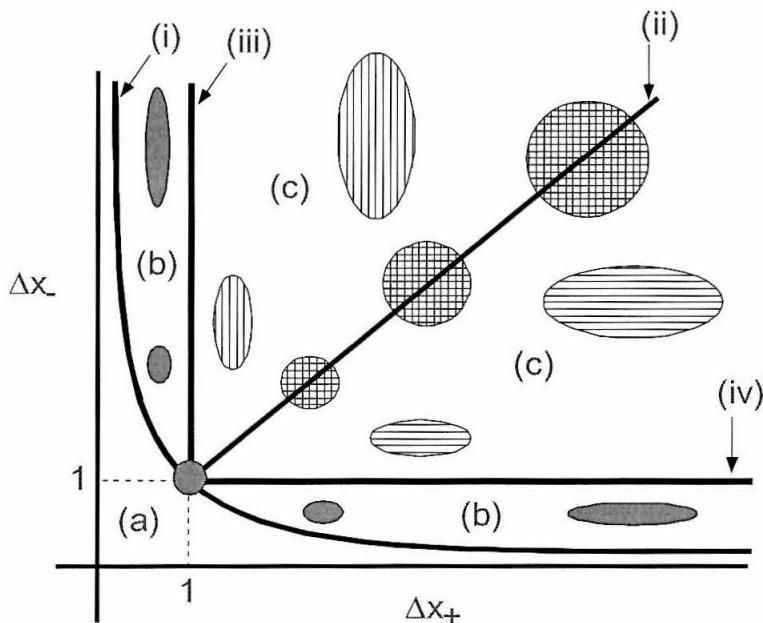


Figure 5.3: Quadrature space of the squeezed states of the electromagnetic field. Curve (i) indicates minimum uncertainty states which satisfy $\Delta X_- \Delta X_+ = 1$. Curve (ii) corresponds to thermal states for which $\Delta X_- = \Delta X_+ > 1$. Curves (iii) and (iv) are for states with $\Delta X_+ = 1$ and $\Delta X_- = 1$, respectively. States in region (a) are forbidden by the uncertainty relation. States in region (b) are quantum squeezed states characterized by the fact that either $\Delta X_+ < 1$ or $\Delta X_- < 1$. States in region (c) are classically squeezed states with both $\Delta X_+ \geq 1$ and $\Delta X_- \geq 1$ and also with unequal quadratures $\Delta X_- \neq \Delta X_+$. The special state $\Delta X_- = \Delta X_+ = 1$ corresponds to the electromagnetic vacuum.

all states not satisfying Eq. (5.18)), the two-photon excitation rate is proportional to N^2

$$\rho_{33}^{Classical.} \simeq v^2(\theta) N^2 \quad (5.19)$$

which always has slope $\frac{d(\log \rho_{33})}{d(\log N)} = 2$ and clearly does not have the distinctive linear component of Eq. (5.14).

5.2 Experiment

5.2.1 Setup

Turning now to the experiment, we have the setup shown in Fig. 5.4 which is almost identical to that described in Section 3.2 with the addition of Block V which is the part of the setup where the squeezed states are generated. The operation of Block V has been discussed in the previous chapter (Section 4.1) with more details about Block V shown in Fig. 4.3.

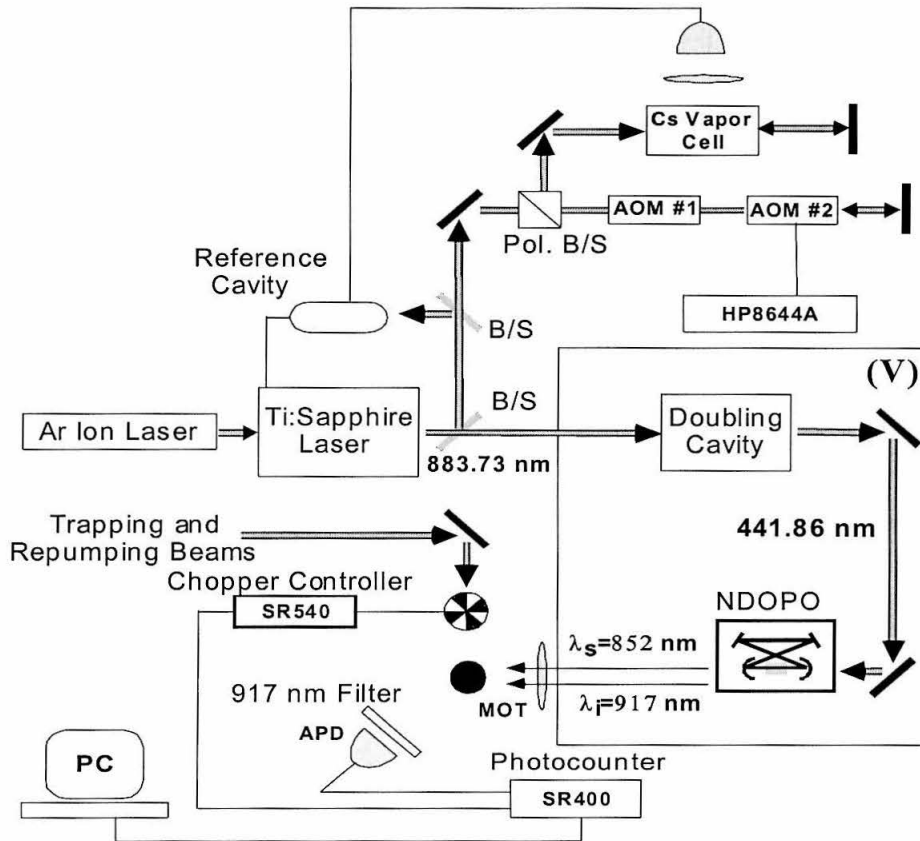


Figure 5.4: Experimental setup for two-photon excitation with non-classical fields.

Recall that in Fig. 5.4 the Ti:Sapphire laser is locked to the two-photon transition $6S_{1/2}F = 4 \rightarrow 6D_{5/2}F'' = 6$, which is achieved by locking to a Doppler-free

spectroscopy signal from an auxiliary *Cs* vapor cell. The output of the Ti:Sapphire laser, at $\lambda_o \simeq 884 \text{ nm}$, is frequency doubled to $\lambda_p \simeq 442 \text{ nm}$ and is used for pumping the NDOPO. The output of the NDOPO is tuned so that the signal ($\lambda_s \simeq 852 \text{ nm}$) and idler ($\lambda_i \simeq 917 \text{ nm}$) beams are resonant with the one photon transitions $6S_{1/2}F = 4 \rightarrow 6P_{3/2}F' = 5$ and $6P_{3/2}F' = 5 \rightarrow 6D_{5/2}F'' = 6$, respectively.³ The squeezed light from the OPO is focused onto the atomic sample which in our case is a MOT. The MOT is formed by diode laser beams that are chopped ON and OFF at 4 KHz . Finally, to measure the excitation rate, the fluorescent decay of the atoms from the $6D_{5/2}F'' = 6 \rightarrow 6P_{3/2}F' = 5$ transition at $\lambda_F \simeq 917 \text{ nm}$ is monitored.

The detector is an avalanche photodiode (APD) of quantum efficiency at 917 nm $\eta \simeq 0.25$, and is carefully shielded to reduce background. Two interference filters are placed in front of it with total transmission at 917 nm equal to $T_{917} \simeq 0.74$. The solid angle over which light is collected is defined by the 1-1 telescope shown in Fig. 2.2, which has opening angle $\theta \simeq 60^\circ$ and hence the solid angle that is covered is equal to $\sigma \equiv \frac{\Omega}{4\pi} = \frac{1}{2} (1 - \cos \frac{\theta}{2}) \simeq 0.07$. Combining the solid angle coverage, filter transmission and detector quantum efficiency gives an overall detection efficiency $\zeta_{tot} \simeq \eta T_{917} \sigma \simeq 0.01$.

5.2.2 ON/OFF Protocol

The measurement cycle consists of two parts, the so-called ON and OFF phases of the experiment which differ from each other only with regard to the state of the trapping beams which are either turned on or off, respectively (see Fig. 5.5). The frequency of the ON/OFF cycle is regulated by the mechanical chopper shown in Fig. 5.4 and is adjusted to be 4 KHz . During the ON part of the cycle, Fig. 5.5a, the trap is formed and the two-photon transition is excited by the combination of the trapping beams and the OPO output, providing a measure for the OPO output intensity R_1 . During the OFF part of the cycle, Fig. 5.5b, the two-photon transition is excited by the signal and idler beams of the OPO and the fluorescent decay R_2 gives a measure

³It is estimated that the fields at 884 nm , 852 nm and 917 nm were kept within 1 MHz from resonance with their corresponding atomic transition.

of the nonclassical excitation rate.

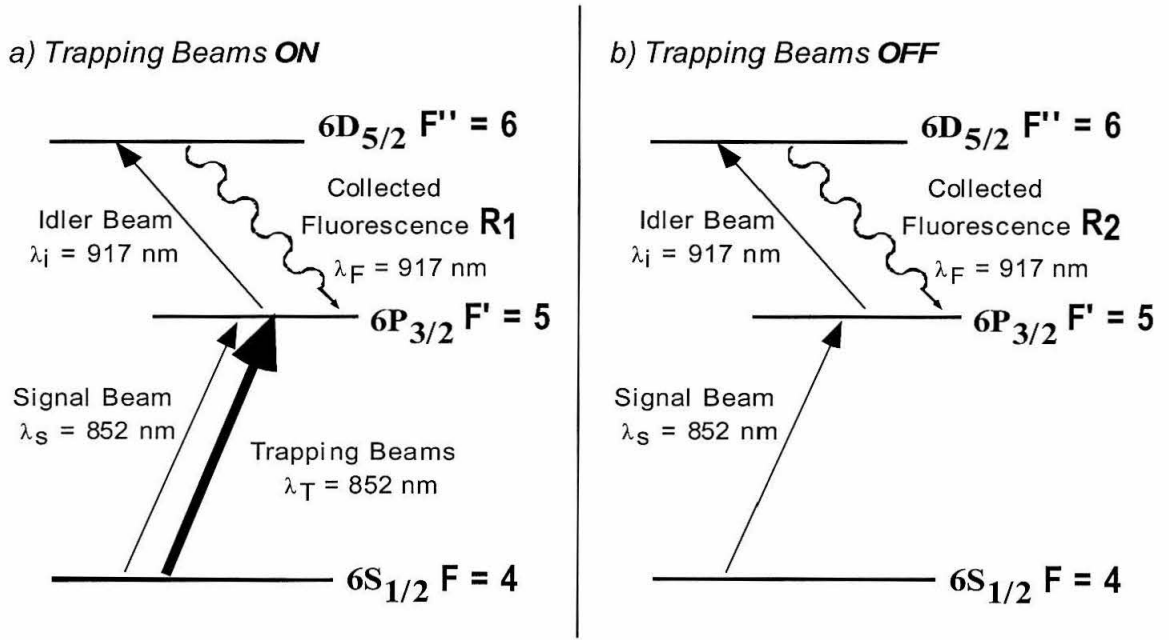


Figure 5.5: a) With the trapping beams turned ON, the rate R_1 is proportional to the intensity of the idler field. b) When the trapping beams are turned OFF, the rate R_2 is proportional to the two-photon excitation rate by the signal and idler beams from the NDOPO.

In particular, during the ON part of the cycle, Fig. 5.5a, the trapping beams saturate the $6S_{1/2}F = 4 \rightarrow 6P_{3/2}F' = 5$ transition and a considerable fraction of the atoms are excited to the $6P_{3/2}F' = 5$ level. The contribution of the signal beam from the NDOPO is negligible because the power in this beam is several orders of magnitude lower than the power of the trapping beams. Therefore, independently of the NDOPO output power, the excited state population of the $6P_{3/2}F' = 5$ level is constant during the ON phase of the experimental cycle. However, the idler beam, resonant with the $6S_{1/2}F = 4 \rightarrow 6P_{3/2}F' = 5$ transition, excites atoms from the intermediate to the upper level at a rate that is proportional to its intensity. Monitoring the fluorescent decay from the $6D_{5/2}F'' = 6 \rightarrow 6P_{3/2}F' = 5$ transition gives R_1 which is a measure of the idler beam intensity I_i , i.e., $R_1 \propto I_i$.

On the other hand, during the OFF part of the experimental cycle, Fig. 5.5b, the trapping beams are turned off and the atoms are excited from the ground state $6S_{1/2}F = 4$ to the upper level $6D_{5/2}F''$ by the combination of the signal and idler beams from the OPO. Thus, monitoring the fluorescent decay from the $6D_{5/2}F'' = 6 \rightarrow 6P_{3/2}F' = 5$ transition gives R_2 which is a measure of the nonclassical excitation probability.

To implement this acquisition protocol, the photon counter is gated to integrate the signal from the APD in two distinct channels that measure R_1 and R_2 . This measurement is complimented by phase-sensitive gain measurements G_+ and G_- similar to those described in Section 4.3.2. To change the gain, and hence the OPO output power, we regulate the pump power. Therefore, for each pump power there is a quadruplet of measurements $\{R_1, R_2, G_+, G_-\}$. The quantities R_1 , G_+ and G_- contain redundant information about the degree of squeezing, or equivalently the power of the squeezed output of the NDOPO, while R_2 is proportional to the nonclassical excitation probability.

5.2.3 Background

One of the critical aspects of the experiment is the accurate determination of background in the R_2 measurement. As estimated earlier in Eq. (5.16) (and also confirmed by our data, see below), the counting rate at the region of interest is $R_2 \sim 1$ / sec; therefore, even a single photon per second leaking into the detector has dramatic effects on the S/N ratio of the experiment. Moreover, dubious sources of background, like scattering of the idler beam into the detector, would scale linearly with the OPO output intensity and mislead our conclusions. For these reasons several precautions and redundant tests have been performed to confirm that we understand and correctly eliminate all sources of background.

First, shielding of the detector was of the highest priority. Even though several layers of isolation have been used, the best background from diffuse scattering that was achieved was ~ 1 /sec. At this level, the main source of background remaining

was the detector itself with darkcounts of $\sim 4/\text{sec}$. A third source of background was the scattered light from the OPO output that contributes up to $4/\text{sec}$ although is more typically less than $0.2/\text{sec}$ for alignments that minimize the scattering into the detector.

Operationally, to measure the background without disturbing any of its sources, an interference filter that passes 917 nm radiation was placed at the OPO output. This filter has a double purpose: first, it turns off the two-photon excitation (since it blocks the signal beam at 852 nm) and, second, it does not disturb the idler beam which could contribute to the scattering background. Notice that scattering of the signal beam that is blocked by the filter does not contribute to the background because of the 917 nm interference filters in front of the detector. To confirm this background measurement, an alternative (independent) method was also used where the magnetic fields of the MOT were turned off. Without the magnetic fields the trap does not form and hence the two-photon excitation is turned off as well. Note that this method is non-intrusive by eliminating only the sample of cold atoms excited by the OPO output, and hence only turns off R_2 without affecting the background. These two methods give within the experimental uncertainty the same background levels and hence confirm each other.

Finally, note that the integration time required to accumulate enough signal so as to distinguish signals of $\sim 1/\text{sec}$ over a background of $\sim 6/\text{sec}$ is roughly 20 min. During this time the whole lab (setup of Fig. 5.4), which includes several mechanical and thermal servos, has to operate without any disruption or drifts. This has proven to be not a trivial task!

5.2.4 Data

Here is a good place to document the numerical transformations on the raw data and make transparent the processing that leads to the counting rates R_1 and R_2 for the one and two-photon excitation rates, respectively. Starting with data acquisition, Fig. 5.6 shows the gating of the counter so as to distinguish between the ON and

OFF parts of the experimental cycle. Usually the width of these gates was about 100

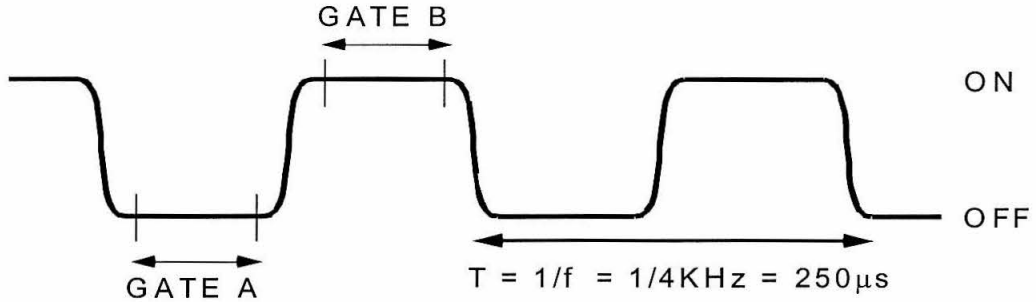


Figure 5.6: Gating of the photon counter. Gate A corresponds to the OFF and Gate B to the ON phases of the experiment.

μs and well within the ON or OFF phase so that edge effects would not contaminate the measurements. The counts of each gate were integrated long enough until 1 sec of data is accumulated (e.g., for 100 μs gates the integration was over 10000 gates), and the sum was sent to a computer in two channels A and B corresponding to the ON and OFF parts of the cycle. So at the end we have two streams of data, for channels A and B , denoted by

$$X_{OFF} = \{x_A^{(1)}, x_A^{(2)}, \dots, x_A^{(N)}\} \quad (5.20)$$

and

$$X_{ON} = \{x_B^{(1)}, x_B^{(2)}, \dots, x_B^{(N)}\} , \quad (5.21)$$

where x_A and x_B are counts per second for each of the channels. By averaging the data points in each channel, we get the mean counting rates per second R_{OFF} and R_{ON} with their corresponding uncertainties defined as usual by

$$R_{OFF/ON} = \frac{1}{N} \sum_{i=1}^N x_{A/B}^{(i)} \quad (5.22)$$

and

$$e_{R_{OFF/ON}} = \frac{1}{N} \sqrt{\sum_{i=1}^N \left(x_{A/B}^{(i)} - \frac{1}{N} \sum_{i=1}^N x_{A/B}^{(i)} \right)^2} \quad (5.23)$$

| G_+ | G_- | R_1 | R_2 |
|-------|-------|-------|------------|
| 0 | 0 | 0 | 0.00±0.50 |
| 2.00 | - | 7132 | 2.79±0.65 |
| 2.25 | - | 6374 | 2.39±0.61 |
| 1.75 | - | 6262 | 1.57±0.43 |
| 1.24 | - | 1465 | 0.61±0.51 |
| 3.00 | - | 14614 | 9.64±0.66 |
| 3.57 | - | 18389 | 14.85±0.91 |
| 2.38 | - | 12424 | 5.35±0.45 |
| 7.50 | - | 33677 | 49.19±2.78 |
| 6.00 | - | 26343 | 30.09±1.78 |
| 4.75 | - | 17944 | 12.82±1.09 |
| - | - | 13291 | 9.96±0.68 |
| - | - | 9182 | 4.84±0.48 |
| 2.25 | - | 4384 | 1.84±0.26 |
| - | - | 3063 | 0.75±0.46 |
| - | - | 2594 | 0.66±0.62 |
| 1.24 | - | 1947 | 0.23±0.25 |
| 1.46 | - | 3831 | 1.67±0.37 |
| 1.25 | - | 2689 | 0.44±0.42 |

Table 5.1: Excitation with non-classical fields, data from experiment 11/17/94.

Three types of measurements were performed with this procedure. First, the atoms were illuminated by the NDOPO output to determine the rates $R_{OFF/ON}^{OPO}$, then the background was measured to obtain $R_{OFF/ON}^{Bgd}$ and finally the OPO output was blocked and the atoms in the trap were illuminated by a fixed power of an 884 nm beam to obtain $R_{OFF/ON}^{884}$. This last measurement was used to normalize the data to account for trap density fluctuations. Note that the 884 nm beam was propagating in the same direction as the squeezed light and hence probed the same region in the MOT that interacted with the squeezed light.

By combining these three measurements, the counting rates R_1 and R_2 are estimated to be

$$R_1 = \left(R_{ON}^{OPO} - R_{ON}^{Bgd} \right) \frac{\overline{R}_{OFF}^{884}}{R_{OFF}^{884}} \quad (5.24)$$

and

$$R_2 = \left(R_{OFF}^{OPO} - R_{OFF}^{Bgd} \right) \frac{\overline{R}_{OFF}^{884}}{R_{OFF}^{884}} \pm \sqrt{\left(e_{R_{OFF}^{OPO}} \right)^2 + \left(e_{R_{OFF}^{Bgd}} \right)^2 + (e_{t.f.})^2}, \quad (5.25)$$

where the background has been subtracted and the trap density fluctuations have been factored out. The counting rate \overline{R}_{OFF}^{884} is an arbitrary reference level for normalizing the density fluctuations and is usually taken to be the mean of the R_{OFF}^{884} measurements. Notice that the normalization for the trap density fluctuations is the same for both the R_1 and R_2 rates. Also note that because of the high counting rate for R_1 , the error of this measurement is negligible and therefore not quoted. Finally, note that the error for the R_2 measurement is a combination of three factors: the Poissonian counting errors $e_{R_{OFF}^{OPO}}$ and $e_{R_{OFF}^{Bgnd}}$, and an estimated 5% fractional error

$$e_{t.f.} \equiv 0.05 \left(R_{OFF}^{OPO} - R_{OFF}^{Bgnd} \right) \frac{\overline{R}_{OFF}^{884}}{R_{OFF}^{884}} \quad (5.26)$$

due to the trap density fluctuations.

| G_+ | G_- | R_1 | R_2 |
|-------|-------|-------|------------|
| 0 | 0 | 0 | 0.00±0.50 |
| 4.9 | 3.13 | 22479 | 25.04±1.61 |
| 3.2 | 1.25 | 13701 | 10.26±0.83 |
| 2.3 | 0.78 | 9000 | 4.24±0.43 |
| 1.8 | 0.42 | 6319 | 2.68±0.33 |
| 1.5 | 0.26 | 4566 | 1.88±0.28 |
| 1.3 | 0.20 | 4048 | 1.50±0.53 |
| 1.3 | 0.16 | 2544 | 0.35±0.32 |

Table 5.2: Excitation with non-classical fields, data from experiment 11/29/94.

Tables 5.1 - 5.5 show the data for the five experiments performed. Note that G_- is the value of the phase-sensitive gain for the idler as determined by Eq. (4.15).

5.2.5 Control Experiment

In addition to the two-photon excitation with nonclassical fields (the spontaneously generated signal and idler beams from the NDOPO), a control experiment of excitation with classical fields (two coherent beams resonant with the $6S_{1/2}F = 4 \rightarrow 6P_{3/2}F' = 5$ and $6P_{3/2}F' = 5 \rightarrow 6D_{5/2}F'' = 6$ transitions, respectively) was also performed. To generate the coherent beams, a small signal beam resonant with the

| G_+ | G_- | R_1 | R_2 |
|-------|-------|-------|------------|
| 0 | 0 | 0 | 0.00±0.50 |
| 3.3 | 2.00 | 25356 | 17.53±1.06 |
| 2.0 | 0.95 | 13142 | 6.08±0.51 |
| 1.4 | 0.43 | 6516 | 1.87±0.25 |
| 1.2 | 0.20 | 3181 | 0.51±0.18 |
| 2.7 | 1.75 | 20602 | 13.02±0.84 |
| 6.7 | 5.00 | 44457 | 55.13±3.00 |
| - | - | 31968 | 26.95±1.50 |
| - | - | 25055 | 16.06±1.08 |
| 4.0 | 2.25 | 20173 | 13.81±0.96 |
| 2.0 | 0.75 | 9909 | 3.39±0.34 |
| 1.5 | 0.38 | 4437 | 0.70±0.23 |

Table 5.3: Excitation with non-classical fields, data from experiment 12/06/94.

| G_+ | G_- | R_1 | R_2 |
|-------|-------|-------|------------|
| 0 | 0 | 0 | 0.00±0.2 |
| 6.07 | 4.25 | 17400 | 35.06±2.07 |
| 3.67 | 2.25 | 9909 | 11.30±0.76 |
| 1.83 | 0.63 | 4576 | 3.06±0.61 |
| 1.67 | 0.45 | 3363 | 1.59±0.39 |
| 1.67 | 0.45 | 2744 | 1.41±0.44 |
| 1.68 | 0.63 | 3565 | 2.27±0.38 |

Table 5.4: Excitation with non-classical fields, data from experiment 12/20/94-a.

$6S_{1/2}F = 4 \rightarrow 6P_{3/2}F' = 5$ transition was injected into the OPO and was parametrically amplified; see Fig. 5.7. As a result, an additional (idler) beam was generated by the NDOPO that was resonance with the $6P_{3/2}F' = 5 \rightarrow 6D_{5/2}F'' = 6$ transition as described in the previous chapter, Section 4.3.

These two beams (the signal and idler output beams of the NDOPO) are in a superposition of coherent states with a small contribution from the squeezed vacuum that is simultaneously generated. To remove the squeezing, a strong attenuator (transmission 3×10^{-4}) is placed at the output of the OPO (Fig. 5.7). The power of the coherent signal and idler beams is regulated by controlling the power of the injected coherent beam. The same set of measurements to obtain R_1 and R_2 as before are taken with this arrangement.

This experiment was performed twice, once on 12/22/94 and once on 1/12/95.

| G_+ | G_- | R_1 | R_2 |
|-------|-------|-------|------------------|
| 0 | 0 | 0 | 0.00 ± 0.20 |
| 4.17 | - | 7049 | 11.96 ± 0.84 |
| 1.35 | 0.22 | 1277 | 1.52 ± 0.40 |
| 2.41 | 0.68 | 3581 | 4.50 ± 0.53 |
| 3.27 | 1.53 | 6352 | 9.72 ± 0.70 |
| 1.27 | 0.14 | 756 | 0.37 ± 0.32 |
| 1.27 | 0.14 | 795 | 0.79 ± 0.31 |
| 1.85 | - | 3123 | 3.62 ± 0.48 |
| - | - | 9800 | 23.32 ± 1.48 |
| 5.22 | 2.81 | 7927 | 16.14 ± 1.00 |
| 1.43 | 0.31 | 1319 | 0.72 ± 0.26 |
| 2.31 | 0.75 | 3149 | 2.91 ± 0.33 |

Table 5.5: Excitation with non-classical fields, data from experiment 12/20/94-b.

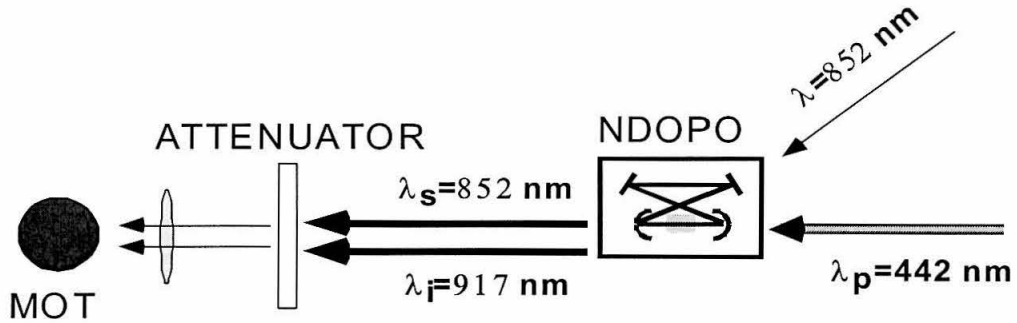


Figure 5.7: Setup for generating two coherent beams at 852 nm and 917 nm in resonance with the $6S_{1/2}F = 4 \rightarrow 6P_{3/2}F' = 5$ and $6P_{3/2}F' = 5 \rightarrow 6D_{5/2}F'' = 6$ transitions, respectively.

In the first experiment the gain of the NDPO was $G_+ \simeq 2.5$ and in the second $G_+ \simeq 5.0$. Table 5.6 lists the data from these experiments.

5.3 Summary

In this chapter the theory and experimental realization of two-photon excitation with nonclassical fields has been presented. Two different theoretical approaches were outlined, the simple Mollow description [77] and the more complete integration of the master equation.[44, 45]. In both treatments the rate of two-photon excitation is pre-

| 12/22/94 | | 1/12/95 | |
|----------|------------------|---------|--------------------|
| R_1 | R_2 | R_1 | R_2 |
| 0 | 0.00 ± 0.50 | 0 | 0.00 ± 0.50 |
| 13350 | 25.66 ± 1.55 | 69923 | 987.00 ± 50.56 |
| 5455 | 4.46 ± 0.58 | 44240 | 378.00 ± 19.55 |
| 2775 | 1.28 ± 0.32 | 24301 | 115.00 ± 6.09 |
| 1355 | 0.37 ± 0.29 | 14704 | 41.52 ± 2.41 |
| 1672 | -0.24 ± 0.52 | 11519 | 19.62 ± 1.17 |
| 1941 | 0.95 ± 0.35 | 5072 | 3.50 ± 0.42 |
| 3835 | 2.33 ± 0.42 | 2093 | 1.19 ± 0.37 |
| 8090 | 10.00 ± 0.79 | 1068 | 0.33 ± 0.34 |
| | | 1410 | 0.43 ± 0.33 |

Table 5.6: Excitation with coherent fields, data from experiments on 12/22/94 and 1/12/95.

dicted to approach asymptotically a linear dependence for small enough intensities with the particular functional form $\rho_{33} \propto N^2 + \xi |M|^2$, Eqs. (5.10) and (5.15). By analyzing different types of states it has been shown that the linear component exists only for nonclassical states as defined by $N < M \leq \sqrt{N(N+1)}$. The experimental realization was then presented in detail. Both the setup, acquisition protocols and data filtering have been carefully explained and the data have explicitly been reported. Finally, a control experiment of two-photon excitation with coherent fields was described. In the next chapter the data from these experiments will be analyzed and the results will be discussed.

Chapter 6 Two-Photon Excitation Rate with Nonclassical Fields: Analysis, Statistics and Results

In the previous chapter the theory and experimental realization of nonclassical two-photon excitation was presented. Here, the data obtained in the experiments of Chapter 5 (Tables 5.1-5.5 and 5.6) will be analyzed and, based on statistical arguments, it will be demonstrated that an asymptotically linear dependence has been observed. In particular, it will be shown that the rate of nonclassical two-photon excitation is best described by the combination of a linear plus a quadratic term of the excitation intensity which is in sharp contrast with the observations of classical excitation in the control experiments for which the dependence is purely quadratic. Absolute comparison with theory is achieved by incorporating the gain measurements and estimating the “knee” position defined to be the point at which the contributions from the quadratic and linear terms are equal. Furthermore, by normalizing the data to the theory, a combination of all data points on a single graph will be presented which will clearly demonstrate in a visual manner as well the deviation from the classical quadratic law.

6.1 Statistical Analysis Part I: Functional Form of

R_2 vs. R_1

6.1.1 Fitting Procedure

The first issue in the analysis is to identify the correct functional form that describes the R_2 versus R_1 data. As explained in the previous chapter, the excited state pop-

ulation ρ_{33} is proportional to the experimentally determined rate R_2 ,

$$\rho_{33} = \sigma_2 R_2, \quad (6.1)$$

while the intensity of the excitation fields I is proportional to R_1 ,

$$I = \sigma_1 R_1. \quad (6.2)$$

Here σ_1 and σ_2 are constants of proportionality which include the experimental efficiencies, atomic cross sections and trap conditions. In general σ_1 and σ_2 will differ from experiment to experiment, and therefore the data from different runs can not be all represented on a single graph without some sort of normalization. Equations (6.1) and (6.2) also imply that investigating the functional dependence of ρ_{33} as a function of intensity I , $\rho_{33} = F(I)$, is equivalent to investigating $R_2 = f(R_1)$. Recall that our goal is to demonstrate that the rate of nonclassical two-photon excitation is a combination of a linear term plus a quadratic term, $F(I) = a_1 I + a_2 I^2$ (see Eq. (5.15)) and hence we must show that $f(R_1) = a'_1 R_1 + a'_2 R_1^2$.

From a mathematical point of view, identifying the best functional form f that fits a given set of data is not an easy task. However, with some physical insight the choices in this case can be limited to the following four alternative models that will be examined in detail. The first of these is the quadratic model

$$f_Q(R_1) \equiv \beta_1 R_1^2, \quad (6.3)$$

which describes classical excitation corresponding to an excitation probability that scales quadratically with intensity. Then, the quadratic plus constant model

$$f_{Q+C}(R_1) \equiv \beta_2 R_1^2 + \beta_3 \quad (6.4)$$

describes a ‘‘pitfall’’ case in the experiment, corresponding to a classical quadratic rate plus a constant background contribution β_3 that has not been correctly identified and

removed from the data. If such a contribution is present, then at low intensities ($I \rightarrow 0 \Rightarrow R_1 \rightarrow 0$) the data will exhibit a divergence from the quadratic law that could mislead to an interpretation as nonclassical excitation. The third model is a power law which is neither quadratic nor linear but rather depends on an arbitrary power,

$$f_P(R_1) \equiv \beta_4 R_1^{\beta_5}. \quad (6.5)$$

Finally, the fourth model is a quadratic plus linear function

$$f_{Q+L}(R_1) \equiv \beta_6 R_1^2 + \beta_7 R_1, \quad (6.6)$$

which is in accordance with the theoretical prediction for nonclassical excitation, Eq. (5.15). Note that the model f_{Q+L} could also be observed if we had dubious sources of background, such as scattered light, that scale linearly with intensity. This, however, has been excluded by the procedures for background determination explained in Section 5.2.3.

Based on these four models, the statistical question imposed is which of them best describes the data of the nonclassical excitation experiments and which the data of the classical excitation (control) experiments. Note that the procedures (such as background determination and data acquisition protocol), as well as the counting rates at the low end of the data, are for both types of experiments identical. Therefore, if there are deficiencies or pitfalls in the experiments with nonclassical excitation, they should also be present in the classical excitation experiments. On the other hand, if differences are discovered between the two types of experiments, then these differences are most likely due to intrinsic differences in the underlying physical processes.

The analysis begins by fitting the data from each experiment to the four models of Eqs. (6.3)-(6.6). The fitting is done as usual by minimizing the $\chi^{(2)}$ “score” function defined by

$$\chi^{(2)} = \sum_{i=1}^n \left(\frac{R_2^{(i)} - f(R_1^{(i)})}{e_{R_2^{(i)}}} \right)^2, \quad (6.7)$$

where n is the number of points in each experiment, $\{R_1^{(i)}, R_2^{(i)}, e_{R_2^{(i)}}\}$ are data points, and f is one of the test functions f_Q, f_{Q+C}, f_P and f_{Q+L} . The “goodness” of each fit is quantified in terms of the $\chi^{(2)}$ of the fit and also the significance level S defined by

$$S \equiv \int_{\chi^{(2)}}^{\infty} F_{n-d}(x) dx, \quad (6.8)$$

where F_{n-d} is the $\chi^{(2)}$ distribution with $n - d$ degrees of freedom, and where n is the number of points in the experiment and d the number of fit parameters.[78] It is noted however that in some special cases, some or all of the fits could be degenerate as for example when the data are described by a purely quadratic relation, which in an ideal case would result in a set of fit parameters $\{\beta_1, \beta_2, \beta_3, \beta_4, \beta_5, \beta_6, \beta_7\} = \{\beta_1, \beta_1, 0, \beta_1, 2, \beta_1, 0\}$ that implies $f_Q = f_{Q+C} = f_P = f_{Q+L} = \beta_1 R_1^2$.

As indicted in the previous chapter, the nonclassical excitation experiment was performed five times (11/17/94, 11/29/94, 12/06/94, 12/20/94-a and 12/20/94-b) and the control experiment twice (12/22/94 and 1/12/95), Tables 5.1-5.5 and 5.6. The results of fitting the test functions to these data sets are shown in Table 6.1.¹

| Experiment | f_Q | | f_{Q+C} | | f_P | | f_{Q+L} | |
|------------|---------|--------------|-----------|--------------|--------|--------------|-----------|--------------|
| | S | $\chi^{(2)}$ | S | $\chi^{(2)}$ | S | $\chi^{(2)}$ | S | $\chi^{(2)}$ |
| 11/17/94 | 0.00001 | 54.1 | 0.0024 | 39.6 | 0.0001 | 48.0 | 0.001 | 40.8 |
| 11/29/94 | 0.04 | 13.2 | 0.55 | 5.9 | 0.53 | 5.1 | 0.68 | 4.0 |
| 12/06/94 | 0.001 | 29.0 | 0.08 | 18.1 | 0.29 | 11.9 | 0.33 | 11.4 |
| 12/20/94a | 0.22 | 7.1 | 0.59 | 4.6 | 0.71 | 3.0 | 0.88 | 1.7 |
| 12/20/94b | 0.002 | 27.6 | 0.14 | 16.0 | 0.24 | 12.6 | 0.50 | 9.3 |
| 12/22/94 | 0.82 | 3.6 | 0.92 | 3.2 | 0.90 | 2.9 | 0.89 | 2.9 |
| 1/12/95 | 0.0001 | 31.3 | 0.0003 | 30.8 | 0.09 | 13.5 | 0.009 | 20.3 |

Table 6.1: Significant levels S and $\chi^{(2)}$ values for fits to the test functions. The number of free parameters $n - d$ in the experiments of $\{11/17/94, \dots, 1/12/95\}$ are for f_Q equal to $\{18, 7, 12, 6, 11, 8, 9\}$ and for f_{Q+C}, f_P and f_{Q+L} equal to $\{17, 6, 11, 5, 10, 7, 8\}$.

By inspection of Table 6.1 several observations can be made. First, for the nonclassical excitation experiments (11/17/94, 11/29/94, 12/06/94, 12/20/94-a and 12/20/94-b) it is obvious that the f_Q model is significantly inferior to the other test

¹More details about the fits in each experiment are shown in Appendix B.

functions as evident from the relatively small confidence level with respect to the rest. Second, for the same set of nonclassical experiments, the fit to f_{Q+L} (which indicates a nonclassical excitation rate) is consistently bigger (although not by a big margin) from the other two alternatives f_{Q+C} and f_P . Third, all fits to the experiment of 11/17/94 are much worse than they are for the rest of the experiments which possibly indicates pathologies in this particular experiment such as unrecorded fluctuations in the trap density, OPO gain fluctuations or laser drifts. Next, for the control experiments (12/22/94 and 1/12/95) the best fit in both cases is the power model $f_P \equiv \beta_4 R_1^{\beta_5}$ for which, however, the power dependencies are $\beta_5 = 1.9$ and 2.1 , respectively; see Appendix B. In addition, the experiment of 12/22/94 has almost identical significance levels for all four test functions which is a direct result of the special case noted earlier, namely that the models become degenerate for a set of data that is described by a quadratic relation. This degeneracy, and hence quadratic dependance, is also true for the last experiment (1/12/95), although it is not evident from its significant levels and $\chi^{(2)}$ values. For both control experiments it is clear from the actual fit parameters that the fitted models are indistinguishable and suggest an almost perfect quadratic dependance.

6.1.2 The \bar{S} statistic

The next task is to define cumulative statistics to quantify the combined knowledge from all experiments. This crucial step in understanding the results should be carefully addressed. The situation is similar to any generic measurement of a given quantity x , for which several data points are taken and then by averaging them a best estimate \bar{x} for the quantity x is established. Here, “data points” are the various experiments and the quantity x is the hypothesis that a given functional form f describes the data.

For each experiment we have probability measures (the significance levels) for the truth of the hypothesis that model $f \in \{f_Q, f_{Q+C}, f_P, f_{Q+L}\}$ describes the data. Therefore, a natural measure of the “average” probability of the hypothesis that the

data of any particular experiment are described by the model f , is the geometric mean \bar{S} of the significant levels of all the experiments with squeezed excitation, namely

$$\bar{S}_j \equiv \sqrt[5]{S_1^{(j)} S_2^{(j)} S_3^{(j)} S_4^{(j)} S_5^{(j)}} \quad (6.9)$$

where $S_i^{(j)}$ is the significance level of the fit of the j^{th} model function (from f_Q , f_{Q+C} , f_P and f_{Q+L}) to the i^{th} experiment (from 11/17/94, 11/29/94, 12/06/94, 12/20/94-a and 12/20/94-b). Applying this definition gives $\bar{S}_Q = 0.003$, $\bar{S}_{Q+C} = 0.10$, $\bar{S}_P = 0.08$, $\bar{S}_{Q+L} = 0.15$. If the first experiment, of 11/17/94, is excluded on the basis that it is an ‘‘outlier,’’ and by redefining \bar{S} to be the fourth root of the product of the significant levels of the remaining four experiments gives $\bar{S}'_Q = 0.01$, $\bar{S}'_{Q+C} = 0.24$, $\bar{S}'_P = 0.40$, $\bar{S}'_{Q+L} = 0.54$.

To quantify how much better the linear plus quadratic model fits the data as compared to any of the alternative model, the quantity Π is defined,

$$\Pi \equiv \min \left\{ \frac{\bar{S}_{Q+L}}{\bar{S}_Q}, \frac{\bar{S}_{Q+L}}{\bar{S}_{Q+C}}, \frac{\bar{S}_{Q+L}}{\bar{S}_P} \right\}. \quad (6.10)$$

Note that in this definition taking the min of the ratios is equivalent to considering the worse case, i.e., comparing the probability of f_{Q+L} with the second most likely model. Taking into account all five experiments of nonclassical excitation gives $\Pi = 1.5$, while excluding the first experiment results in $\Pi' = 2.25$. Hence in the first case the data are at least 1.5 times more likely to be described by the f_{Q+L} model than by any of the other test functions, while in the second case this probability increases to 2.25.

6.1.3 The \bar{C} statistic

An alternative statistic that can be defined is the significance level of the cumulative $\chi^{(2)}$ value

$$\chi_{TOT,j}^{(2)} \equiv \chi_{1,j}^{(2)} + \chi_{2,j}^{(2)} + \chi_{3,j}^{(2)} + \chi_{4,j}^{(2)} + \chi_{5,j}^{(2)}, \quad (6.11)$$

where $\chi_{i,j}^{(2)}$ is the $\chi^{(2)}$ value from the fit of the j^{th} model function (from f_Q , f_{Q+C} , f_P and f_{Q+L}) to the i^{th} experiment (from 11/17/94, 11/29/94, 12/06/94, 12/20/94-a and

12/20/94-b). The static \overline{C}_j is defined to be the significance level as calculated from Eq. (6.8) where n is the total number of data points from all five experiments and d is five times the number of fit parameters in f_j . Applying this statistic to the values in Table 6.1 for the nonclassical excitation experiments gives $\overline{C}_Q = 2 \times 10^{-8}$, $\overline{C}_{Q+C} = 0.001$, $\overline{C}_P = 0.004$ and $\overline{C}_{Q+L} = 0.04$. Excluding as before the first experiment gives $\overline{C}'_Q = 0.0001$, $\overline{C}'_{Q+C} = 0.07$, $\overline{C}'_P = 0.44$ and $\overline{C}'_{Q+L} = 0.72$.

Similarly with the previous case, the ‘‘likelihood’’ that the data are described by a linear plus quadratic model relatively to any of the other models is quantified in terms of ratios of the statistic \overline{C} , defined by

$$\Sigma \equiv \min \left\{ \frac{\overline{C}_{Q+L}}{\overline{C}_Q}, \frac{\overline{C}_{Q+L}}{\overline{C}_{Q+C}}, \frac{\overline{C}_{Q+L}}{\overline{C}_P} \right\}. \quad (6.12)$$

As before, taking into account all five experiments of nonclassical excitation gives that $\Sigma = 10$, while excluding the first experiment results in $\Sigma' = 1.64$. Hence, in this case as well, the data are most likely described by the linear plus quadratic model with a probability that is at least 1.64 times as big as the probability that they are described by any other model.

6.1.4 f_Q vs f_{Q+L}

In the above discussion all four test functions have been treated equally although from a physical standpoint some are better choices than others. Starting from f_{Q+C} , it is noted that the issue of an additive constant has been extensively studied by the measurements of the background and redundant procedures implemented to check for such a constant during the experiments (see Section 5.2.3). Furthermore, the f_P test function, although it may describe phenomenologically the data, has no good physical interpretation and can be excluded as well. In addition as noted earlier, degeneracy of the models forces these alternative fit functions (f_{Q+C} and f_P) to curves very similar with f_Q or f_{Q+L} and makes the distinction among all four choices less profound. Nevertheless, for completeness the results have been carefully presented for all models and even in this case distinction can be made in favor of f_{Q+L} .

Having said all that, the study of alternative functional forms can be limited to the two choices of f_Q and f_{Q+L} which characterize a classical quadratic and a nonclassical combination of a linear plus quadratic excitation rates, respectively. The distinction between these two is much more profound as seen from the ratios of the cumulative significant levels defined by the \bar{S} and \bar{C} statistics and are equal to:

- $\frac{\bar{S}_{Q+L}}{\bar{S}_Q} = 50$ (= 54 if the 11/17/94 experiment is excluded)
- $\frac{\bar{C}_{Q+L}}{\bar{C}_Q} = 2 \times 10^6$ (= 7200 if the 11/17/94 experiment is excluded)

Therefore, the distinguishability for the nonclassical excitation experiments between the f_Q and f_{Q+L} models is very clear and in favor of f_{Q+L} . Note that the measure of distinguishability provided by the \bar{S} statistic seems to be an underestimate relative to the estimate by the \bar{C} statistic (which appears to be an overestimate). Figure 6.1 shows the 12/20/94-b nonclassical excitation experiment overlaid by the f_Q and f_{Q+L} fits which even by “eye” are distinguishable and the f_{Q+L} fit is favored.

Moreover, the two control experiments of excitation with classical fields are described by purely quadratic functions and the alternative models yield degenerate curves best approximated by f_Q , as explained earlier. Figure 6.2 shows the data from the 12/22/94 experiment, plotted together with the best f_Q fit. Clearly, the fit leaves no doubt that the data are well described by a quadratic law in contrast with the nonclassical excitation experiments.

6.2 Statistical Analysis Part II: The G factor

Beyond the analysis of the R_2 versus R_1 data, there is one more piece of information, the gain measurements, that has not been utilized yet. The OPO gain is experimentally determined in two ways, by measuring G_{852} and G_{917} (see Eqs (4.13) and (4.15)), which are related to the operation of the OPO via the relations for G_s and G_i given in Eqs. (4.16) and (4.17). In particular, the intensity output of the squeezed field can be estimated directly from the gain measurements and hence offers an alternative route to investigate the functional dependence of R_2 versus intensity. In addition,

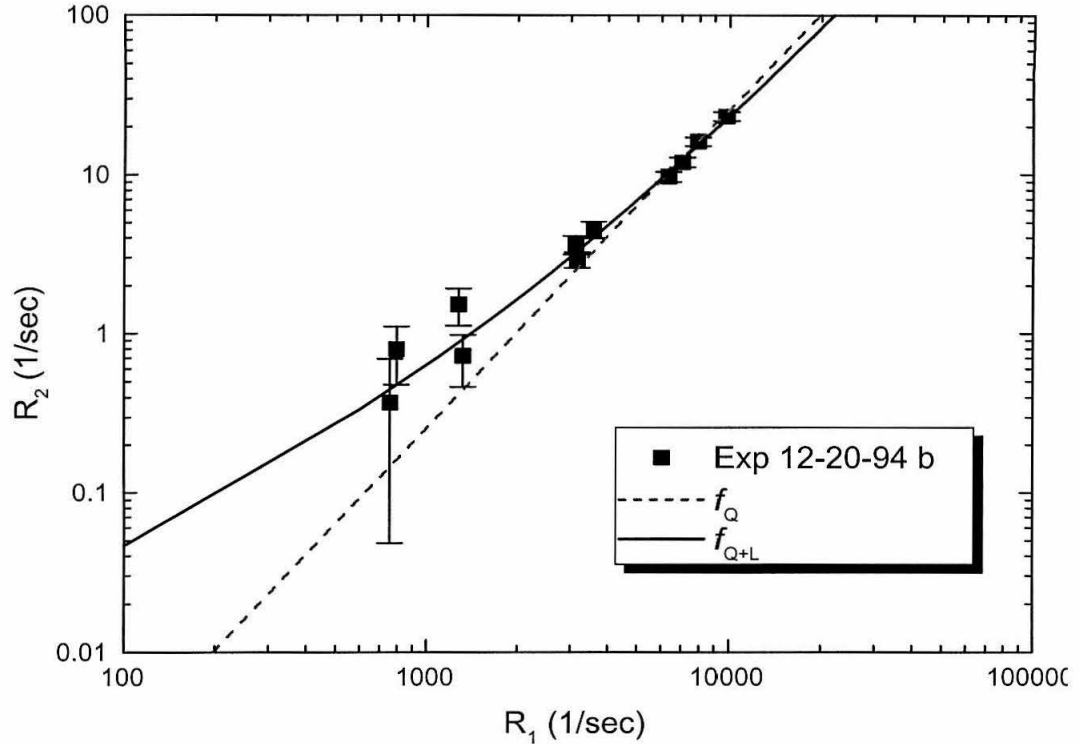


Figure 6.1: R_2 versus R_1 from the nonclassical two-photon excitation experiment of 12/20/94-b. The solid line is a quadratic plus linear fit (f_{Q+L}) and the dotted line is a quadratic fit (f_Q).

the relation of R_1 to the intensity (which should scale proportionally to each other) could also be verified.

The photon flux in the idler beam of the squeezed output of the NDOPO (and hence the output intensity I) scales proportionally to the intracavity photon number n_{917} in the idler beam, which is given by

$$n_{917} \equiv \langle \hat{a}_{917}^\dagger \hat{a}_{917} \rangle = \frac{1}{2} \frac{x^2}{1 - x^2}, \quad (6.13)$$

where x is the pumping parameter defined in Eq. (4.1). [79, 80] Then, the intracavity photon number n_{917} is expressed in terms of the OPO gain G_s , Eq. (4.16) (or equivalently G_i , Eq. (4.17)), which is what we experimentally measure as discussed in Sec. 4.3.2, by

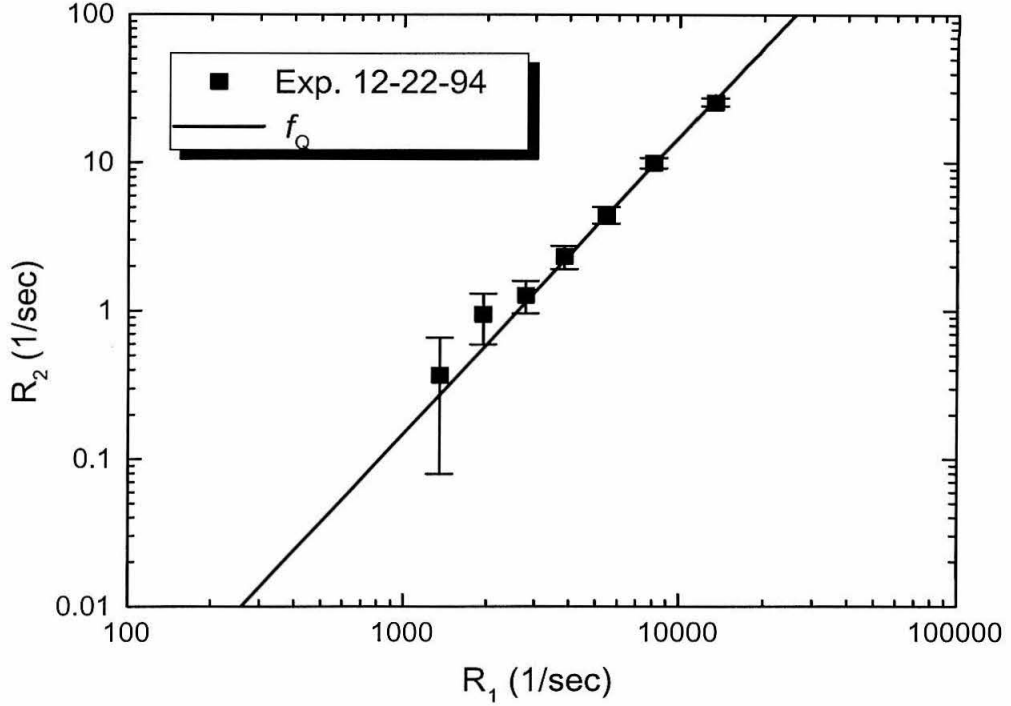


Figure 6.2: R_2 versus R_1 from the two-photon classical excitation experiment of 12/22/94. The solid line is a quadratic fit (f_Q) to the data.

$$n_{917} = \frac{1}{2} \left(\sqrt{G_s} - 1 \right) = \frac{1}{4} \left(\sqrt{4G_i + 1} - 1 \right), \quad (6.14)$$

and similarly n_{917} and G_i are related to each other by

$$n_{917} = \frac{1}{4} \left(\sqrt{4G_i + 1} - 1 \right). \quad (6.15)$$

Therefore, the question that needs to be addressed is whether or not the counting rates R_1 and R_2 are the expected functions of G_s , namely

$$R_1 = \alpha_1 \left(\sqrt{G_s} - 1 \right), \quad (6.16)$$

and

$$R_2 = \alpha_2 \left(\sqrt{G_s} - 1 \right) + \alpha_3 \left(\sqrt{G_s} - 1 \right)^2, \quad (6.17)$$

which follow trivially from Eqs. (5.14) and (6.14).² Notice that Eqs (6.16) and (6.17), together with $R_2 = f_{Q+L}(R_1)$, form an overspecified system that is redundant in the sense that by establishing Eq. (6.16) and given that $R_2 = f_{Q+L}(R_1)$ has already been shown, then Eq. (6.17) automatically follows.

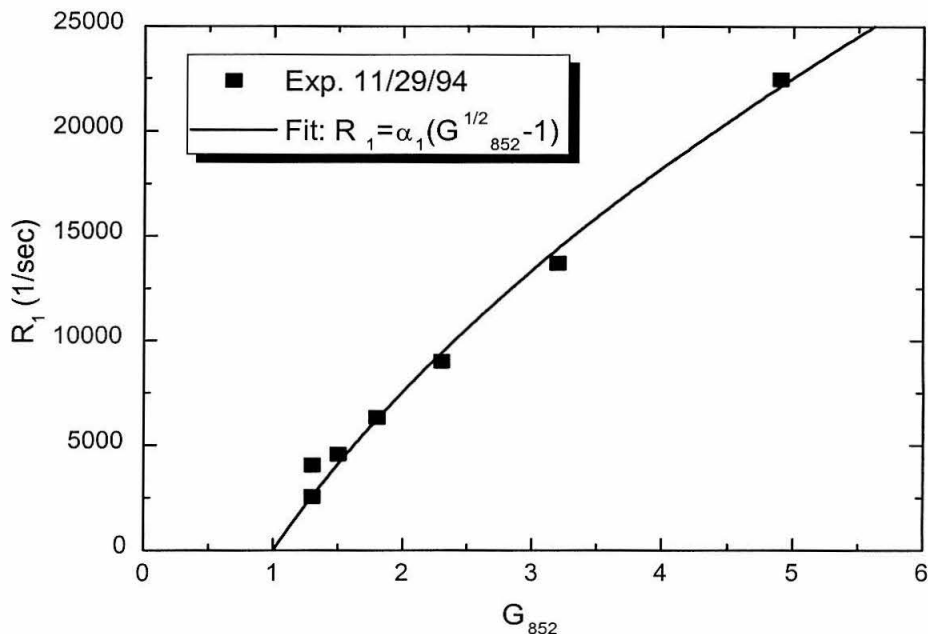


Figure 6.3: One photon counting rate R_1 versus the OPO gain G_{852} from the data of 11/29/94. The solid line is a fit of the form $R_1 = \alpha_1 \left(\sqrt{G_{852}} - 1 \right)$.

Instead of showing the full blown analysis of alternative functional forms for R_1 and R_2 vs. $G_{s,i}$, only two examples are shown here in support of the argument

²Note that during our experiments there was some confusion as to which gain we are measuring; see Appendix A, Sec A.2. In particular, while we thought that we were measuring $G'_s = \left(\frac{1+x^2}{1-x^2} \right)^2$, we were in fact measuring $G_s = \frac{1}{(1-x^2)^2}$. The implication of this is that n_{917} is expressed in different forms relative to G'_s and G_s . As can easily be shown $n_{917} = \frac{1}{2} \left(\sqrt{G_s} - 1 \right)$ and $n_{917} = \frac{1}{4} \left(\sqrt{G'_s} - 1 \right)$, hence, independently of our mistake, n_{917} has the same functional dependance on G_s and G'_s and hence the subsequent analysis of relating the gain measurements to R_1 and R_2 (Eq. (6.16) and (6.17)) is not affected. However, the relation of R_1 and R_2 to G_i is different from what we though it should have been, but this was not used either explicitly at any part of our work.

that the gain measurements are consistent with the linear plus quadratic dependence discussed in the previous section. Figure 6.3 shows the R_1 vs G_{852} data from the experiment of 11/29/94, plotted together with the best fit to the data of the form $R_1 = \alpha_1 (\sqrt{G_{852}} - 1)$. Clearly the agreement is quite good and supports the argument that the values of R_1 are proportional to the intensity. For completeness, in Fig. 6.4, the R_2 data from the same experiment are plotted as a function of the gain G_{852} with the solid line indicating a fit to Eq. (6.17) while the dashed line shows a purely quadratic fit.

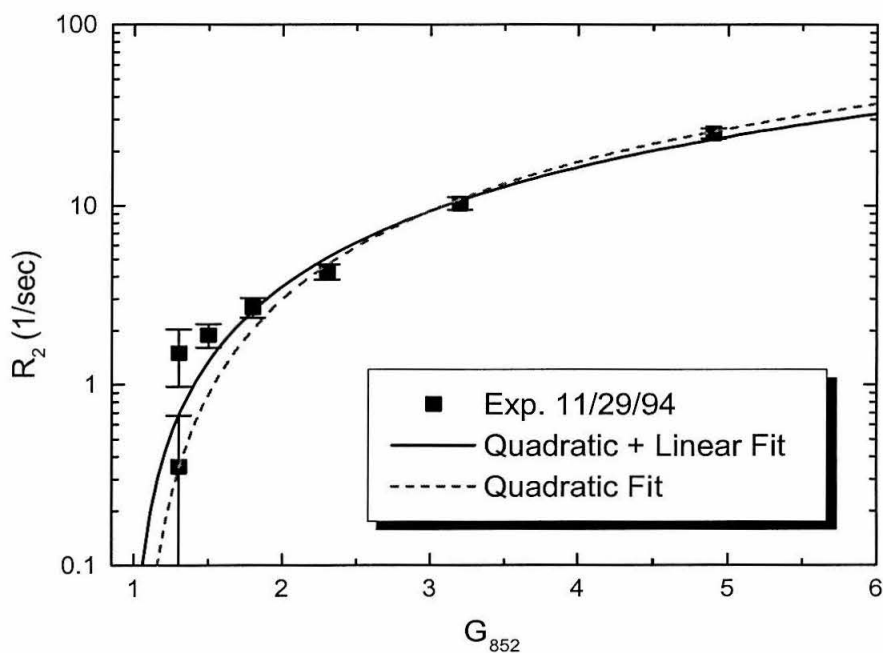


Figure 6.4: Two-photon counting rate R_2 versus the OPO gain G_{852} from the data of 11/29/94. The solid line is a fit of the form $R_2 = \alpha_2 (\sqrt{G_{852}} - 1) + \alpha_3 (\sqrt{G_{852}} - 1)^2$. The dashed lines shows the quadratic fit of the form $R_2 = \alpha'_3 (\sqrt{G_{852}} - 1)^2$.

6.3 “Knee” Position

Beyond the functional form that best describes the data, a natural question to ask is how the data compare in absolute terms with the theory. Answering this question

is not easy because the parameters σ_1 and σ_2 in Eqs. (6.1) and (6.2) differ from experiment to experiment and furthermore the efficiencies, atomic cross sections and trap conditions that determine these parameters have not been carefully measured. One absolute comparison that can be made, however, is the “knee” position, defined to be the intensity at which the contribution from the quadratic part of the R_2 vs. R_1 relation equals the contribution from the linear part. To relate the knee position to the nonclassical correlations of the excitation field, it is chosen to express this special point of “equipartition” in terms of the OPO gain G_s^{knee} .

From the theory of Ficek and Drummond [44, 45], the rate of two-photon excitation scales as

$$R_2 \propto \left(1 + \frac{\gamma_3}{\gamma_2}\right) N^2 + N, \quad (6.18)$$

(see Eq. (5.14)), which implies that knee position is at

$$N^{knee,FD} = \frac{\gamma_2}{\gamma_2 + \gamma_3} \simeq 0.61. \quad (6.19)$$

To obtain the numerical value of $N^{knee,FD}$, the values $\gamma_2 \simeq 5 \text{ MHz}$ and $\gamma_3 \simeq 3.2 \text{ MHz}$ have been used. The OPO gain at the knee point can be shown to be, [79] (see also Appendix C)

$$G_s^{knee,FD} = 1.33. \quad (6.20)$$

The theory of Ficek and Drummond from which the above prediction for the knee position is derived, is a broadband theory in contrast with the actual experiment for which the bandwidth of squeezing was finite ($\sim 7 - 9 \text{ MHz}$). For this reason, Dr. A. S. Parkins carried out a numerical integration of the master equation [81] to produce more accurate results; see Appendix C. The prediction for the knee position based on this theory is almost identical to $G_s^{knee,FD}$, and has the same value to the second decimal point,

$$G_s^{knee} = 1.33. \quad (6.21)$$

It should be noted, that even though both the broadband theory of Ficek and Drummond and the narrowband theory of A. S. Parikns predict the same gain for the

“knee” position, as far as we can tell, this is of no fundamental significance.

Turning now to the experiments, the knee position is determined from the $f_{Q+L}(R_1)$ fits to the data. In particular, from the fit $R_2 = \beta_6 R_1^2 + \beta_7 R_1$ the knee position is calculated in terms of R_1 to be

$$R_1^{knee} = \frac{\beta_7}{\beta_6}. \quad (6.22)$$

Then, by fitting $R_1 = \alpha_1 (\sqrt{G_s} - 1)$ (Eq. (6.16)) to the R_1 versus G_{852} data, the gain at the knee point is estimated to be

$$G_s^{knee} = \left(\frac{\beta_7}{\alpha_1 \beta_6} + 1 \right)^2 \pm e_G, \quad (6.23)$$

with

$$e_G \equiv \frac{2\beta_7}{\alpha_1 \beta_6} \left(\frac{\beta_7}{\alpha_1 \beta_6} + 1 \right) \sqrt{\left(\frac{e_{\alpha_1}}{\alpha_1} \right)^2 + \left(\frac{e_{\beta_6}}{\beta_6} \right)^2 + \left(\frac{e_{\beta_7}}{\beta_7} \right)^2 - \frac{2\text{cov}(\beta_6, \beta_7)}{\beta_7 \beta_6}}. \quad (6.24)$$

The uncertainty e_G of G_s^{knee} comes from error propagation of the uncertainties e_{α_1} , e_{β_6} and e_{β_7} of α_1 , β_6 and β_7 , found by the fits. The quantity $\text{cov}(\beta_6, \beta_7)$ is the covariance of β_6 and β_7 estimated from the variance-covariance matrix of the fits.

| Experiment | α_1 | $\beta_6 (\times 10^{-7})$ | $\beta_7 (\times 10^4)$ | $\text{cov}(\beta_6, \beta_7)$ | G_s^{knee} |
|------------|--------------|----------------------------|-------------------------|--------------------------------|--------------|
| 11/17/94 | 18182 ± 691 | 0.37 ± 0.04 | 1.2 ± 0.5 | -6.72 × 10 ⁻¹⁴ | 1.39 ± 0.20 |
| 11/29/94 | 18239 ± 423 | 0.42 ± 0.04 | 1.5 ± 0.4 | -1.84 × 10 ⁻¹³ | 1.43 ± 0.17 |
| 12/06/94 | 27141 ± 1339 | 0.24 ± 0.01 | 1.1 ± 0.3 | -2.88 × 10 ⁻¹⁴ | 1.37 ± 0.13 |
| 12/20/94a | 11592 ± 259 | 1.01 ± 0.06 | 1.9 ± 0.6 | -6.52 × 10 ⁻¹³ | 1.35 ± 0.16 |
| 12/20/94b | 6695 ± 220 | 1.88 ± 0.18 | 4.5 ± 1.1 | -1.67 × 10 ⁻¹² | 1.84 ± 0.32 |

Table 6.2: Fit parameters and OPO gain at the knee position, G_s^{knee} , for the non-classical excitation experiments.

The values of the fit parameters and the gain at the knee point derived from Eqs. (6.23) and (6.24) are shown in Table 6.2. The average of G_s^{knee} (calculated using the least squares estimator $\bar{x} \pm \bar{e} = \sum \frac{x_i}{e_i^2} / \sum \frac{1}{e_i^2} \pm 1 / \sqrt{\sum \frac{1}{e_i^2}}$) is equal to

$$\overline{G_s^{knee}} = 1.41 \pm 0.08. \quad (6.25)$$

Figure 6.5 shows graphically these results. Note that our data for the gain at the knee point are systematically higher than the theoretically predicted value, although after taking the average, they are only 1σ away from this value. Although we have no quantitative explanation for this discrepancy, we believe that it may be related to imperfections in the experiment as compared with the theory, which include laser detunings, frequency drifts, density fluctuations in the trap and the imperfection of the OPO output as discussed in Chapter 4. One possible explanation for the deviation of our data from the full theory is that there are nonzero detunings which move the “knee” position as discussed in Appendix D. However, a full investigation of the effects of detunings has not been carried out and although we do have some calculations (see Appendix D) that show that the knee position moves around with detunings, it remains an issue for future investigation.

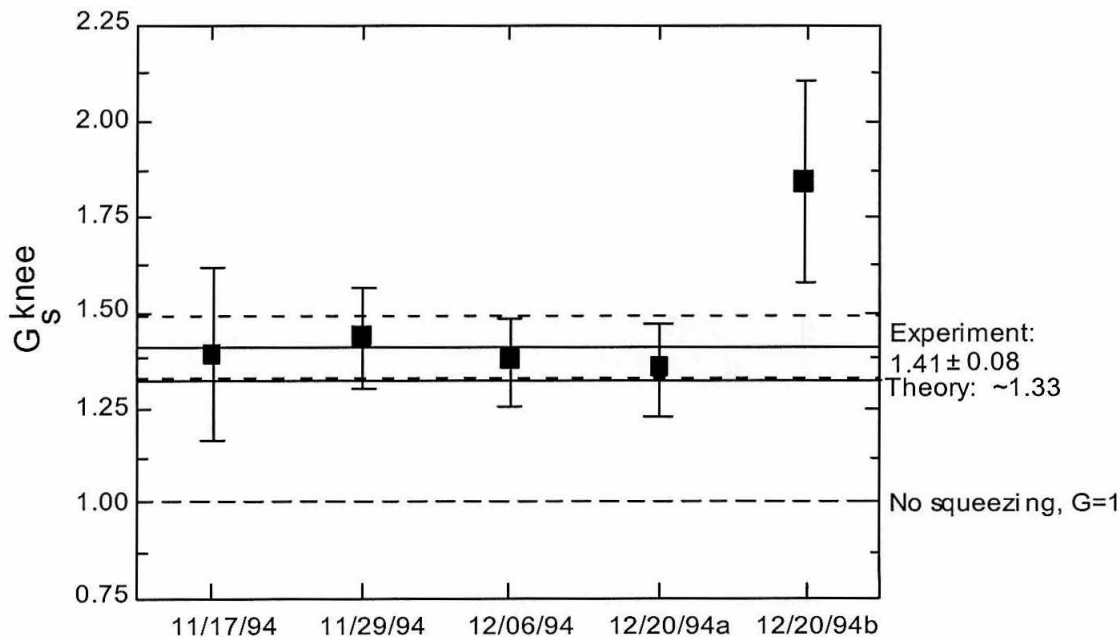


Figure 6.5: Gain at the knee position G_s^{knee} for the non-classical excitation experiments. The solid line at $G = 1.33$ is the prediction from the full theory and is approximately the same as the value predicted from the theory of Ficek and Drummond. The solid line at $G = 1.41$ is the average of the experimental values and the two dotted lines symmetrically around it are the 1σ error bars.

6.4 Combining all Data

To complete the analysis, a normalization procedure is implemented to combine all experiments into a single plot and compare them to theory. Experimentally, the quantities that have been measured are the one and two-photon excitation rates R_1 and R_2 , and the OPO gain G^{exp} . These parameters are related to the theoretical predictions for the excited state population ρ_{33} , the OPO output intensity characterized by the photon flux in the idler beam n_{917} and the OPO gain G^{th} via the simple proportionality relations $R_2 = \frac{1}{\sigma_2}\rho_{33}$ and $R_1 = \frac{1}{\sigma_1}n_{917}$ (see Eqs. (6.1) and (6.2)) and the equality condition for the gain $G^{\text{exp}} = G^{\text{th}}$. Hence, the goal of normalizing the data to the theory reduces to identifying the parameters σ_1 and σ_2 .

The normalization procedure begins by considering the following set of equations based on theory

$$\rho_{33} = \lambda_1 n_{917} + \lambda_2 n_{917}^2, \quad (6.26)$$

$$n_{917} = \lambda_3 \left(\sqrt{G^{\text{th}}} - 1 \right), \quad (6.27)$$

$$\rho_{33} = \lambda_4 \left(\sqrt{G^{\text{th}}} - 1 \right) + \lambda_5 \left(\sqrt{G^{\text{th}}} - 1 \right)^2, \quad (6.28)$$

which relate in a redundant way the quantities $\{\rho_{33}, n_{917}, G^{\text{th}}\}$ to each other. The coefficients λ_i are determined by fitting Eqs. (6.26)-(6.28) to a set of values of $\{\rho_{33}, n_{917}, G^{\text{th}}\}$ obtained by numerically integrating the appropriate master equation for our system; Refs. [79, 81] and Appendix C. These values are found to be $\lambda_1 = 0.985 \times 10^{-6}$, $\lambda_2 = 18.05 \times 10^{-6}$, $\lambda_3 = 0.459$, $\lambda_4 = \lambda_1 \lambda_3 = 4.52 \times 10^{-7}$, and $\lambda_5 = \lambda_2 \lambda_3^2 = 3.80 \times 10^{-6}$.

Counterparts to Eqs. (6.26)-(6.28) are the following functions that describe the experimental data

$$R_2 = \mu_1 R_1 + \mu_2 R_1^2, \quad (6.29)$$

$$R_1 = \mu_3 \left(\sqrt{G^{\text{exp}}} - 1 \right), \quad (6.30)$$

$$R_2 = \mu_4 \left(\sqrt{G^{\text{exp}}} - 1 \right) + \mu_5 \left(\sqrt{G^{\text{exp}}} - 1 \right)^2, \quad (6.31)$$

with the parameters μ_i determined from fits to the experiments. By comparing Eqs. (6.26)-(6.28) to Eqs. (6.29)-(6.31), the parameters μ_i and λ_i are seen to be related to each other by

$$\lambda_1 = \mu_1 \frac{\sigma_2}{\sigma_1}, \quad (6.32)$$

$$\lambda_2 = \mu_2 \frac{\sigma_2}{\sigma_1^2}, \quad (6.33)$$

$$\lambda_3 = \mu_3 \sigma_1, \quad (6.34)$$

$$\lambda_4 = \mu_4 \sigma_2, \quad (6.35)$$

$$\lambda_5 = \mu_5 \sigma_2. \quad (6.36)$$

Taking the log of these equations leads to a linearized set of equations

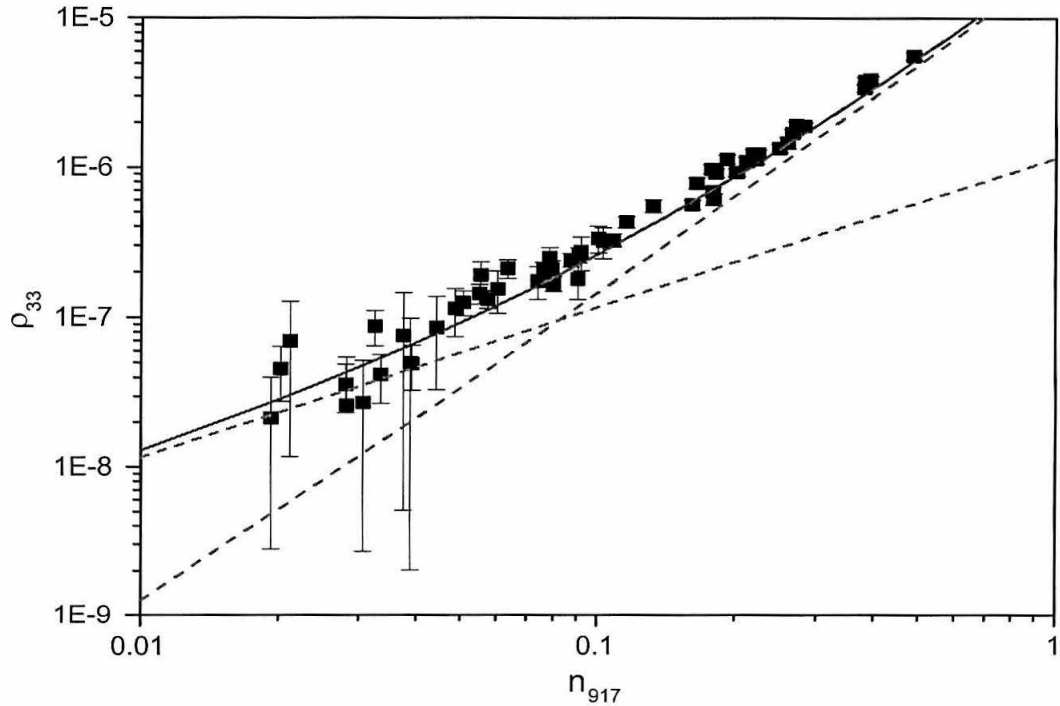


Figure 6.6: Excited state population ρ_{33} due to nonclassical two-photon excitation as a function of OPO output intensity expressed in terms of the intracavity photon number for the idler field, n_{917} . The solid line is the full theory and the dotted lines are the linear and quadratic asymptotes to the theory. The data points are the normalized data from the five experiments.

$$\begin{pmatrix} -1 & 1 \\ -2 & 1 \\ 1 & 0 \\ 0 & 1 \\ 0 & 1 \end{pmatrix} \begin{pmatrix} \ln \sigma_1 \\ \ln \sigma_2 \end{pmatrix} = \begin{pmatrix} \ln \frac{\lambda_1}{\mu_1} \\ \ln \frac{\lambda_2}{\mu_2} \\ \ln \frac{\lambda_4}{\mu_4} \\ \ln \frac{\lambda_4}{\mu_4} \\ \ln \frac{\lambda_5}{\mu_5} \end{pmatrix} \quad (6.37)$$

from which the normalization parameters σ_1 and σ_2 are calculated using the well known least squares procedure for a set of linear equations.

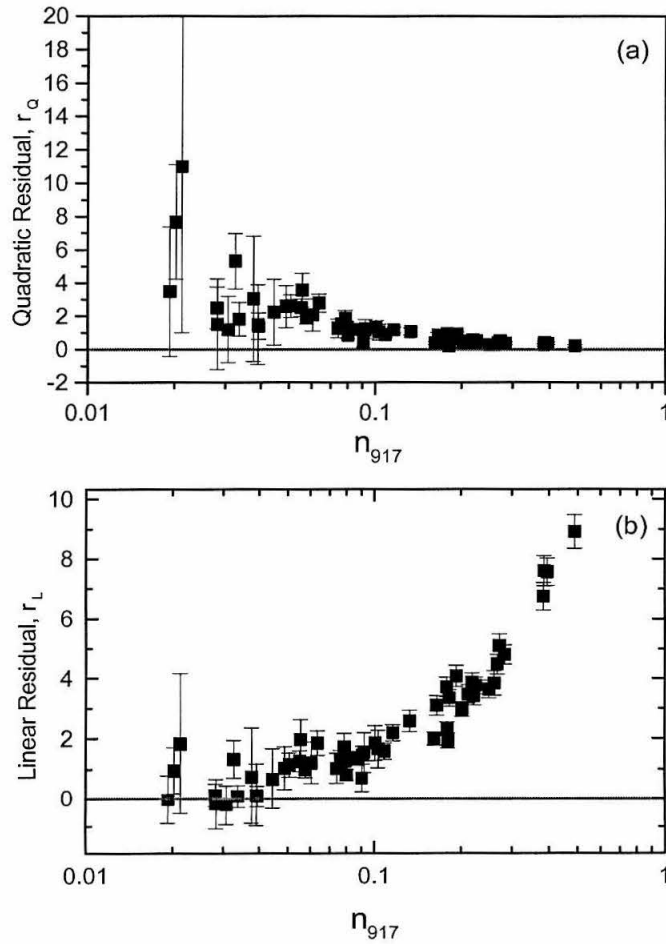


Figure 6.7: Residuals of the normalized data (a) relative to the quadratic and (b) relative to the linear asymptotes to the theory.

The fact that the normalization parameters σ_1 and σ_2 are determined from an overspecified system of linear equations implies that *a priori* there is no guarantee that there are two such parameters that would simultaneously satisfy all five conditions. For example, if Eqs. (6.26)-(6.28) do not describe the data, then there is no reason why just two parameters (σ_1 and σ_2) should scale the data to these functional forms. On the other hand, a consistency of the linear system of these five equations (Eq. (6.37)) would further indicate that the data are described by the suggested theory.

For each experiment the normalization parameters σ_1 and σ_2 are calculated and then the data are scaled accordingly. Figure 6.6 shows the result of this normalization procedure along with the full theory from the integration of the master equation and the linear and quadratic asymptotes to this theory. The data at the low end of the scale extend to a region of slope $\lesssim 1.3$ which is far below the classical value of 2 (quadratic dependence). To further demonstrate the properties of the data with respect to the linear and quadratic asymptotes, Fig. 6.7 shows the residuals with respect to these curves. Here the set of points for the quadratic residual $\{r_Q \pm e_{r_Q}, n_b\}$ is calculated from the set of experimental data points $\{\rho_{33} \pm e_{\rho_{33}}, n_b\}$ and the theoretical prediction for the dependence of ρ_{33} on n_b , which is broken into two parts according to

$$\rho_{33} = \rho_{33}^L + \rho_{33}^Q. \quad (6.38)$$

Here ρ_{33}^L is the linear part and ρ_{33}^Q is the quadratic part of the theory, see Appendix C and are given by

$$\rho_{33}^L = 1.16 \times 10^{-6} n_b, \quad (6.39)$$

and

$$\rho_{33}^Q = 24.31 \times 10^{-6} n_b^2 \left(1 - 0.487 e^{-\frac{n_b}{0.5566}} \right), \quad (6.40)$$

respectively; see Fig. (C.1). Then the quadratic residuals are defined to be

$$r_Q^{(i)} \pm e_{r_Q}^{(i)} \equiv \left[\frac{\rho_{33}^{(i)}}{\rho_{33}^Q(n_b^{(i)})} - 1 \right] \pm \frac{e_{\rho_{33}}^{(i)}}{\rho_{33}^Q(n_b^{(i)})}, \quad (6.41)$$

where the index i signifies the i^{th} point from the experimental data points. Similarly, the linear residual is defined to be

$$r_L^{(i)} \pm e_{r_L}^{(i)} \equiv \left[\frac{\rho_{33}^{(i)}}{\rho_{33}^L(n_b^{(i)})} - 1 \right] \pm \frac{e_{\rho_{33}}^{(i)}}{\rho_{33}^L(n_b^{(i)})}. \quad (6.42)$$

6.5 Summary

In conclusion, the analysis of the two-photon experiment has demonstrated from various aspects that the data obtained from nonclassical excitation experiments exhibit nonclassical behavior. Observations for the excitation rate as a function of intensity indicate rates that scale with intensity with slopes as low as 1.3 in sharp contrast with classical theory from which a quadratic relation is expected. The difference from classical excitation was confirmed by control experiments which exhibit no statistically significant deviation from classical predictions (slope $\sim 2.0 \pm 0.1$). The analysis has concentrated in three main areas: a) identifying the functional form that best describes the data, b) comparing in absolute terms theory with experiment in terms of the so called “knee” point and c) normalizing all data to the theory. In the first part it has been shown that the linear plus quadratic model f_{Q+L} describes the data better than any of the alternative models that were considered, which was quantified by the cumulative statistics \overline{S} and \overline{C} . For the absolute comparison with theory, the gain point at which the contributions from the quadratic and linear components become equal was calculated from the data to be $G_s^{\text{exp}} = 1.41 \pm 0.08$, which is to be compared to the theoretical prediction $G_s^{\text{th}} = 1.33$. Finally for the normalization of the data to the theory, two parameters σ_1 and σ_2 for each experiment were used, which were determined from the values of the fitting parameters and the full theory of the system.

Part III

QUANTUM INTERFERENCE

Chapter 7 Multiple-Field, Two-Photon Excitation and Quantum Interference

The subject of quantum interference (QI) and control of QI has been extensively studied, with applications in a variety of fields ranging from atomic and molecular physics to chemistry. It includes the study of quantum state synthesis in Rydberg atoms[82], control of chemical reaction[83], control of phase-sensitive yields of above-threshold ionization [84] and control of photodissociation processes[85], to mention just a few examples. In addition, of particular interest to basic atomic physics, has been the study of lasing without inversion,[86, 87, 88, 89, 90] and the phenomenon of electromagnetically induced transparency,[91, 92, 93, 94, 95] and the associated enhancement of the index of refraction accompanied by vanishing absorption,[96, 97, 98, 99] all of which are direct effects of QI in atomic systems. Finally, in this admittedly brief (incomplete) survey of literature in the vast field of QI, more relevant to the present work, is the study of inhibition or enhancement of two-photon absorption by Agarwal et al.,[100] and that of the manipulation of excited state populations by Luo et al.[101]

Within the domain of this extensive theoretical and experimental studies, here a recent experiment [102] and the theory developed to study the underlying physics will be presented. This particular experiment demonstrated a new atomic system that exhibits QI with potential applications in frequency metrology and ultra-high frequency mixing. In particular, the excited state population ρ_{33} of a three-level atom excited via two-photon absorption is sensitive to the relative phase of three lasers used for the excitation. An extension of the initial work provided promising experimental results [103] for improvements of several orders of magnitude in the bandwidth of homodyne detection of nonclassical states of the electromagnetic field with the particular demonstration having been carried out for a frequency offset of 25 THz be-

tween squeezed signal and idler fields. The common theme in both the experiments of Refs.[102, 103] is QI, which provides the tool not only to demodulate and observe beatnotes of lasers that differ in frequency by 10-100's of THz, but also to control atomic multiphoton excitation rates by controlling the relative phase of the exciting lasers. Alternatively, by monitoring the two-photon excitation rate, stabilization of the relative phase of individual lasers could be achieved.[102] Independently from the work to be presented here, V. Blanchet et al. have recently also demonstrated QI in a similar experiment.[104]

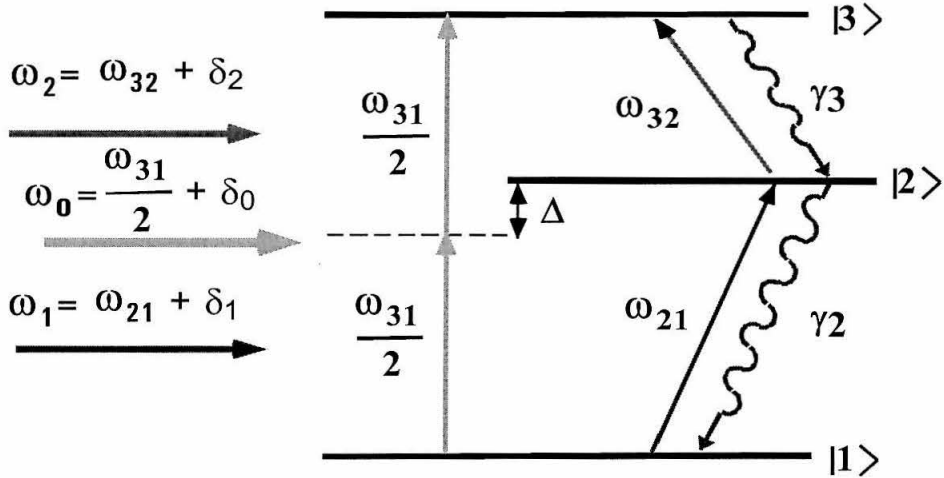


Figure 7.1: The two-photon transition $|1\rangle \rightarrow |3\rangle$ is excited by three fields via two alternative excitation pathways, which lead to QI.

To be more specific, the physical system under consideration consists of a three-level atom, Fig. 7.1, excited by three lasers at frequencies $(\omega_1, \omega_2, \omega_0)$ chosen so that they are close to the atomic eigenfrequencies $(\omega_{21}, \omega_{32}, \frac{1}{2}\omega_{31})$, respectively. Atomic excitation can then proceed in two alternative ways, namely either via the near resonant dipole absorption of two photons from the ω_1 and ω_2 laser beams or via the far detuned quadrupole (i.e., simultaneous two-photon) absorption from the ω_0 beam. The presence of these two alternative excitation pathways gives rise to QI with the “*control knob*” being the relative optical phase of the three lasers.

After this brief introduction, in the remainder of this chapter, theoretical and experimental developments of the last two years related to QI in the atomic system of Fig. 7.1 will be described. First in Section 7.1 the physical system that will be analyzed is presented. Then, in Section 7.2, a perturbative model valid for weak field excitation will be discussed [105] followed by a “full” theoretical analysis based on the master equation for the system in Section 7.3.[106] To complement this theoretical discussion, a “Quantum Interference Calculator” (QuInC) has been developed and will be briefly outlined in Section 7.4.[50] Section 7.5 deals with a proof-of-principle experiment.[102] In Section 7.6 a generalization to multiphoton processes will be suggested and in Section 7.7 the idea of internal correlations in the atomic population will be put forward. Finally, the chapter concludes with a brief summary.

7.1 The 3-level Atom and Excitation Scheme

The basic structure of the system to be analyzed is shown in Fig. 7.1. A three-level atom with eigenstates $|1\rangle$, $|2\rangle$, $|3\rangle$ in a ladder configuration is taken to have eigenfrequencies $(\omega_{21}, \omega_{32}, \frac{1}{2}\omega_{31})$ defined by $\omega_{ij} = \frac{E_i - E_j}{\hbar}$. The atom is further characterized by the generalized decay rates $\{\gamma_1, \gamma_2, \gamma_3, \gamma_{12}, \gamma_{23}, \gamma_{13}\}$ where γ_{ii} are the population and γ_{ij} $i \neq j$ the coherence decay rates.

The total excitation in the system consists of three parts corresponding to three laser fields of distinct frequencies illuminating the atom, namely $(\omega_1, \omega_2, \omega_0)$, and is given by

$$\mathcal{E} = \mathcal{E}_0 + \mathcal{E}_1 + \mathcal{E}_2 \quad (7.1)$$

where

$$\mathcal{E}_i = \epsilon_i e^{-i\Phi_i} \text{ for } i = 0, 1, 2, \quad (7.2)$$

with $\Phi_i \equiv \omega_i t + \phi_i$. Here ϵ_i is the amplitude and ϕ_i the spatial phase of the field at the site of the atom. The frequencies of the three lasers are chosen to be “close” to

the eigenfrequencies of the atom with corresponding detunings $(\delta_1, \delta_2, \delta_0)$ defined by

$$\begin{aligned}\omega_1 &= \omega_{21} + \delta_1, \\ \omega_2 &= \omega_{32} + \delta_2, \\ \omega_0 &= \frac{\omega_{31}}{2} + \delta_0.\end{aligned}\tag{7.3}$$

Throughout the analysis it is assumed that $\delta_i \ll \omega$ for $i = 0, 1, 2$ and ω being any of the transition or excitation frequencies in the problem, thus allowing the elimination of certain rapidly oscillating terms of the form $e^{-i(\omega_i - \delta_j)t}$. When this assumption is relaxed, interesting effects associated with low frequency fields at $\omega_i - \delta_j$ appear and will be the subject of future study.

In addition to the δ_i 's the quantity Δ is defined to be

$$\Delta \equiv \left| \frac{\omega_{31}}{2} - \omega_{32} \right| = \left| \frac{\omega_{31}}{2} - \omega_{21} \right|\tag{7.4}$$

and represents the non-degeneracy frequency distance of the intermediate excited state from the frequency of the two-photon eigenfrequency of the atom (see Fig. 7.1). Throughout the following treatments it is also assumed that $\Delta \gg \delta_i$ for $i = 0, 1, 2$.

To prelude the analysis, it is pointed out that the QI in the system relies on a particular relative phase of the three lasers used for the excitation and arises from imbalance between the dipole allowed ($|1\rangle \rightarrow |2\rangle \rightarrow |3\rangle$) and quadrupole ($|1\rangle \rightarrow |3\rangle$) excitation pathways. More explicitly, two amplitudes contribute to ρ_{33} , with the first ($a_{1 \rightarrow 2 \rightarrow 3}$) arising from the two polarizations of the $|1\rangle \rightarrow |2\rangle$ and $|2\rangle \rightarrow |3\rangle$ transitions (oscillating as $e^{-i(\omega_1 + \omega_2)t}$) and the second ($a_{1 \rightarrow 3}$) from the direct $|1\rangle \rightarrow |3\rangle$ excitation (oscillating as $e^{-i2\omega_0 t}$). Hence, the overall excitation population is given by $\rho_{33} \sim |a_{1 \rightarrow 2 \rightarrow 3} + a_{1 \rightarrow 3}|^2$, which has an oscillating cross term proportional to $[e^{-i(2\omega_0 - \omega_1 - \omega_2)t} + cc]$. Therefore, the excited state population ρ_{33} has an oscillating component which has the phase $\Phi \equiv \Phi_1 + \Phi_2 - 2\Phi_0$ as its argument, so that external variation of any of the Φ_i can be viewed as a “control knob” of QI in the system. The phase Φ can also be written as $\Phi = \Delta\omega \cdot t + \Delta\phi$ with $\Delta\omega \equiv \omega_1 + \omega_2 - 2\omega_0$ and

$\Delta\phi \equiv \phi_1 + \phi_2 - 2\phi_0$. Hence the atom acts as a nonlinear mixer that demodulates the frequencies $(\omega_1, \omega_2, \omega_0)$ with ω_0 being the analog of the local oscillator (LO) in the usual non-linear mixer theory and the distance $\delta\omega \equiv |\omega_1 - \omega_0| \simeq |\omega_2 - \omega_0|$ being the LO to “sideband” separation at which the nonlinear mixer operates. By realizing that in atomic systems this separation $\delta f = \frac{\delta\omega}{2\pi}$ ranges up to 100’s of THz, it is recognized that this scheme offers new opportunities in the field of nonlinear mixing and demodulation of optical fields.[102]

7.2 Perturbative Analysis

7.2.1 Equation of Motion

The starting point for the formal analysis is the general Schrodinger equation for the density operator,[107, 108] which in this case simplifies to

$$\begin{aligned} \dot{\rho}_{ij} &= -(\gamma_{ij} + i\omega_{ij})\rho_{ij} - \frac{i}{\hbar}[V, \rho]_{ij} \\ &= -(\gamma_{ij} + i\omega_{ij})\rho_{ij} - \frac{i}{\hbar} \sum_{k=1}^3 (V_{ik}\rho_{kj} - \rho_{ik}V_{kj}) , \end{aligned} \quad (7.5)$$

where ρ is the reduced density matrix ($\rho_{ij} = |i\rangle\langle j|$) representing the atom. The first term in the above equation describes the free Hamiltonian evolution of the atom, while the second term describes the atom-field interaction via the interaction potential V that couples the various atomic levels with the radiation field. Note that in the present work, all fields are taken to be in coherent states. In the usual perturbation approach it is assumed that only dipole interactions are allowed and hence only V_{12} and V_{23} are non-zero while $V_{13} = 0$ and $V_{ii} = 0$ for $i = 1, 2, 3$. The real matrix elements $V_{ij} = V_{ji}$ have the form:

$$V_{21} = \frac{\mu_1}{2} [(\mathcal{E}_0 + \mathcal{E}_1) e^{-i\vartheta_1} + c.c.] ,$$

$$V_{32} = \frac{\mu_2}{2} [(\mathcal{E}_0 + \mathcal{E}_2) e^{-i\vartheta_2} + c.c.] , \quad (7.6)$$

where ϑ_1 and ϑ_2 are phases that arise from the fact that the atomic dipole moments $\mu_{12} = \mu_1 e^{-i\vartheta_1}$ and $\mu_{23} = \mu_2 e^{-i\vartheta_2}$ are taken to be complex quantities with μ_1 and μ_2 real. The two-photon absorption from the ω_0 beam that leads to the direct excitation of the $|1\rangle \rightarrow |3\rangle$ transition is thus modeled within this formalism as two far detuned (from the intermediate level $|2\rangle$), dipole absorptions as described by the components of V_{21} and V_{32} proportional to \mathcal{E}_0 . The rest of the terms in V_{21} and V_{32} proportional to \mathcal{E}_1 and \mathcal{E}_2 , respectively, correspond to the near resonant dipole absorptions, the combination of which completes the stepwise pathway for excitation via the $|1\rangle \rightarrow |2\rangle \rightarrow |3\rangle$ transition.

The next step is to perform a change of variables that casts the problem into a dimensionless form. Towards this end the dimensionless time parameter τ is introduced,

$$\tau \equiv \gamma t , \quad (7.7)$$

where γ is the geometric mean of the decay constants γ_2 and γ_3 ,

$$\gamma \equiv \sqrt{\gamma_2 \gamma_3} . \quad (7.8)$$

In addition, the dimensionless parameter α is defined to be the square root of the ratio of the linewidths of the second and third excited states of the atom,

$$\alpha \equiv \sqrt{\frac{\gamma_2}{\gamma_3}} . \quad (7.9)$$

Finally all frequencies and detunings are normalized to γ , i.e.,

$$\begin{aligned} \omega &\rightarrow \frac{\omega}{\gamma} \equiv \omega \text{ for all } \omega\text{'s} \\ \delta &\rightarrow \frac{\delta}{\gamma} \equiv \delta \text{ for all } \delta\text{'s and} \end{aligned} \quad (7.10)$$

$$\Delta \rightarrow \frac{\Delta}{\gamma} \equiv \Delta .$$

With this new parametrization, by expanding the master equation given by Eq. (7.5) and keeping only the lowest order terms in the interaction potentials V_{ij} , the following set of equations of motion is derived:

$$\dot{\rho}_{11} \simeq 0 , \quad (7.11)$$

$$\dot{\rho}_{12} \simeq -\left(\frac{\alpha}{2} - i\omega_{21}\right) \rho_{12} + iV'_{12}\rho_{11} , \quad (7.12)$$

$$\dot{\rho}_{22} \simeq -\alpha\rho_{22} - iV'_{21}(\rho_{12} - \rho_{21}) , \quad (7.13)$$

$$\dot{\rho}_{13} \simeq -\left(\frac{1}{2\alpha} - i\omega_{31}\right) \rho_{13} + iV'_{23}\rho_{12} , \quad (7.14)$$

$$\dot{\rho}_{23} \simeq -(\beta - i\omega_{32}) \rho_{23} - i(V'_{21}\rho_{13} - \rho_{22}V'_{23}) , \quad (7.15)$$

$$\dot{\rho}_{33} \simeq -\frac{1}{\alpha}\rho_{33} - iV'_{32}(\rho_{23} - \rho_{32}) , \quad (7.16)$$

where β is defined by

$$\beta \equiv \frac{1}{2} \left(\alpha + \frac{1}{\alpha} \right) , \quad (7.17)$$

and the new interaction potentials V'_{ij} are given by

$$\begin{aligned} V'_{21} &= \frac{\mu_1}{2\hbar\gamma} [(\mathcal{E}_0 + \mathcal{E}_1) e^{-i\vartheta_1} + c.c.] \\ &= \frac{\mu_1}{2\hbar\gamma} [(\epsilon_0 e^{-i(\omega_0\tau + \phi_0 + \vartheta_1)} + \epsilon_1 e^{-i(\omega_1\tau + \phi_1 + \vartheta_1)}) + c.c.] , \end{aligned} \quad (7.18)$$

and

$$\begin{aligned} V'_{32} &= \frac{\mu_2}{2\hbar\gamma} [(\mathcal{E}_0 + \mathcal{E}_2) e^{-\vartheta_2} + c.c.] \\ &= \frac{\mu_2}{2\hbar\gamma} [(\epsilon_0 e^{-i(\omega_0\tau + \phi_0 + \vartheta_2)} + \epsilon_2 e^{-i(\omega_2\tau + \phi_2 + \vartheta_2)}) + c.c.] . \end{aligned} \quad (7.19)$$

7.2.2 Solution for ρ_{33} and QI

Within the context of a perturbative solution, the above system of differential equations (Eqs. (7.11)-(7.16)) is solved by first assuming that the ground state population

ρ_{11} is fixed and then integrating the equations in the order they appear, while substituting the solutions in turn into subsequent equations. It is easy to see that the first equation is of 0th order in the interaction potentials V_{ij} , the second of 1st order, the third and fourth of 2nd order, the fifth of 3rd order and finally the sixth equation is of 4th order in the V_{ij} 's.

The details of integration and the solutions of the equations of motion (Eqs. (7.11)-(7.16)) are documented elsewhere [105]. Here, only the solution to the excited state population ρ_{33} of the third excited level will be given. In particular, the analytic solution for ρ_{33} , cast in a very suggestive way for QI, is found to be

$$\rho_{33}(\tau) = \mathbf{X}^2 - 2 \mathbf{X} \mathbf{Y} \sin(\Theta + \Phi) + \mathbf{Y}^2 \quad (7.20)$$

with \mathbf{X} and \mathbf{Y} defined by

$$\mathbf{X} = \sqrt{\frac{Q_o^2}{(4\delta_0^2 + \frac{1}{4\alpha^2})}} , \quad (7.21)$$

$$\mathbf{Y} = \sqrt{\frac{\Omega_1^2}{(\delta_1^2 + \frac{1}{4}\alpha^2)} \frac{\Omega_2^2}{((\delta_1 + \delta_2)^2 + \frac{1}{4\alpha^2})}} . \quad (7.22)$$

Clearly the quantities \mathbf{X} and \mathbf{Y} in Eq. (7.20) play the role of path amplitudes and indeed from their definitions (Eqs. (7.21) and (7.22)) they are evidently the excitation probability amplitudes for the $|1\rangle \rightarrow |3\rangle$ and $|1\rangle \rightarrow |2\rangle \rightarrow |3\rangle$ excitation pathways, respectively.

The three dimensionless Rabi frequencies involved in the definitions of \mathbf{X} and \mathbf{Y} have been defined to be

$$\Omega_1 \equiv \frac{\mu_1 \epsilon_1}{2\hbar\gamma} , \quad (7.23)$$

$$\Omega_2 \equiv \frac{\mu_2 \epsilon_2}{2\hbar\gamma} \quad (7.24)$$

and

$$Q_o \equiv \frac{\mu_1 \mu_2 \epsilon_0^2}{4\gamma^2 \Delta \hbar^2} . \quad (7.25)$$

Note that Q_o is an effective two-photon Rabi frequency that is proportional to the intensity rather than the amplitude of the field, and to the square rather than the linear expectation value of the position operator for the electron. Also notice that for a three-level atom $\langle r \rangle_{12} \langle r \rangle_{23} = \langle r^2 \rangle_{13}$.

The size of the interference term in Eq. (7.20) (second term) depends on the phase $\Phi + \Theta$, where Φ and Θ are defined according to

$$\tan \Phi = \frac{4\delta_1\delta_0(\delta_1 + \delta_2) + \frac{1}{2}(\delta_1 + \delta_2) + \frac{1}{2\alpha^2}\delta_1 - \delta_0}{2\alpha\delta_0(\delta_1 + \delta_2) + \frac{1}{\alpha}\delta_1(2\delta_0 - \delta_1 - \delta_2) + \frac{1}{4\alpha}} \quad (7.26)$$

and

$$\Theta \equiv (2\omega_0 - \omega_2 - \omega_1)\tau + (2\phi_o - \phi_2 - \phi_1) = (2\delta_0 - \delta_1 - \delta_2)\tau + (2\phi_o - \phi_1 - \phi_2) , \quad (7.27)$$

respectively. Observe that the phase Φ is static and that the only dynamical phase in the problem is Θ which can be a function of time either because the excitation frequencies ω_i do not satisfy a “triangle equality” $2\omega_0 - \omega_2 - \omega_1 = 0$ or because the phases ϕ_i of these fields vary at the site of the atom, $\phi_i(\tau)$ as via Doppler shifts for a moving atom, $2k_0 - k_1 - k_2 \neq 0$ (which of course amounts to a frequency shift). In either case, ρ_{33} as a function of time will vary due to the interference term in Eq. (7.20), with the temporal modulation analogous to a spatial fringe pattern and the depth of modulation analogous to the corresponding visibility.[109] With this terminology, the fringe pattern for the QI arising in Eq. (7.20) is expressible as a single sinusoid with $\Phi + \Theta$ as its argument. The population $\rho_{33}(\tau)$ has a mean value of

$$\rho_{33}^o = \mathbf{X}^2 + \mathbf{Y}^2 \quad (7.28)$$

and a “visibility” (depth of modulation) \mathcal{V} defined by [109]

$$\mathcal{V} \equiv \frac{\rho_{33}^{MAX} - \rho_{33}^{MIN}}{\rho_{33}^{MAX} + \rho_{33}^{MIN}} = \frac{2 \mathbf{X}\mathbf{Y}}{\mathbf{X}^2 + \mathbf{Y}^2} . \quad (7.29)$$

With these definitions at hand, ρ_{33} can be rewritten as

$$\rho_{33}(\tau) \simeq \rho_{33}^o [1 + \mathcal{V} \sin(\Theta + \Phi)] . \quad (7.30)$$

7.3 “Full” Theory

Although the preceding analysis gives simple analytic results that have an intuitive meaning, the solution is limited to weak field excitation and interesting saturation and inversion effects are not within the scope of that calculation. For this reason, further analysis was performed that incorporates the case of strong field excitation by applying a semiclassical formalism based upon the master equation with the usual dipole interaction Hamiltonian to describe one-photon absorption and with an effective interaction Hamiltonian to describe quadrupole (two-photon) absorption. As a result, a set of optical Bloch equations was derived, the solutions of which fully describe QI in the three-level atom excited by three fields of arbitrary strength in the semiclassical regime. It is noted that although this formalism is different from that of the previous section, solutions derived here apply not only to the strong excitation limit, but also encompass the weak excitation of perturbative approach as a special case. However, the generality of the current approach is gained at a loss of some of the simplicity of the solutions of Section 7.2. In particular, while in the perturbation theory, analytical expressions for the excited state population and visibility of the QI have been derived, giving insight into the underlying physical process, in the present work only a matrix solution is given (valid under a “closed-triangle” constraint, see below), which however can easily be numerically inverted to generate explicit results.

7.3.1 Hamiltonian Formalism

The starting point of this analysis is the master equation in the interaction picture, given by [110]

$$\frac{\partial \rho}{\partial t} = -\frac{i}{\hbar} [H_I, \rho] - \frac{1}{2} \sum_{i,j=1}^2 \gamma'_{i+1j+1} (\rho S_i^+ S_j^- + S_i^+ S_j^- \rho - 2S_j^- \rho S_i^+) e^{i(\omega_i - \omega_j)t} , \quad (7.31)$$

where the first term arises from the reversible interaction of the atom with the input fields while the second term describes spontaneous emission. In the above equation the S_i^\pm are transition operators defined by $S_i^+ = |i+1\rangle\langle i|$ and $S_i^- = (S_i^+)^\dagger$ for $i = 1, 2$. The decay rates γ'_{ij} are defined by $\gamma'_{22} \equiv \gamma_2$, $\gamma'_{33} \equiv \gamma_3$ while the diagonal terms $\gamma'_{23} = \gamma'_{32}$ correspond to the transfer rate that couples the $2 \rightarrow 3$ and $2 \rightarrow 1$ coherences.[110] However, γ'_{23} and γ'_{32} will not play any role in the final solutions because they represent rapidly oscillating terms that can be neglected.[110] Recall that this is a consequence of the assumption that the spacings between the atomic energy levels are not equal and, in fact, are very large as compared to the atomic linewidths.

The interaction Hamiltonian H_I is taken to be

$$\begin{aligned}
H_I = & -i\hbar\gamma\Omega_1 [S_1^+ e^{-i(\delta_1 t + \phi_1)} - S_1^- e^{i(\delta_1 t + \phi_1)}] \\
& -i\hbar\gamma\Omega_2 [S_2^+ e^{-i(\delta_2 t + \phi_2)} - S_2^- e^{i(\delta_2 t + \phi_2)}] \\
& -i\hbar\gamma^2 Q_o [|3\rangle\langle 1| e^{-i2(\delta_0 t + \phi_0)} - |1\rangle\langle 3| e^{i2(\delta_0 t + \phi_0)}] \\
& -\hbar\gamma^2 Q_o (\beta_3 |3\rangle\langle 3| - \beta_1 |1\rangle\langle 1|)
\end{aligned} \tag{7.32}$$

where γ is defined in Eq. (7.8) and the Rabi frequencies Ω_1, Ω_2 and Q_o given by Eqs. (7.23), (7.24) and (7.25), respectively.

The first and second terms in Eq. (7.32) are the usual semiclassical terms under the rotating-wave approximation for dipole induced resonance fluorescence driven by coherent fields $\mathcal{E}_1, \mathcal{E}_2$ for the $1 \rightarrow 2$ and $2 \rightarrow 3$ transitions, respectively.[110, 111] The last two terms are “*effective*” interaction Hamiltonian terms,[112, 113, 114, 115, 116, 117] and account for the interaction of the atom with the \mathcal{E}_o field which is responsible for the quadrupole (two-photon) transition that couples the ($|1\rangle, |3\rangle$) states directly via the simultaneous absorption of two photons from the \mathcal{E}_o field. In particular, the third term describes the two-photon absorption for the $|1\rangle \rightarrow |3\rangle$ excitation and is of identical qualitative form to that of dipole transitions with the exception that the effective driving Rabi frequency is of higher order, ($Q \propto \mu_1 \mu_2 \epsilon^2$, [113]). The fourth term in Eq. (7.32) is due to dynamical Stark shifts induced by \mathcal{E}_o and is a necessary

addition to the “*effective*” Hamiltonian that describes the interaction of the atoms with \mathcal{E}_o in order to properly account for the case of strong driving \mathcal{E}_o fields.[113, 117] The parameters β_1 and β_3 quantify the strength of the intensity-dependent Stark shifts of the $|1\rangle$ and $|3\rangle$ levels, respectively, due to the virtual transition to the intermediate ($|2\rangle$) level.[117] These parameters, β_1 and β_3 , can be shown from Ref.[113], Eq. (63) to be related to each other and in particular to satisfy the following equation

$$\beta_1 = \frac{1}{\beta_3} = \frac{|\mu_2|}{|\mu_1|} \simeq \sqrt{\frac{\gamma_3}{\gamma_2}}, \quad (7.33)$$

where the last equality follows from Eq. (21) in Ref. [44].

Finally, note that while the inclusion of the fourth term is necessary to account correctly for effects associated with strong \mathcal{E}_o fields, the corresponding strong field effects associated with the \mathcal{E}_1 and \mathcal{E}_2 fields are built into the model since the full microscopic Hamiltonian is used to describe the interaction of the atom with \mathcal{E}_1 and \mathcal{E}_2 . In particular, by setting $\mathcal{E}_o = 0$ this theory reduces to the case studied in Ref. [110] (which likewise accounts for strong \mathcal{E}_1 and \mathcal{E}_2 fields with $\mathcal{E}_o = 0$). In fact, it has been verified that the two theories (that of Ref. [110] and the present) predict identical results.

7.3.2 Equation of Motion

Similarly with perturbation theory the master equation in this case, Eq. (7.31), is cast in a dimensionless form by changing time variables according to Eq. (7.7). After some algebra the following equation of motion for the atomic populations ρ_{22} and ρ_{33} are derived:

$$\dot{\rho}_{22} = -\alpha\rho_{22} + \frac{1}{\alpha}\rho_{33} - \Omega_1 (\rho_{12}e^{-i\theta_1} + \rho_{21}e^{i\theta_1}) + \Omega_2 (\rho_{23}e^{-i\theta_2} + \rho_{32}e^{i\theta_2}), \quad (7.34)$$

$$\dot{\rho}_{33} = -\frac{1}{\alpha}\rho_{33} - \Omega_2 (\rho_{23}e^{-i\theta_2} + \rho_{32}e^{i\theta_2}) - Q_o (\rho_{13}e^{-i2\theta_o} + \rho_{31}e^{i2\theta_o}), \quad (7.35)$$

while the atomic coherences ρ_{12} , ρ_{23} and ρ_{13} are shown to satisfy

$$\dot{\rho}_{12} = - \left(\frac{\alpha}{2} + i \frac{1}{\alpha} Q_o \right) \rho_{12} + \Omega_2 \rho_{13} e^{-i\theta_2} + Q_o \rho_{32} e^{i2\theta_o} + \Omega_1 (2\rho_{22} + \rho_{33} - 1) e^{i\theta_1} , \quad (7.36)$$

$$\dot{\rho}_{23} = - \left[\frac{1}{2} \left(\alpha + \frac{1}{\alpha} \right) + i \alpha Q_o \right] \rho_{23} - \Omega_1 \rho_{13} e^{-i\theta_1} - Q_o \rho_{21} e^{i2\theta_o} - \Omega_2 (\rho_{22} - \rho_{33}) e^{i\theta_2} , \quad (7.37)$$

$$\dot{\rho}_{13} = - \left[\frac{1}{2\alpha} + i \left(\alpha + \frac{1}{\alpha} \right) Q_o \right] \rho_{13} + \Omega_1 \rho_{23} e^{i\theta_1} - \Omega_2 \rho_{12} e^{i\theta_2} + Q_o (\rho_{22} + 2\rho_{33} - 1) e^{i2\theta_o} . \quad (7.38)$$

The differential equations for the rest of the components of the density matrix follow trivially from the trace condition $Tr(\rho) = 1$ which gives ρ_{11} and from the relation $\rho_{ij} = \rho_{ji}^*$ which gives ρ_{21} , ρ_{32} and ρ_{31} . Note that due to the trace condition the density matrix has only eight independent components. Furthermore, it is noted that the definitions used here for all parameters (namely γ , α , δ_1 , δ_2 , δ_0 , Ω_1 , Ω_2 and Q_o) are identical to those used in the perturbation theory which greatly simplifies the quantitative comparison of the results of the two theories.

Before proceeding further, it is worth pointing out the physical significance of various terms in Eqs. (7.34)-(7.38) to gain insight into the underlying dynamics of the system. First by examining Eq. (7.34) it is obvious that the population ρ_{22} is increased due to the decay from level $|3\rangle$ and decreased due to decay to the ground state $|1\rangle$, where in the dimensionless representation used here, the corresponding rates of these two processes are given by α and $\frac{1}{\alpha}$, respectively. In addition the presence of the Ω_1 and Ω_2 fields couples the ρ_{12} and ρ_{23} coherences to the population of the second excited level, while the Q_o field which drives the $|1\rangle \rightarrow |3\rangle$ transition has no direct influence on the population of the $|2\rangle$ level. Next, from Eq. (7.35) it is clear that the population ρ_{33} is depleted due to decay to the intermediate level $|2\rangle$, while the presence of the Ω_2 and Q_o fields couple it directly to the ρ_{23} and ρ_{13} coherences, respectively. Similar comments apply to the differential equations for the coherences ρ_{12} , ρ_{23} , and ρ_{13} , Eqs. (7.36)-(7.38). Finally, it is observed that the intensity dependent Stark shifts, due to the \mathcal{E}_o field (terms proportional to iQ_o), enter the above system of coupled differential equations only through the equations of motion of the atomic

coherences.

7.3.3 Solution

To solve the system of coupled differential equations (7.34)-(7.38), the problem is formulated in a matrix form where, with appropriate changes of variables, all components of the matrix become real quantities. Although the algebra is somewhat involved, it is nonetheless straightforward and here only the results will be given. First, a set of new quantities is defined according to

$$W_i \equiv \rho_{ii} , \quad (7.39)$$

for $i = 2, 3$ for the populations. For the coherences ρ_{12} and ρ_{21} introduce

$$X_1 \equiv \rho_{12}e^{-i\theta_1} + \rho_{21}e^{i\theta_1} , \quad (7.40)$$

$$X_2 \equiv \frac{\rho_{12}e^{-i\theta_1} - \rho_{21}e^{i\theta_1}}{i} , \quad (7.41)$$

and similarly, for ρ_{23} and ρ_{32} define

$$Y_1 \equiv \rho_{23}e^{-i\theta_2} + \rho_{32}e^{i\theta_2} , \quad (7.42)$$

$$Y_2 \equiv \frac{\rho_{23}e^{-i\theta_2} - \rho_{32}e^{i\theta_2}}{i} , \quad (7.43)$$

and for ρ_{13} and ρ_{31} define

$$Z_1 \equiv \rho_{13}e^{-i2\theta_0} + \rho_{31}e^{i2\theta_0} , \quad (7.44)$$

$$Z_2 \equiv \frac{\rho_{13}e^{-i2\theta_0} - \rho_{31}e^{i2\theta_0}}{i} . \quad (7.45)$$

These transformations lead to equations and solutions for $\{W_2, W_3, X_1, X_2, Y_1, Y_2, Z_1, Z_2\}$ from which the atomic populations are immediately identified, while for the

coherences the simple inverse transformations

$$\rho_{12} = \rho_{21}^* = \frac{X_1 + iX_2}{2} e^{i\theta_1} , \quad (7.46)$$

$$\rho_{23} = \rho_{32}^* = \frac{Y_1 + iY_2}{2} e^{i\theta_2} , \quad (7.47)$$

$$\rho_{13} = \rho_{31}^* = \frac{Z_1 + iZ_2}{2} e^{i2\theta_o} , \quad (7.48)$$

must be applied.

Finally, the system of coupled differential equations of the density matrix components, Eqs. (7.34)-(7.38), transforms to

$$\frac{d\overrightarrow{\Psi}^T}{d\tau} = \mathbf{M}(\tau) \cdot \overrightarrow{\Psi}^T + \overrightarrow{\mathbf{m}}^T , \quad (7.49)$$

where

$$\overrightarrow{\Psi} \equiv (W_2, W_3, X_1, X_2, Y_1, Y_2, Z_1, Z_2) , \quad (7.50)$$

and where $\overrightarrow{\mathbf{m}}$ is the “initial condition” of the problem defined by

$$\overrightarrow{\mathbf{m}} = (0, 0, -2\Omega_1, 0, 0, 0, -2Q_o, 0) . \quad (7.51)$$

The real matrix $\mathbf{M}(\tau)$ is defined by

$$\mathbf{M}(\tau) = \begin{pmatrix} -\alpha & \frac{1}{\alpha} & -\Omega_1 & 0 & \Omega_2 & 0 & 0 & 0 \\ 0 & -\frac{1}{\alpha} & 0 & 0 & -\Omega_2 & 0 & -Q_o & 0 \\ 4\Omega_1 & 2\Omega_1 & -\frac{\alpha}{2} & \Delta_1 & Q_o c & Q_o s & \Omega_2 c & -\Omega_2 s \\ 0 & 0 & -\Delta_1 & -\frac{\alpha}{2} & Q_o s & -Q_o c & \Omega_2 s & \Omega_2 c \\ -2\Omega_2 & 2\Omega_2 & -Q_o c & -Q_o s & -\beta & \Delta_2 & -\Omega_1 c & \Omega_1 s \\ 0 & 0 & -Q_o s & Q_o c & -\Delta_2 & -\beta & -\Omega_1 s & -\Omega_1 c \\ 2Q_o & 4Q_o & -\Omega_2 c & -\Omega_2 s & \Omega_1 c & \Omega_1 s & -\frac{1}{2\alpha} & \Delta_o \\ 0 & 0 & \Omega_2 s & -\Omega_2 c & -\Omega_1 s & \Omega_1 c & -\Delta_o & -\frac{1}{2\alpha} \end{pmatrix} , \quad (7.52)$$

where $\beta = \frac{1}{2}(\alpha + \frac{1}{\alpha})$ and $c \equiv \cos \Theta$ and $s \equiv \sin \Theta$ with the angle Θ given by

$$\Theta \equiv 2\theta_o - \theta_1 - \theta_2 = (2\delta_o - \delta_1 - \delta_2)\tau + (2\phi_o - \phi_1 - \phi_2) . \quad (7.53)$$

The detunings Δ_i , $i = 0, 1, 2$ include both the intensity dependent Stark shifts induced by the \mathcal{E}_o field and the frequency offsets of the excitation lasers from the unshifted atomic energy levels and are given by

$$\begin{aligned} \Delta_1 &= \delta_1 + \frac{1}{\alpha}Q_o \\ \Delta_2 &= \delta_2 + \alpha Q_o \\ \Delta_o &= 2\delta_o + \left(\alpha + \frac{1}{\alpha}\right)Q_o \end{aligned} \quad (7.54)$$

Note that as was the case with perturbation, there is only one dynamical phase (Θ) in the problem, which is a particular relative phase between the three exciting fields. A minor detail is that although Eq. (7.53) is identical to Eq. (7.27), there is a hidden $\pi/2$ difference between these two phases that traces back to the original Hamiltonians, namely Eq. (7.5) and Eq. (7.31), and in particular to the fact that H_I in Eq. (7.5) is taken to be proportional to V_{ij} compared to iV_{ij} of Eq. (7.31). Therefore, direct comparisons of the Θ -dependent results from the two theories over the region of common validity will be shifted by $\pi/2$, which is simply a notational difference.

Note that the matrix $M(\tau)$ is, in general, time dependent via the quantity Θ , which is either explicitly time dependent for $2\delta_o - \delta_1 + \delta_2 \neq 0$ or if the union of ϕ_i is a function of time (e.g., as for a moving atom). However, in the special case that the “closed triangle” condition $2\delta_o - \delta_1 - \delta_2 = 0$ holds, and $\phi_i \neq \phi_i(\tau)$, the matrix M becomes time independent and the steady-state solution $\frac{d\overrightarrow{\Psi}^T}{d\tau} = 0$ is formally given by

$$\overrightarrow{\Psi}_{ss}^T = -\mathbf{M}^{-1} \cdot \mathbf{m}^T . \quad (7.55)$$

In the subsequent discussion, we analyze only this special case for which a simple numerical matrix inversion is required and mainly concentrate on the solutions as a

function of the angle Θ . More complex numerical integration of Eq. (7.49) will yield solutions in more general cases where the “closed triangle” condition is not necessarily satisfied.

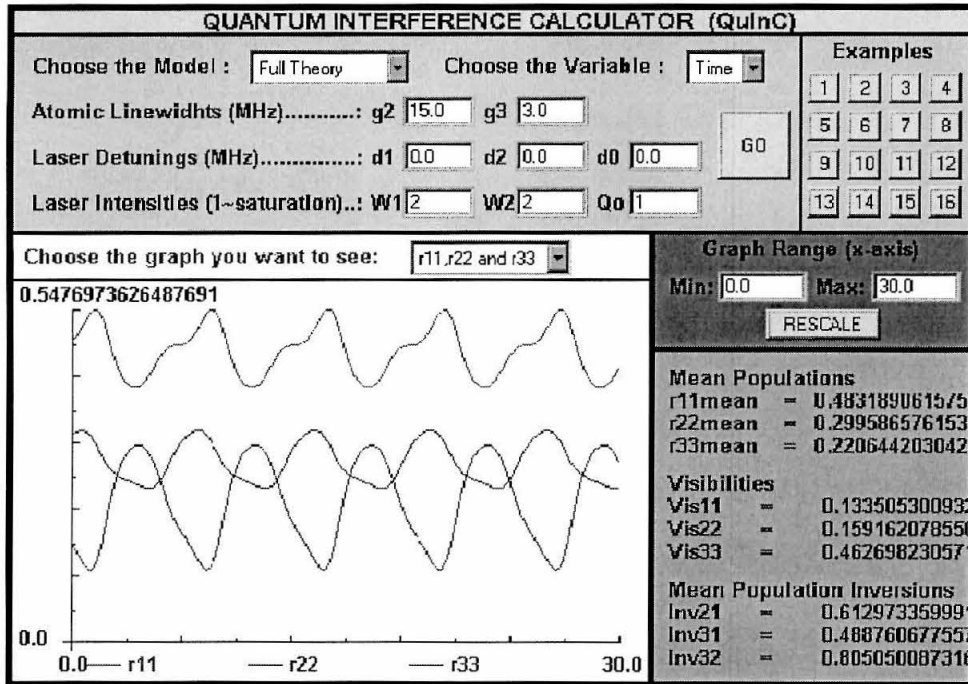


Figure 7.2: Quantum Interference Calculator (QuInC) is available on the WWW at <http://www.cco.caltech.edu/~qoptics/QIHome/QuInC/QuInC.html>

7.4 QuInC

The theory presented in the previous two sections reveals a very rich phenomenology in the two-photon excitation process of a three-level atom in schemes such as the one shown in Fig. 7.1. The effects of QI are profound in the modulated atomic populations, in phase-sensitive atomic inversions, in “unusual” (asymmetric and with multiple peaks) excitation spectra and in the visibility of the QI fringe patterns. These effects have all been discussed in detail elsewhere [105, 106] and for that reason here no specific examples will be given. The multidimensionality of the solution space

which is spanned by the atomic properties summarized in $\alpha = \sqrt{\frac{\gamma_2}{\gamma_3}}$, the strength of the excitation lasers characterized by Ω_1 , Ω_2 and Q_o , the detunings δ_1 , δ_2 and δ_0 and the relative phase of the excitation amplitudes Θ , suggests that there are many more unexplored regimes beyond those discussed in Refs. [105, 106]. For this reason, in order to allow the reader to investigate further the possibilities of the QI scheme outlined here, a Quantum Interference Calculator (QuInC) has been developed; see Fig. 7.2. The calculator implements Eq. (7.20) and (7.55) for a set of user defined parameters and calculates excited state populations and fringe visibilities. The program is written in Java and is made publicly available on the WWW.[50]

7.5 Experiment

To demonstrate that QI is indeed observable in two-photon excitation by three lasers, a proof-of-principle experiment was conducted.[102] The atomic system used in this experiment was again the $6S_{1/2}F = 4 \rightarrow 6P_{3/2}F' = 5 \rightarrow 6D_{5/2}F'' = 6$ transition in *Cs*; see Fig. 1.2. The experimental setup is shown in Fig. 7.3 and it is very similar to that of the previous experiments (see Section 3.2, Fig. 3.3, and Section 5.2, Fig. 5.4) with some minor modifications indicated in Block VI. In particular, in order to generate the three coherent excitation beams, a small portion of one of the trapping beams (which was shifted to be resonant with the $6S_{1/2}F = 4 \rightarrow 6P_{3/2}F' = 5$ transition) is injected into the OPO which amplifies it and generates a conjugate (idler) beam. The idler is also in a coherent state and its frequency is resonant with the $6P_{3/2}F' = 5 \rightarrow 6D_{5/2}F'' = 6$ transition as described in Section 4.3. Note that as before the Ti:Sapphire laser is kept in resonance with the two-photon $6S_{1/2}F = 4 \rightarrow 6D_{5/2}F'' = 6$ transition frequency at 884 *nm*. Before reaching the MOT the coherent signal and idler outputs of the OPO are mixed with a portion of the master laser and so the atoms are illuminated by three beams with corresponding wavelengths $\lambda_1 = 852$ *nm*, $\lambda_2 = 917$ *nm* and $\lambda_0 = 884$ *nm* in resonance with the relevant atomic transitions, realizing in this way the excitation scheme of Fig. 7.1.

the setup in Fig.7.3 is accomplished by a PZT at the path of the ω_0 beam which is scanned at a rate that produces a frequency shift $\omega_m \sim 10 \text{ Hz}$ of the ω_0 beam (i.e., $\omega_o \rightarrow \omega_o \pm \omega_m$).

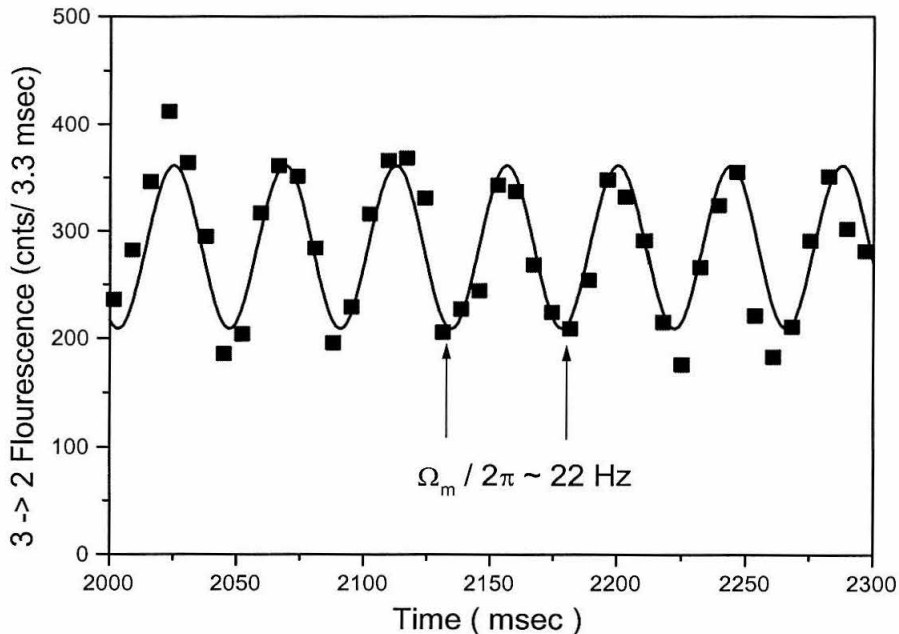


Figure 7.4: Fluorescence from the $6D_{5/2}F'' = 6 \rightarrow 6P_{3/2}F' = 5$ transition as a function of time for excitation of the atoms in the MOT by a combination of three coherent beams with corresponding wavelengths 852 nm , 917 nm and 884 nm . The phase of the 884 nm beam is modulated with a PZT at a frequency $\frac{\omega_m}{2\pi} \simeq 11 \text{ Hz}$.

Figure 7.4 shows a segment of a characteristic time sequence of data points acquired in the experiment. Plotted along the y - axis is the fluorescence from the $6D_{5/2}F'' = 6 \rightarrow 6P_{3/2}F' = 5$ decay and the x - axis is time. Since the fluorescence is proportional to the excited state population ρ_{33} , the data may also be interpreted as a measure of ρ_{33} as a function of time. The solid line is a sinusoidal fit to the data with variable amplitude, phase, offset and frequency. The observed modulation is a clear indication of QI and exhibits some of the characteristic aspects of the theory presented earlier. In particular, note that the modulation frequency is equal to $\frac{\Omega_m}{2\pi} \simeq 22 \text{ Hz}$, which is twice the modulation frequency of the ω_o beam by the PZT

(which for this run was 11 *Hz*) as expected from the definition of Θ , Eq. (7.27) and (7.53). The other important feature demonstrated by this experiment is that the visibility (contrast) of the signal is large enough so that from a practical point of view it can be used in applications, some of which will be proposed in the following two chapters. Adopting the language of fringes and visibility from the interference of optical fields,[109] the signal in Fig. 7.4 has visibility defined in Eq. (7.29) which in this case is approximately $\mathcal{V}_{\text{exp}} = 0.30$.

To compare directly the experimental results in Fig. 7.4 with the theory developed earlier in the chapter, the visibility for the conditions of the experiment is calculated based on the perturbation theory, Eq. (7.20) and full theory, Eq. (7.55) models. Note that while in the perturbation theory there is an analytic expression for \mathcal{V} , Eq. (7.29), in the case of the full theory the value for \mathcal{V} must be calculated numerically. The parameters that enter both calculations are $\{\alpha = \sqrt{\frac{\gamma_2}{\gamma_3}}, \Omega_1, \Omega_2, Q_o, \delta_1, \delta_2, \delta_0\}$ and for the experiment $\alpha \simeq \sqrt{\frac{5}{3}} \simeq 1.29$, the Rabi frequencies are estimated from the powers of the excitation beams, measured to be $P_1 \simeq P_2 \simeq 0.5 \text{ nW}$ and $P_0 \simeq 5 \text{ mW}$, and the detunings, which are all experimentally arranged to be close to zero, $\delta_1 \simeq \delta_2 \simeq \delta_0 \simeq 0$. Observe that in perturbation theory only the ratio $\frac{\Omega_1 \Omega_2}{Q_o} = \sqrt{\frac{P_1 P_2}{P_0^2}} \Delta \simeq 0.35$ enters the visibility calculation. Based on these parameters the value of \mathcal{V} is calculated to be $\mathcal{V}_{\text{pert}} \simeq 0.84$ which is significantly higher than the measured value of $\mathcal{V}_{\text{exp}} \simeq 0.30$. Realizing, however, that the excitation intensities are close to saturation, ($P_1^{\text{sat}} \simeq P_2^{\text{sat}} \simeq 0.5 \text{ nW}$ and $P_0^{\text{sat}} \simeq 10 \text{ mW}$), it is of no surprise that perturbation fails. Applying the full theory model with parameters $\Omega_1 = \Omega_2 = 1$ and $Q_o = 0.35$ (in analogy with perturbation), the estimated visibility is $\mathcal{V}_{\text{full}} \simeq 0.29 \approx \mathcal{V}_{\text{exp}}$, although admittedly, the correspondence is too good given the uncertainties in the parameters $\{\alpha, \delta_1, \delta_2, \delta_0, \Omega_1, \Omega_2, Q_o\}$ and in the spatial overlap of the excitation fields.

7.6 Multiphoton Excitations

Having discussed the case of quantum interference in two-photon excitation, it is natural then to ask about quantum interference in higher order multiphoton processes. Taking the simplest possible approach, we consider a generic multiphoton system shown in Fig. 7.5, where the n^{th} atomic state is excited from the ground state by using several lasers, and inquire as to the nature of quantum interference. Without

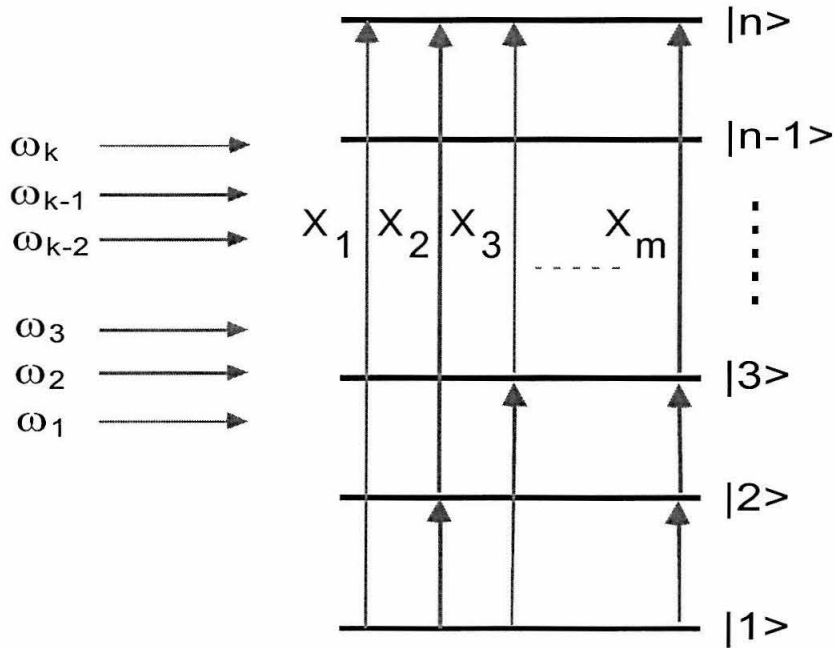


Figure 7.5: Multiphoton excitation with multiple lasers $\{\omega_1, \omega_2, \dots, \omega_k\}$. Several excitation paths $\{\mathbf{X}_1, \mathbf{X}_2, \dots, \mathbf{X}_m\}$ contribute to the overall excited state population ρ_{nn} , resulting in QI.

going into details that are beyond the scope of the present discussion, it is noted that if several lasers are employed for the excitation resulting in m distinct excitation pathways for reaching the n^{th} level, then corresponding amplitudes $\{\mathbf{X}_1, \mathbf{X}_2, \dots, \mathbf{X}_m\}$ will be associated with each of these paths. While in the two-photon case these amplitudes were quadratic in electric field amplitudes, in this more general case the amplitudes will be proportional to a set of powers $\{p_1, p_2, \dots, p_m\}$ of the field, i.e., $\mathbf{X}_i \sim$

ϵ^{pi} , depending on how many “photons” are involved in the i^{th} excitation pathway. A simple generalization of Eq. (7.20), together with the assumption of phase coherence between the excitation amplitudes, allows to write the excited state population as

$$\rho_{nn} = \sum_{i=1}^m \mathbf{X}_i^2 + \sum_{i=1}^{m-1} \sum_{j=i+1}^m \mathbf{X}_i \mathbf{X}_j \sin \Theta_{ij} \quad (7.56)$$

where Θ_{ij} are generalized relative phases corresponding to the phase Θ in the two-photon excitation. The complexity of the above expression and most importantly the nonlinearity of Eq. (7.56) in the field amplitudes suggests the possibility of a very complex behavior in the system. The full implications of such extensions have not been worked out yet, but they do promise a variety of interesting effects for future investigation.

7.7 Internal State Correlations

Lastly, the fact that for sufficiently strong excitation all three atomic levels can have large phase-sensitive populations is examined. Figure 7.6 shows a particular example of such large modulation calculated applying the full theory model. Evidently, all three populations ρ_{11} , ρ_{22} and ρ_{33} , have comparable sizes and modulations in contrast with the perturbative regime where $\rho_{33} \ll \rho_{22} \ll \rho_{11}$.

On the other hand, the effects of quantum interference are usually manifested as modulation of only the final state of the system that is excited in the presence of multiple excitation pathways as for example in the classic Young’s double slit experiment best described by Feynman.[118] However, in this case, due to the additional trace constrain $Tr(\rho) = 1$, modulation can arise for the ground (initial) and intermediate state populations as well as that of the final state. For strong excitation, the compound nature of the atomic population feeds back the effects of interference of the excitation amplitudes even to the ground state. Hence, the usual meaning of “initial” and “final” states is lost and this “feedback” by virtue of the trace condition makes all states subject to modulation from QI.

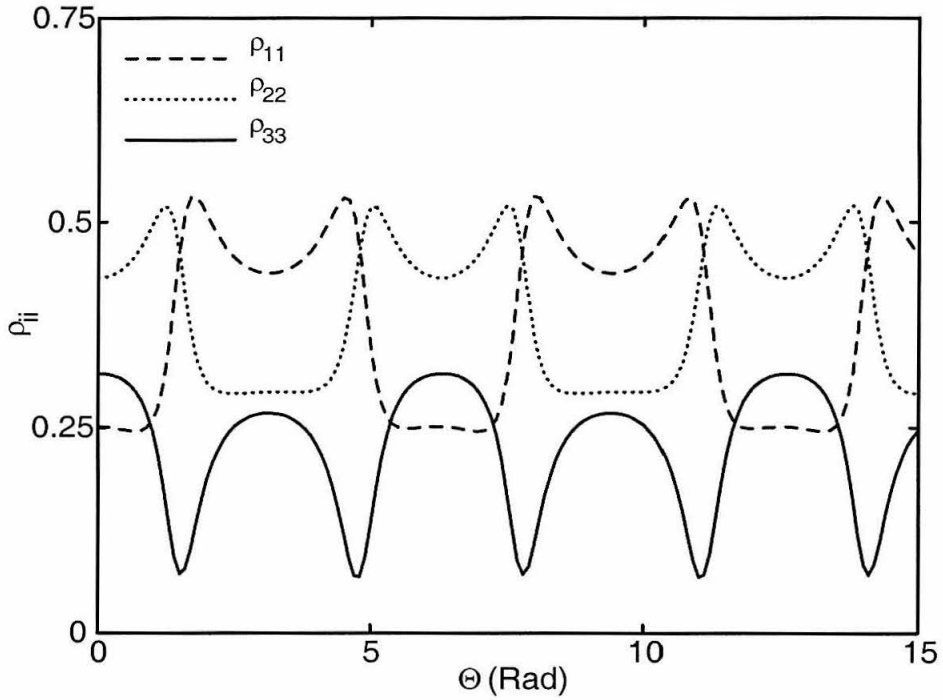


Figure 7.6: Atomic state populations ρ_{11} , ρ_{22} and ρ_{33} as functions of the phase Θ , calculated from the full theory model using $\alpha = \sqrt{\frac{3}{15}}$, $\delta_1 = -\frac{30}{\sqrt{45}}$, $\delta_2 = -\frac{10}{\sqrt{45}}$, $\delta_0 = \frac{\delta_1 + \delta_2}{2}$ and $\Omega_1 = \Omega_2 = Q_o = 2$.

In somewhat more quantitative terms, the system (i.e., the atom) is divided in two parts by considering the combined atomic population of any two of the three levels together and the third by itself, i.e., $\rho_1 \equiv \rho_{ii} + \rho_{jj}$ and $\rho_2 \equiv \rho_{kk}$ for $i, j, k \in \{1, 2, 3\}$ and $i \neq j \neq k$. The trace condition then trivially gives that $\rho_1 = 1 - \rho_2$ and leads to perfect anticorrelation between ρ_1 and ρ_2 , which is more formally described by

$$\zeta \equiv \langle (\rho_1 - \bar{\rho}_1)^2 \rangle = \langle (\rho_2 - \bar{\rho}_2)^2 \rangle = -\langle (\rho_1 - \bar{\rho}_1)(\rho_2 - \bar{\rho}_2) \rangle, \quad (7.57)$$

with the covariance matrix \mathcal{C} of the variables ρ_1 and ρ_2 taking the simple form

$$\mathcal{C}(\rho_1, \rho_2) = \zeta \begin{pmatrix} 1 & -1 \\ -1 & 1 \end{pmatrix}. \quad (7.58)$$

Moreover, one can also show that the full covariance matrix for the populations of the system ρ_{11} , ρ_{22} and ρ_{33} , can be written in terms of only three (instead of six) parameters, ζ_1 , ζ_2 and ζ_3 , in the following form

$$\mathcal{C}(\rho_{11}, \rho_{22}, \rho_{33}) = \begin{pmatrix} \zeta_1 & \zeta_3 & -(\zeta_1 + \zeta_3) \\ \zeta_3 & \zeta_2 & -(\zeta_2 + \zeta_3) \\ -(\zeta_1 + \zeta_3) & -(\zeta_2 + \zeta_3) & \zeta_1 + \zeta_2 + 2\zeta_3 \end{pmatrix}. \quad (7.59)$$

Here $\zeta_1 \equiv \langle (\rho_1 - \bar{\rho}_1)^2 \rangle$, $\zeta_2 \equiv \langle (\rho_2 - \bar{\rho}_2)^2 \rangle$ and $\zeta_3 \equiv \langle (\rho_1 - \bar{\rho}_1)(\rho_2 - \bar{\rho}_2) \rangle$.

7.8 Summary

In conclusion, this chapter outlines the work that has been done on QI in two-photon excitation of a three-level atom ($|1\rangle$, $|2\rangle$, $|3\rangle$) by the combination of three excitation lasers (ω , ω_2 , ω_3) in near resonance with the $|1\rangle \rightarrow |2\rangle$, $|2\rangle \rightarrow |3\rangle$ and $|1\rangle \rightarrow |3\rangle$ transitions, respectively. Quantum interference in the system arises from the presence of multiple excitation pathways. Theoretical models based on a perturbative treatment and the master equation have been developed to study the effects in the weak and strong field excitation regimes. A proof-of-principle experiment was conducted that demonstrated that QI is observable with fairly large visibility $\mathcal{V}_{\text{exp}} \simeq 0.30$, which compares favorably with theory. Extension of this work to multiphoton excitation has been suggested and interesting effects of internal correlations in the atomic populations have been described.

Chapter 8 Ultrafast Homodyne Detection

In view of the developments in quantum interference presented in the previous chapter and the work on nonclassical two-photon excitation presented in Chapters 5 and 6, it is natural to wonder as to what would happen if quantum interference is combined with nonclassical excitation. In the discussion of QI presented in the previous chapter and Refs. [102, 105, 106], two-photon excitation by classical fields has been extensively considered. There the total excitation field \mathcal{E} is taken to be composed of three parts \mathcal{E}_0 , \mathcal{E}_1 and \mathcal{E}_2 (i.e., $\mathcal{E} = \mathcal{E}_0 + \mathcal{E}_1 + \mathcal{E}_2$) and each of them is assumed to be in a coherent state and in near resonance with the quadrupole $|1\rangle \rightarrow |3\rangle$, dipole $|1\rangle \rightarrow |2\rangle$ and dipole $|2\rangle \rightarrow |3\rangle$ transitions of a three-level atom, respectively (see Section 7.1). Here, the goal is to investigate what happens when the coherent \mathcal{E}_1 and \mathcal{E}_2 fields are replaced by the squeezed signal and idler \mathcal{E}_s and \mathcal{E}_i outputs of an NDOPO. This excitation scheme is depicted in Figure 8.1 and will be the subject of the present chapter.

To motivate the subsequent discussion a close analogy can be drawn between the usual balance homodyne detection of squeezing [75, 76] and QI in two-photon excitation as shown in Fig. 8.1.[103] In the case of balanced homodyne detection (Fig. 8.2a), a coherent local oscillator (LO) beam is mixed with the signal and idler beams from an OPO on a 50/50 beamsplitter. The frequency of the LO ω_{LO} is chosen to be at the center of the signal and idler frequencies ω_s and ω_i so that $\omega_{LO} = \frac{\omega_s + \omega_i}{2}$. The light from each of the output ports of the beamsplitter is detected on photodiodes producing photocurrents i_1 and i_2 which are subtracted to produce the difference current $\Delta i = i_1 - i_2$. The Fourier transform of Δi has nonzero frequency content at the beatnote frequency $\Omega_o = \frac{\omega_s - \omega_i}{2}$ due to nonclassical correlations between the signal and idler beams [13] which are detected in this way on a spectrum analyzer.

By contrast, in the case of QI in two-photon excitation, an atom is illuminated by

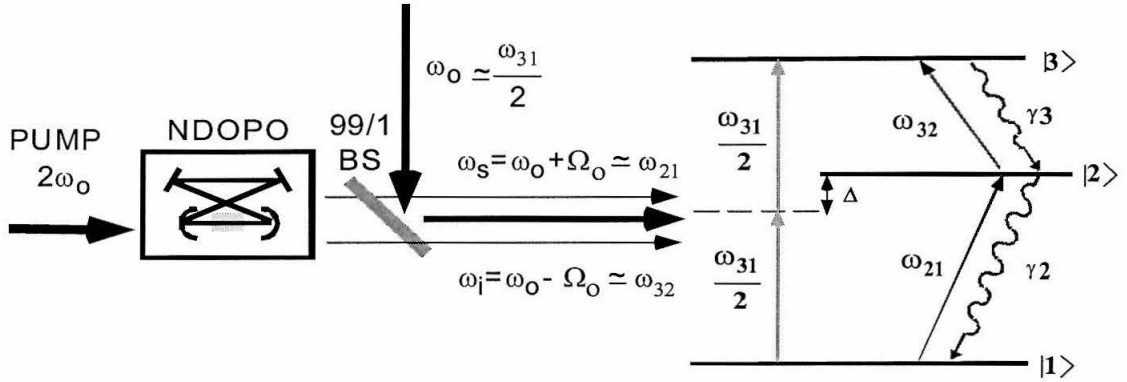


Figure 8.1: Two-photon excitation by a combination of a coherent RO field with frequency ω_o , in resonance with the two-photon $|1\rangle \rightarrow |3\rangle$ transition, and the signal and idler outputs of an NDOPO at frequencies ω_s and ω_i in resonance with the dipole $|1\rangle \rightarrow |2\rangle$ and $|2\rangle \rightarrow |3\rangle$ transitions, respectively.

the combination of the signal and idler output beams from an OPO in conjunction with a coherent reference oscillator (RO) beam (Fig. 8.2b). Here the RO plays the role of the LO in homodyne and its frequency is chosen likewise to be $\omega_{RO} = \frac{\omega_s + \omega_i}{2}$. The atom's response to the three fields results in a modulated signal due to QI as discussed in the previous chapter. Viewed differently, the atom acts as a nonlinear mixer that combines the frequencies of the signal, idler and RO beams to produce a demodulated beatnote signal around $\Omega = 0$ (dc-frequency), (recall that $\rho_{33} \sim |a_{1 \rightarrow 2 \rightarrow 3} + a_{1 \rightarrow 3}|^2 \propto |e^{-i2\omega_o t} + e^{-i(\omega_s + \omega_i)t}|^2$). Hence the size of modulation is proportional to the product of the signal and idler fields, providing in this way a handle on the nonclassical correlations between the two.

Somewhat more formally, the contrast between homodyne detection of squeezed light and QI with squeezed light can be quantified with respect to the corresponding observables, which in the first case is the Fourier transform $\Psi(\Omega)$ of the autocorrelation function of the photocurrent and in the second case a photocounting time series whose Fourier transform is defined to be $\Phi(\Omega)$. Based on an extension of Mollow's

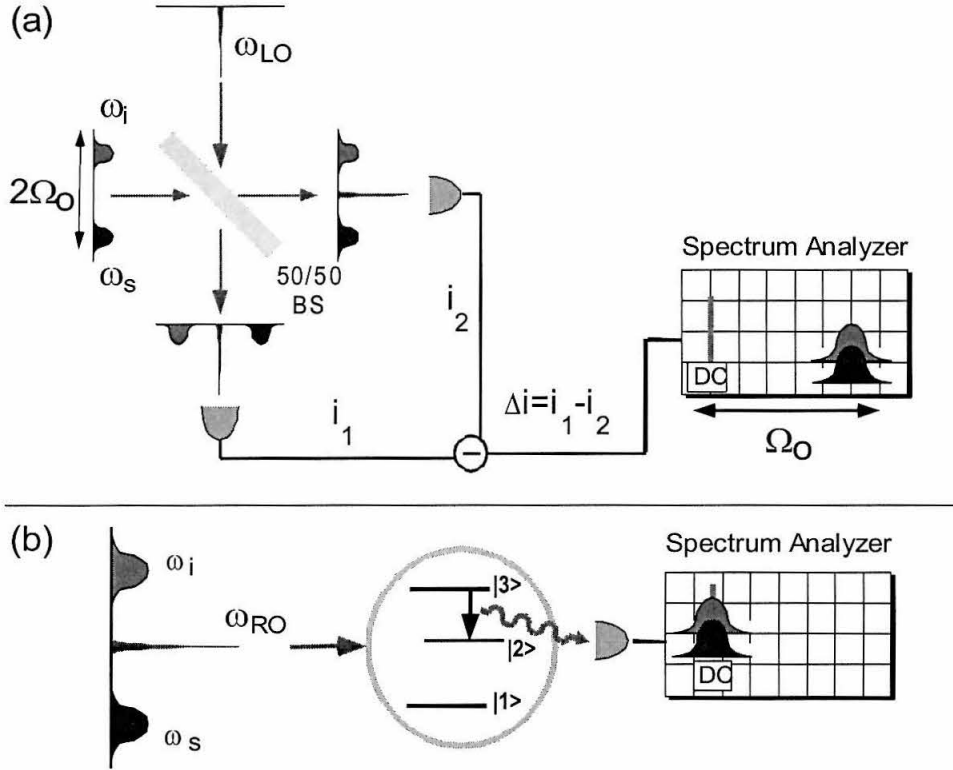


Figure 8.2: a) Homodyne detection of squeezing. b) Detection of nonclassical correlations with QI where an atom is utilized as a nonlinear mixer.

treatment,[77] these two signals have been shown in Ref. [103] to be equal to

$$\Psi(\Omega) = \epsilon_{LO}^4 \left[1 + \frac{2N_{eff}}{\epsilon_{LO}^2} \right] \delta(\Omega) + 2\epsilon_{LO}^2 [N(\Omega) + |M(\Omega)| \cos(2\phi_{LO} + \phi_s)] \quad (8.1)$$

and

$$\Phi(\Omega) = \epsilon_{RO}^4 \left[1 + \frac{2M_{eff}}{\epsilon_{RO}^2} \cos(2\phi_{LO} + \phi_s) \right] \delta(\Omega) + 2\epsilon_{RO}^2 N(\Omega) . \quad (8.2)$$

Here the coherent LO (RO) field is given by $\mathcal{E}_{LO} = \epsilon_{LO} e^{-i(\omega_{LO} + \phi_{LO})t}$ ($\mathcal{E}_{RO} = \epsilon_{RO} e^{-i(\omega_{RO} + \phi_{RO})t}$) where ϵ_{LO} (ϵ_{RO}) is the amplitude and ϕ_{LO} (ϕ_{RO}) the spatial phase of the field at the site of the atom. The parameters $N(\Omega)$ and $M(\Omega) = |M(\Omega)| e^{i\phi_s}$ are defined by Eqs. (5.9) and (5.8) and characterize the quantum field. Their “effective”

values have been defined to be $N_{eff} \equiv \int N(\Omega') d\Omega'$ and $M_{eff} \equiv \int |M(\Omega')| d\Omega'$.

Summarized in Eqs. (8.1) and (8.2) are the characteristics, features and distinctive differences of the two methods. More specifically, it is clear from Eq. (8.1) that in homodyne detection the term that gives information about the nonclassical correlation M peaks at the same frequency that $M(\Omega)$ peaks at, which is $\Omega_o = \frac{\omega_s - \omega_i}{2}$. Realizing that photodetectors are limited in bandwidth to few 10's of GHz , it is clear that this sets an upper limit to the range of detectable nonclassical correlations, which can be quantified by the dimensionless quantity $\Delta f \equiv \frac{\omega_s - \omega_i}{\omega_o}$. In the optical and near IR regions, the range Δf is therefore limited to $\Delta f \lesssim 10^{-5}$. On the other hand, in the case of detection with QI, information about M appears in the term proportional to M_{eff} at dc-frequency and in principle the detectable range Δf is not limited. In fact, for the atomic system considered here for which an experimental realization [103] will be outlined below, $\Delta f \simeq 0.07$. Note that for large values of Δf the form of amplitude quadratures changes and interesting effects (which up to now have been beyond any observational capabilities) have been predicted.[120, 121]

The gain in the detectable range Δf comes, however, at the expense of an unambiguous classification of classical versus quantum states. In particular, in homodyne detection by choosing $\cos(2\phi_o + \phi_s) = -1$ the second term in Eq. (8.1) becomes proportional to $N - |M|$ and hence directly tests the quantum squeezing condition $N^2 < |M|^2 \leq N(N+1)$ which is only valid if $N - |M| < 0$. On the other hand with the method of QI only the condition $|M| \neq 0$ can be directly verified by detecting a non-zero modulation in Eq. (8.2). To overcome this deficiency complementary methods to the QI detection scheme have been proposed.[103]

After this brief introduction, in Section 8.1 the full theory developed to model the system of Fig. 8.1 will be outlined [119]. Section 8.2 presents an experiment that demonstrates that nonclassical correlations between the signal and idler beams from the NDOPO, which are separated in frequency by 25 THz , are indeed observable as a result of QI with the atom acting as a nonlinear mixer.[103]

8.1 Theory

8.1.1 Excitation Field

The basic structure of the atomic system under consideration and notation to be used here has been introduced in Section 7.1. However, the excitation field is replaced for the purposes of the current discussion by $\widehat{\mathcal{E}} = \widehat{\mathcal{E}}_0 + \widehat{\mathcal{E}}_q$, which is composed of two parts. First, the field $\widehat{\mathcal{E}}_0$ is taken to be in a coherent state with eigenvalue given by $\mathcal{E}_0 = \epsilon_0 e^{-i(\omega_0 t + \phi_0)}$, where ϵ_0 is the amplitude and ϕ_0 the spatial phase of the field at the position of the atom. This field \mathcal{E}_0 will be referred to as the reference oscillator (RO). The second part of the field, $\widehat{\mathcal{E}}_q$, is taken to be the output of a subthreshold NDOPO. As usual,[12] the output of the NDOPO consists of two energy carrying sidebands, namely the signal and idler fields with spectral distributions centered at frequencies $\omega_{s,i} = \omega'_0 \pm \Delta'$, which are positioned symmetrically around the frequency ω'_0 . Note that the NDOPO may generate many such pairs of sidebands, but due to atomic resonance conditions described below, only a single pair is relevant for the problem considered here. For the purposes of the present analysis, it is assumed that the frequency ω_0 of the coherent field $\widehat{\mathcal{E}}_0$ is the same as of the central frequency ω'_0 for the signal and idler fields ($\omega_0 = \omega'_0$). Therefore, the electromagnetic field illuminating the atoms consists of three frequency components centered at ω_0 , $\omega_s = \omega_0 + \Delta'$ and $\omega_i = \omega_0 - \Delta'$. The detunings of the components of the driving field from the atomic eigenfrequencies are defined to be δ_0 , δ_i and δ_s and are given by

$$\begin{aligned}\omega_0 &= \frac{\omega_{31}}{2} + \delta_0, \\ \omega_s &= \omega_{21} + \delta_s, \\ \omega_i &= \omega_{32} + \delta_i.\end{aligned}\tag{8.3}$$

Since $\omega_{s,i} = \omega_0 \pm \Delta'$, this implies that

$$\begin{aligned}\delta_s &= \delta_0 + (\Delta' - \Delta), \\ \delta_i &= \delta_0 - (\Delta' - \Delta).\end{aligned}\tag{8.4}$$

In the subsequent analysis, it is assumed that $\omega_0 \approx \frac{\omega_{13}}{2}$, i.e., δ_0 is small, and that $\Delta \approx \Delta'$, with the residual detunings δ_s and δ_i of order the atomic linewidths (γ_2, γ_3). The quantum field $\widehat{\mathcal{E}}_q$ is also assumed to be a broadband field with respect to the atomic linewidths (γ_2, γ_3), so that δ_s and δ_i do not enter the description of the dynamics of the system. This assumption eliminates the complexity of finite-bandwidth squeezed excitation.[81] However, the coherent part of the total excitation field $\widehat{\mathcal{E}}_0$ is by definition narrowband, so that the detuning δ_0 will be important in the system's dynamics.

Finally the quantum field $\widehat{\mathcal{E}}_q(t)$ in the time domain is described by the expectation values of the correlation functions N and M of the creation and annihilation operators $\widehat{a}(\omega)$ and $\widehat{a}^\dagger(\omega)$ in frequency domain. These correlation functions are N_1, N_2 and M , and are defined similarly to Eqs. (5.9) and (5.8):

$$N_1 \equiv \langle \widehat{a}^\dagger(\omega_s) \widehat{a}(\omega_s) \rangle , \quad (8.5)$$

$$N_2 \equiv \langle \widehat{a}^\dagger(\omega_i) \widehat{a}(\omega_i) \rangle , \quad (8.6)$$

and

$$M \equiv |M(\omega)| e^{i\phi_s} = \langle \widehat{a}(\omega_s) \widehat{a}(\omega_i) \rangle . \quad (8.7)$$

8.1.2 Hamiltonian Formulation and Master Equation

The system under consideration is similar to the one studied by Ficek and Drummond in Ref. [44], with the important addition of the RO field $\widehat{\mathcal{E}}_0$. Hence the starting point in the analysis is the master equation of Ref. [44]. Since the bulk of the formalism used here to deal with the quantum fields is drawn from Ref. [44], it will be briefly explained and taken as is. Note, however, that the addition of the classical RO field as part of the total excitation field leads to a rich new phenomenology arising from quantum interference of excitation pathways, which is a new arena within the context of the interaction of squeezed light with atoms.

With this in mind, the total Hamiltonian H_{tot} of the system is written as

$$H_{tot} = H_A + H_F + H_{int} , \quad (8.8)$$

where H_A describes the free evolution of atomic operators and is given by

$$H_A |m\rangle = E_m |m\rangle , \quad (8.9)$$

for each of the atomic eigenstates $m = 1, 2, 3$. H_F is the free-field Hamiltonian given by

$$H_F = \hbar \int a^\dagger(\omega) a(\omega) \omega d\omega , \quad (8.10)$$

where the coherent state field $\widehat{\mathcal{E}}_0$ has been ignored in H_F since it contributes only a c-number to the overall energy. The interaction of the field with the atom is described by H_{int} , defined to be

$$H_{int} = i\hbar \int d\omega \left[\left[\sum_i \sum_{j \neq i} g_{ij}(\omega) S_{ij} \right] a(\omega) - H.c. \right] \\ - i\hbar \gamma^2 Q_o \left[(S_{31} e^{-i2(\delta_o t + \phi_o)} - S_{13} e^{i2(\delta_o t + \phi_o)}) + i(\beta_3 S_{33} - \beta_1 S_{11}) \right] , \quad (8.11)$$

where g_{ij} are coupling coefficients and S_{ij} atomic operators defined by $S_{ij} = |i\rangle \langle j|$, $i, j = 1, 2, 3$. As usual these operators satisfy the commutation relation

$$[S_{ij}, S_{pq}] = S_{iq} \delta_{jp} - S_{pj} \delta_{qi} , \quad (8.12)$$

where δ_{ij} is the Kroniker delta function. Note that in the electric dipole-approximation, $g_{13} = 0$. The parameter Q_o is a ‘‘Rabi-like’’ frequency defined in Eq. (7.25) and as before $\gamma = \sqrt{\gamma_2 \gamma_3}$. Note that the first term of Eq. (8.11) describes the interaction of the atoms with the quantum field $\widehat{\mathcal{E}}_q$ and has been extensively discussed in Ref. [44]. This first term is responsible for driving the $|1\rangle \leftrightarrow |2\rangle$ and $|2\rangle \leftrightarrow |3\rangle$ atomic transitions. To account for the additional coherent-state component $\widehat{\mathcal{E}}_0$ of the field the second term of Eq. (8.11) is added and is of the same form as that introduced in the semiclassical analysis in the previous chapter. It accounts for the driving of the

$|1\rangle \rightarrow |3\rangle$ transition and the intensity dependent Stark shifts via the β_1 and β_3 terms defined in Eq. (7.33).

Without getting into the details of the derivation, which are explicitly presented in Ref. [119], it is simply stated here that starting from the above Hamiltonian the master equation for the system of Fig. 8.1 can be shown to be

$$\begin{aligned}
\frac{\partial \rho}{\partial t} = & -\frac{1}{2}\gamma M \sum_{i,j=1}^2 (S_i^+ \rho S_j^+ - S_j^+ S_i^+ \rho + S_j^- \rho S_i^- - \rho S_i^- S_j^-) e^{-i(\omega_i + \omega_j - 2\omega_o)t} \\
& -\frac{1}{2}\gamma M^* \sum_{i,j=1}^2 (S_i^- \rho S_j^- - S_j^- S_i^- \rho + S_j^+ \rho S_i^+ - \rho S_i^+ S_j^+) e^{-i(\omega_i + \omega_j - 2\omega_o)t} \\
& - \sum_{i,j=1}^2 N_i \gamma_{ij} (\rho S_j^- S_i^+ + S_j^- S_i^+ \rho - 2S_i^+ \rho S_j^-) e^{i(\omega_i - \omega_j)t} \\
& - \sum_{i,j=1}^2 (N_i + 1) \gamma_{ij} (\rho S_i^+ S_j^- + S_i^+ S_j^- \rho - 2S_j^- \rho S_i^+) e^{i(\omega_i - \omega_j)t} \\
& - \gamma^2 Q_o [(S_{31}\rho - \rho S_{31}) e^{-2i(\delta_0 t + \phi_o)} - (S_{13}\rho - \rho S_{13}) e^{2i(\delta_0 t + \phi_o)}] \\
& + i\gamma^2 Q_o [\beta_3 (S_{33}\rho - \rho S_{33}) - \beta_1 (S_{11}\rho - \rho S_{11})], \tag{8.13}
\end{aligned}$$

where the first five terms correspond to the results of Ficek and Drummond of Ref.[44]a Eq. (20), while the last two terms are due to $\widehat{\mathcal{E}}_0$. In the above equation γ_{ii} , $i = 1, 2$, are equal to half the radiative decay constants for the $|1\rangle \rightarrow |2\rangle$ and $|2\rangle \rightarrow |3\rangle$ transitions (hence, $\gamma_{11} = \frac{\gamma_2}{2}$ and $\gamma_{22} = \frac{\gamma_3}{2}$). The additional damping terms γ_{12} and γ_{21} (as defined in Eq. (21) of Ref.[44]a) are in general non-zero, but because it is assumed that the atom has non-equidistant energy levels, with Δ large, these terms are rapidly oscillating and may be dropped. Terms corresponding to Stark shifts due to the weak quantum field $\widehat{\mathcal{E}}_q$ as well as Lamb shifts have been neglected. More details and explicit derivation of Eq. (8.13) can be found in Refs. [44, 119].

8.1.3 Equations of Motion

The next step is to expand Eq. (8.13) and arrive at a set of coupled differential equations for the elements of the density matrix. In particular, for the atomic populations ρ_{22} and ρ_{33} it is found that

$$\begin{aligned} \frac{\partial \rho_{22}}{\partial \tau} &= -M \rho_{13} e^{-2i\delta_0 \tau} - M^* \rho_{31} e^{2i\delta_0 \tau} + \alpha N_1 (1 - \rho_{22} - \rho_{33}) \\ &\quad - \alpha (N_1 + 1) \rho_{22} - \frac{1}{\alpha} N_2 \rho_{22} + \frac{1}{\alpha} (N_2 + 1) \rho_{33} \end{aligned} \quad (8.14)$$

and

$$\begin{aligned} \frac{\partial \rho_{33}}{\partial \tau} &= \frac{1}{2} M \rho_{13} e^{-2i\delta_0 \tau} + \frac{1}{2} M^* \rho_{31} e^{2i\delta_0 \tau} + \frac{1}{\alpha} N_2 \rho_{22} - \frac{1}{\alpha} (N_2 + 1) \rho_{33} \\ &\quad - Q_o (\rho_{13} e^{-2i(\delta_0 \tau + \phi_o)} + \rho_{31} e^{2i(\delta_0 \tau + \phi_o)}) , \end{aligned} \quad (8.15)$$

while the atomic population of the ground state can be calculated from the trace condition $Tr(\rho) = 1$. For the atomic coherences ρ_{12} , ρ_{23} , and ρ_{13} it is similarly found that

$$\begin{aligned} \frac{\partial \rho_{12}}{\partial \tau} &= \frac{1}{2} M^* \rho_{32} e^{2i\delta_0 \tau} - \frac{1}{2} \left[N_2 \frac{1}{\alpha} + N_1 \alpha + (N_1 + 1) \alpha \right] \rho_{12} \\ &\quad - i \frac{1}{\alpha} Q_o \rho_{12} + Q_o \rho_{32} e^{2i(\delta_0 \tau + \phi_o)} , \end{aligned} \quad (8.16)$$

$$\begin{aligned} \frac{\partial \rho_{23}}{\partial \tau} &= \frac{1}{2} M^* \rho_{21} e^{2i\delta_0 \tau} - \frac{1}{2} \left[N_2 \frac{1}{\alpha} + (N_2 + 1) \frac{1}{\alpha} + (N_1 + 1) \alpha \right] \rho_{23} \\ &\quad - i \alpha Q_o \rho_{23} - Q_o \rho_{21} e^{2i(\delta_0 \tau + \phi_o)} , \end{aligned} \quad (8.17)$$

and

$$\begin{aligned} \frac{\partial \rho_{13}}{\partial \tau} &= -M^* \rho_{22} e^{2i\delta_0 \tau} + \frac{1}{2} M^* (1 - \rho_{22}) e^{2i\delta_0 \tau} - \frac{1}{2} \left[N_1 \alpha + (N_2 + 1) \frac{1}{\alpha} \right] \rho_{13} \\ &\quad - i \left(\alpha + \frac{1}{\alpha} \right) Q_o \rho_{13} + Q_o (2\rho_{33} + \rho_{22} - 1) e^{2i(\delta_0 \tau + \phi_o)} , \end{aligned} \quad (8.18)$$

while the rest of the atomic coherences can be calculated from the relation $\rho_{ij} = \rho_{ji}^*$. Note that Eqs. (8.14)-(8.18) have been transformed into dimensionless form as was done in the previous chapter and the parameter $\alpha = \sqrt{\frac{\gamma_2}{\gamma_3}}$ is the same as before.

8.1.4 Solution for the Atomic Populations

The quantities of interest here are the atomic populations ρ_{22} and ρ_{33} whose derivation is simplified because the above set of differential equations decouples into two groups of linearly independent differential equations. In particular to solve for the atomic populations only the closed set of differential equations for ρ_{22} , ρ_{33} , ρ_{13} and ρ_{31} needs to be considered. Therefore, in steady state ($\frac{\partial \rho_{22}}{\partial \tau} = 0$, $\frac{\partial \rho_{33}}{\partial \tau} = 0$, $\frac{\partial(\rho_{13}e^{-2i\delta_0\tau})}{\partial \tau} = 0$ and $\frac{\partial(\rho_{31}e^{2i\delta_0\tau})}{\partial \tau} = 0$) the differential equations reduce to simple algebraic ones given by

$$M\tilde{\rho}_{13} + M^*\tilde{\rho}_{13}^* = \alpha N_1 - \left(\alpha + 2\alpha N_1 + \frac{1}{\alpha}N_2 \right) \rho_{22} + \left(\frac{1}{\alpha} - \alpha N_1 + \frac{1}{\alpha}N_2 \right) \rho_{33}, \quad (8.19)$$

$$\left(Q_o e^{-2i\phi_o} - \frac{1}{2}M \right) \tilde{\rho}_{13} + \left(Q_o e^{2i\phi_o} - \frac{1}{2}M^* \right) \tilde{\rho}_{13}^* = \frac{1}{\alpha}N_2\rho_{22} - \frac{1}{\alpha}(N_2 + 1)\rho_{33}, \quad (8.20)$$

$$\tilde{\rho}_{13} = \frac{1}{A} \left(-\frac{3}{2}M^* + Q_o e^{2i\phi_o} \right) \rho_{22} + 2\frac{1}{A}Q_o e^{2i\phi_o} \rho_{33} + \frac{1}{A} \left(\frac{1}{2}M^* - Q_o e^{2i\phi_o} \right). \quad (8.21)$$

where $\tilde{\rho}_{13}$ is defined to be

$$\tilde{\rho}_{13} \equiv \rho_{13}e^{-2i\delta_0\tau} \quad (8.22)$$

and the quantity A is given by

$$A \equiv \frac{1}{2} \left[N_1\alpha + (N_2 + 1)\frac{1}{\alpha} \right] + i \left[2\delta_0 + \left(\alpha + \frac{1}{\alpha} \right) Q_o \right]. \quad (8.23)$$

After some algebra to eliminate $\tilde{\rho}_{13}$ and $\tilde{\rho}_{31}$ from Eqs (8.19)-(8.21), it is found that the atomic populations ρ_{22} and ρ_{33} are given in terms of the following two linear equations

$$\Lambda_1\rho_{22} + \Xi_1\rho_{33} = 1, \quad (8.24)$$

and

$$\Lambda_2\rho_{22} + \Xi_2\rho_{33} = 1. \quad (8.25)$$

For the special case when the coherent-field $\widehat{\mathcal{E}}_0$ is resonant with the two-photon transition, (i.e., for $\delta_0 = 0$) and assuming that $\widehat{\mathcal{E}}_0$ is a weak field so that the Stark shift contribution (i.e., $(\alpha + \frac{1}{\alpha}) Q_o$) can be neglected, the quantities Λ_1 , Ξ_1 , Λ_2 and Ξ_2 can be shown to be equal to

$$\Lambda_1 = \frac{3|M|^2 - 2Q_o|M|\cos\Phi - \frac{1}{2}[N_1\alpha + (N_2 + 1)\frac{1}{\alpha}](\alpha + 2\alpha N_1 + \frac{1}{\alpha}N_2)}{|M|^2 - 2|M|Q_o\cos\Phi - \frac{1}{2}\alpha N_1[N_1\alpha + (N_2 + 1)\frac{1}{\alpha}]}, \quad (8.26)$$

$$\Xi_1 = \frac{-4Q_o|M|\cos\Phi + \frac{1}{2}[N_1\alpha + (N_2 + 1)\frac{1}{\alpha}](\frac{1}{\alpha} - \alpha N_1 + \frac{1}{\alpha}N_2)}{|M|^2 - 2|M|Q_o\cos\Phi - \frac{1}{2}\alpha N_1[N_1\alpha + (N_2 + 1)\frac{1}{\alpha}]}, \quad (8.27)$$

$$\Lambda_2 = \frac{4Q_o^2 + 3|M|^2 - 8Q_o|M|\cos\Phi - \frac{1}{\alpha}[N_1\alpha + (N_2 + 1)\frac{1}{\alpha}]N_2}{4Q_o^2 + |M|^2 - 4Q_o|M|\cos\Phi}, \quad (8.28)$$

and

$$\Xi_2 = \frac{8Q_o^2 - 4Q_o|M|\cos\Phi + \frac{1}{\alpha}[N_1\alpha + (N_2 + 1)\frac{1}{\alpha}](N_2 + 1)}{4Q_o^2 + |M|^2 - 4Q_o|M|\cos\Phi}, \quad (8.29)$$

while in the more general case these expressions became much more complicated. In Eqs. (8.26)-(8.29) the phase Φ is a combination of the phases of the squeezing ϕ_s and of the RO ϕ_o and is given by

$$\Phi = 2\phi_o + \phi_s. \quad (8.30)$$

Hence, the solutions for the atomic populations ρ_{22} and ρ_{33} are given by

$$\rho_{22} = \frac{\Xi_1 - \Xi_2}{\Lambda_2\Xi_1 - \Xi_2\Lambda_1} \quad (8.31)$$

and

$$\rho_{33} = \frac{\Lambda_2 - \Lambda_1}{\Lambda_2\Xi_1 - \Xi_2\Lambda_1}. \quad (8.32)$$

Note that from the above solution it is clear that the atomic populations have a phase-sensitive modulation determined through the dependence of Λ_i and Ξ_i on Φ , which is the only phase left in the final answer. Furthermore, all phase-sensitive terms are of the form $|M|Q_o\cos\Phi$, corresponding to interference between the RO field as described by Q_o and the quantum field output of the NDOPO as described by the correlations of the field-quadrature fluctuations given by M . However, since

no cross (interference) terms between N_1 , N_2 and Q_o exist, it is obvious that these correlation functions are incoherent with each other and with Q_o . Indeed, as shown in Ref.[13], the signal and idler outputs of the NDOPO when viewed in isolation from each other are described by their total intensities N_1 and N_2 , respectively, and correspond to incoherent, thermal fields and hence should not be expected to interfere with Q_o although they do contribute to the overall excitation probability by virtue of the energy they carry. More explicitly, note that for excitation with thermal fields ($M = 0$) the coupling between ρ_{33} and ρ_{13} due to the signal and idler fields vanishes. By contrast, the quantum correlations between the signal and idler fields as given by M drive a non-zero coupling of ρ_{13} with ρ_{33} as does Q_o , thus giving rise to QI (assuming the RO and squeezed fields are phase coherent).

Although at this point the discussion will turn away from the theoretical considerations, it is noted that an extensive discussion of the consequences of these results is presented in Ref. [119]. There, important experimental constraints of a finite focusing angle of the squeezing onto the atoms are investigated. It has been shown that for a small focusing angle θ the excited state populations ρ_{33} and ρ_{22} are given by

$$\rho_{22} \approx N_1 v(\theta) + O[v^2(\theta)] \quad , \quad (8.33)$$

and

$$\rho_{33} \approx [4\alpha^2 Q_o^2 + (|M|^2 \alpha^2 + N_1 N_2) v^2(\theta) - 4\alpha^2 Q_o |M| v(\theta) \cos \Phi] + O[v^3(\theta)] \quad , \quad (8.34)$$

where

$$v(\theta) = \frac{1}{2} \left[1 - \frac{1}{4} (3 + \cos^2 \theta) \cos \theta \right] \quad , \quad \theta \in (0, \pi) \quad . \quad (8.35)$$

Note that Eq. (8.34) can be rewritten as

$$\rho_{33} \approx (X_o^2 - 2X_o X_{q1} \cos \Phi + X_{q1}^2) + X_{q2}^2 \quad , \quad (8.36)$$

where the quantities $X_o \equiv 2\alpha Q_o$ and $X_q \equiv \sqrt{X_{q1}^2 + X_{q2}^2}$ (with $X_{q1} \equiv \alpha |M| v(\theta)$ and

$X_{q_2} \equiv \sqrt{N_1 N_2} v(\theta)$) are excitation amplitudes due to the coherent field $\widehat{\mathcal{E}}_0$ and the quantum field $\widehat{\mathcal{E}}_q$, respectively. Written in this form, ρ_{33} is obviously the result of two quantum interfering pathways with amplitudes X_o and X_{q_1} , plus a third incoherent contribution whose amplitude is X_{q_2} . The physical interpretation of this observation is that excitation via the RO and M interfere via the ρ_{13} coherence where excitation via N_1 and N_2 proceeds incoherently as discussed earlier so that their contribution to the total excitation probability adds incoherently.

In addition, in Ref. [119] effects of phase-sensitive inversion due to squeezing have been analyzed and new methods for detecting nonclassical effects of the interaction of squeezed light with atom have been presented.

8.2 Experiment

Turning now to the experimental observation of QI with squeezed light the discussion begins with the description of the setup shown in Fig. 8.3 which is similar with the setup of the previous experiments and in particular with the setup for the experiment of QI with coherent beams described in the previous chapter. Since most of the setup has been described already, here only two minor modifications are noted. First, the beamsplitter that combines the squeezed light with the coherent 884 nm RO beam is a 99/1 beamsplitter so as to minimize the losses of squeezing and second the detection strategy has been changed because the signal is very weak and instead of accumulating the photocounting time series on the PC, the signal is Fourier transformed and viewed on a spectrum analyzer.

The power of the RO beam was measured to be $P_{884} \approx 5 \text{ mW}$ and that of the signal and idler outputs of the NDOPO was estimated from parametric gain measurements to be $P_{852} \approx P_{917} \approx 1 \text{ pW}$. The three co-propagating beams (RO, signal and idler) are focused with a waist of 10 μm into the atomic Cs sample in the MOT. Their intensities are $\frac{I_{884}}{I_{884}^s} \approx 1$ and $\frac{I_{852}}{I_{852}^s} \approx \frac{I_{917}}{I_{917}^s} \approx 10^{-3}$, where I_{884}^s , I_{852}^s and I_{917}^s are the saturation intensities of the quadrupole $6S_{1/2}F = 4 \rightarrow 6D_{5/2}F'' = 6$ and dipole $6S_{1/2}F = 4 \rightarrow 6P_{3/2}F' = 5$ and $6P_{3/2}F' = 5 \rightarrow 6D_{5/2}F'' = 6$ transitions, respectively.

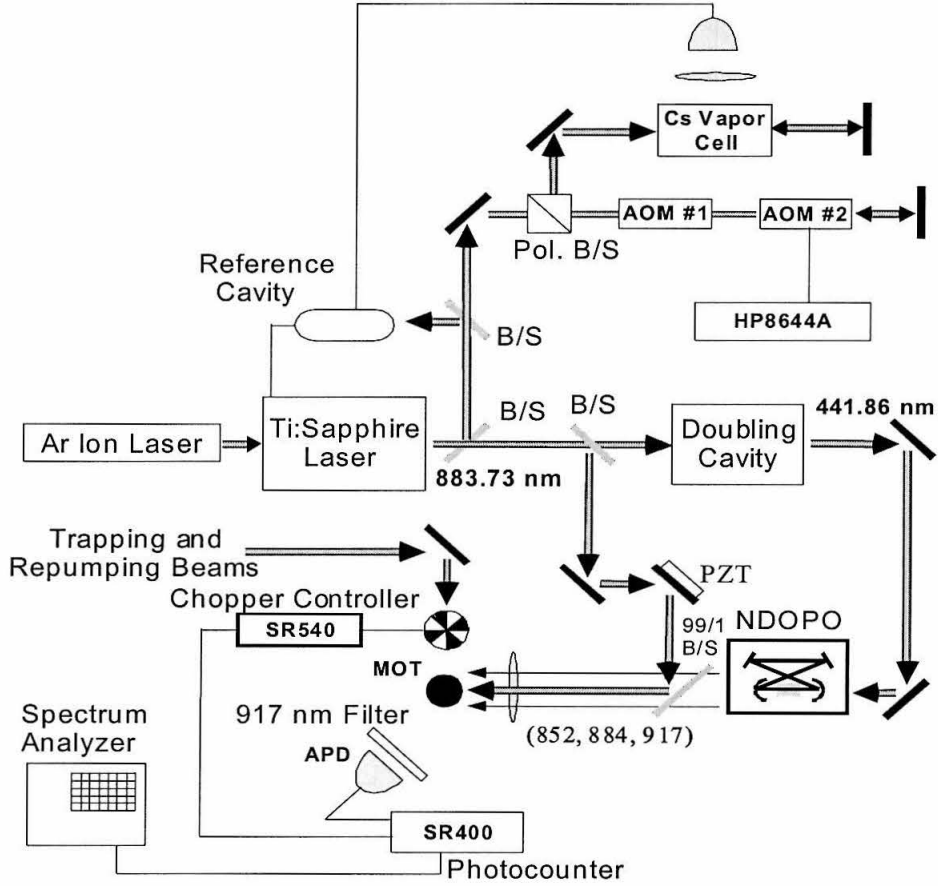


Figure 8.3: Experimental setup for observation of QI with squeezed light.

The excited state population ρ_{33} is monitored as before by observing the fluorescence I_F from the $6D_{5/2}F'' = 6 \rightarrow 6P_{3/2}F' = 5$ decay. With the given intensities for the excitation fields and for the efficiencies in the setup, the collected counting rates are $C_{sq} \approx 2$ /sec for excitation by the squeezed field alone and $C_{RO} \approx 10^4$ /sec for excitation by the coherent RO field alone. Modulation of the excited state population ρ_{33} due to QI is induced by scanning a PZT along the path of the RO beam at a rate $\frac{\omega_m}{2\pi} \approx 11$ Hz. As a result, the phase of the RO has the following time dependence

$$\phi_{RO}(t) = \omega_m t + \phi_{RO}^{(0)}, \quad (8.37)$$

where $\phi_{RO}^{(0)}$ is the static spatial phase of the RO field at the side of the atom.

Because the focussing angle of squeezing onto the atoms is only $\theta \approx 5^\circ$, the excited state population ρ_{33} is given by Eq. (8.34) and therefore the observed signal $I_F \propto \rho_{33}$ is of the form

$$I_F \approx \left[C_{RO} + 2\sqrt{C_{RO}C_{sq}} \cos \left(2\omega_m t + 2\phi_{RO}^{(0)} + \phi_s \right) \right] T \quad (8.38)$$

where T is the photcounter integration time. Here terms of order C_{sq} have been neglected since $C_{sq} \ll C_{RO}$. Note that the accumulated data is a time series of I_F , given by $\{I_F(t_o), I_F(t_o + T), I_F(t_o + 2T), \dots\}$. Therefore, in order to observe QI fringes two constraints must be satisfied: first, the Nyquist sampling theorem which requires that $T \leq \frac{1}{2\omega_m}$ and second a coherence constraint which requires that $\frac{1}{\tau_{coh}} \lesssim \omega_m$. Here τ_{coh} is the coherence time between the RO and squeezed fields (i.e., the average time before stochastic jumps scramble the phase $2\phi_{RO}^{(0)} + \phi_s$) which for the experiment is estimated to be 100 *ms*. The combination of these two constraints imposes an upper limit on the integration time, $T \leq \frac{\tau_{coh}}{2}$, and hence an upper limit for the signal I_F . Rewriting I_F as $I_F = \langle I_F \rangle + \delta I_F$ where $\langle I_F \rangle$ is the mean value of the signal and δI_F the modulation due to QI, implies that for the counting rates C_{sq} and C_{RO} of the experiment $\langle I_F \rangle \lesssim 500$ and $\delta I_F \lesssim 12$. Taking into account the uncertainty due to the Poissonian (counting) statistics of $\langle I_F \rangle$ which is of order $\sqrt{\langle I_F \rangle} \approx 22$ implies that direct observation of the QI modulation δI_F in the time domain is not possible. Therefore, an alternative strategy is implemented where the signal I_F is Fourier transformed and viewed on a spectrum analyzer. Note that based on these considerations in order to observe QI with squeezing in the time domain (similarly with the case for QI with coherent fields, Fig. 7.4), the condition $\frac{\delta I_F}{\sqrt{\langle I_F \rangle}} \simeq \sqrt{2C_{sq}\tau_{coh}} > 1$ must be satisfied. In addition, when the assumption $C_{sq} \ll C_{RO}$ is relaxed so that $C_{sq} \sim C_{RO} \sim C$ then $\langle I_F \rangle \simeq (C_{RO} + 2C_{sq})T$ and hence the signal to noise threshold for observation of QI in the time domain becomes $\frac{\delta I_F}{\sqrt{\langle I_F \rangle}} \simeq \sqrt{\frac{2}{3}C\tau_{coh}} > 1$.

Figure 8.4 shows two traces from the spectrum analyzer. The first one is a control

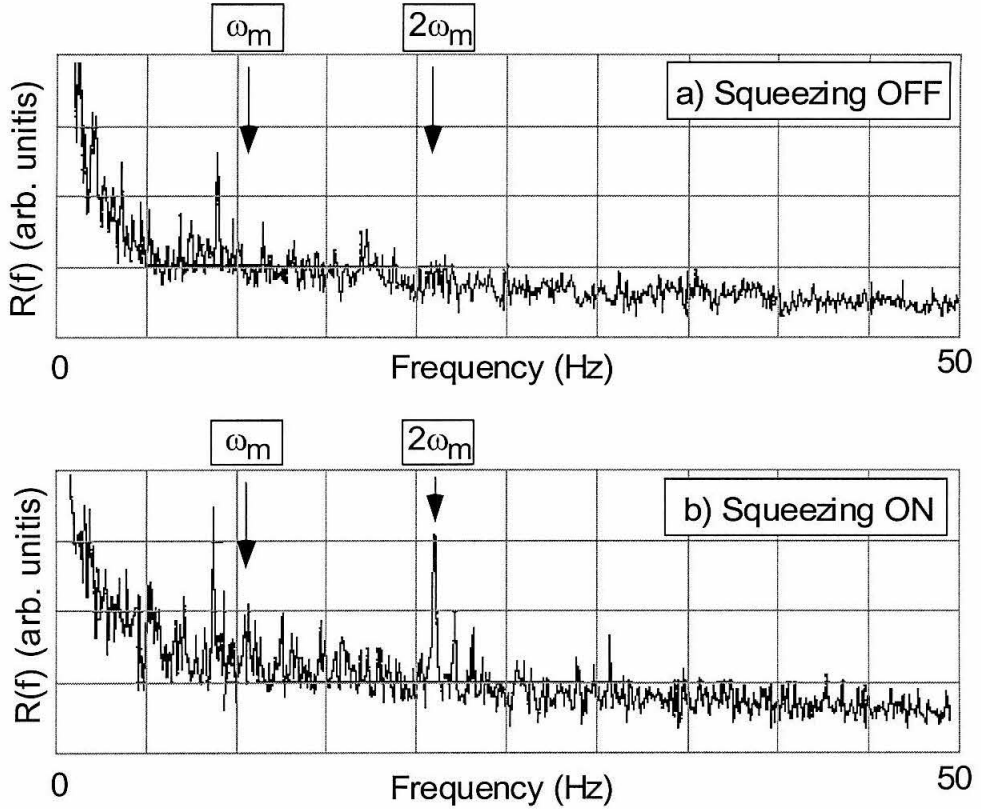


Figure 8.4: Power spectrum $R(f)$ of the photocounting time series I_F . a) Control spectrum with the squeezing turned off for which no modulation at either ω_m or $2\omega_m$ is observed; b) spectrum with the squeezing on for which a peak at frequency $2\omega_m$ appears.

trace for which the squeezing is turned off by detuning the temperature of the nonlinear $KNbO_3$ crystal in the OPO, and as evident there is no modulation at either ω_m or $2\omega_m$ (recall that $\frac{\omega_m}{2\pi} \sim 11 \text{ Hz}$). The second trace is with the squeezing turned on and a peak appears at $\sim 22 \text{ Hz}$ which is equal to $2\omega_m$. The peak that appears in Fig. 8.4b is a signature of the quantum correlations between the signal and idler outputs of the NDOPO although strictly speaking it only demonstrates that $M = \langle \hat{\mathcal{E}}_{852} \hat{\mathcal{E}}_{917} \rangle \neq 0$ but not necessarily that the quantum criterium $N^2 < |M|^2 \leq N(N+1)$ (where $N = \langle \hat{\mathcal{E}}_{852}^\dagger \hat{\mathcal{E}}_{852} \rangle = \langle \hat{\mathcal{E}}_{917}^\dagger \hat{\mathcal{E}}_{917} \rangle$) is satisfied. Alternative methods to directly compare N with M using QI are currently under investigation and some indirect methods have already been proposed.[103]

8.3 Summary

In conclusion, in this chapter the illumination of a three-level atom by a combination of a coherent RO field and the squeezed output of an NDOPO has been studied. As a result of multiple excitation pathways for two-photon excitation, QI in the excited state population ρ_{33} has been predicted. A theoretical model based on the master equation of the system has been developed to enable detail calculations of features of QI in the system.[119] An experimental realization with Cs has shown that QI with squeezed light is indeed observable. Realizing that the modulation terms due to QI in the excited state population ρ_{33} are proportional to the nonclassical correlations, $M = \langle \hat{\mathcal{E}}_s \hat{\mathcal{E}}_i \rangle$ suggests that by using this method detection of squeezing can be achieved. Furthermore, by drawing an analogy between the behavior of the atom in this system and conventional nonlinear mixers, it has been pointed out that atoms have much greater “bandwidth.” In particular, for the experimental realization presented, correlations have been detected between the signal and idler beams from an NDOPO which are separated in frequency by 25 THz. In the next chapter the use of atoms as nonlinear mixers will be examined in more detail.

Chapter 9 Atoms as Ultrafast Nonlinear Mixers

The modulation in the excited state population ρ_{33} due to QI discussed in the last two chapters can also be interpreted as nonlinear mixing of three fields with the atom acting as the mixer and the modulation in ρ_{33} being the demodulated signal.[102] Figure 9.1 shows schematically this analogy. In this generic representation, three fields with amplitudes ϵ_0 , ϵ_1 and ϵ_2 , and corresponding frequencies ω_0 , ω_1 and ω_2 , are the input to the nonlinear mixer which in this case is simply a three-level atom. The atom “processes” the input fields, and the output is the demodulated beatnote of them, $V_{out} \propto 1 + \xi \epsilon_0^2 \epsilon_1 \epsilon_2 \cos [(2\omega_0 - \omega_1 - \omega_2) t]$ (see Eq. (7.20)). Here V_{out} is the voltage from a photodetector that monitors the excited state population ρ_{33} and ξ depends on atomic parameters. Note that the static phase $2\phi_0 - \phi_1 - \phi_2 + \Phi$ that appears in Eq. (7.20) has been neglected for simplicity. In addition, although in the preceding discussion monitoring of ρ_{33} has been accomplished by detecting the fluorescent decay from the $|3\rangle \rightarrow |2\rangle$ transition, alternative methods to observe ρ_{33} such as excitation to a different level or ionization from the $|3\rangle$ excited level, may also be implemented.

The important advantage of atomic nonlinear mixers (ANM’s) is that they operate at optical frequencies and that the distance between the fields that can be demodulated with this technique (quantified by $\delta f = \frac{\omega_1 - \omega_2}{2\pi}$) can reach 100’s of *THz*. Conventional nonlinear mixers, which in the optical range are simply fast photodetectors, can only reach 10’s of *GHz*. Hence, ANM’s are several orders of magnitude “faster” than ordinary photodetectors (albeit in rather narrow windows) and can offer alternative solutions to comparing fields which are separated by large frequency intervals. In the remainder of this chapter, details and implications of atomic nonlinear mixing will be discussed with emphasis on potential applications.[122]

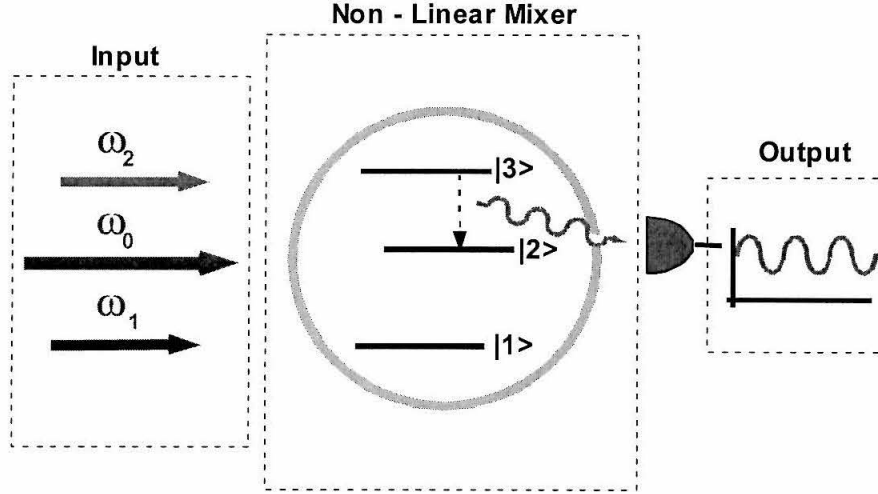


Figure 9.1: A three level atom acting as a nonlinear mixer. Three input fields at frequencies ω_1 , ω_2 and ω_3 are “mixed” to result in a “demodulated” output signal.

9.1 Characterization of Atomic Nonlinear Mixers

Atomic nonlinear mixers based on QI are wavelength specific and operate at narrow frequency ranges due to the vanishing response of atoms to excitation by fields that are far off resonance from the eigenfrequencies. To quantify the frequency response of ANM’s, consider an atom with energy levels $\{|1\rangle, |2\rangle, |3\rangle\}$ and eigenfrequencies $\{\frac{\omega_{31}}{2}, \omega_{21}, \omega_{32}\}$ corresponding to the two-photon $|1\rangle \rightarrow |3\rangle$ and one-photon $|1\rangle \rightarrow |2\rangle$ and $|2\rangle \rightarrow |3\rangle$ transition frequencies. The atom is excited by three fields $\{\mathcal{E}_0, \mathcal{E}_1, \mathcal{E}_2\}$ with amplitudes $\{\epsilon_0, \epsilon_1, \epsilon_2\}$ and frequencies $\{\omega_0, \omega_1, \omega_2\}$ as defined in Eq. (7.2). For simplicity, the spatial phases of these fields are set to zero. The detunings of the excitation field frequencies from the atomic eigenfrequencies are $\{\delta_0, \delta_1, \delta_2\}$ as defined in Eq. (7.3). Assuming perturbation theory (see Section 7.2) we find that the excited state population ρ_{33} is given by Eq. (7.20). Note that the perturbation limit requires that $\rho_{33} \ll 1$ which from Eq. (7.20) is equivalent to requiring that $\mathbf{X}, \mathbf{Y} \ll 1$.

9.1.1 ANM Frequency Response with Fixed Excitation Power

The response of the ANM is quantified by two parameters: the mean excited state population $\rho_{33}^o = \mathbf{X}^2 + \mathbf{Y}^2$ and the visibility of the demodulated signal $\mathcal{V} = \frac{2\mathbf{X}\mathbf{Y}}{\mathbf{X}^2 + \mathbf{Y}^2}$ (see Eqs. (7.28) and (7.29)). Recall that \mathbf{X} and \mathbf{Y} (defined by Eqs. (7.21) and (7.22)) are the excitation amplitudes associated with the two alternative excitation pathways, namely the simultaneous two-photon absorption from the ω_0 field ($|1\rangle \rightarrow |3\rangle$) and the stepwise absorption of one photon from each of the ω_1 and ω_2 fields ($|1\rangle \rightarrow |2\rangle \rightarrow |3\rangle$), respectively. Optimum performance of the ANM occurs when both ρ_{33}^o and \mathcal{V} are as large as possible. To achieve optimum visibility (i.e., maximize the fringe contrast of the demodulated signal V_{out}), the amplitudes \mathbf{X} and \mathbf{Y} must be adjusted to be equal (e.g., by tuning the field amplitudes) so that $\mathcal{V} = 1$. Furthermore, to maximize the mean signal ρ_{33}^o for fixed power levels of the excitation fields, the frequency detunings must be all zero. Combining these two conditions (i.e., $\mathbf{X} = \mathbf{Y}$ and $\delta_0 = \delta_1 = \delta_2 = 0$) gives that for optimized performance the Rabi frequencies (or equivalently the excitation field amplitudes) must satisfy

$$\frac{\Omega_1\Omega_2}{Q_o} = \frac{\epsilon_1\epsilon_2}{\epsilon_0^2}\Delta = \frac{\alpha}{2}, \quad (9.1)$$

where Δ is defined by Eq. (7.4) and $\alpha = \sqrt{\frac{\gamma_2}{\gamma_3}}$. Assuming this condition is satisfied, the mean excited state population $\tilde{\rho}_{33}^o$ is equal to

$$\tilde{\rho}_{33}^o = 8\alpha^2 Q_o^2 = 32\Omega_1^2\Omega_2^2 \quad (9.2)$$

and the visibility of the demodulated signal is $\mathcal{V} = 1$.

Having defined a measure of ‘‘optimum’’ performance for the ANM (Eqs. (9.1) and (9.2)), the frequency response can now be quantified with respect to these optimum conditions. In particular, for fixed field amplitudes that satisfy the ‘‘optimum’’ condition in Eq. (9.1), the following two measures are defined:

$$\rho(\delta_1, \delta_2, \delta_0) \equiv \frac{\rho_{33}^o}{\tilde{\rho}_{33}^o} = \frac{1}{8\alpha^2(4\delta_0^2 + \frac{1}{4\alpha^2})} + \frac{1}{32(\delta_1^2 + \frac{1}{4}\alpha^2)((\delta_1 + \delta_2)^2 + \frac{1}{4\alpha^2})} \quad (9.3)$$

and $\mathcal{V}(\delta_1, \delta_2, \delta_0) \equiv \mathcal{V}\left(\frac{\Omega_1 \Omega_2}{Q_o} = \frac{\alpha}{2}\right)$, which is derived from Eq. (7.29) to be

$$\mathcal{V}(\delta_1, \delta_2, \delta_0) = \frac{\alpha \sqrt{(4\delta_0^2 + \frac{1}{4\alpha^2}) (\delta_1^2 + \frac{1}{4}\alpha^2) ((\delta_1 + \delta_2)^2 + \frac{1}{4\alpha^2})}}{(\delta_1^2 + \frac{1}{4}\alpha^2) ((\delta_1 + \delta_2)^2 + \frac{1}{4\alpha^2}) + \frac{\alpha^2}{4} (4\delta_0^2 + \frac{1}{4\alpha^2})} \quad (9.4)$$

Recall that the δ_i are dimensionless quantities, since they are normalized by $\gamma = \sqrt{\gamma_2 \gamma_3}$.

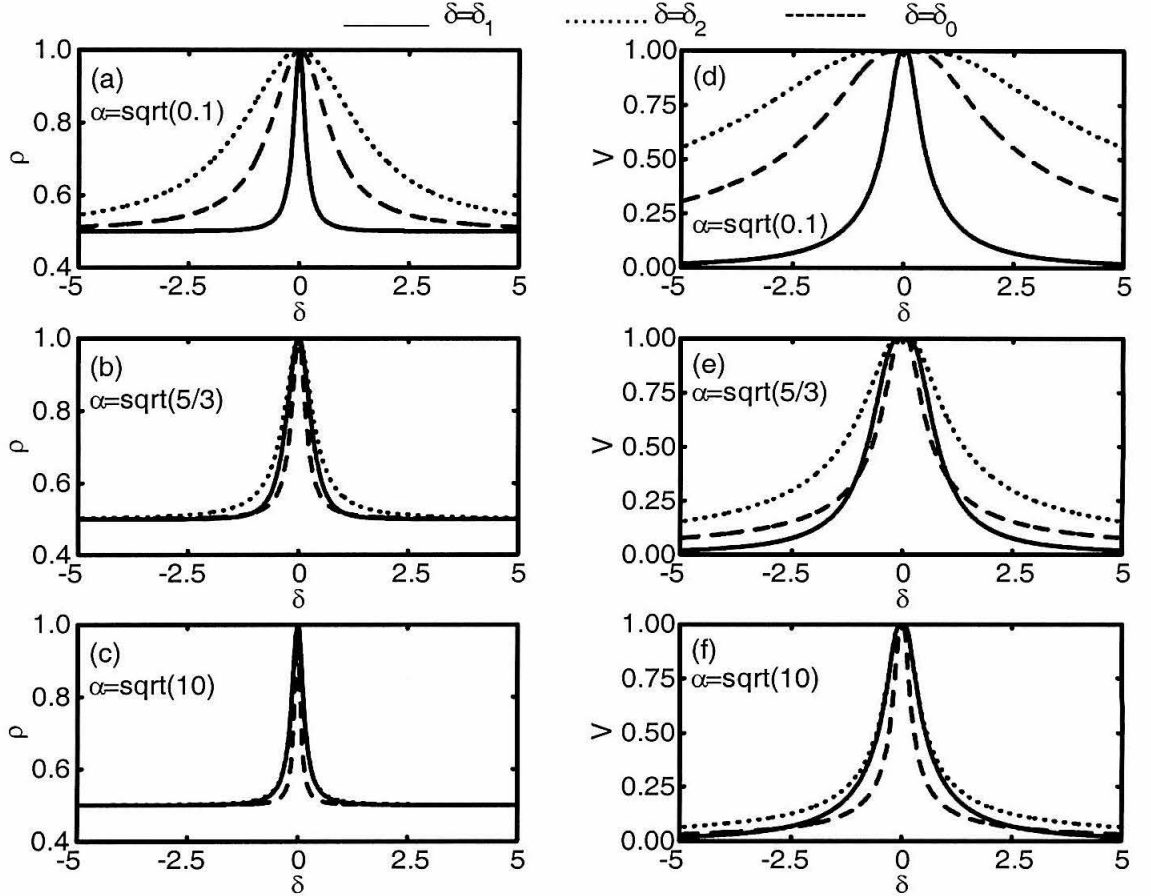


Figure 9.2: Frequency response of ρ in (a), (b) and (c) and \mathcal{V} in (d), (e) and (f) as functions of the detuning δ . Solid lines are for $\delta_1 = \delta$, $\delta_2 = 0$, $\delta_0 = 0$; dotted lines are for $\delta_1 = 0$, $\delta_2 = \delta$, $\delta_0 = 0$; dashed lines are for $\delta_1 = 0$, $\delta_2 = 0$, $\delta_0 = \delta$. The value of $\alpha = \sqrt{\frac{\gamma_2}{\gamma_3}}$ is for (a) and (d) $\alpha = \sqrt{\frac{1}{10}}$, for (b) and (e) $\alpha = \sqrt{\frac{5}{3}}$ and for (c) and (f) $\alpha = \sqrt{\frac{10}{1}}$. Note that δ is in units of $\gamma = \sqrt{\gamma_2 \gamma_3}$.

To elaborate further on the physical meaning of the frequency response measures defined in Eqs. (9.3) and (9.4), it is first noted that $\rho(\delta_1, \delta_2, \delta_0)$ quantifies the dependence of the mean excited state population on the detunings, normalized by the optimum value of $\tilde{\rho}_{33}^o$. Therefore, when the fields are resonant with the atomic eigenfrequencies, this measure is equal to unity, $\rho(\delta_1 = 0, \delta_2 = 0, \delta_0 = 0) = 1$. As the detunings move away from zero, the value of ρ decays, indicating that the mean detectable signal V_{out} decreases accordingly. Similarly, $\mathcal{V}(\delta_1, \delta_2, \delta_0)$ quantifies the visibility drop due to nonzero frequency detunings. Both ρ and \mathcal{V} are complicated functions of $\{\delta_1, \delta_2, \delta_0, \alpha\}$ and hence a full description of all their features is beyond the scope of the present discussion. However, few special cases are shown in Fig. 9.2. In particular, the frequency dependence of ρ and \mathcal{V} is shown as a function of one of the three detunings while the other two are kept equal to zero. Note that for this choice of detunings $\rho \geq \frac{1}{2}$ which is not necessarily the case if more than one of the detunings are different from zero. Furthermore, notice that the linewidths of all curves in Fig. 9.2 are of order of few $\gamma = \sqrt{\gamma_2\gamma_3}$.

To quantify the ‘‘linewidth’’ of the response functions, it can be shown that for the special case that $\delta_2 = \delta_0 = 0$, the FWHM of the visibility function \mathcal{V} (Eq. (9.4)) is equal to

$$\Delta_{FMHM}^{(1)}(\delta_0 = \delta_2 = 0) = \frac{1}{2\alpha} \sqrt{2 \left(-(1 + \alpha^4) + \sqrt{(1 + \alpha^4)^2 + 8\alpha^4 (3 + 2\sqrt{3})} \right)}. \quad (9.5)$$

Similarly, for the cases that $\delta_1 = \delta_0 = 0$ and $\delta_1 = \delta_2 = 0$, the FWHM of \mathcal{V} is given by

$$\Delta_{FWHM}^{(2)}(\delta_0 = \delta_1 = 0) = \frac{\sqrt{2}}{\alpha} \sqrt{(3 + 2\sqrt{3})} \simeq \frac{3.6}{\alpha}, \quad (9.6)$$

and

$$\Delta_{FWHM}^{(0)}(\delta_1 = \delta_2 = 0) = \frac{1}{2} \frac{\sqrt{2}}{\alpha} \sqrt{(3 + 2\sqrt{3})} \simeq \frac{1.8}{\alpha}, \quad (9.7)$$

respectively. Notice that $\Delta_{FWHM}^{(2)} = 2\Delta_{FWHM}^{(0)}$ and that they both scale as $\frac{1}{\alpha}$, which

means that in a practical application for which δ_0 or δ_2 is large, a good choice of an ANM would be such that $\alpha \ll 1$, or equivalently such that $\gamma_2 \ll \gamma_3$. On the other hand, $\Delta_{FWHM}^{(1)}$ is a more complicated function and in fact it has a maximum at $\alpha = 1$ for which $\Delta_{FWHM}^{(1)}(\alpha = 1) \simeq 1.65$. Figure 9.3 shows the $\Delta_{FWHM}^{(i)}$ as functions of α . Notice that for large values of α , the linewidths $\Delta_{FWHM}^{(1)}$ and $\Delta_{FWHM}^{(2)}$ become equal, $\Delta_{FWHM}^{(1)} = \Delta_{FWHM}^{(2)}$.

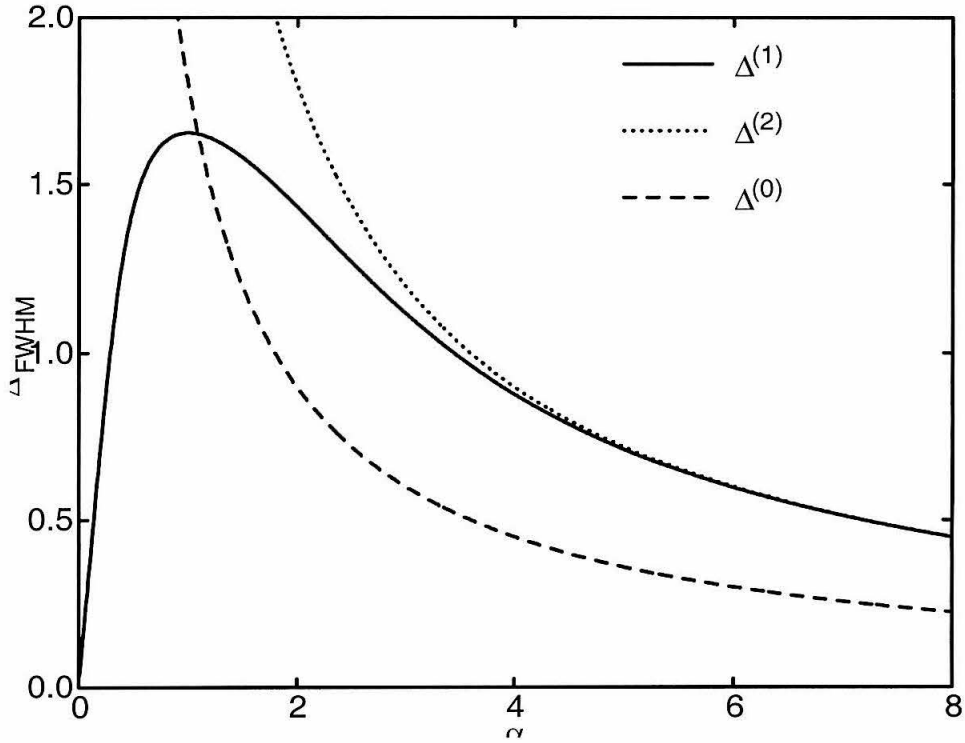


Figure 9.3: Full width at half maximum $\Delta_{FWHM}^{(i)}$, $i = 0, 1, 2$ for the visibility \mathcal{V} as a function of $\alpha = \sqrt{\frac{\gamma_2}{\gamma_3}}$. Note that $\Delta_{FWHM}^{(i)}$ is in units of $\gamma = \sqrt{\gamma_2 \gamma_3}$.

9.1.2 ANM Frequency Response with Variable Excitation Power

So far in the discussion of frequency response of ANM, the power of the excitation fields was fixed according to Eq. (9.1). However, if the power is allowed to change,

then the effective bandwidth of the ANM's is limited only by the available power in each of the fields since in principle, for any detuning, the excitation amplitudes \mathbf{X} and \mathbf{Y} can be kept constant by adjusting the field powers. In practice, of course, the available laser power is limited and furthermore for large detunings other atomic energy levels come into play.

Nevertheless, detunings can be compensated to a large extent by increasing the field power. It is clear from Eq. (7.21) that in order to keep \mathbf{X} constant for large detunings of the \mathcal{E}_0 field, $\delta_0 \gg \alpha, \frac{1}{\alpha}, \delta_1, \delta_2$, the ratio $\frac{P_0}{\delta_0}$ must be also kept constant. Similarly from Eq. (7.22) in order to keep \mathbf{Y} constant while δ_1 is increased, the ratio $\frac{P_1}{\delta_1^4}$ must be fixed while if δ_2 is increased the ratio $\frac{P_2}{\delta_2^2}$ must be fixed. Notice that the required power P_0 to keep \mathbf{X} constant increases linearly with δ_0 while to keep \mathbf{Y} constant, P_1 must be scaled as δ_1^4 and P_2 as δ_2^2 . Also note that although mathematically it is valid to increase P_2 to compensate for δ_1 , physically this does not work because if δ_2 is small, then P_2 will saturate the $|2\rangle \rightarrow |3\rangle$ transition which will limit \mathbf{Y} , (recall that Eq. (7.22) applies only in the perturbative limit). Similarly, increasing P_1 to compensate for δ_2 does not work either.

As an example of the detunings that can be compensated by increased laser power, consider the experiment described in Section 7.5.[102] There the excitation powers were $P_{884} \simeq 5 \text{ mW}$ and $P_{852} \simeq P_{917} \simeq 0.5 \text{ nW}$. Assuming that the power could be increased to 1 *Watt* for each of the beams, it is easy to calculate that similar results with Fig. 7.4 could be observed for detunings as large as $\delta_{884} \simeq 42$, $\delta_{852} \simeq 62$ and $\delta_{917} \simeq 5940$ which since $\gamma \simeq 3.9 \text{ MHz}$ translate to 160 *MHz*, 240 *MHz* and 23 *GHz*, respectively.

9.2 Database of Atomic Nonlinear Mixers

Although atomic nonlinear mixers are limited in bandwidth and work only for specific wavelengths due to the resonance conditions that must be satisfied, there is nevertheless an abundance of possible excitation schemes where this method could be applied to. In particular, any three-level atom that can be excited by three fields via two

alternative excitation pathways will act as a nonlinear mixer for these three fields. For the purposes of the present discussion, only atoms in a ladder (Ξ) configuration will be considered, although V and Λ systems could also be used; see Fig. 9.4. Likewise, the discussion is limited to the alkali elements Li , K , Na , Rb and Cs for which databases of their energy levels are readily available.[123, 124] Of course other atoms and even molecules would work in the same fashion.

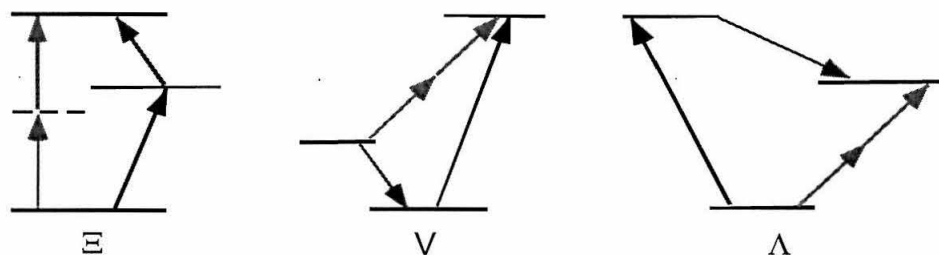


Figure 9.4: From the three possible two-photon excitation schemes, Ξ , V and Λ , only the first one is considered here. The other two also exhibit QI and could be also used as nonlinear mixers.

To consider all possible three-level configurations that can be used as ANM's, all combinations $\{n_1L_1J_1, n_2L_2J_2, n_3L_3J_3\}$ of energy levels in each atom must be considered. Here n_i is the principal quantum number, L_i is the orbital angular momentum and J_i the total angular momentum of the i^{th} energy level of the atom. These combinations are limited by three constraints. First, because the discussion here is only for Ξ systems, the condition $E_{n_1} < E_{n_2} < E_{n_3}$, where E_{n_i} is the energy of the i^{th} level, is imposed. Second, to avoid microwave frequencies and the very closely spaced Rydberg states, the wavelength of each of the three transitions is constrained to be $\lambda_{ij} < 2000 \text{ nm}$, where λ_{ij} is the wavelength of the $|i\rangle \rightarrow |j\rangle$ transition. Finally, for the transitions to be allowed, the parity selection rules $|L_1 - L_2| = |L_2 - L_3| = 1$ and the conservation of angular momentum selection rules $|J_1 - J_2| = 0, \pm 1$ and $|J_2 - J_3| = 0, \pm 1$ must be satisfied. Note that these constraints allow systems for which n_1L_1 is not necessarily the ground state. For these systems, it is assumed that considerable atomic population can be built up in the n_1L_1 level by excitation

from the ground state. Applying these criteria to the energy levels of *Li*, *K*, *Na*, *Rb* and *Cs* [123, 124] gives about 6900 distinct three-level systems which can be used as ANMs.

Figure 9.5 shows the sideband-to-carrier separation Δf as a function of the carrier wavelength λ_c for the data base of 6900 ANM's. Here the carrier frequency is defined to be the two-photon resonance frequency $\frac{\omega_{31}}{2}$ corresponding to the quadrupole $|1\rangle \rightarrow |3\rangle$ transition and the sideband-to-carrier separation is defined by $\Delta f \equiv \frac{1}{2\pi} \left| \omega_{21} - \frac{\omega_{31}}{2} \right| = \frac{1}{2\pi} \left| \omega_{32} - \frac{\omega_{31}}{2} \right|$, where as before the frequencies ω_{21} and ω_{32} are the resonance frequencies for the $|1\rangle \rightarrow |2\rangle$ and $|2\rangle \rightarrow |3\rangle$ transitions, respectively. Notice that our experimental demonstration of Section 7.5 [102] where demodulation of fields with $\Delta f = 12.5 THz$ has been observed, is rather insignificant compared to what is possible according to Fig. 9.5, where Δf can be as large as $\sim 240 THz$!

9.3 Frequency Metrology

The capability for optical demodulation demonstrated in the experiment described in Section 7.5, together with the numerous possibilities for nonlinear mixing illustrated in Fig. 9.5 suggest exploiting QI in two-photon excitation for applications in frequency metrology. In particular, to obtain an absolute measurement of a given target frequency in terms of a handful of reference frequencies, one faces the daunting challenge of bridging intervals that are often comparable to the optical frequency itself. Numerous schemes to “conquer” these large frequency intervals have been investigated,[125, 126, 127, 128] including resonant multiwave mixing in atomic vapors.[129, 130]

Within this context, we have proposed a new method for absolute comparison of an (arbitrary) target frequency ω_t to one or more reference frequencies $\omega_{r_1}, \omega_{r_2}, \dots$, [128] by exploiting atoms as ultrafast nonlinear mixing elements. As for the actual implementation of the proposed scheme, the first step is to construct from the set of available frequencies $\Omega_o = \{\omega_{r_1}, \omega_{r_2}, \dots\}$ and ω_t a new set $\Omega_1 = \{\omega'_1, \omega'_2, \dots, \omega'_{N_1}\}$ via sum and difference frequency generation and harmonic conversion, where one allows

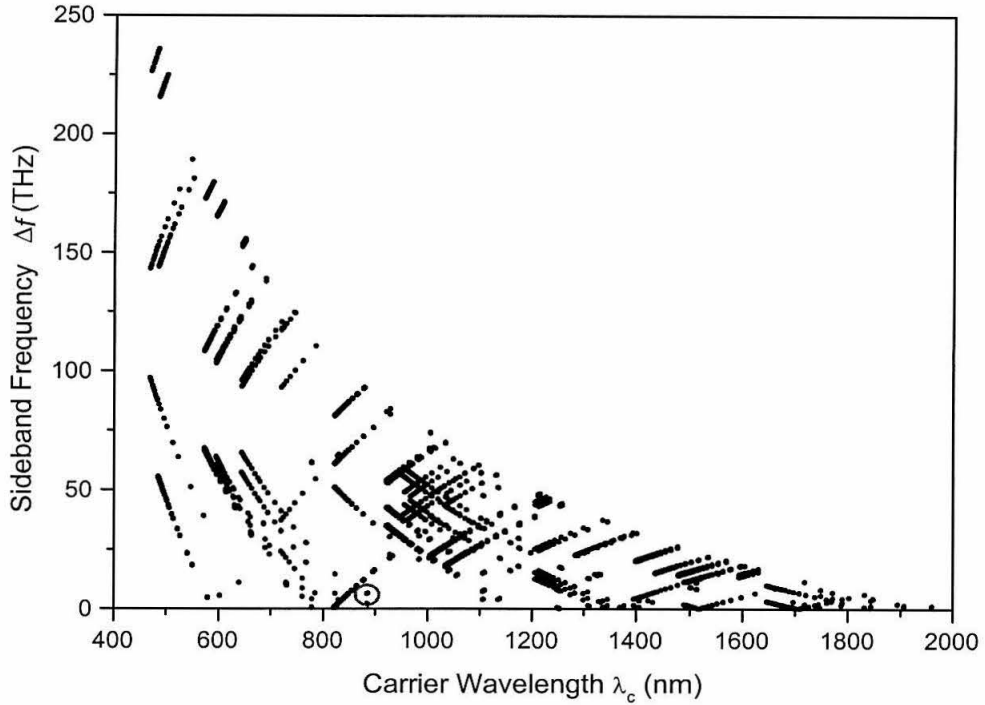


Figure 9.5: ANM characteristics for the sideband-to-carrier separation Δf versus the carrier wavelength λ_c for the database of 6900 transitions in the alkali elements. The circled point corresponds to the experimental demonstration with $\lambda_c \simeq 884 \text{ nm}$ and $\Delta f \simeq 12.5 \text{ THz}$.

for combinations of the form $\omega_i \pm \omega_j$ with $\{\omega_i, \omega_j\} \subseteq \Omega_o \cup \omega_t$. This process may be repeated for up to k stages to generate a final set of frequencies Ω_k with the number of resulting frequencies growing exponentially in k ; see Fig. 9.6.

Of course, finally we need only three of these frequencies to mix with the aid of an atom. To decide which three must actually be generated, all possible triplets $(\omega'_a, \omega'_b, \omega'_c)$ from the set $\Omega = \{\omega_t\} \cup \Omega_o \cup \Omega_1 \dots \cup \Omega_k$ that can be traced back to ω_t must be considered. From this large number of possibilities, only those triplets that satisfy $\omega'_a + \omega'_b - 2\omega'_c < \Delta\omega'$, where $\Delta\omega'$ is the maximum offset that can be either directly detected or compensated via electro-optic modulation ($\Delta\omega' \leq 500 \text{ GHz}$), must be kept. These triplets are then cross-referenced to the database of two-photon transitions with a search algorithm that optimizes a criterion such as the sum Σ of

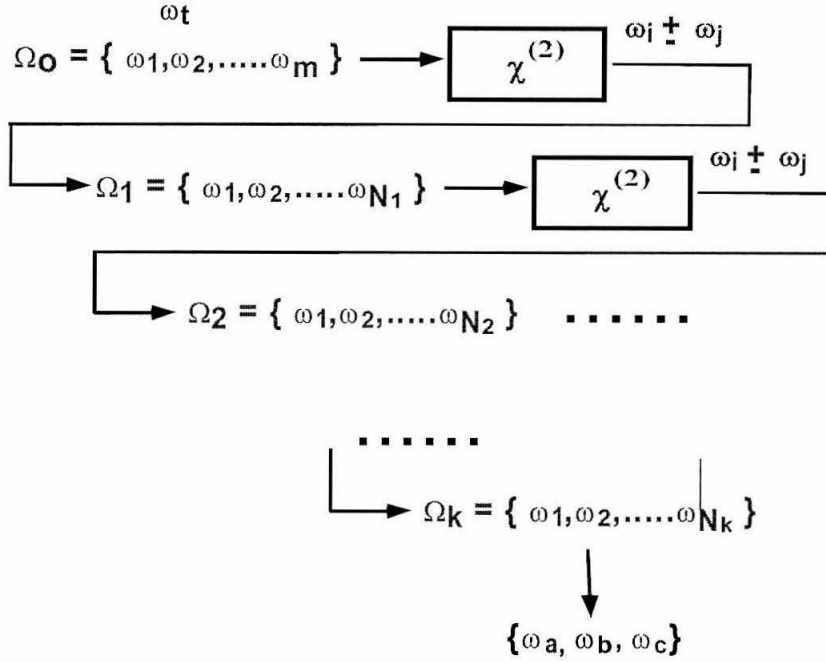


Figure 9.6: By frequency sum and difference generation and harmonic conversion ($\omega_i \pm \omega_j$), an initial set of reference frequencies Ω_o together with the target frequency ω_t results after k stages of nonlinear transformations into a new set of frequencies Ω_k . From Ω_k the three “best” frequencies $\{\omega_a, \omega_b, \omega_c\}$ for the particular application are chosen.

absolute detunings, $\Sigma = |\omega'_a - \omega_{12}| + |\omega'_b - \omega_{23}| + |\omega'_c - \frac{1}{2}\omega_{13}|$, and thereby chooses the particular atomic transition for the measurement and a set of three frequencies $\{\omega_a, \omega_b, \omega_c\}$ that must be generated.

The three frequencies ω_a , ω_b and ω_c chosen with the above procedure are linear combinations of the frequency standards $\omega_{r_i} \in \Omega_o$ and target frequencies ω_t which can be expressed as

$$\omega_n = p_n \omega_t + \sum q_{n_i} \omega_{r_i} , \quad (9.8)$$

where $n \in \{a, b, c\}$ and the coefficients p_n and q_{n_i} are integers. Then, by illuminating the chosen atom with the three frequencies ω_a , ω_b and ω_c , two-photon excitation is induced by two alternative pathways leading to QI which is observed as a modulation of the excited state population. The frequency of this modulation is given by $\Omega_B =$

$\omega_a + \omega_b - 2\omega_c$ which in combination with Eq. (9.8) implies that

$$\omega_t = \frac{\Omega_B - \sum (q_{a_i} + q_{b_i} - 2q_{c_i}) \omega_{r_i}}{(p_a + p_b - 2p_c)}. \quad (9.9)$$

Clearly an additional constraint must be satisfied in order for ω_t to be measurable by this technique, namely $p_a + p_b - 2p_c \neq 0$.

Once the target frequency has been measured with respect to the references which by definition are stable and well determined, the target itself becomes a new reference frequency. In this way new frequency standards may be established. Furthermore, by setting frequency standards as the targets, the internal consistency of the existing set of standards may be verified.

9.4 Optical Communication

A specific application of the methods described in the previous section is in optical communication. In particular, by using ANMs the goal is to establish frequency standards in the $1.5 - 1.55 \mu m$ range which is relevant for optical communications.[131] As fiber networks become more crowded with techniques such as wavelength division multiplexing (WDM), the need for such standards increases and the ability to operationally define a frequency reference that is well measured and stabilized with respect to other already established frequency standards could have significant market value as well. Preliminary studies have indicated that the methods outlined in the previous section allow for the determination of practically any frequency in the range of $200 - 2000 nm$. Therefore, this dense coverage clearly suggests that ANMs could also be applied for the task of establishing frequency standards in optical communication. Realizing this possibility we have filed a patent application for ANMs and the method of QI for demodulating frequencies that are separated by large intervals. Details and examples of these applications will appear in a future publication.[122]

9.5 Summary

In conclusion, in this chapter the properties of ANM's have been analyzed and measures to determine their frequency response have been defined. By analyzing these measures general dependencies of the ANM “bandwidth” on the atomic linewidths have been discussed. By expanding the view to systems other than the one that has been studied so far (i.e., the $6S_{1/2} \rightarrow 6P_{3/2} \rightarrow 6D_{5/2}$ transition in *Cs*), a database of 6900 possible transitions in the alkali elements *Li*, *Na*, *K*, *Rb* and *Cs* has been constructed. Each of these transitions can be utilized as an ANM which due to QI can demodulate the beatnote of three incident laser fields which could differ up to 100's of *THz*. Applying ANMs to frequency metrology, we have suggested a novel method for bridging large frequency intervals and establishing new frequency standards has been suggested. A particular application of this method in optical communication could have significant technology implications. Work in these areas is continuing, and more details will appear in the near future.[122]

Chapter 10 Epilogue

Reflecting back on my research of the last six years, it is a fair judgement to say that it has been a very rewarding experience with several important milestones along the way. The goal of this Thesis was to outline these developments and to describe in detail crucial aspects of the experiments. Complementing the Thesis are several publications which, with some unavoidable overlap, present the same subjects from a different point of view. In particular, five papers have already been published,[7, 48, 49, 102, 103] three have been submitted for publication,[105, 106, 119] and two are under preparation.[122] In addition, a patent has been filed for the idea of utilizing atoms as ultrafast nonlinear mixers.

To summarize, it is noted that motivated by theoretical developments and predictions about the interaction of squeezed light with atoms, I was the principal student to initiated a research program to study specific examples of these effects. Unique capabilities for producing tunable squeezing in resonance with atomic transitions that were developed earlier in our labs were adapted to perform the nonclassical excitation experiment described in Chapters 5 and 6. In preparation for these experiments, several issues had to be resolved, including the construction of a MOT and the development of experimental tools to perform spectroscopy on the atoms in the MOT. Furthermore, the excited level of the particular transition that we chose to study was not well known, and for that reason a classical high precision spectroscopy experiment was performed. After all this preparatory work, we finally attempted and successfully completed the task of observing a nonclassical effect of the interaction of atoms with squeezed light. This was the deviation from quadratic form and an asymptotically linear excitation rate in the two-photon excitation of a three-level atom by the signal and idler outputs of an NDOPO. Note that to the present day this is the only instance of such an observation.

Subsequent to the above experiments, I entered a different arena of research and

studied QI in two-photon excitation by multiple fields. A proof-of-principle experiment strikingly demonstrated that atoms can act as ultrafast nonlinear mixers due to QI, which motivated me to further pursue the study of these phenomena. Most of my efforts have been concentrated in the theoretical analysis of QI for which perturbative and master equation solutions have been derived. By analyzing these solutions I have discovered several interesting phenomena which have been discussed elsewhere. Furthermore, by generalizing the particular system that was studied experimentally, I have created a database of 6900 possible transitions that can be used in similar fashion. Based on these discoveries my colleagues and I have suggested novel techniques for frequency metrology and optical communications.

In addition, combining these results with nonclassical excitation, we proposed new techniques for observing nonclassical correlations that have been up to now beyond reach due to the limitations in bandwidth in the existing detectors. Again, to demonstrate the feasibility of our suggestions, we have performed a proof-of-principle experiment, and to back our results I developed a theoretical model based on the master equation of the system.

Last but not least there has also been a significant effort to observe the interaction of squeezed light with a two-level atom in a microcavity,[2] which, however, was not covered in this Thesis. In these cavity QED experiments, the atoms behave as one-dimensional systems and the coupling of squeezing to them should be greatly simplified. Several experiments have been performed and significant theoretical work has been done in order to understand the system. The results will be published in the near future; they have already been extensively discussed in Quentin Turchette's Ph.D. Thesis. Two main accomplishments of this research are worth mentioning here. First a unique unidirectional coupling of two independent quantum systems (the mode of the OPO and the atom in the microcavity), which were physically separated by several meters from each other, was accomplished. Second observations of the interaction of squeezed light with a two-level atom have been recorded as a function of several parameters. However, the situation was somewhat analogous with the experiment described in Section 8.2, where although there have been observations

of the interaction with squeezed light, there was no direct proof that this was due to the nonclassical character of the squeezed excitation. Despite this deficiency, these experiment represents the only other instance besides the experiment of Section 5.2 that investigates the fundamental alteration of radiation processes for the interaction of squeezing with atoms.

It is my hope that the foundations established by my work will contribute to further developments and better understanding of the interaction of nonclassical states of light with atoms, and that my work on QI will open new avenues in the fields of frequency metrology and ultrafast nonlinear mixing.

Appendix A OPO Gain for the Single and Double-Sided Cavity

A crucial parameter for the OPO characterization is the gain, which is determined operationally by observing the amplification and deamplification of a small injected beam into the cavity. The characterization of our own OPO in this fashion was explained in detail in Chapter 4. Here, based on input-output relations and a coupling term between the pump and the signal and idler fields, I derive theoretical expressions for the OPO gain, in terms of the pumping parameter x (see Eq. (4.1)), for a variety of cases.

A.1 Degenerate OPO (DOPO)

We begin with the DOPO case. Figure A.1 shows a very general case of an OPO pumped by a classical field b of frequency 2ω . Here, we are only considering subthreshold OPO's for which the pump is not depleted, and since it is also non-resonant with the OPO cavity, it is shown in Fig. A.1 to go through the OPO unaltered. The fundamental mode at frequency ω inside the cavity is denoted by α and is coupled to the pump mode b by a coupling constant μ , which is due to the nonlinear properties of the crystal (assumed to be also constant). Furthermore, we consider two small coherent injected fields (denoted by a and a') at the fundamental frequency ω , which enter the OPO cavity either through the output coupler M_{out} or through the high reflector M_1 , which are characterized by losses given in terms of the linewidths γ and γ' , respectively. Finally, with this configuration, the output field is called a_{out} and will be the one we measure to determine the OPO gain. The goal here is to express a_{out} in terms of the rest of the parameters and hence derive a theoretical expression for the operationally determined gain, Eq. (4.2), as a function of the pumping pa-

parameter x . Furthermore, to model additional losses in the OPO, e.g., light induced absorption, a loss factor, called γ'' , is introduced. Note, that either, or both, of the two input coherent fields (a , a') can be turned off, and the formulas will reduce to the corresponding specific case. In particular, in our experiments $a = 0$. However, because we will only consider semiclassical fields, when both a and a' are turned off, then $a_{out} = 0$.

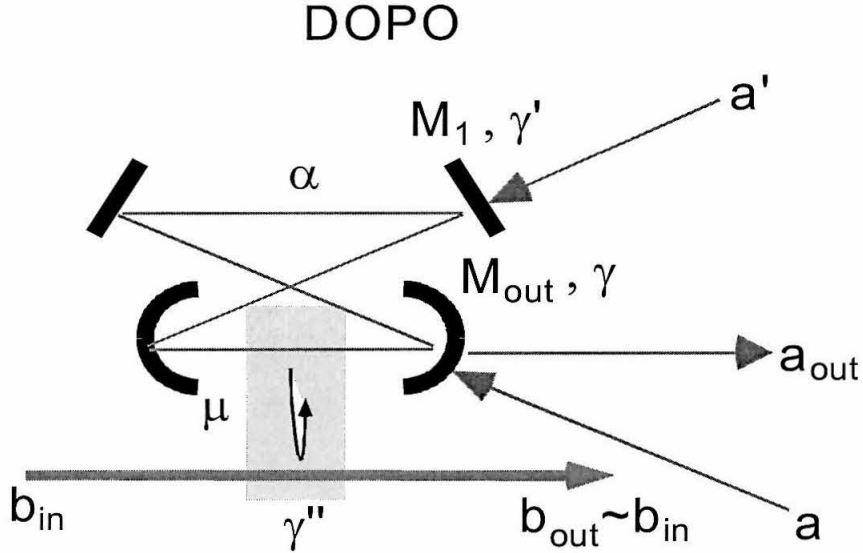


Figure A.1: DOPO configuration.

The starting point in the analysis is the following rate equation for the intracavity field α ,

$$\frac{d\alpha}{dt} = -(\gamma + \gamma' + \gamma'' + i\omega)\alpha + 2\sqrt{\mu}\alpha^\dagger b + \sqrt{2\gamma}a + \sqrt{2\gamma'}a'. \quad (\text{A.1})$$

Clearly, the first term describes the decay of the intracavity field due to the various losses (γ , γ' and γ'') while the last two terms are due to the injected fields a and a' . The second term comes from the coupling of the fundamental mode α with the pump b . [73, 74] The various fields have the following forms:

$$\alpha = \tilde{\alpha}e^{-i(\omega t + \phi_\alpha)}, \quad (\text{A.2})$$

$$a = \tilde{a}e^{-i(\omega t + \phi_a)}, \quad (\text{A.3})$$

$$a' = \tilde{a}'e^{-i(\omega t + \phi_{a'})}, \quad (\text{A.4})$$

and

$$b = \tilde{b}e^{-i(2\omega t + \phi_b)}, \quad (\text{A.5})$$

where the quantities with “ \sim ” over them are taken to be the real and slowly varying components of the fields. Hence, from Eq. (A.1) one finds that in steady state (i.e., $\frac{d\tilde{\alpha}}{dt} = 0$)

$$\tilde{\alpha} = \frac{\frac{\sqrt{2\gamma}}{(\gamma + \gamma' + \gamma'')} \tilde{a}e^{i(\phi_\alpha - \phi_a)} + \frac{\sqrt{2\gamma'}}{(\gamma + \gamma' + \gamma'')} \tilde{a}'e^{i(\phi_\alpha - \phi_{a'})}}{1 - xe^{i(2\phi_\alpha - \phi_b)}}. \quad (\text{A.6})$$

Here x is the threshold parameter given by

$$x \equiv \frac{\tilde{b}}{\tilde{b}_{th}}, \quad (\text{A.7})$$

where \tilde{b}_{th} is defined to be

$$\tilde{b}_{th} \equiv \frac{(\gamma + \gamma' + \gamma'')}{2\sqrt{\mu}}. \quad (\text{A.8})$$

Note that the above definition of x is in accord with the definition of Eq. (4.1).

Equation (A.6) has several interesting features. First, if both a and a' are non-zero then there will be interference between the two which will ultimately determine the intracavity field in addition to the nonlinear properties of the cavity. If however one of them is zero, then the phase ϕ_α will be “locked” to the phase of the injected beam and then the only phase sensitive term will be the one in the denominator. This is in fact the case we are interested in, namely when one of the two injected fields is zero. To derive the output field we use the input-output relation

$$\tilde{a}_{out} = -\tilde{a} + \sqrt{2\gamma}\tilde{\alpha} \quad (\text{A.9})$$

A.1.1 Probe Injected Through M_1

The first case we consider is when $a = 0$. Then,

$$\tilde{a}_{out} = \sqrt{2\gamma} \frac{\frac{\sqrt{2\gamma'}}{(\gamma+\gamma'+\gamma'')}\tilde{a}'}{1 - xe^{i(2\phi_{a'}-\phi_b)}}, \quad (\text{A.10})$$

which implies that the power gain (which is what we experimentally measure, see Eq. (4.2)) is equal to

$$G \equiv \left| \frac{\tilde{a}_{out}(x)}{\tilde{a}_{out}(x=0)} \right|^2 = \frac{1}{1 - 2x \cos \theta + x^2}, \quad (\text{A.11})$$

where $\theta \equiv 2\phi_{a'} - \phi_b$. Experimentally, the phase sensitive gain is characterized by G_{\pm} which gives the two extrema of G as the angle $\phi_{a'}$ is varied by a PZT at the path of the injected beam. Hence,

$$G_{\pm} = \frac{1}{(1 \mp x)^2}. \quad (\text{A.12})$$

A.1.2 Probe Injected Through M_{out}

In this case $a' = 0$, and the output field is derived to be

$$\tilde{a}_{out} = \left[-1 + \frac{2 \left(\frac{\gamma}{\gamma+\gamma'+\gamma''} \right)}{1 - xe^{i(2\phi_a-\phi_b)}} \right] \tilde{a}, \quad (\text{A.13})$$

which implies that the gain is equal to

$$G = \frac{1 + 2\frac{x}{\Gamma} \cos \theta + \frac{x^2}{\Gamma^2}}{1 - 2x \cos \theta + x^2}, \quad (\text{A.14})$$

where $\theta = 2\phi_a - \phi_b$ and $\Gamma = -1 + \frac{2\gamma}{\gamma+\gamma'+\gamma''}$. As the phase θ is scanned (e.g., by a PZT at the path of the injected beam a) then the gain is also modulated and the maximum and minimum of it can be calculated from Eq. (A.14). To compute G_{\pm} from Eq. (A.14) we note that there are two different cases, namely $\Gamma \neq 0$ and $\Gamma = 0$.

In the first case, the extrema of the gain occur at $\theta = 0$ and π and take the values

$$G_{\pm}(\Gamma \neq 0) = \left(\frac{1 \pm \frac{x}{\Gamma}}{1 \mp x} \right)^2. \quad (\text{A.15})$$

For the second case, $\Gamma = 0 \Rightarrow \gamma = \gamma' + \gamma''$, one needs to be more careful. In particular, the output field is given in this case by

$$\tilde{a}_{out} = \left(\frac{x e^{i\theta}}{1 - x e^{i\theta}} \right) \tilde{a} \quad (\text{A.16})$$

which means that when the gain is turned off, i.e., $x = 0$, then the output is equal to zero, $\tilde{a}_{out} = 0$ and hence the definition of the gain, Eq. (A.11), diverges. Furthermore, in the special case that $\gamma \gg \gamma', \gamma'', \Gamma \simeq 1$ and $G_{\pm}(\Gamma = 1) = \left(\frac{1 \pm x}{1 \mp x} \right)^2$ in accord with the formulas derived in Ref. [12].

Finally, notice that while in the case when the probe is injected through the output mirror M_{out} the additional losses in the cavity alter the gain (through Γ), when the probe is injected through the high reflector M_1 then the gain is independent of additional losses.

A.2 Non-Degenerate OPO (NDOPO)

We now turn our attention to the NDOPO. The set up we are considering is shown in Fig. A.2. The notation is similar to the one used for the DOPO with the only difference being that we now have two non-degenerate modes (signal and idler, denoted by a_1 and a_2) that are present in the cavity. In the most general case, different linewidths γ and couplings μ can be present, and for this reason all parameters have been duplicated with the subscripts 1 and 2 to distinguish between the characteristics for the signal and idler modes. Finally, in this very general representation of the NDOPO, a maximum of four injected inputs are possible, a_1, a_2, a'_1 and a'_2 ; see Fig. A.2.

The starting point of the analysis is again the rate equations for the intracavity

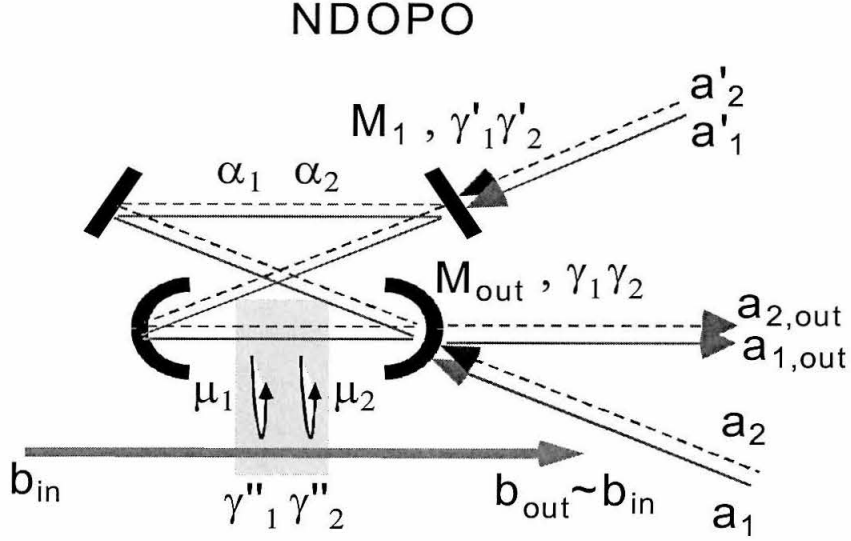


Figure A.2: NDOPO configuration.

fields α_1 and α_2 , which are given in analogy with Eq. (A.1) by

$$\frac{d\alpha_1}{dt} = -(\gamma_1 + \gamma'_1 + \gamma''_1 + i\omega_1)\alpha_1 + 2\sqrt{\mu_1}\alpha_2^*b + \sqrt{2\gamma_1}a_1 + \sqrt{2\gamma'_1}a'_1, \quad (\text{A.17})$$

and

$$\frac{d\alpha_2}{dt} = -(\gamma_2 + \gamma'_2 + \gamma''_2 + i\omega_2)\alpha_2 + 2\sqrt{\mu_2}\alpha_1^*b + \sqrt{2\gamma_2}a_2 + \sqrt{2\gamma'_2}a'_2. \quad (\text{A.18})$$

In generalizing Eq. (A.1) to Eqs. (A.17) and (A.18), the Hermitian conjugates of the α_1 and α_2 fields were taken to be $\alpha_1^\dagger = a_2^*$ and $\alpha_2^\dagger = a_1^*$. Following similar steps as before, we solve for the slowly varying components $\tilde{\alpha}_1$ and $\tilde{\alpha}_2$ of the intracavity fields in the steady state case. First by simplifying Eqs. (A.17) and (A.18), we obtain that

$$\tilde{\alpha}_1 - (x_1 e^{i\theta}) \tilde{\alpha}_2^* = \frac{\sqrt{2\gamma_1} e^{i(\phi_{\alpha_1} - \phi_{a_1})}}{(\gamma_1 + \gamma'_1 + \gamma''_1)} \tilde{a}_1 + \frac{\sqrt{2\gamma'_1} e^{i(\phi_{\alpha_1} - \phi_{a'_1})}}{(\gamma_1 + \gamma'_1 + \gamma''_1)} \tilde{a}'_1, \quad (\text{A.19})$$

and

$$\tilde{\alpha}_2 - (x_2 e^{i\theta}) \tilde{\alpha}_1^* = \frac{\sqrt{2\gamma_2} e^{i(\phi_{\alpha_2} - \phi_{a_2})}}{(\gamma_2 + \gamma'_2 + \gamma''_2)} \tilde{a}_2 + \frac{\sqrt{2\gamma'_2} e^{i(\phi_{\alpha_2} - \phi_{a'_2})}}{(\gamma_2 + \gamma'_2 + \gamma''_2)} \tilde{a}'_2, \quad (\text{A.20})$$

where $x_i \equiv \frac{2\sqrt{\mu_i}}{(\gamma_i + \gamma'_i + \gamma''_i)} \tilde{b}$, $i = 1, 2$ and $\theta \equiv \phi_{\alpha_1} + \phi_{\alpha_2} - \phi_b$. Hence, $\tilde{\alpha}_1$ and $\tilde{\alpha}_2$ are equal to

$$\tilde{\alpha}_1 = \frac{1}{(1 - x_1 x_2)} \left[\frac{\sqrt{2\gamma_1} e^{i(\phi_{\alpha_1} - \phi_{a_1})}}{(\gamma_1 + \gamma'_1 + \gamma''_1)} \tilde{a}_1 + \frac{\sqrt{2\gamma'_1} e^{i(\phi_{\alpha_1} - \phi_{a'_1})}}{(\gamma_1 + \gamma'_1 + \gamma''_1)} \tilde{a}'_1 \right] + \frac{x_1 e^{i\theta}}{(1 - x_1 x_2)} \left[\frac{\sqrt{2\gamma_2} e^{-i(\phi_{\alpha_2} - \phi_{a_2})}}{(\gamma_2 + \gamma'_2 + \gamma''_2)} \tilde{a}_2 + \frac{\sqrt{2\gamma'_2} e^{-i(\phi_{\alpha_2} - \phi_{a'_2})}}{(\gamma_2 + \gamma'_2 + \gamma''_2)} \tilde{a}'_2 \right], \quad (\text{A.21})$$

and

$$\tilde{\alpha}_2 = \frac{1}{(1 - x_1 x_2)} \left[\frac{\sqrt{2\gamma_2} e^{i(\phi_{\alpha_2} - \phi_{a_2})}}{(\gamma_2 + \gamma'_2 + \gamma''_2)} \tilde{a}_2 + \frac{\sqrt{2\gamma'_2} e^{i(\phi_{\alpha_2} - \phi_{a'_2})}}{(\gamma_2 + \gamma'_2 + \gamma''_2)} \tilde{a}'_2 \right] + \frac{x_2 e^{i\theta}}{(1 - x_1 x_2)} \left[\frac{\sqrt{2\gamma_1} e^{-i(\phi_{\alpha_1} - \phi_{a_1})}}{(\gamma_1 + \gamma'_1 + \gamma''_1)} \tilde{a}_1 + \frac{\sqrt{2\gamma'_1} e^{-i(\phi_{\alpha_1} - \phi_{a'_1})}}{(\gamma_1 + \gamma'_1 + \gamma''_1)} \tilde{a}'_1 \right]. \quad (\text{A.22})$$

These expressions, along with the input-output relations

$$\tilde{a}_{1,out} = -\tilde{a}_1 + \sqrt{2\gamma_1} \tilde{\alpha}_1, \quad (\text{A.23})$$

and

$$\tilde{a}_{2,out} = -\tilde{a}_2 + \sqrt{2\gamma_2} \tilde{\alpha}_2, \quad (\text{A.24})$$

give the signal and idler output fields. In an experiment to measure the gain of the OPO, one will usually inject only a single beam into the cavity. Therefore, we assume that $a_2 = a'_2 = 0$ and consider the two cases as before, where either $\{a_1 = 0, a'_1 \neq 0\}$ or $\{a_1 \neq 0, a'_1 = 0\}$.

A.2.1 Probe Injected Through M_1

In this case ($a_1 = 0$, $a'_1 \neq 0$, $a_2 = a'_2 = 0$) the output fields are given by

$$\tilde{a}_{1,out} = \frac{1}{(1 - x_1 x_2)} \frac{2\sqrt{\gamma_1 \gamma'_1}}{(\gamma_1 + \gamma'_1 + \gamma''_1)} \tilde{a}'_1, \quad (\text{A.25})$$

and

$$\tilde{a}_{2,out} = \frac{x_2}{(1 - x_1 x_2)} e^{i\theta} \frac{2\sqrt{\gamma_2 \gamma'_1}}{(\gamma_1 + \gamma'_1 + \gamma''_1)} \tilde{a}'_1. \quad (\text{A.26})$$

The gain of the OPO is then defined in accord with Eq. (4.13) and (4.15) to be

$$G_1 \equiv \left| \frac{\tilde{a}_{1,out}(x_1, x_2)}{\tilde{a}_{1,out}(b=0)} \right|^2 = \frac{1}{(1 - x_1 x_2)^2} \quad (\text{A.27})$$

and

$$G_2 \equiv \left| \frac{\tilde{a}_{2,out}(x_1, x_2)}{\tilde{a}_{1,out}(b=0)} \right|^2 = \frac{\gamma_2}{\gamma_1} \left(\frac{x_2}{1 - x_1 x_2} \right)^2 \quad (\text{A.28})$$

Note that $b = 0$ is equivalent to setting $x_1 = 0$ and $x_2 = 0$. Finally, note that for the special case when $\gamma_1 = \gamma_2$ and $x_1 = x_2$, the relation $G_2 = G_1 \left(1 - \frac{1}{\sqrt{G_1}}\right)$ holds.

A.2.2 Probe Injected Through M_{out}

The last case to consider is for $a_1 \neq 0$, $a'_1 = 0$ and as before $a_2 = a'_2 = 0$. Here the output fields are

$$\tilde{a}_{1,out} = \left[-1 + \frac{1}{(1 - x_1 x_2)} \frac{2\gamma_1}{(\gamma_1 + \gamma'_1 + \gamma''_1)} \right] \tilde{a}_1, \quad (\text{A.29})$$

and

$$\tilde{a}_{2,out} = \frac{x_2 e^{i\theta}}{(1 - x_1 x_2)} \frac{2\sqrt{\gamma_1 \gamma_2}}{(\gamma_1 + \gamma'_1 + \gamma''_1)} \tilde{a}_1. \quad (\text{A.30})$$

Then the gain for the signal and idler fields is equal to

$$G_1 \equiv \left| \frac{\tilde{a}_{1,out}(x_1, x_2)}{\tilde{a}_{1,out}(b=0)} \right|^2 = \left[\frac{1 - \frac{2\gamma_1}{(\gamma_1 + \gamma'_1 + \gamma''_1)} \frac{1}{(1 - x_1 x_2)}}{1 - \frac{2\gamma_1}{(\gamma_1 + \gamma'_1 + \gamma''_1)}} \right]^2, \quad (\text{A.31})$$

and

$$G_2 \equiv \left| \frac{\tilde{a}_{2,out}(x_1, x_2)}{\tilde{a}_{1,out}(b=0)} \right|^2 = \left[\frac{\frac{2\sqrt{\gamma_1\gamma_2}}{(\gamma_1+\gamma'_1+\gamma''_1)} x_2}{1 - \frac{2\gamma_1}{(\gamma_1+\gamma'_1+\gamma''_1)} (1-x_1x_2)} \right]^2. \quad (\text{A.32})$$

In the special case when $\gamma_1 \gg \gamma'_1, \gamma''_1$ (e.g., in our experiment), these expressions simplify to

$$G_1 = \left(\frac{1+x_1x_2}{1-x_1x_2} \right)^2, \quad (\text{A.33})$$

and

$$G_2 = \frac{\gamma_2}{\gamma_1} \frac{4x_2^2}{(1-x_1x_2)^2} \quad (\text{A.34})$$

which if $\gamma_2 = \gamma_1$ and $x_1 = x_2$ implies further that $G_1 - G_2 = 1$, in accord with the formulas derived from Ref. [12].

A.3 Summary

In this appendix we have studied the properties of the amplified or deamplified coherent output from a DOPO and NDOPO when a small coherent injected beam enters the cavity either through the output coupler or one of the high-reflectors. Analytic expressions for the gain have been derived in each case that correspond to what one would normally measure in an experiment. The goal throughout this exercise is to relate the experimentally measured quantity G with the fundamental parameter x for the OPO from which the squeezed output properties can be inferred.

Appendix B Nonclassical Two-Photon Experiment: Data Plots, Fits and Fit Parameters

The goal in this appendix is to show details of our data for the nonclassical excitation experiments discussed in Chapters 5 and 6. For each of the experiments we show three graphs. In the first graph, the data points R_1 vs. R_2 are plotted on a log-log scale along with the best quadratic plus linear fit (solid lines) of the form $R_2 = f_{Q+L}(R_1) = \beta_6 R_1^2 + \beta_7 R_1$ (see Eq. (6.6)), and the best quadratic fit (dashed lines) of the form $R_2 = f_Q(R_1) = \beta_1 R_1^2$ (see Eq. (6.3)). In the two bottom panels we indicate the residuals of the data to these two fits. The i^{th} point of the quadratic plus linear residual is defined by

$$r_{Q+L}^{(i)} \pm e_{r_{Q+L}}^{(i)} \equiv \left[\frac{R_2^{(i)}}{f_{Q+L}(R_1^{(i)})} - 1 \right] \pm \left[\frac{e_{R_2}^{(i)}}{f_{Q+L}(R_1^{(i)})} - 1 \right], \quad (\text{B.1})$$

and similarly the i^{th} point of the quadratic residual is given by

$$r_Q^{(i)} \pm e_{r_Q}^{(i)} \equiv \left[\frac{R_2^{(i)}}{f_Q(R_1^{(i)})} - 1 \right] \pm \left[\frac{e_{R_2}^{(i)}}{f_Q(R_1^{(i)})} - 1 \right], \quad (\text{B.2})$$

where $\{R_1^{(i)}, R_2^{(i)}\}$ is the i^{th} data point of the particular experiment. The error bars $e_{r_{Q+L}}$ and e_{r_Q} of the residuals are computed from the experimental uncertainties e_{R_2} of R_2 as indicated in the above expressions.

Finally, for completeness, we show for each of the experiments the fit parameters β_1, \dots, β_7 for the f_Q , f_{Q+C} , f_P and f_{Q+L} model functions; see Eqs. (6.3)-(6.6).

B.1 Exp. 11-17-94 (Nonclassical Excitation)

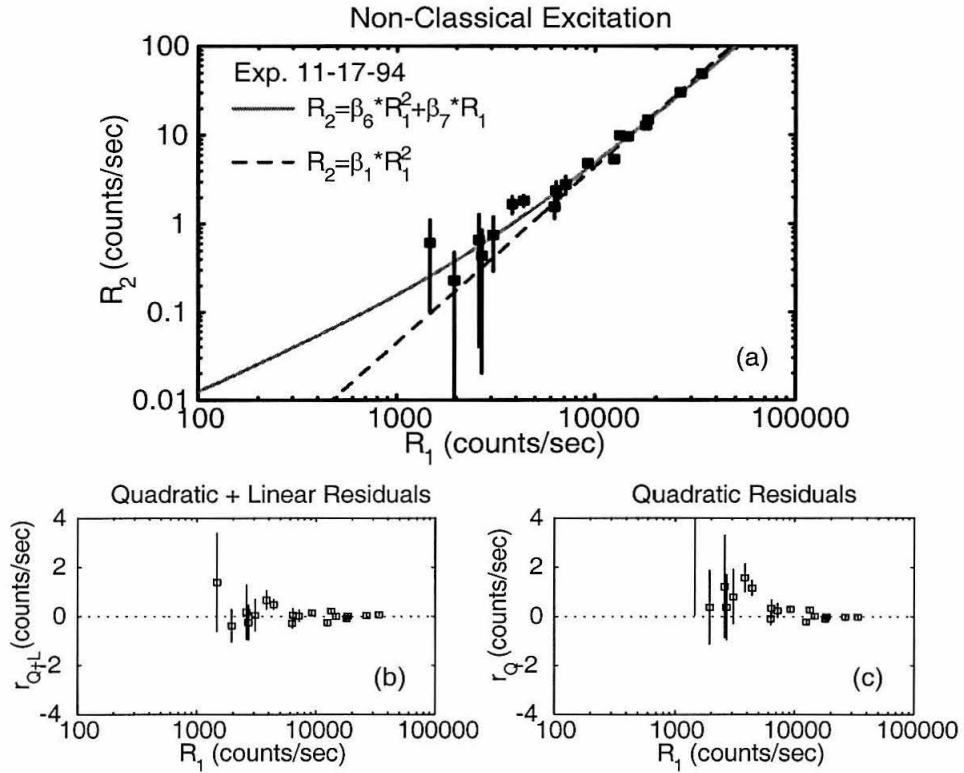


Figure B.1: a) R_2 vs. R_1 data from the 11-17-94 experiment. The solid line is the best linear plus quadratic fit and the dashed line the best quadratic fit. b) Quadratic plus linear residual, define in Eq. (B.1) c) Quadratic residual, defined in Eq. (B.2)

- $\beta_1 = 4.42 \times 10^{-8}$
- $\beta_2 = 4.21 \times 10^{-8}$
- $\beta_3 = 0.46$
- $\beta_4 = 1.98 \times 10^{-7}$
- $\beta_5 = 1.85$
- $\beta_6 = 3.71 \times 10^{-8}$
- $\beta_7 = 1.20 \times 10^{-4}$

B.2 Exp. 11-29-94 (Nonclassical Excitation)

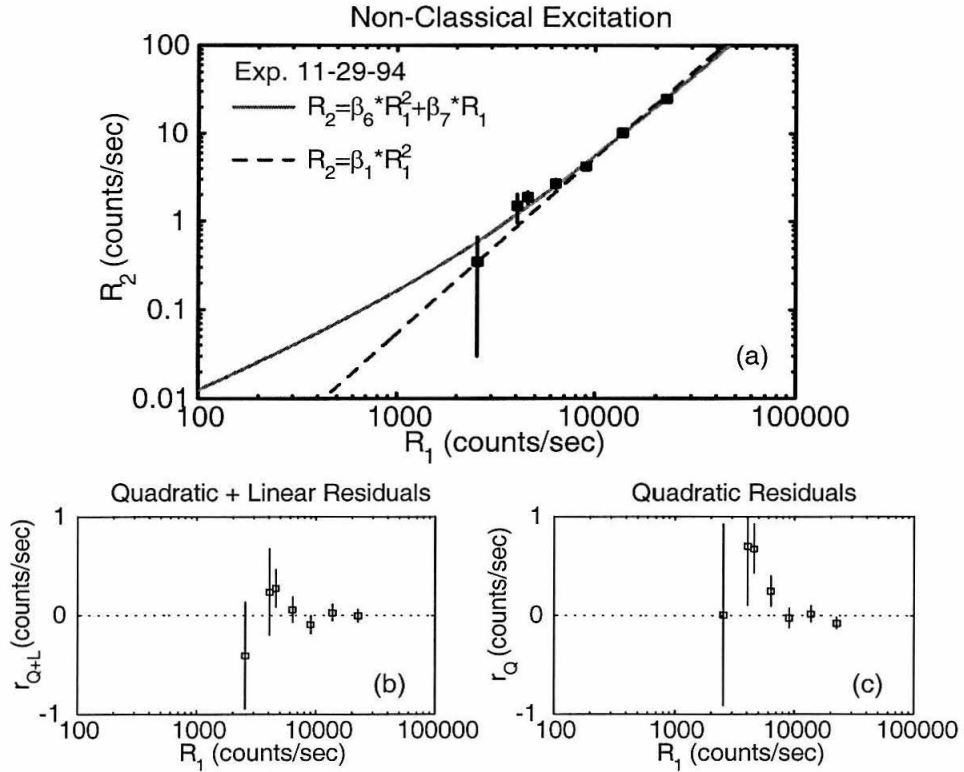


Figure B.2: a) R_2 vs. R_1 data from the 11-29-94 experiment. The solid line is the best linear plus quadratic fit and the dashed line the best quadratic fit. b) Quadratic plus linear residual, define in Eq. (B.1) c) Quadratic residual, defined in Eq. (B.2)

- $\beta_1 = 5.38 \times 10^{-8}$
- $\beta_2 = 5.01 \times 10^{-8}$
- $\beta_3 = 0.47$
- $\beta_4 = 5.24 \times 10^{-7}$
- $\beta_5 = 1.76$
- $\beta_6 = 4.46 \times 10^{-8}$
- $\beta_7 = 1.19 \times 10^{-4}$

B.3 Exp. 12-06-94 (Nonclassical Excitation)

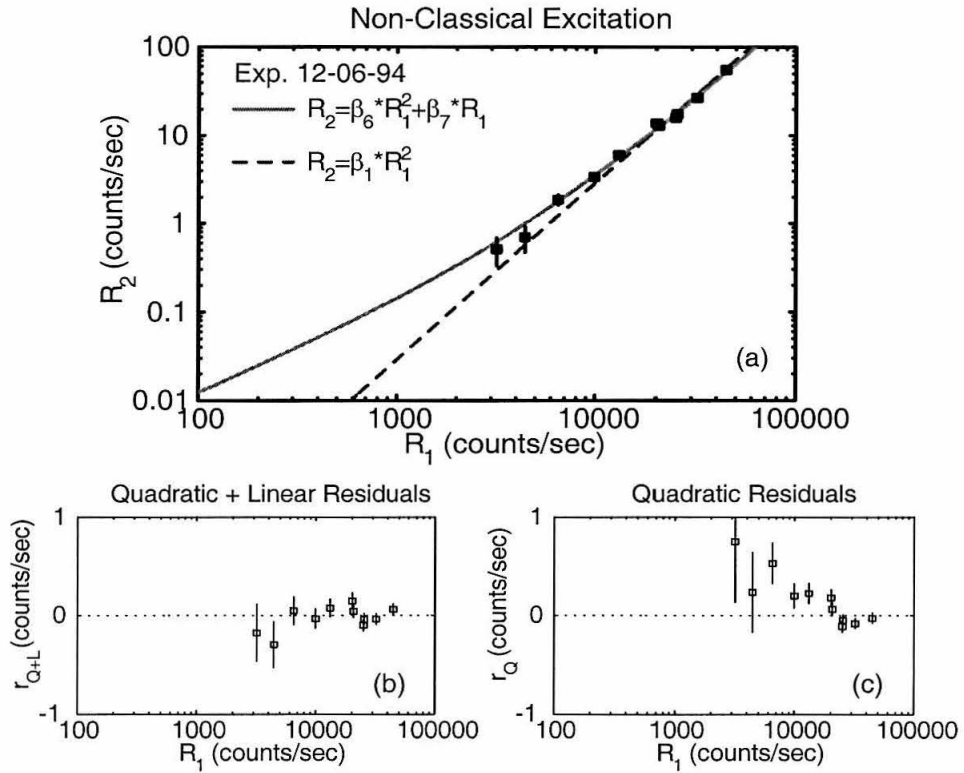


Figure B.3: a) R_2 vs. R_1 data from the 12-06-94 experiment. The solid line is the best linear plus quadratic fit and the dashed line the best quadratic fit. b) Quadratic plus linear residual, define in Eq. (B.1) c) Quadratic residual, defined in Eq. (B.2)

- $\beta_1 = 2.88 \times 10^{-8}$
- $\beta_2 = 2.78 \times 10^{-8}$
- $\beta_3 = 0.39$
- $\beta_4 = 2.70 \times 10^{-7}$
- $\beta_5 = 1.78$
- $\beta_6 = 2.37 \times 10^{-8}$
- $\beta_7 = 1.20 \times 10^{-4}$

B.4 Exp. 12-20-94a (Nonclassical Excitation)

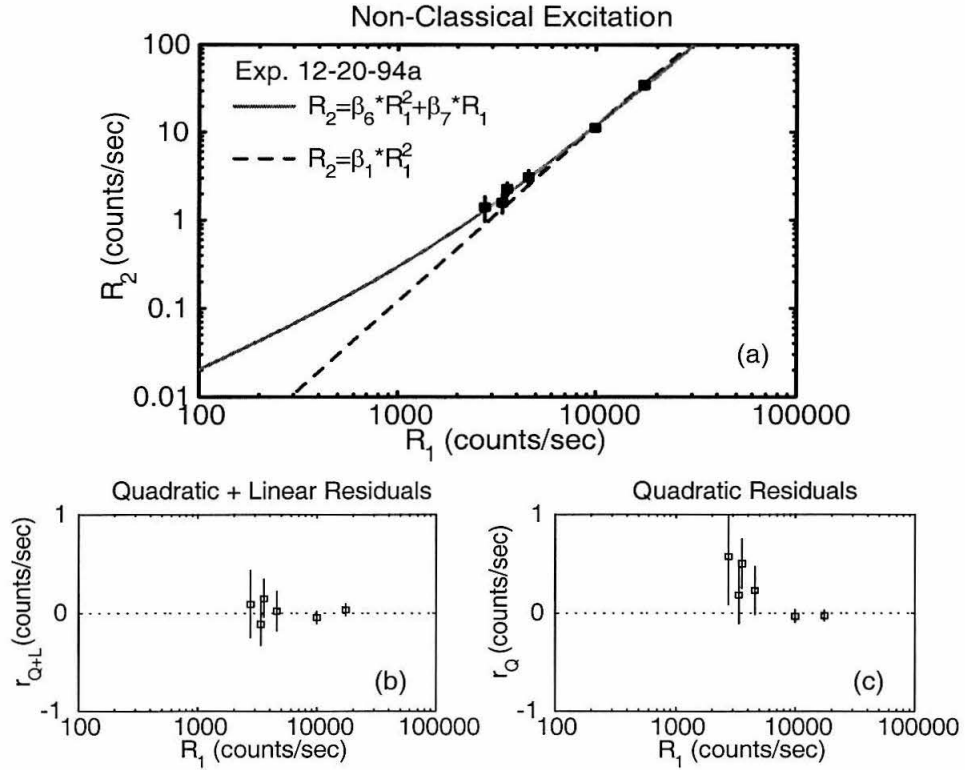


Figure B.4: a) R_2 vs. R_1 data from the 12-20-94a experiment. The solid line is the best linear plus quadratic fit and the dashed line the best quadratic fit. b) Quadratic plus linear residual, define in Eq. (B.1) c) Quadratic residual, defined in Eq. (B.2)

- $\beta_1 = 1.19 \times 10^{-7}$
- $\beta_2 = 1.16 \times 10^{-7}$
- $\beta_3 = 0.24$
- $\beta_4 = 6.64 \times 10^{-7}$
- $\beta_5 = 1.82$
- $\beta_6 = 1.01 \times 10^{-7}$
- $\beta_7 = 1.94 \times 10^{-4}$

B.5 Exp. 12-20-94b (Nonclassical Excitation)

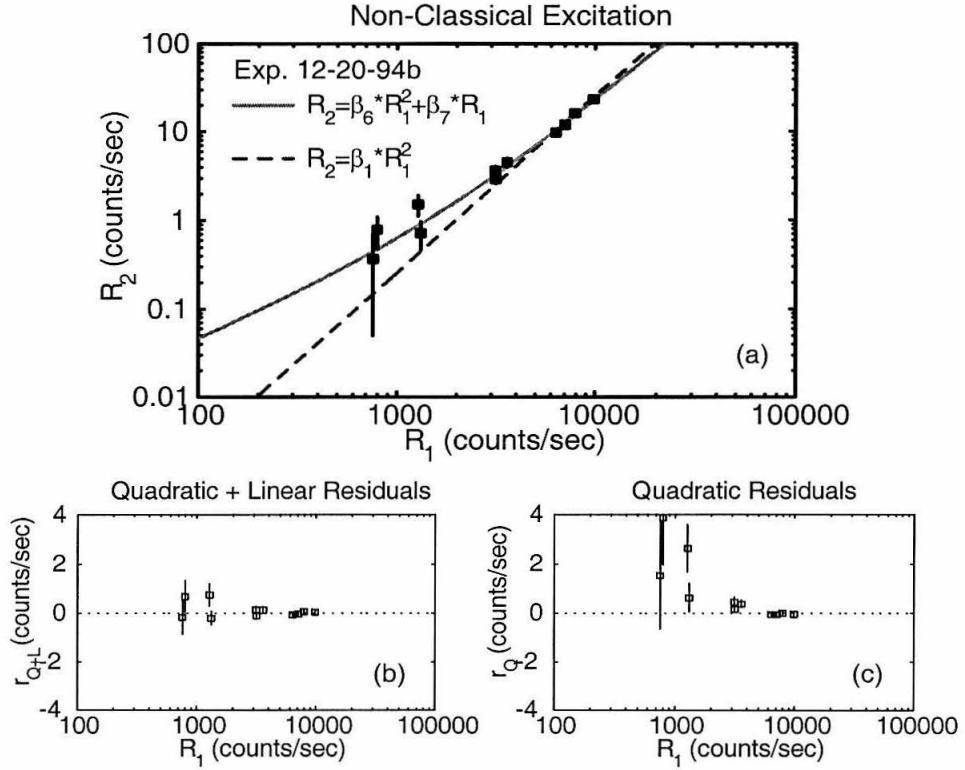


Figure B.5: a) R_2 vs. R_1 data from the 12-20-94b experiment. The solid line is the best linear plus quadratic fit and the dashed line the best quadratic fit. b) Quadratic plus linear residual, define in Eq. (B.1) c) Quadratic residual, defined in Eq. (B.2)

- $\beta_1 = 2.56 \times 10^{-7}$
- $\beta_2 = 2.45 \times 10^{-7}$
- $\beta_3 = 0.40$
- $\beta_4 = 4.81 \times 10^{-7}$
- $\beta_5 = 1.67$
- $\beta_6 = 1.88 \times 10^{-7}$
- $\beta_7 = 4.46 \times 10^{-4}$

B.6 Exp. 12-22-94 (Coherent Excitation)

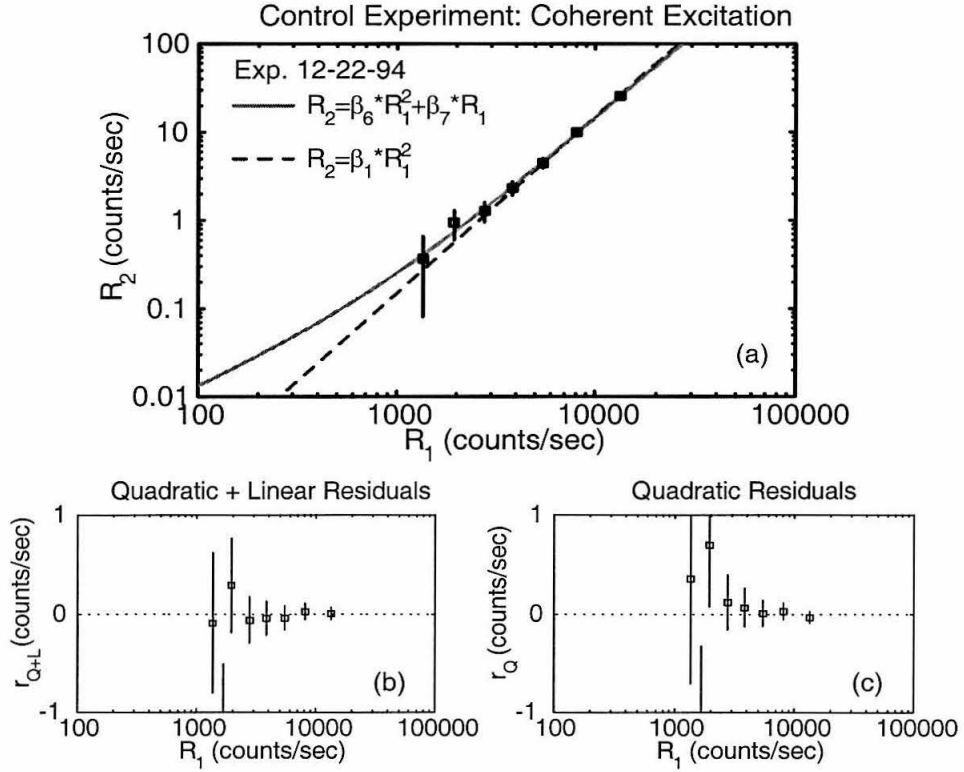


Figure B.6: a) R_2 vs. R_1 data from the 12-22-94 experiment. The solid line is the best linear plus quadratic fit and the dashed line the best quadratic fit. b) Quadratic plus linear residual, define in Eq. (B.1) c) Quadratic residual, defined in Eq. (B.2)

- $\beta_1 = 1.49 \times 10^{-7}$
- $\beta_2 = 1.46 \times 10^{-7}$
- $\beta_3 = 0.11$
- $\beta_4 = 3.18 \times 10^{-7}$
- $\beta_5 = 1.92$
- $\beta_6 = 1.34 \times 10^{-7}$
- $\beta_7 = 1.19 \times 10^{-4}$

B.7 Exp. 01-12-95 (Coherent Excitation)

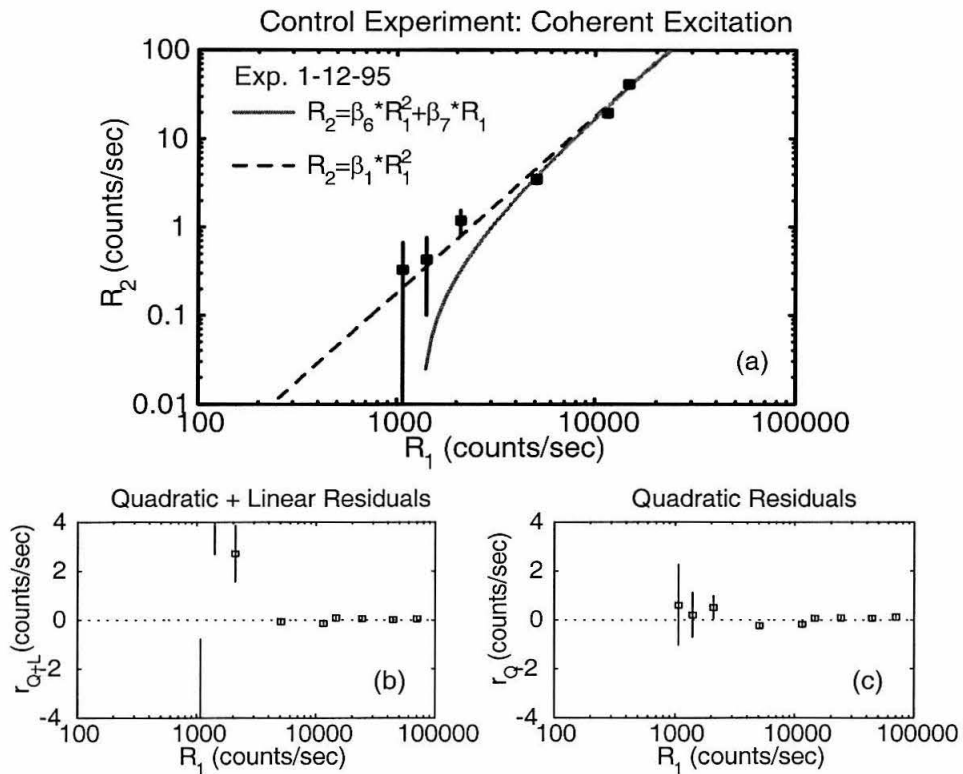


Figure B.7: a) R_2 vs. R_1 data from the 01-12-95 experiment. The solid line is the best linear plus quadratic fit and the dashed line the best quadratic fit. b) Quadratic plus linear residual, define in Eq. (B.1) c) Quadratic residual, defined in Eq. (B.2)

- $\beta_1 = 1.80 \times 10^{-7}$
- $\beta_2 = 1.81 \times 10^{-7}$
- $\beta_3 = -0.12$
- $\beta_4 = 4.99 \times 10^{-8}$
- $\beta_5 = 2.13$
- $\beta_6 = 1.96 \times 10^{-7}$
- $\beta_7 = -2.57 \times 10^{-4}$

Appendix C Results from Numerical Integration of the Master Equation for the Nonclassical Two-Photon Excitation Experiment

In order to better model the nonclassical excitation experiment described in Ch. 5 and Ch. 6, A. S. Parkins has numerically integrated the master equation of the system taking into account the finite bandwidth of squeezing, which was not included in Ficek and Drummond's work.[44, 45] The results he has derived and details of relating his parameters to our experiment are presented in this Appendix. Note that numerical results shown here are from private communication between A. S. Parkins and the Caltech group that conducted the experiment, while the rest of the calculations are due to the present author.

C.1 Master Equation

The master equation that describes the interaction of the signal (a) and idler (b) modes of the NDOPO with a three-level atom is a special case of what was discussed in Ref. [81]. In particular, A. S. Parkins has considered the following master equation for the density matrix ρ of the three-level atom:

$$\begin{aligned} \frac{\partial \rho}{\partial t} = & \frac{1}{2} [\varepsilon a^\dagger b^\dagger - \varepsilon^* ab, \rho] \\ & + \frac{1}{2} \kappa_a (2a\rho a^\dagger - a^\dagger a\rho - \rho a^\dagger a) + \frac{1}{2} \kappa_b (2b\rho b^\dagger - b^\dagger b\rho - \rho b^\dagger b) \\ & - \sqrt{\eta_a \kappa_a \gamma_{21}} \{ [\sigma_{12}^+, a\rho] + H.c \} - \sqrt{\eta_b \kappa_b \gamma_{32}} \{ [\sigma_{23}^+, b\rho] + H.c \} \\ & + \frac{1}{2} \gamma_{21} (2\sigma_{12}^- \rho \sigma_{12}^+ - \sigma_{12}^+ \sigma_{12}^- \rho - \rho \sigma_{12}^+ \sigma_{12}^-) \end{aligned}$$

$$+\frac{1}{2}\gamma_{32} (2\sigma_{23}^- \rho \sigma_{23}^+ - \sigma_{23}^+ \sigma_{23}^- \rho - \rho \sigma_{23}^+ \sigma_{23}^-) \quad (\text{C.1})$$

Here, $\sigma_{ij}^- = (\sigma_{ij}^+)^\dagger \equiv |i\rangle \langle j|$ are atomic raising and lowering operators. The linewidths γ_{21} and γ_{32} are the FWHM of the atomic linewidths of the intermediate and upper state of the three-level atom, respectively, while κ_a and κ_b are the FWHM linewidths of the ‘‘cold’’ OPO cavity for the signal and idler modes. Note, that implicit in equation Eq. (C.1) is that the signal mode a drives the $|1\rangle \rightarrow |2\rangle$ transition, while the idler mode b drives the $|2\rangle \rightarrow |3\rangle$ transition. The parameters η_a and η_b ($\eta_{a,b} \leq 1$) are coupling efficiencies between the OPO output modes a and b and the three-level atom. Finally the parameter ε is the pump strength with which the OPO is driven.

C.2 Parameters and Notation

Expressed in terms of ε , the parameters N and M that characterize the squeezing are given by

$$N = \langle \hat{a}^\dagger(\omega_a) \hat{a}(\omega_a) \rangle = \langle \hat{b}^\dagger(\omega_b) \hat{b}(\omega_b) \rangle = \frac{\kappa_a \kappa_b \varepsilon^2}{\left(\frac{1}{4}\kappa_a \kappa_b - \varepsilon^2\right)^2}, \quad (\text{C.2})$$

and

$$M = \langle \hat{a}(\omega_a) \hat{b}(\omega_b) \rangle = \frac{\varepsilon \sqrt{\kappa_a \kappa_b} \left(\frac{1}{4}\kappa_a \kappa_b + \varepsilon^2\right)}{\left(\frac{1}{4}\kappa_a \kappa_b - \varepsilon^2\right)^2}. \quad (\text{C.3})$$

These expressions can be rewritten in terms of the pumping parameters $x_1 = \frac{\varepsilon}{\frac{1}{2}\kappa_a}$ and $x_2 = \frac{\varepsilon}{\frac{1}{2}\kappa_b}$ (see Appendix A) to give the more familiar expressions

$$N = \frac{4x_1 x_2}{(1 - x_1 x_2)^2} = \left(\frac{2x}{1 - x^2}\right)^2, \quad (\text{C.4})$$

and

$$M = \frac{2\sqrt{x_1 x_2} (1 + x_1 x_2)}{(1 - x_1 x_2)^2} = \frac{2x (1 + x^2)}{(1 - x^2)^2}, \quad (\text{C.5})$$

where the last equality in Eqs. (C.4) and (C.5) come from the simplifying assumption that $\kappa_a = \kappa_b = \kappa$ and hence $x_1 = x_2 = x$. Clearly, as expected for minimum

uncertainty states, $M^2 = N(N + 1)$. Furthermore, the expressions with $x_1 = x_2 = x$ are identical to those derived in Ref. [12]; see Eq. (56) and (57) therein.¹

Lastly, we must express the output photon flux and output intensity from the OPO in terms of the pumping parameters x_1 and x_2 . These are given by

$$f_i = \kappa_i n_i, \quad (\text{C.6})$$

and

$$I_i = \hbar\omega_i f_i, \quad (\text{C.7})$$

for $i = a, b$, where f_i is the photon number flux of the signal and idler modes ($i = a$ and $i = b$, respectively), I_i is the intensity and n_i is the intracavity photon number. Note that $n_i \neq N$, because one must integrate over the bandwidth of the OPO in order to obtain the total photon number. In particular,

$$n_a = \langle a^\dagger(t) a(t) \rangle = \frac{1}{2\pi} \int d\omega' e^{i(\omega - \omega')} \langle \widehat{a}^\dagger(\omega_a) \widehat{a}(\omega'_a) \rangle \quad (\text{C.8})$$

and similarly for the idler mode b ; see Eq. (5) in Ref. [12]. Generalization of the results shown in Ref. [12] (Eq. (23)) leads to the photon flux for the signal,[79] which is given by

$$f_a = \kappa_a n_a = \kappa_a \frac{\frac{\kappa_b}{\kappa_a + \kappa_b} \varepsilon^2}{\frac{1}{4} \kappa_a \kappa_b - \varepsilon^2} = \frac{\kappa_a \kappa_b}{\kappa_a + \kappa_b} \frac{x_1 x_2}{(1 - x_1 x_2)}, \quad (\text{C.9})$$

and similarly the flux of the idler field,[79] which is given by

$$f_b = \kappa_b n_b = \kappa_b \frac{\frac{\kappa_a}{\kappa_a + \kappa_b} \varepsilon^2}{\frac{1}{4} \kappa_a \kappa_b - \varepsilon^2} = \frac{\kappa_a \kappa_b}{\kappa_a + \kappa_b} \frac{x_1 x_2}{(1 - x_1 x_2)}. \quad (\text{C.10})$$

¹Combining the expression for N given in Eq. (C.4) with the expression for the operationally determined gain G_s (Eq. (A.27)), it is easy to see that

$$G_s = \frac{1}{4} \left(\sqrt{N + 1} + 1 \right)^2.$$

Hence,

$$n_a = \frac{\kappa_b}{\kappa_a + \kappa_b} \frac{x_1 x_2}{(1 - x_1 x_2)} = \frac{1}{2} \frac{x^2}{1 - x^2}, \quad (\text{C.11})$$

and

$$n_b = \frac{\kappa_a}{\kappa_a + \kappa_b} \frac{x_1 x_2}{(1 - x_1 x_2)} = \frac{1}{2} \frac{x^2}{1 - x^2}, \quad (\text{C.12})$$

where the last equality in Eqs. (C.11) and (C.12) holds for the special case where $\kappa_a = \kappa_b = \kappa$.²

| ε | $\rho_{33} (\times 10^{-8})$ | ε | $\rho_{33} (\times 10^{-8})$ | ε | $\rho_{33} (\times 10^{-8})$ |
|---------------|------------------------------|---------------|------------------------------|---------------|------------------------------|
| 0.10 | 0.0337 | 0.75 | 2.340 | 1.80 | 34.969 |
| 0.15 | 0.0762 | 0.80 | 2.741 | 1.90 | 44.307 |
| 0.20 | 0.1364 | 0.85 | 3.190 | 2.00 | 56.229 |
| 0.25 | 0.2149 | 0.90 | 3.695 | 2.10 | 71.557 |
| 0.30 | 0.3128 | 0.95 | 4.259 | 2.20 | 91.373 |
| 0.35 | 0.4312 | 1.00 | 4.891 | 2.30 | 117.206 |
| 0.40 | 0.5714 | 1.10 | 6.388 | 2.40 | 151.182 |
| 0.45 | 0.7350 | 1.20 | 8.259 | 2.50 | 196.316 |
| 0.50 | 0.9241 | 1.30 | 10.599 | 2.60 | 257.167 |
| 0.55 | 1.1408 | 1.40 | 13.526 | 2.70 | 339.970 |
| 0.60 | 1.3876 | 1.50 | 17.196 | 2.80 | 454.404 |
| 0.65 | 1.6675 | 1.60 | 21.808 | 2.90 | 614.895 |
| 0.70 | 1.9838 | 1.70 | 27.619 | | |

Table C.1: Data from numerical integration of the master equation appropriate for the nonclassical excitation experiment of Ch. 4 and 5. (From private communication with A. S. Parkins, Feb. 1995).

C.3 Results

The integration of the master equation described in the previous section was carried out for the following set of parameters, corresponding to our experiment:

- $\kappa_a = 7.3 \text{ MHz}$ and $\kappa_b = 8.6 \text{ MHz}$,

²It is clear from this discussion that the OPO output intensities of the signal and idler beams are not exactly the same. In particular, the ratio of the two is given by

$$\frac{I_a}{I_b} = \frac{\lambda_b}{\lambda_a}.$$

For our experiment $\lambda_a \simeq 852 \text{ nm}$ and $\lambda_b \simeq 917 \text{ nm}$, hence $I_{852} \approx 1.08 I_{917}$.

- $\gamma_{21} = 5.0 \text{ MHz}$ and $\gamma_{32} = 3.2 \text{ MHz}$,
- $\eta_a = \eta_b = 0.0005$ ($\eta = \frac{\Omega}{4\pi} = \frac{1}{2} (1 - \cos \frac{\theta}{2})$, where Ω is the solid angle covered by the squeezing; θ is the focusing angle which in our case is $\theta \approx 5.6^\circ$),
- $\delta_{12} = \delta_{23} = 0$ (detunings of the a and b fields from the atomic transition frequencies).

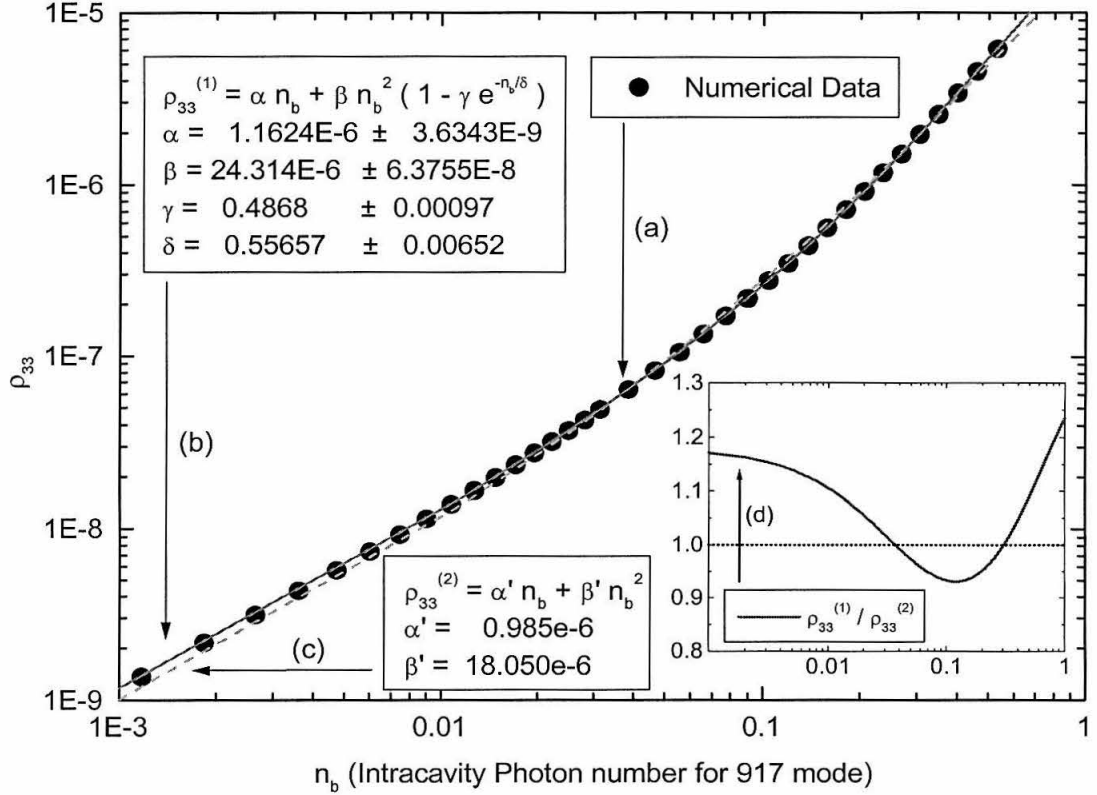


Figure C.1: a) Circles: Excited state population ρ_{33} as a function of the intracavity photon number of the idler mode n_b from numerical integration of the master equation by A. S. Parkins. b) Solid line: “Phenomenological” fit to the numerical data of the form $\rho_{33}^{(1)} = \alpha n_b + \beta n_b^2 (1 - \gamma e^{-n_b/\delta})$. c) Dashed line: Best linear plus quadratic fit to the numerical data of the form $\rho_{33}^{(2)} = \alpha' n_b + \beta' n_b^2$. d) Insert: Ratio of the two fits shown in (b) and (c), $\frac{\rho_{33}^{(1)}}{\rho_{33}^{(2)}}$.

The results are shown in Table C.1, where the values of the excited state population ρ_{33} are tabulated as a function of the strength of the pumping field ε . By converting the values of ε to intracavity photon numbers of the idler beam, $n_b = n_{917}$ as given in Eq. (C.12), we plot in Fig. C.1 the excited state population ρ_{33} as a function of n_b . To obtain an analytic expression for the full theory, we fit to the numerical data a “phenomenological” function of the form

$$\rho_{33}^{(1)} = \alpha n_b + \beta n_b^2 \left(1 - \gamma e^{-\frac{n_b}{\delta}}\right), \quad (\text{C.13})$$

which is approximately a linear plus quadratic function with a correction that enters via the γ and δ terms. Alternatively, the numerical data may also be fitted to a purely linear plus quadratic function of the form

$$\rho_{33}^{(2)} = \alpha' n_b + \beta' n_b^2, \quad (\text{C.14})$$

which however, does not describe the data as well as the $\rho_{33}^{(1)}$ model of Eq. (C.13). The difference between the two fits of Eqs. (C.13 and (C.14) is depicted in the insert of Fig. C.1, where the ratio of the two is plotted as a function of n_b .

C.4 “Knee Position”

The “knee” position is defined to be the point at which the excited state population ρ_{33} is due to equal parts from the linear and quadratic contributions to the excitation. For a function of the form $y = ax + bx^2$ this is equal to the point $x = \frac{a}{b}$. On a log-log scale, i.e., in a plot of $\log y$ vs. $\log x$ the “knee” position is the point at which the slope of the graph is equal to 1.5, as can easily be seen from

$$\left. \frac{d \log y}{d \log x} \right|_{x=\frac{a}{b}} = \left. \frac{a + 2bx}{a + bx} \right|_{x=\frac{a}{b}} = \frac{3}{2}. \quad (\text{C.15})$$

Applying the definition of Eq. (C.15) to the two fits to the numerical data (Eqs. (C.13) and (C.14)), gives that the knee position for $\rho_{33}^{(1)}$ is at $n_b^{\text{knee},1} = 0.0704$, and

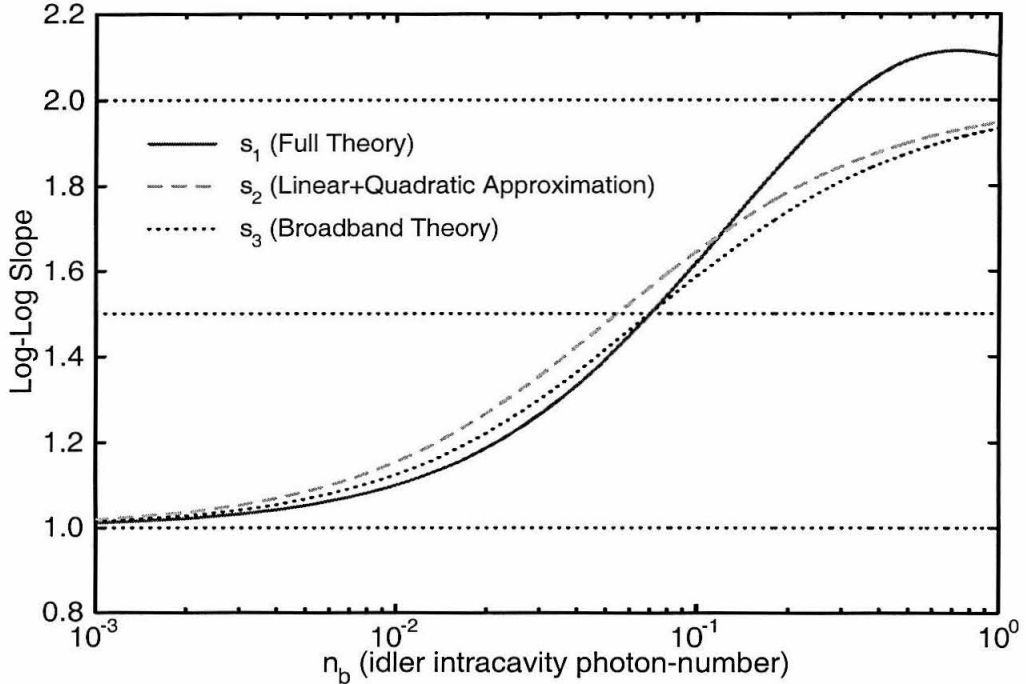


Figure C.2: Log-log slope $\frac{d \log \rho_{33}}{d \log n_b}$ as a function of the idler intracavity photon-number n_b . a) Slope of $\rho_{33}^{(1)}$ (solid line); b) slope of $\rho_{33}^{(2)}$ (dashed line); c) slope of ρ_{33}^{FD} ($\eta \ll 1$) (dotted line).

for $\rho_{33}^{(2)}$ at $n_b^{knee,2} = 0.0546$. These values of n_b can be converted to values of gain, G_s , corresponding to what we measure experimentally, by the use of Eqs. (A.27) and (C.12) which relate the two via

$$G_s = \left(\frac{(\kappa_a + \kappa_b)}{\kappa_a} n_b + 1 \right)^2. \quad (\text{C.16})$$

Hence, for the parameters of our experiment, we conclude that the model $\rho_{33}^{(1)}$ predicts gain $G_s^{knee,1} = 1.33$ at the “knee” point (which is very close to the value predicted from the theory of Ficek and Drummond; see Sec. 6.3), and the model $\rho_{22}^{(2)}$ gain $G_s^{knee,2} = 1.25$.

To elaborate somewhat further, we note that the log-log slope for $\rho_{33}^{(1)}$ is given

explicitly by

$$s_1 \equiv \frac{d \log \rho_{33}^{(1)}}{d \log n_b} = \frac{\alpha + 2\beta n_b - \beta\gamma \left(2 - \frac{n_b}{\delta}\right) n_b e^{-\frac{n_b}{\delta}}}{\alpha + \beta n_b - \beta\gamma n_b e^{-\frac{n_b}{\delta}}}, \quad (\text{C.17})$$

and for the $\rho_{33}^{(2)}$ by

$$s_2 \equiv \frac{d \log \rho_{33}^{(2)}}{d \log n_b} = \frac{\alpha' + 2\beta' n_b}{\alpha' + \beta' n_b}. \quad (\text{C.18})$$

For the parameters α , β , γ , δ , α' and β' shown in Fig. C.1, appropriate for the numerical data describing our experiment, the two slopes s_1 and s_2 are shown in Fig. C.2 as a function of n_b . The slope s_2 of the linear plus quadratic model varies smoothly, as expected, between the values of 1 and 2. The physical interpretation of this behavior is, of course, that for small enough excitation intensities (i.e., small n_b) the excitation rate is asymptotically linear (slope of 1), while for large n_b we approach the classical regime where the slope is 2 and the excitation probability scales quadratically with intensity. On the other hand, the more accurate description of the numerical data by $\rho_{33}^{(1)}$ has a slope that also starts at 1 for small enough intensities and approaches 2 for large intensities, but there is also a region where it “overshoots” and exhibits slopes bigger than 2.

For completeness, in Fig. C.2 we also show the slope of the broadband theory, as calculated by Ficek and Drummond.[44, 45] In particular, Ficek and Drummond have shown that in the broadband theory, the excited state population is given by

$$\rho_{33}^{FD} (\eta \ll 1) \simeq v^2 (\theta) \frac{\gamma_{21}}{\gamma_{32}} \left[\left(1 + \frac{\gamma_{32}}{\gamma_{21}}\right) N^2 + N \right], \quad (\text{C.19})$$

see Eq. (23) in Ref. [45]. Here, for simplicity, we assume that the coupling efficiency η is the same as the parameter $v(\theta)$ by Ficek and Drummond. In addition, because the theory of Ficek and Drummond is a broadband theory, we assume that $N \sim 4 \frac{\kappa_a + \kappa_b}{\kappa_a} n_b$ (which can be obtained from Eqs. (C.4) and (C.12) by assuming that $n_b \ll 1$) and hence, the log-log slope is given by

$$s_3 \equiv \frac{d \log [\rho_{33}^{FD} (\eta \ll 1)]}{d \log n_b} \simeq \frac{8 \left(\frac{\kappa_a + \kappa_b}{\kappa_a}\right) \left(1 + \frac{\gamma_{32}}{\gamma_{21}}\right) n_b + 1}{4 \left(\frac{\kappa_a + \kappa_b}{\kappa_a}\right) \left(1 + \frac{\gamma_{32}}{\gamma_{21}}\right) n_b + 1}, \quad (\text{C.20})$$

which is shown in Fig. C.2. Solving as before for the knee point (i.e., setting $s_3 = 1.5$) gives that $n_b = 0.0700$ and hence, $G_s = 1.33$.

Appendix D Effect of Detunings on the “Knee” Position in the Nonclassical Two-Photon Excitation Experiment

In an attempt to investigate in more detail the effects of detunings in the nonclassical two-photon excitation experiment described in Ch. 5 and 6, A. S. Parkins has carried out numerical calculations with parameters close to the experimental settings. Here, the results of these calculations are briefly outlined.

There are two detunings in the problem that can affect the two-photon excitation rate. First there is the δ_{21} detuning defined to be

$$\delta_{21} \equiv \omega_{21} - \omega_a, \quad (\text{D.1})$$

and then there is the δ_{32} detuning, similarly defined by

$$\delta_{32} \equiv \omega_{32} - \omega_b. \quad (\text{D.2})$$

Here, ω_{21} and ω_{32} are the eigenfrequencies of the $|1\rangle \rightarrow |2\rangle$ and $|2\rangle \rightarrow |3\rangle$ transitions, respectively, and ω_a and ω_b are the frequencies of the signal and idler modes of the OPO that drive these two transitions.

The results from the numerical integration of the master equation of the system are shown in Table D.1. Here, the master equation given by Eq. (C.1) is integrated for each set of detunings (δ_1, δ_2) for a series of different values of ε to produce the excited state population ρ_{33} as a function of n_b , which is calculated from Eq. (C.12). The “knee” point n_b^{knee} is then defined to be the point at which the log-log slope is equal to 1.5 and from this value the gain at the “knee” point is calculated using Eq. (C.16). Except for the detunings, the rest of the parameters used here are the same

as in Sec. C.3, which correspond to the experimental conditions.

| $\delta_{21} (MHz)$ | $\delta_{32} (MHz)$ | n_b^{knee} | G_s^{knee} | $\rho_{33}^{knee} (\times 10^{-8})$ |
|---------------------|---------------------|--------------|--------------|-------------------------------------|
| 0.0 | 0.0 | 0.0695 | 1.326 | 14.70 |
| 1.0 | 0.0 | 0.0646 | 1.301 | 9.76 |
| 0.0 | 1.0 | 0.0627 | 1.292 | 9.62 |
| 0.5 | 0.5 | 0.0633 | 1.295 | 9.71 |
| 1.0 | 1.0 | 0.0510 | 1.235 | 4.24 |
| -1.0 | 1.0 | 0.0721 | 1.339 | 15.0 |
| 1.0 | -1.0 | 0.0721 | 1.339 | 15.0 |
| -2.0 | 2.0 | 0.0809 | 1.384 | 16.0 |
| -3.0 | 3.0 | 0.0949 | 1.456 | 17.3 |
| -5.0 | 5.0 | 0.1330 | 1.663 | 19.1 |

Table D.1: “Knee” position and detunings: data from numerical integration of the master equation for two-photon excitation with nonclassical fields.

Bibliography

- [1] Z. Ficek and P. D. Drummond, *Physics Today* **50**, 34 (1997).
- [2] N. Ph. Georgiades, C. J. Hood, Q. A. Turchette, H. J. Kimble and A. S. Parkins, to be submitted in *Phys. Rev. A* (1997).
- [3] E. S. Polzik, J. Carri and H. J. Kimble, *Phys. Rev. Lett.* **68**, 3020 (1992).
- [4] E. S. Polzik, J. Carri and H. J. Kimble, *Appl. Phys. B* **55**, 279 (1992).
- [5] E. L. Raab, M. Prentiss, A. Cable, S. Chu and D. Pritchard, *Phys. Rev. Lett.* **59**, 2631 (1987).
- [6] C. Monroe, W. Swann, H. Robinson and H. C. Wieman, *Phys. Rev. Lett.* **65**, 1571 (1990).
- [7] N. Ph. Georgiades, E. S. Polzik and H. J. Kimble, *Opt. Lett.* **19**, 1474 (1994).
- [8] For a summary of spectroscopic measurements in optical lattices, see *Phys. Today* **46**(6), 17 (1993).
- [9] C. Tai, W. Happer and R. Gupta, *Phys. Rev. A* **12**, 723 (1975).
- [10] M. Zhu, C. W. Oates and H. J. Hall, *Opt. Lett.* **18**, 1186 (1993).
- [11] R. W. Fox, S. L. Gilbert, L. Hollberg and J. H. Marquardt, *Opt. Lett.* **18**, 1456 (1993).
- [12] M. J. Collet and R. Loudon, *J. Opt. Soc. Am.* **B4**, 1525 (1987).
- [13] H. J. Kimble, in *Fundamental Systems in Quantum Optics*, eds. J. Dalibard, J. M. Raimond and J. Zinn-Justin (Elsevier Science, Amsterdam, 1992).
- [14] G. J. Milburn, *Optica Acta* **31**, 671 (1984).

- [15] G. J. Milburn Phys. Rev. A **34**, 4882 (1986).
- [16] C. W. Gardiner, Phys. Rev. Lett. **56**, 1917 (1986).
- [17] A. S. Parkins, in *Modern Nonlinear Optics*, edited by M. Evans and S. Kielich (J. Wiley, New York, 1993), Vol. 2, pp. 607-666.
- [18] R. Vyas and S. Singh, Phys. Rev. A **45**, 8095 (1992).
- [19] H. J. Carmichael, A. S. Lane and D. F. Walls, Phys. Rev. Lett. **58**, 2539 (1987).
- [20] A. S. Parkins, Phys. Rev. A **42**, 6873 (1990).
- [21] S. Swain, Phys. Rev. Lett. **73**, 1493 (1994).
- [22] S. Swain and P. Zhou, Phys. Rev. A **52**, 4845 (1995).
- [23] C. M. Savage and D. F. Walls, Phys. Rev. Lett. **57**, 2164 (1996).
- [24] A. S. Parkins, Phys. Rev. A **53**, 2893 (1996).
- [25] A. S. Parkins and C. W. Gardiner, Phys. Rev. A **40**, 2534 (1989).
- [26] M. V. Satyanarayana, P. Rice, R. Vyas and H. J. Charmichael, J. Opt. Soc. Am. B **6**, 228 (1989).
- [27] M. A. Marte, H. Ritsch and D. F. Walls, Phys. Rev. Lett. **61**, 1093 (1988).
- [28] P. R. Rice, X. S. Yin, J. Walden, J. Geabanacloche, L. M. Pedrotti and J. E. Mullen, Phys. Rev. A **50**, 4176 (1994).
- [29] C. Ginzler, R. Schack and A. Schenzle, J. Opt. Soc. Am B **8**, 1704 (1991).
- [30] M. A. M. Marte and D. F. Walls, Phys. Rev. A **37**, 1235 (1988).
- [31] Z. Ficek, W. S. Smyth and S. Swain, Phys. Rev. A **52**, 4126 (1995).
- [32] Z. Ficek and B. J. Dalton, Opt. Comm. **102**, 231 (1993).
- [33] J. I. Cirac and L.L. Sanchezsoto, Phys. Rev. A **42**, 3051 (1990).

- [34] T. A. B. Kennedy and D. F. Walls, *Phys. Rev. A* **42**, 3051 (1990).
- [35] A. S. Parkins and C. W. Cardiner, *Phys. Rev. A* **40**, 3796 (1989).
- [36] P. R. Rice and L. M. Pedrotti, *J. Opt. Soc. Am B* **9**, 2008 (1992).
- [37] W. S. Smyth and S. Swain, *Phys. Rev. A* **53**, 2846 (1996).
- [38] R. Graham, D. F. Walls and W. P. Zhang, *Phys. Rev. A* **44**, 7777 (1991).
- [39] Z. M. Zhang, L. Xu and J. L. Chai, *Phys. Lett A* **151**, 65 (1990).
- [40] G. S. Agarwal and R. R. Puri, *Phys. Rev. A* **41**, 3782 (1990).
- [41] S. Smart and S. Swain, *Phys. Rev. A* **45**, 6862 (1992).
- [42] J. Geabanacloche, *Phys. Rev. Lett.* **62**, 1603 (1989).
- [43] H. Javanainen and P. L. Gould, *Phys. Rev. A* **41**, 5088 (1990).
- [44] Z. Ficek and P. D. Drummond, *Phys. Rev. A* **43**, 6247 (1991).
- [45] Z. Ficek and P. D. Drummond, *Phys. Rev. A* **43**, 6258 (1991).
- [46] S. Smart and S. Swain, *J. Mod. Opt.* **40**, 1939 (1993).
- [47] S. Smart and S. Swain, *J. Mod. Opt.* **41**, 1055 (1994).
- [48] N. Ph. Georgiades, E. S. Polzik, K. Edamatsu, H. J. Kimble and A. S. Parkins, *Phys. Rev. Lett.* **75**, 3426 (1995).
- [49] K. Edamatsu, N. Ph. Georgiades, H. J. Kimble and A. S. Parkins, *Prog. Cryst. Growth and Charact. of Mater.* **33**, 335 (1996).
- [50] Caltech Quantum Optics homepage on the world wide web:
<http://www.cco.caltech.edu/~qoptics>.
- [51] Quentin Turchette, Ph.D. Thesis, Caltech (1997).
- [52] M. Stephens and C. Wieman, *Phys. Rev. Lett.* **72**, 3787 (1994).

- [53] K. Lindquist, M. Stephens and C. Wieman, *Phys. Rev. A* **46**, 4082 (1992).
- [54] K. E. Gibble, S. Kasapi and S. Chu, *Opt. Lett.* **17**, 526 (1992).
- [55] K. Libbrecht and J. L. Hall, *Rev. Sci. Instrum.* **64**, 2133 (1993).
- [56] A. L. Migdall, J. V. Prodan and W. D. Phillips, *Phys. Rev. Lett.* **54**, 2596 (1985).
- [57] O. S. Heavens, *J. Opt. Soc. Am.* **51**, 1058 (1961).
- [58] B. Cagnac, G. Grynberg and F. Biraben, *J. Physique France*, **34**, 845 (1973).
- [59] G. Grynberg and B. Cagnac, *Rep. Prog. Phys.* **40**, 791 (1977).
- [60] *Quantum Electronics*, Ch.6, A. Yariv, 3rd ed., Wiley, (1989).
- [61] H. Kofermann, *Nuclear Moments*, New York, Academic Press (1958).
- [62] L. Armstrong, *Theory of the hyperfine structure of free atoms*, New York, Wiley-Interscience (1971).
- [63] I. I. Sobelman, *Atomic spectra and radiative transitions*, 2nd ed., Berlin; New York: Springer-Verlag, (1992).
- [64] *Optical Resonance and Two-Level Atoms*, L. Allen and J. H. Eberly, p. 69, Dover Publications, Inc. (1975).
- [65] *See special issue on OPO's*, *JOSA B* **10**, No. 9 and No. 10 (1993).
- [66] *See special issue on squeezed states of light*, *JOSA B* **4** (1987).
- [67] *See special issue*, *J. of Mod. Opt.* **34** (1987).
- [68] *See special issue on quantum noise reduction in optical systems*, *Appl. Phys. B* **55** (1992).
- [69] Z. Y. Ou and H. J. Kimble, *Opt. Lett.* **18**, 1053 (1993).

- [70] Z. Y. Ou, S. F. Pereira, E. S. Polzik and H. J. Kimble, *Opt. Lett.* **17**, 640 (1992).
- [71] H. Mabuchi, E. S. Polzik, H. J. Kimble, *JOSA B* , **11**, 2023 (1994).
- [72] R. W. P. Drever, J. L. Hall, F. V. Kowalski, J Hough, G. M. Ford, A. J. Munley and H. Ward, *Appl. Phys. B* **31**, 97 (1983).
- [73] S. Schiller, S. Kohler, R. Paschotta and J. Mlynek, *Appl. Phys. B* **60**, S77-S88 (1995).
- [74] K. Schneider, Ph.D. Thesis (Diplomarbeit), Ch. 2, University of Konstanz (1995).
- [75] H. P. Yuen and V. W. S. Chan, *Opt. Lett.* **8**, 177 (1983).
- [76] G. L. Abbas, V. W. S. Chan and T. K. Yee, *Opt. Lett.* **8**, 419 (1983).
- [77] B. R. Mollow, *Phys. Rev.* **175**, 1555 (1968).
- [78] L. Montanet, R. M. Barnett, D. E. Groom, T. G. Trippe, C. G. Wohl B. Armstrong, G. S. Wagman, H. Murayama, J. Stone, et al., *Review of Particle Properties*, *Phys. Rev. D* **50**, 1275, Part I, (1994).
- [79] Private communication with A. S. Parkins.
- [80] M. J. Collet, R. Loudon and C. Gardiner, *J. of Mod. Optics* **34**, 881 (1987).
- [81] C. Gardiner and A. S. Parkins, *Phys. Rev. A* **50**, 1792 (1994).
- [82] M. W. Noel and C. R. Stroud, *Phys. Rev. Lett.* **75**, 1252 (1995).
- [83] L. Zou, V. Kleman, X. Li, S. P. Lu, K. Trentelman, and R. J. Gordon, *Science* **270**, 77 (1995).
- [84] D. W. Schumacher, F. Weihe, H. Q. Muller and P. H. Bucksbaum, *Phys. Rev. Lett.* **73**, 1344 (1994).

- [85] M. Shapiro and P. Brumer, Institute of Physics Conference Series, **154**, 231 (1997).
- [86] M. O. Scully, S-Y. Zhu, A. Gavridiles, Phys. Rev. Lett. **62**, 1033 (1989).
- [87] A. Imamoglu, S. E. Harris, Opt. Lett. **14**, 1344 (1989).
- [88] A. S. Zibrov, M. D. Lukin, D. E. Nikonov, L. Hollberg, M. O. Scully, V. L. Velichansky, H. G. Robinson, Phys. Rev. Lett., **75**, 1499 (1995).
- [89] G. G. Padmabandu, G. R. Welch, I. N. Shubin, E.S. Fry, D. E. Nikonov, M. D. Lukin and M. O. Scully, Phys. Rev. Lett. **76**, 2053 (1996).
- [90] S. Y. Zhu, L. M. Narducci and M. O. Scully, Phys. Rev. A, **52**, 4791 (1995); C. Mavroyannis, Phys. Rev. A, **46**, R6785 (1992).
- [91] S. E. Harris, Phys. Rev. Lett. **70**, 552 (1993).
- [92] G. S. Agarwal, Phy. Rev. Lett. **71**, 1351 (1993).
- [93] S. E. Harris, Phys. Rev. Lett. **72**, 52 (1994).
- [94] S. E. Harris Phys. Rev. Lett. **77**, 5357 (1996).
- [95] *For a review see* S. E. Harris, Phys. Today, p. 36, July (1997), *and references therein.*
- [96] A. S. Zibrov, M. D. Lukin, L. Hollberg, D. E. Nikonov, M. O. Scully, H. G. Robinson and V. L. Velichansky, Phys. Rev. Lett., **76**, 3935 (1996).
- [97] M. O Scully and S. Y. Zhu, Opt. Comm. **87**, 134 (1992).
- [98] P. Zhou and S. Swain, Phys. Rev. Lett. **78**, 832 (1997).
- [99] H. Schmidt and A Imamoglu, Opt. Lett. **21**, 1936 (1996).
- [100] G. S. Agarwal and W. Harshawardhan, Phys. Rev. Lett. **77**, 1039 (1996).
- [101] Z. F. Luo and Z. Z. Xu, J. of Phys. B **27**, 217 (1994).

- [102] N. Ph. Georgiades, E. S. Polzik and H. J. Kimble, *Opt. Lett.* **21**, 1688 (1996).
- [103] N. Ph. Georgiades, E. S. Polzik and H. J. Kimble, *Phys. Rev. A* **55**, 1605 (1997).
- [104] V. Balanchet, c. Niclole, Mohamet-Aziz Bouchene and Bertand Girard, *Phys. Rev. Lett.* **78**, 2716, (1997).
- [105] N. Ph. Georgiades, E. S. Polzik and H. J. Kimble, “*Quantum Interference in Two-Photon Excitation: Part I. Weak-Field Excitation*”, submitted for publications in *Phys. Rev. A* (1997).
- [106] N. Ph. Georgiades, E. S. Polzik and H. J. Kimble, “*Quantum Interference in Two-Photon Excitation: Part II. Non-Perturbative Solution*”, submitted for publications in *Phys. Rev. A* (1997).
- [107] M. Sargent III, S Ovadia, M. H. Lu, *Phys. Rev. A* **32**, 1596, (1985).
- [108] W. H. Louisell, *Quantum Statistical Properties of Radiation*, Ch. 6, Wiley Interscience (1990).
- [109] M. Born and E. Wolf, *Principle of Optics*, p. 267, Pergamon Press, 6th Edition,(1993).
- [110] Z. Ficek, B. J. Dalton and P. L. Knight, *Phys. Rev. A* **51**, 4062 (1995).
- [111] H. Carmichael, *Lecture Notes in Physics m18*, An Open Systems Approach to Quantum Optics, pp. 35-37, Springer-Verlag (1993).
- [112] M. Sargent III, S. Ovadia and M. H. Lu, *Phys. Rev. A* **32**, 1596 (1985).
- [113] A. W. Boone and S. Swain, *Quant. Opt.* **1**, 27 (1989).
- [114] K.J. McNeil and D. F. Walls, *J. Phys. A* **7**, 617 (1974).
- [115] K. J. McNeil and D. F. Walls, *J. Phys. A* **8**, 104 (1975).
- [116] Z. Chen and H. Freedhoff, *J. of Phys. B* **24**, 3373 (1991).

- [117] T. Nasreen and M. S. K. Razmi, *Phys. Rev. A* **46**, 4161 (1992).
- [118] The Feynman Lectures on Physics, Feynman, Leighton and Sands, Vol III, Ch. 3, Addison Wesley (1965).
- [119] N. Ph. Georgiades, E. S. Polzik and H. J. Kimble, “*Quantum Interference in Two-Photon Excitation with Squeezed and Coherent Fields*”, submitted for publication in *Phys. Rev. A* (1997).
- [120] B. Yurke, *Phys. Rev. A* **32**, 311 (1985).
- [121] C. M. Caves and B. L. Schumaker, in *Quantum Optics IV*, eds. J. D. Harvey and D. F. Walls (Springer-Verlag, 1986), pp 20-30.
- [122] N. Ph. Georgiades, E. S. Polzik and H. J. Kimble, “*Applications of Atomic Nonlinear Mixers*”, in preparation.
- [123] Atomic energy levels for *Li, Rb* and *Cs* are taken from the “*Atomic Energy Levels, Vols. I, II and III*” by C. E. Moore, National Bureau of Standards (US), Washington, DC (1949).
- [124] Atomic energy levels for *Na* and *K* are taken from data on the internet at <http://aeldata.phy.nist.gov/archive/el.html> by NIST.
- [125] H. Schnatz, B. Lipphardt, J. Helmcke, F. Riehle, G. Zinner, *Phys. Rev. Lett.* **76**, 18 (1996).
- [126] H. R. Telle, D. Meschede and T. W. Hänsch, *Opt. Lett.* **15**, 532 (1990).
- [127] D. Lee, and N. C. Wong, *Opt. Lett.* **17**, 13 (1992).
- [128] D. A. Van Baak and L. Hollberg, *Opt. Lett* **19**, 1586 (1994).
- [129] V.M Klementyev, Yu. A. Matyugin, and V. P. Chebotayev, *Zh. Eksp. Teor. Fiz. Pis'ma Red* **24**, 8 (1976).

- [130] D. A. Jennings, C. R. Pollock, F. R. Petersen, R. E. Drullinger, K. M. Evenson, J. S. Wells, J. L. Hall and H. P. Layer, *Opt. Lett.* **8**,136(1983).
- [131] D. J. E. Knight, *Laser Physics* **4**, 345 (1994).